



**HAL**  
open science

# Development of new methodologies for the detection, measurement and on going monitoring of ground deformation using spaceborne SAR data

Javier Duro

► **To cite this version:**

Javier Duro. Development of new methodologies for the detection, measurement and on going monitoring of ground deformation using spaceborne SAR data. Other. Université Paris-Est, 2010. English. NNT : 2010PEST1020 . tel-00638089

**HAL Id: tel-00638089**

**<https://theses.hal.science/tel-00638089>**

Submitted on 3 Nov 2011

**HAL** is a multi-disciplinary open access archive for the deposit and dissemination of scientific research documents, whether they are published or not. The documents may come from teaching and research institutions in France or abroad, or from public or private research centers.

L'archive ouverte pluridisciplinaire **HAL**, est destinée au dépôt et à la diffusion de documents scientifiques de niveau recherche, publiés ou non, émanant des établissements d'enseignement et de recherche français ou étrangers, des laboratoires publics ou privés.

**UNIVERSITÉ PARIS-EST**

**ÉCOLE DOCTORALE : MATHÉMATIQUES ET SCIENCES ET  
TECHNOLOGIES DE L'INFORMATION ET DE LA COMMUNICATION (MSTIC)**

**ALTAMIRA INFORMATION, S.A.R.L.**

**Thèse de doctorat**

**Traitement du Signal et des Images**

**JAVIER DURO**

DÉVELOPPEMENT DE NOUVELLES MÉTHODES UTILISANT LES IMAGES RSO  
SATELLITALES POUR LA DÉTECTION, LA MESURE ET LE SUIVI DES MOUVEMENTS DE  
TERRAIN

*VERSION FINAL*

*VERSION PUBLIQUE*

**Thèse dirigée par Benoît Deffontaines**

**Co-dirigée par Bénédicte Fruneau et Alain Arnaud**

12 novembre 2010

**Jury :**

President / rapporteur : Jordi J. Mallorquí

Rapporteur : Jean-Paul Xavier

Examineur : Jordi Inglada

Cette thèse de doctorat a été effectuée dans le cadre d'une convention CIFRE entre :

Laboratoire Mathématiques et Sciences et Technologies de l'Information et de la Communication (MSTIC) de l'Université Paris-Est

Directeur Robert Eymard

Adresse ENPC Aile Vicat bureau V426, 6-8 avenue Blaise Pascal

F-77454 Marne la Vallée cedex 2

Tel : +33 (0)1 64 15 38 49 - Fax : +33 (0)1 64 15 36 91

<http://www.univ-paris-est.fr/fr/-ecole-doctorale-mathematiques-et-stic-mstic/>

Altamira Information, S.A.R.L.

Directeur Alain Arnaud

Adresse Parc Technologique du Canal 10, avenue de l'Europe

F-31520 Ramonville Saint-Agne

Tel.: +33 (0)5 34 32 02 60 - Fax: +33 (0)5 34 32 02 00

<http://www.altamira-information.com>

All rights reserved. No part of the material protected by this copyright notice may be reproduced or utilized in any form or by means, electronic or mechanical, including photocopying, recording or by any other information storage and retrieval system, without written permission from the publisher: École doctorale Université Paris-Est MSTIC and Altamira Information, S.A.R.L.

# Résumé

Les techniques d'interférométrie sur réflecteurs persistants, ou points stables (PSI), sont des outils particulièrement efficaces pour le suivi des déformations du sol et offrent les avantages typiques des systèmes de télédétection radar à synthèse d'ouverture (RSO) : une large couverture spatiale combinée à une résolution relativement élevée. Ces techniques sont basées sur l'analyse d'un jeu d'images RSO acquises sur une zone donnée. Elles permettent de régler le problème de décorrélation grâce à l'identification d'éléments particuliers (au sein de la cellule de résolution) dont la rétrodiffusion radar est de haute qualité et stable sur toute une série d'interférogrammes. Ces techniques sont fort efficaces pour l'analyse de zones urbaines où les constructions constituent de bons réflecteurs avec une réflexion supérieure à celle du sol ; il en va de même pour des zones de campagne où la densité d'infrastructures est plus limitée. La technique PSI requiert un modèle temporel approximatif a priori pour la détection des déformations, bien que la caractérisation de l'évolution temporelle de la déformation soit communément l'un des objectifs des études.

Le travail réalisé porte sur une technique PSI particulière, appelée Stable Point Network (SPN), Réseau de Points Stables, qui a été totalement développée par Altamira Information en 2003. Le travail présente de manière concise les caractéristiques de la technique et décrit les principaux produits générés: carte moyenne de déformation, séries temporelles de déformation des points mesurés, et les cartes de résidu d'erreur topographique utilisées pour géocoder de façon précise les produits PSI.

Le principal objectif de cette thèse est l'identification et l'analyse des points faibles de la chaîne de traitement SPN et le développement de nouveaux outils et méthodologies pour résoudre les problèmes identifiés. Dans un premier temps, les performances de la technique SPN sont examinées et illustrées sur des cas pratiques (basés sur des sites test réels et à partir de données provenant de différents capteurs) et à l'aide de simulations.

Les principaux points faibles de la technique sont identifiés et commentés, notamment le manque de paramètres automatiques de contrôle qualité, l'évaluation de la qualité des données d'entrée, la sélection de bons points pour la mesure ainsi que l'utilisation d'un modèle fonctionnel pour le déroulement de phase (franges interférométriques) basé sur une tendance linéaire de la déformation dans le temps.

Différentes solutions sont ensuite envisagées. Nous nous intéressons tout particulièrement au contrôle qualité automatique dans la procédure de coregistration, en utilisant l'analyse du positionnement interpixel de certains points naturels, comme par exemple des pixels identifiés dans les images. L'amélioration de la sélection finale des points de mesure (carte PSI) s'obtient grâce à l'analyse de la signature du signal radar des cibles les plus puissantes présentes au sein de

l'image, afin de sélectionner uniquement le centre du lobe principal du point de mesure. D'autres développements apportent plus de robustesse dans des étapes clefs, ainsi l'analyse du rotationnel des estimations en lien étroit avec un réseau de mesures relatives, ou l'implémentation d'une méthodologie différente pour l'intégration qui peut être lancée en parallèle afin d'être comparée avec l'intégration classique. Enfin le principal inconvénient de la technique, c'est-à-dire l'utilisation d'un modèle linéaire de détection des déformations du sol fait l'objet d'un développement d'une nouvelle méthode d'ajustement qui permet des changements de tendance durant la période de temps considérée.

Ces différentes améliorations sont évaluées en utilisant des données simulées mais également avec des cas réels d'applications. La nouvelle méthodologie pour la détection de déformations du sol non linéaires a en particulier été testée sur la ville de Paris où l'on dispose d'une grande quantité de données SAR ERS1/ 2 et ENVISAT. Ces images couvrent une large période temporelle (1992 à 2008) sur laquelle des déformations non linéaires ont été répertoriées.

**Mots clés:** Télédétection, interférométrie radar à synthèse d'ouverture (InSAR), interférométrie sur réflecteurs persistants (PSI), détection de déformations du sol non linéaires.

# Abstract

Persistent Scatterer Interferometric techniques are very powerful geodetic tools for land deformation monitoring that offer the typical advantages of the satellite remote sensing SAR (Synthetic Aperture Radar) systems: a wide coverage at a relatively high resolution. Those techniques are based on the analysis of a set of SAR images acquired over a given area. They overcome the decorrelation problem by identifying elements (in resolution cells) with a high quality returned SAR signal which remains stable in a series of interferograms. These techniques have been useful for the analysis of urban areas, where manmade objects produce good reflections that dominate over the background scattering, as well as in field areas where the density of infrastructures is more limited. Typically, PSI technique requires an approximate a priori temporal model for the detection of the deformation, even though characterizing the temporal evolution of a deformation is commonly one of the objectives of any study.

This work is focused on a particular PSI technique, which is named Stable Point Network (SPN) and that it has been completely developed by Altamira Information in 2003. The work concisely outlines the main characteristics of this technique, and describes its main products: average deformation maps, deformation time series of the measured points, and the so-called maps of the residual topographic error, which are used to precisely geocode the PSI products.

The main objectives of this PhD are the identification and analysis of the drawbacks of this processing chain, and the development of new tools and methodologies in order to overcome them. First, the performances of the SPN technique are examined and illustrated by means of practical cases (based on real test sites made with data coming from different sensors) and simulated scenarios.

Thus, the main drawbacks of the technique are identified and discussed, such as the lack of automatic quality control parameters, the evaluation of the input data quality, the selection of good points for the measurements and the use of a functional model to unwrap the phases based on a linear deformation trend in time.

Then, different enhancements are proposed. In particular, the automatic quality control of the coregistration procedure has been introduced through the analysis of the interpixel position of some natural point targetslike pixels identified within the images. The enhancements in the selection of the final points of measurements (the final PSI map) come by means of the analysis of the SAR signal signature of the strong targets presented within the image, in order to select only the center of the main lobe as point of measurement. The introduction of robustness within some critical steps of the technique is done by means of the analysis of the rotational of the estimates in close loops within a network of relative measurements, and by means of the implementation of a different integration methodology, which can be ran in parallel in order to compare it with

the classical one. Finally, the main drawback of the technique, the use of a linear model for the detection of ground deformations, is addressed with the development of a new fitting methodology which allows possible change of trends within the analyzed time span.

All those enhancements are evaluated with the use of real examples of applications and with simulated data. In particular, the new methodology for detecting nonlinear ground deformations has been tested in the city of Paris, where a large stacking of ERS1/2 and ENVISAT SAR images is available. Those images are covering a very large time period of analysis during which some known nonlinear ground deformations occurred.

**Keywords:** Remote sensing, SAR interferometry (InSAR), Persistent Scatterers Interferometry (PSI), non-linear ground deformation monitoring.

# Acknowledgments

I am indebted to many people who helped me during the completion of this PhD research; without them this work would never have been possible. First of all I would like to thank my advisors at the Université Marne-la-Vallée in Paris, Benoît Deffontaines and Bénédicte Fruneau, who welcomed me in their research group; their effort and advice helped to make this PhD possible, as well as the full research team at the laboratoire géomatériaux et géologie de l'ingénieur (G2I). Furthermore, I am specially grateful to Alain Arnaud for believing and supporting this project within Altamira Information; his advice and mentorship guided this work.

I would also especially like to thank all the members of the technical staff of Altamira Information in Barcelona; they put hard work and effort into providing some of the results which illustrate this document. In particular, I am very grateful to Geraint Cooksley and Oscar Mora for the useful discussions, comments and reviews that improved this thesis. I am also especially grateful to Fifamè Koudogbo who made the final and very complete revision of the document. Thanks are also due to Erlinda Biescas for her continuous support and contributions in the processing of TerraSAR-X data and other software developments. I am also grateful to Marc Gaset and David Albiol for their great contribution in some of the processings and developments of SPN. I would also like to thank Patrick Ordoqui for his incredible contribution to the software implementation and in the design of the processing network of the company. I would like to highlight the support of other people from Altamira's technical staff: Mónica Sánchez, Javier García, Marta Agudo and Diego López.

I would also like to give special thanks to other people who helped me with the administrative tasks and with the translations to French and English: Ester Vendrell, Anne Urdiroz and Marie-Josée Banwell.

I am also grateful to other people with whom I had the good fortune of working and learning in the past: Nuno Miranda, Josep Closa, Bertrand Rogron.

Finally, I would also like to express my gratitude to my wife Verónica, not only for her continuous support, but also for her help in the final design of some of the drawings of this document.

This work was given financial support from the ANRT, under the CIFRE convention's number 20060193. The ERS/ENVISAT radar data used in this thesis were provided by the European Space Agency under contract 16702/02/ILG. The TerraSAR-X data used was within the AO MTH0263. The RADARSAT-1 is a copyright of CSA under the DELTA project.

# Contents

<b>1</b>	<b>Overview</b>	<b>1</b>
1.1	Introduction . . . . .	1
1.2	Main objective . . . . .	4
1.3	Outline of this thesis . . . . .	4
<b>2</b>	<b>Background</b>	<b>7</b>
2.1	Synthetic Aperture Radar . . . . .	7
2.1.1	Acquisition system and geometry . . . . .	7
2.1.1.1	Image Doppler centroid . . . . .	11
2.1.1.2	SAR image distortions . . . . .	13
2.1.2	The phase of the SAR signal . . . . .	15
2.1.2.1	The travel phase . . . . .	15
2.1.2.2	The reflection phase . . . . .	17
2.1.2.3	The construction phase . . . . .	17
2.2	SAR interferometry . . . . .	19
2.2.1	Phase stability conditions . . . . .	20
2.2.2	Estimation of the interferometric phase quality . . . . .	22
2.2.3	Sources of decorrelation . . . . .	22
2.2.3.1	Geometric decorrelation . . . . .	24
2.2.4	Phase unwrapping . . . . .	27
2.2.4.1	Residue-cut algorithm methods . . . . .	28
2.2.4.2	Least squares estimation techniques . . . . .	28
2.2.4.3	Other algorithms . . . . .	29

2.2.5	SAR interferometry processing steps . . . . .	29
2.2.5.1	Data extraction . . . . .	31
2.2.5.2	SAR focusing . . . . .	31
2.2.5.3	Generation of a descriptor of the illuminated ground surface . . . . .	31
2.2.5.4	Correction of the product annotation timings . . . . .	31
2.2.5.5	Image coregistration . . . . .	32
2.2.5.6	Generation of the interferogram . . . . .	34
2.2.5.7	Compensation of the orbital state vectors inaccuracies . . . . .	35
2.2.5.8	Phase unwrapping . . . . .	35
2.2.5.9	Geocoding . . . . .	35
2.3	InSAR main applications . . . . .	36
2.3.1	Digital Elevation Model generation . . . . .	36
2.3.1.1	Geometric interpretation . . . . .	37
2.3.2	Estimation of ground deformation maps . . . . .	40
2.3.2.1	Complete interferometric phase model . . . . .	41
2.3.2.2	Detection of movement . . . . .	42
<b>3</b>	<b>Persistent Scatterers Interferometry</b>	<b>47</b>
3.1	Review of PSI technology . . . . .	47
3.2	What is a PS . . . . .	48
3.2.1	Why not all targets exhibit a PS behavior? . . . . .	50
3.2.1.1	Type of reflection As it was highlighted above, different kinds of reflection can occur, as depicted in figure 3.2.2. . . . .	50
3.2.1.2	Ground object size . . . . .	51
3.2.1.3	Wavelength . . . . .	52
3.2.1.4	Radar resolution . . . . .	52
3.2.1.5	Functional models . . . . .	53
3.2.2	Estimating PS like pixels on radar images . . . . .	54
3.2.2.1	SAR amplitude stability . . . . .	54
3.2.2.2	Stacking of the interferometric coherence . . . . .	55
3.2.2.3	Other methodologies . . . . .	57

3.3	Stable Point Network technique . . . . .	58
3.3.1	Image extraction procedure . . . . .	59
3.3.2	Image selection procedure . . . . .	60
3.3.3	Image coregistration procedure . . . . .	60
3.3.4	Initial mask of PS procedure . . . . .	60
3.3.5	Stable Point Network analysis procedure . . . . .	61
3.3.5.1	Relationship establishment . . . . .	63
3.3.5.2	Estimation of the model parameters at network arcs . . . . .	63
3.3.5.3	Network integration . . . . .	65
3.3.5.4	Estimation of the Atmospheric Phase Screen (APS) . . . . .	65
3.3.5.5	Final spatial high resolution estimation of the SPN model parameters . . . . .	70
3.3.5.6	Estimation of the deformation time series . . . . .	71
3.3.6	Final selection of points of measurement . . . . .	74
3.3.6.1	Methodology for selecting good SPN points of measurement . . . . .	75
3.3.7	PS geocoding . . . . .	77
3.3.7.1	Precise geocoding procedure . . . . .	78
3.3.7.2	Example of application . . . . .	79
<b>4</b>	<b>Improvements of the SPN technique</b>	<b>83</b>
4.1	Image coregistration quality control . . . . .	83
4.1.1	Detection of super PS . . . . .	84
4.1.1.1	The impulse response function (IRF) . . . . .	84
4.1.1.2	Identification of super PSs . . . . .	87
4.1.2	Evaluation of the coregistration accuracy . . . . .	87
4.1.3	Example of application of the methodology . . . . .	89
4.2	PS-like pixel selection enhancements . . . . .	91
4.2.1	Enhancements of the initial estimation of PS . . . . .	93
4.2.1.1	Relative calibration of the images . . . . .	93
4.2.1.2	Example of application . . . . .	95
4.2.2	Final selection of PSlike pixels enhancements . . . . .	98
4.2.2.1	Origin of ambiguous SPN measurements . . . . .	98

4.2.2.2	Impact of SAR artifacts on SPN measurements . . . . .	102
4.3	SPN linear deformation improvements . . . . .	108
4.3.1	Robustness of the linear deformation pattern in time . . . . .	109
4.3.1.1	Variogram definition . . . . .	110
4.3.1.2	Estimation of the variogram per SLCs . . . . .	111
4.3.1.3	Application . . . . .	113
4.4	SPN non-linear . . . . .	116
4.4.1	Characterization of the SPN linear model fitting procedure by means of simulations . . . . .	116
4.4.1.1	Performance of the estimator in function of the noise . . . . .	118
4.4.2	SPN estimation system for non-linear deformations . . . . .	123
4.4.2.1	Example of monitoring of non-linear deformations by using a priori information: Katrina hurricane test case . . . . .	123
4.4.2.2	Guidelines for detecting possible non-linear deformation areas in SPN . . . . .	128
4.4.2.3	Advanced SPN for the automatic monitoring of non-linear deformations . . . . .	133
4.4.2.4	Application on Paris test site . . . . .	133
<b>5</b>	<b>Summary and Conclusions</b>	<b>143</b>



# Nomenclature

1-D	one-dimensional
2-D	two-dimensional
3-D	three-dimensional
ALOS	Advanced Land Observing Satellite
AOI	Area Of Interest
APS	Amospheric Phase Screen
ASCII	American Standard Code for Information Interchange
CEOS	Committe on Earth Observing Sensors
CNES	Centre National d'Etudes Spatiales
Cosmo-Skymed	Constellation of Small Satellites for Mediterranean basin Observation
CSA	Canadian Space Agency
DA	Dispersion index of the SAR amplitude
DEM	Digital Elevation Model
DIAPASON	Differential Interferometric Automated Process Applied to Survey Of Nature
DInSAR	Differential SAR Interferometry
DLR	Deutsches Zentrum für Luft- und Raumfahrt
ENVISAT	Enviromental Satellite (ESA operated)
Envisat	Environmental Satellite
ERS-1	First European Remote Sensing satellite (ESA operated)
ERS-2	Second European Remote Sensing satellite (ESA operated)
ESA	European Space Agency
FM	Frequency Modulation
GCP	Ground Control Points

InSAR	SAR Interferometry
IRF	Impulsional Response Function
ISLR	Integrated Side Lobe Ratio
JERS	Japanese Earth Resource Satellite
LOS	Line Of Sight
NASA	National Aeronautics and Space Administration
NASDA	National Space Development Agency of Japan
PRF	Pulse Repetition Frequency
PS	Persistent Scatterers
PSI	Persistent Scatterers Interferometry
PSInSAR	Permanent Scatterers technique
PSLR	Peak to Side Lobe Ratio
RADARSAT-1	Canadian radar satellite
RAW	level 0 SAR data
SAR	Synthetic Aperture Radar
SCR	Signal to Clutter Ratio
SLC	Single Look Complex or level 1 data
SNR	Signal to Noise Ratio
SP	Stable Points
SPN	Stable Point Network technique
SVD	Singular Value Decomposition
TerraSAR-X	German radar satellite
TFA	Time Frequency Analysis
UMLV	Université de Marne-la-Vallée
USGS	United States Geological Survey
UTM	Universal Transverse Mercator coordinate system

# Chapter 1

## Overview

### 1.1 Introduction

Since the 1970s, orbiting synthetic aperture radars (SAR) early missions [All83, Ela88, Co067] have proven to be a very interesting tool to reliably map the Earth's surface and acquire information about its physical properties, such as topography, morphology, roughness and the dielectric characteristics of the backscattering layer. Spaceborne SAR sensors are active systems that operate in the microwave domain (cm to dm wavelength) providing global acquisitions that are almost independent from the meteorological conditions. Consequently these systems are very suitable for operational monitoring tasks. Side-looking imaging geometry, pulse compression techniques and synthetic aperture concept are combined together in order to obtain images with a geometric resolution in the range of few meters to tens of meters.

At the end of the 1980s the first results published showed the potential of the use of spaceborne SARs as interferometers (InSAR) [Gab88, All89, Gol, Zeb86, Mas85, Pra90b]. After the launch of the European Space Agency (ESA) satellite ERS-1 [ESAa] in 1991, a large amount of SAR data suitable for interferometry became available. This was the first large scale opportunity to test all the theoretic InSAR concepts and applications, which was done with a great level of success. Availability of SAR data was ensured by the ERS-2 [ESAa] mission (replica of ERS-1 launched in 1995). The Canadian Space Agency (CSA) launched the RADARSAT-1 SAR mission in 1995 and the National Space Development Agency of Japan (NASDA) L-band SAR sensor named JERS (launched in 1992). Since the early 1990s radar interferometry has almost become an operational technique, thanks to, among other reasons, this large amount of accessible data.

Today, spaceborne SAR interferometry is recognized as a very powerful tool for mapping the Earth's land, ice and even the sea surface topography. Differential InSAR (DInSAR) is a unique method for detection and mapping of surface displacements over large temporal and spatial scales with a precision in the order of a centimeter. This is of great importance for earthquake and volcanic research, glaciology and ice sheet monitoring, studying tectonic processes, monitoring land subsidence due to mining, gas, water, and oil withdrawal, human construction activities, etc. [Mas93a, Mas93b, Zeb94, Jou95, Gol93, Pra90b].

Presently, there is a large amount of spaceborne SAR sensors, offering data sets of varying

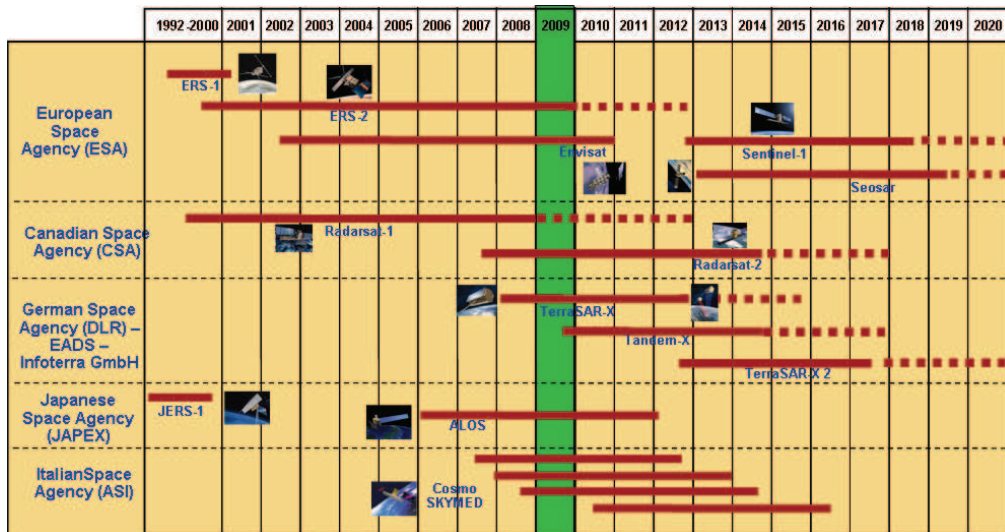


Figure 1.1.1: Most common past, present and future SAR satellite missions life span.

suitability for repeat pass interferometry. SAR images acquired at different wavelengths, with different ranges of swath coverage, resolutions and revisit times are highly accessible. See 1.1.1 for further details about the past, the present and the future SAR sensor missions life span.

The current SAR sensors offer different imaging modes with quite different characteristics. Depending on the particular conditions of the studied ground phenomena one could consider the suitability of selecting one mode or another (as well as the sensor wavelength). For example, the ScanSAR mode (Radarsat-1 and 2, ENVISAT, TerraSAR-X, ALOS) makes interferometric measurements over very large areas possible (up to 400 x 400 Km) at the cost of a decreased resolution and of a higher complexity level in the data handling and processing. Consequently, this mode appears to be very suitable for large scale monitoring, such as required for tectonics, earthquakes, glaciers motion and volcanoes.

New high resolution SAR data acquisition modes as the Spotlight (TerraSAR-X, Cosmo-SkyMed, RADARSAT-2) offers data at less than 1 meter resolution and 10 kilometers coverage. This mode is very suitable for high resolution monitoring, especially in pure urban applications where the density and the complexity of single reflectors are very high. Then, it is possible to isolate the radar response of this single reflector increasing the opportunity and the quality of the measurements and providing higher and more accurate spatial sampling of the studied phenomena.

SAR interferometry is one of the main applications of radar imagery because it fully exploits the geometric precision of the SAR systems (in the order of the sensor wavelength). The SAR images are characterized by two kind of information related to the illuminated ground surface, the amplitude and the phase. The amplitude is related with the mean power returned by each radar resolution cell. Meanwhile the phase is directly related to the travel distance of the emitted wave from the sensor to the illuminated ground surface. The principles of interferometry can be explained as a technique that compares radar images acquired over the same area at different moments in time and from slightly different point of views. By means of the analysis of the evolution of the SAR phase signal of the different acquisitions, information regarding the topographical relief and ground deformation can be extracted. These phase components are superimposed in the interferometric signal jointly with other unwelcome contributions, the most critical one being the one due to the variations in the state of the atmosphere during the image acquisition. It is

very important to detect those unwanted phase artifacts in order to avoid possible errors when interpreting the InSAR data. Nevertheless, SAR interferometry technique has two main drawbacks that must be understood completely in order to evaluate its limitations:

- The measurements are only relative: The phase information of each resolution cell does not only contain information about the travel distance. The phase information is also related to the target's physical properties and the geometric layout due to the acquisition system. The isolation of the travel distance information is possible when differentiating the phases between two passes. The subtraction is efficient only if the target properties do not change and if the observation conditions are almost similar (to have a similar radar construction phase for each resolution cell [Zeb92, Gat94]). When these conditions are met radar interferometry is a measure of differences of distances between two acquisitions [Mas93a].
- The phase measurement is ambiguous: The difference of distances measured by the interferometric signal is only the residual of this double difference modulus the signal wavelength. Then, phase unwrapping techniques must be applied in order to remove this ambiguity and to obtain absolute phase measurements [Gol, Pra90a]. However, this can be a very difficult task, especially when the quality of the interferometric signal is not good.

Finally, in late 1990s and beginning of 2000s, a new InSAR processing technique appeared based on the multi-image SAR images comparison over stable or coherent scatterers [Usa97, Usa99], called Persistent Scatterers Interferometry (PSI). The Permanent Scatterer technique was the first PSI methodology introduced in between 1999 and 2000 [Fer99a, Fer99b, Fer00, Fer01]. It is based on the fact that under certain particular acquisition conditions, some targets over the ground surface present a good and stable SAR response or backscattering [Usa97]. Then, over those particular targets (characterized by a high signal to noise ratio) and by exploiting the phase comparison over all the available data set the phase contribution due to the different natural phenomena can be isolated. In other words, the variation of the interferometric phase due to the topographical relief, the ground deformation and the different atmospheric conditions of each data take can be estimated.

Almost in parallel, some other PSI techniques appeared which consider different approaches to the problem of phase information extraction from a stacking of SAR data. Examples include the Small Baseline Approach Subset (SBAS) technique [Ber02], the Interferometric Point Target Analysis (IPTA) described in [Wer03], the Coherent Point Target (CPT) approach described in [Mor01, Mor03], and the PS's like approach described in [Hoo04] and the one described in [Ada03, Ada04] performed by the InSAR team of the DLR (German Space Agency). At the same time Altamira Information [ALT] developed its own PSI processing technique, the Stable Point Network technique (SPN) [Arn03, Dur03]. It was entirely developed by the company and it is the result of several years of research. Since 2004, Altamira Information has been exploiting the SPN technique commercially as well as in research projects within the private and public domains. During the past years, the SPN technique has been tested in a very large variety of scenarios and in some cases under very difficult conditions. Therefore the robustness and the flexibility of the chain is well known, and so are the main limitations and the constraints within the actual processing work-flow.

## 1.2 Main objective

The primary objective of this work is to study and improve the ground deformation estimation procedures based on Persistent Scatterers Interferometric (PSI) methodologies. The technical basis of the study is Altamira Information's PSI technique, the Stable Point Network (SPN) [Arn03, Dur03]. The improvements of the ground deformation estimates will be corroborated by means of the terrain validation and data interpretation performed by the Laboratoire Geomatériaux et Géologie de l'Ingénieur de l'Université de Marne-la-Vallée (UMLV).

One of the main constraints of the PSI methodologies is the need to perform a phase unwrapping. As in classical InSAR, this is one of the most problematic and risky steps when performing SAR phase measurements. In classical InSAR this is a two dimension problem. The unwrapping must be done only in space (range and azimuth direction over one interferometric pair). Meanwhile, in PSI this problem is extended to three dimensions (space + time). The bibliography lists several methodologies to deal with this problem [Gol, Zeb86, Pra90a, Mas93a], each of them with some particular benefits and drawbacks, always depending on the nature of the studied test case.

In particular, SPN is based on linear ground deformation movement modeling in order to assist the phase unwrapping step. This procedure has been demonstrated to be a very simple and robust estimator [Fer01, Mor01]. However, it becomes a big constraint when analyzing long periods of time and/or with some special ground deformation cases [ESAb], especially when it must be performed automatically, without human decisions and without any prior information about the test site.

The main goal of this PhD is to present a solution for the main constraints of SPN in order to deal with non-linear movements, especially with long time periods of analysis. In addition, the quality control parameters of the chain will be analyzed and extended in order to increase the robustness of the estimator and to reduce the human intervention within the processing workflow steps. The work will be conducted by using simulated as well as real data extracted from several different test cases. The results will be used in order to illustrate the theoretic explanations and the enhancements introduced by the new developments.

## 1.3 Outline of this thesis

This document is divided into five chapters, including this overview and the conclusion. In Chapter 2 the technical background explanations required to understand this work are reviewed. In particular, the chapter addresses the basic concepts of SAR and SAR interferometry with special emphasis on the explanation and understanding of the phase measurements. The main SAR interferometric applications are also reviewed within this chapter, jointly with the steps in order to illustrate the generation of an interferogram.

In Chapter 3 the key characteristics of the PSI processing methodologies are reviewed. An extensive analysis of what is a Persistent Scatterers and how they can be detected in SAR images is presented. The main points of the SPN processing chain are also explained within this chapter.

Chapter 4 contains the principal work of this thesis. The chapter presents the main technical improvements upon the SPN methodology which have contributed to enhance the detection and monitoring of ground deformations. These improvements can be summarized in four main points:

- Enhancements of the automatic coregistration quality control procedure based on a stacking of SAR images.
- Enhancements of the selection of the final SAR imaging pixels which are considered as good quality targets in order to give the estimated ground deformation measurements.
- Enhancements in order to increase the robustness, the precision and the quality control of the current SPN estimation methodology, but also which are very useful for the new one.
- Final and most important point, which gives the main guidelines for detecting possible non-linear ground deformation movements with SPN by means of practical examples based on simulated and real data.

Thus, a new automatic procedure is presented in order to enhance the monitoring of non-linear ground deformations by means of SPN.

The last chapter of this thesis, Chapter 5, summarizes the general results and conclusions of the presented research, which include a survey of the main limitations of SPN, and the development of new procedures to improve the robustness, the processing quality control and the PS identification. The most significant result of this work is the development of a new estimation methodology to monitor non-linear ground deformations.



# Chapter 2

## Background

Persistent scatterer interferometry is based on conventional synthetic aperture radar interferometry (InSAR). In this chapter the basic principles of SAR, classical InSAR and Differential InSAR will be explained. Only the information which is strictly necessary for a good comprehension of the interferometric technique will be given. The main InSAR applications and drawbacks will be briefly reviewed at the end of the chapter. An extensive list of references are suggested for further readings on SAR systems and its applications.

### 2.1 Synthetic Aperture Radar

In this section the basis of Radar and Synthetic Aperture Radar (SAR) will be introduced and discussed. Special emphasis will be put regarding the acquisition system and geometry and the understanding of the signal phase. For further explanation of Radar and in particular of SAR a lot bibliographic information can be found, as for example [Cum05, Cur91, Ela88, Fra99, Mas08, Sch93]

#### 2.1.1 Acquisition system and geometry

Spaceborne SARs are active systems on board satellites which illuminate the Earth's surface with a series of microwave pulses in a side-looking geometry, as depicted in figure 2.1.1. While the sensor is moving through its orbital path it transmits microwave pulses at the rate of the Pulse Repetition Frequency (PRF). The emitted signal interacts with the elements of the Earth's surface and part of this energy is backscattered towards the satellite. The echoes from each emitted pulse are received via the same antenna. Two different scanning mechanism are performed:

- Each transmitted pulse sweeps across the swath (across track or range direction) at the velocity of  $c/\sin\theta_i$ . Being  $c$  the light velocity and  $\theta_i$  the local wave incidence angle (oblique geometry).

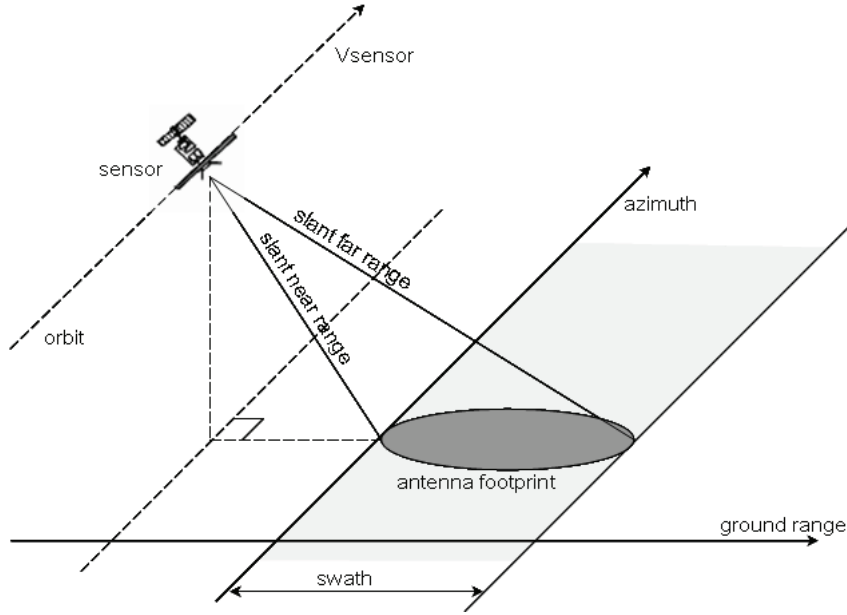


Figure 2.1.1: Illustration of the spaceborne SAR system acquisition geometry.

- Simultaneously the ground surface is scanned in the along track (or azimuth direction) while the antenna footprint is moving at a rate given by the ground velocity  $v_g$  (which depends on the sensor orbit velocity  $v_s$ , the geometry and the rotation of the Earth).

The time scales of these two scanning mechanisms are very different (of about several orders of magnitude). Then, it can be considered that they are both mutually independent. It is important to highlight that the tuning of the PRF is a crucial parameter during the system design as it allows to assume that each received echo signal is the response to a single transmitted pulse.

By this way, the received echoes are arranged side-by-side resulting in a two dimension data matrix, as depicted in figure 2.1.2. The range direction is characterized by the radar principle. The resolution is governed by the duration of the transmitted pulse  $\tau_P$ . Meanwhile, in azimuth the resolution is limited by the antenna footprint size, which is in the order of several kilometers in azimuth and range. The expressions for the range and the azimuth resolution can be found in equations 2.1.1 and 2.1.2.

$$range_{resolution} \approx \frac{c\tau_P}{2} \quad (2.1.1)$$

$$azimuth_{resolution} \approx \frac{R_o\lambda}{L_a} \quad (2.1.2)$$

where  $c$  is the speed of light ( $\sim 3 \cdot 10^8 m/s$ ),  $R_o$  is the slant-range distance ( $\sim 850Km$ ) and  $\lambda$  is the wavelength (few centimeters for microwave SAR systems). To achieve a good resolution it is natural to think that it would be desired to emit a pulse of short duration from a sensor with an antenna of large dimensions. However, in terms of emitted power this is completely inefficient. To generate a short signal in time a high peak power is required in emission in order to have enough energy backscattered from the ground echoes. Furthermore, to get a good resolution in azimuth an antenna of huge dimensions is necessary  $L_a$ , which is physically impossible for on board SAR spaceborne systems.

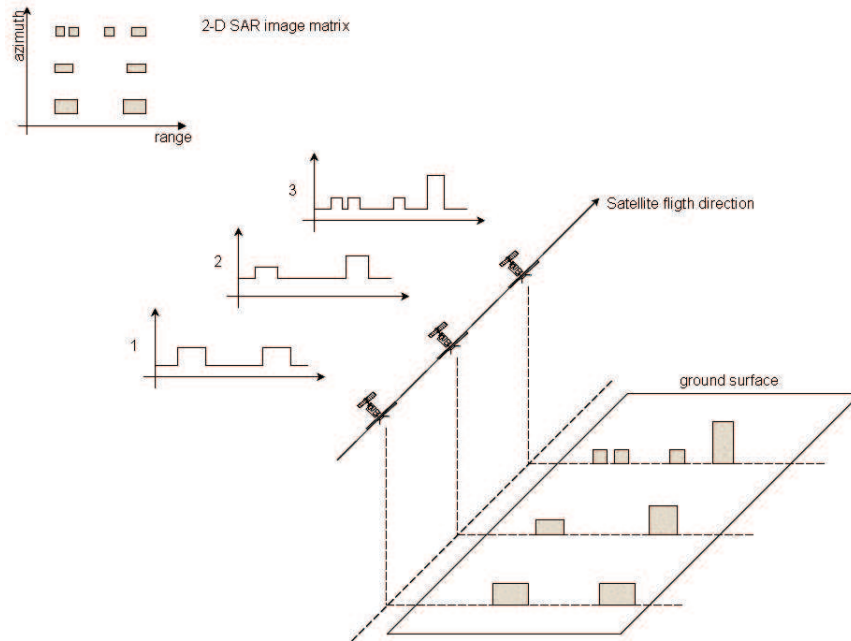


Figure 2.1.2: Illustration of the SAR imaging acquisition matrix formation.

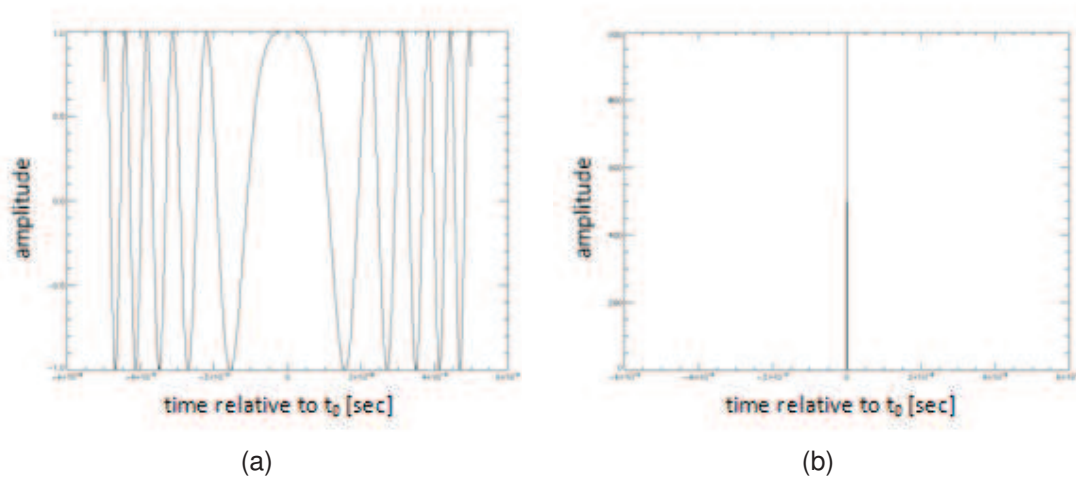


Figure 2.1.3: a) Example of real part of a chirp signal used by radar systems. b) Resulting of the ideal matched filtering applied over the signal in (a).

The solution in range is achieved by the use of long duration phase coded pulse, like for example the chirp function. Those kinds of signals are modulated in frequency, see figure 2.1.3. In other words, the signal has a frequency modulation (FM) which changes in a linear way with time, and consequently, their bandwidth is enlarged. In reception, a chirp function can be compressed to a sinc function by means of correlation with a chirp of the same frequency rate. That operation produces a narrow signal in time, hence with a large bandwidth in the frequency domain, which results in an increase of the resolution. This range compression is often the first step performed in SAR data processing workflow. The range pulse bandwidth is the parameter which have the major influence in the range resolution.

In azimuth, the increase of resolution is achieved by means of the synthetic aperture technique. The SAR images are formed by the coherent recording of the echoes, which allows for tracking the phase history of each scatterer over the extent of the sensor's trajectory. The exploitation of

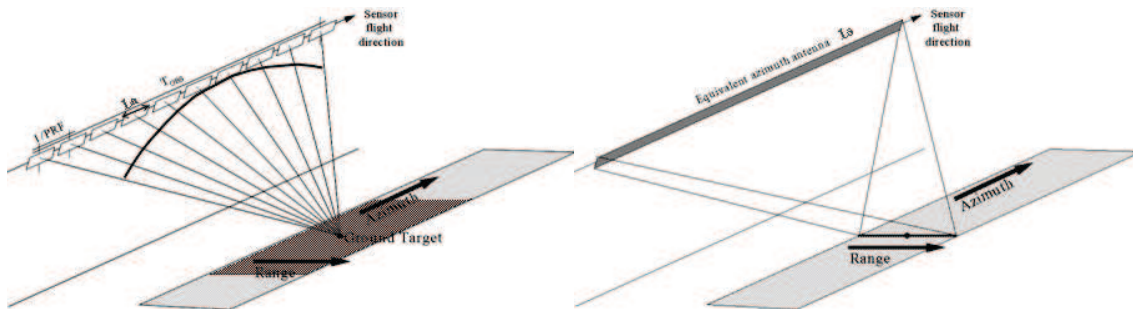


Figure 2.1.4: The principle of synthetic aperture radar. a) During the image formation each ground target is observed several times while the satellites is moving on its orbit's trajectory by a wide azimuth beamwidth related to an antenna length or aperture of  $L_a$ . b) Equivalent antenna of size  $L_s \gg L_a$  which considers the length of the sensor path during the time that a target stays within the radar beam. Since the beamwidth is inversely proportional to the antenna aperture, a synthesized large aperture is equivalent to a narrow beamwidth (to an improved azimuth resolution).

the signal phase by the subsequent image formation process can be regarded as the synthesis of an antenna with a larger azimuth extent, hence the term Synthetic Aperture Radar. In figure 2.1.4 the geometry of the principle of the synthetic aperture technique is illustrated. The echoes of the ground target are recorded by different data takes of the sensor along the orbit (sampled by the PRF). It means, from slightly different point of views and not only when the antenna swath is perpendicular to the target's line of sight with respect to the sensor velocity vector. This originates an hyperbolic evolution of the range distance between the sensor and the target through the different data takes, which is known as the target's Doppler history and is the key parameter for recovering the target's azimuth position and resolution.

At the end, as results of the several observations available of the same target the total observation time ( $T_{OBS}$  in figure 2.1.4.a) of the target is increased. Which is equivalent to say that the target is observed with a largest equivalent antenna. Thus, the synthetic aperture is shown by  $L_s$  in figure 2.1.4.b. It is the length of the sensor path during the time that a target stays within the radar beam. This length governs the amount of data which is available for processing from a given target. Then, as the beamwidth ( $\sim$  resolution) is inversely proportional to the antenna aperture, if by using signal processing it can synthesized a large aperture, the azimuth resolution can be improved by synthesizing the equivalent narrow beamwidth.

The ensemble (within a matrix) of the coherently demodulated echo signals is referred as the SAR raw data, which has a resolution of several kilometers per pixel. The high resolution SAR image is obtained by means of the compression or the focusing step, performed by means of using signal processing techniques over the raw data. Only then, the resolution increases up to some few meters. In order to compress the data in range direction the signal must be correlated with a replica of the emitted chirp. Meanwhile in azimuth direction the Doppler history of each target is exploited in order to sum coherently all the recorded complex samples of the same target. The azimuth focusing should account for the hyperbolic evolution of the azimuth phase in order to align the raw samples before the coherent summation. Figure 2.1.5 shows an example of SAR raw data before and after the focusing. For visualization purposes only the amplitude is presented. It can be observed that the raw data (left image on figure 2.1.5) is blurred, it is almost impossible to identify anything. After the focusing step, (right image on figure 2.1.5) the image becomes sharp, it is possible to identify different structures, textures and roughness due to the different ground reflexion mechanisms. The final image resolutions are governed by the formulas 2.1.3 and 2.1.4.

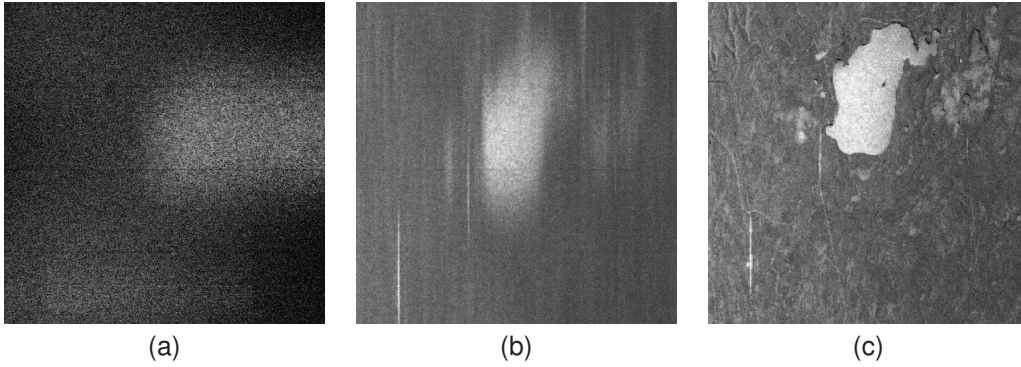


Figure 2.1.5: Illustration example of focusing SAR data with ENVISAT. a) amplitude of a level 0 image. The energy of the targets is spread over an area of several samples in the 2-D. b) amplitude of the 1-D range focused images. The targets are focused in range but still spread in azimuth. c) amplitude of the 1-D range + 1-D azimuth focused image. Finally the energy of the targets is concentrated into their properly slant-range position. This is the final level 1 detected product with the finest resolution achievable.

$$range_{resolution} = \frac{c}{2B_p} \quad (2.1.3)$$

$$azimuth_{resolution} = \frac{L_a}{2} \quad (2.1.4)$$

As it can be noticed in the formula 2.1.3 the final image resolution is related to the final pulse bandwidth ( $B_p$ ) achieved after the range de-chirping. Thanks to the use of chirp signals a large bandwidth signal can be obtained resulting in a range resolution of the order of few meters. In the azimuth direction the achieved resolution (after the compression) depends only on the size of the SAR antenna, as it can be noticed in equation 2.1.4.

As numerical example, for the C-band ENVISAT case, with an antenna size of about 10 meters and a pulse bandwidth of about 16 MHz the resulting azimuth and range resolution are of about 5 per 9 meters approximately. For the X-band TerraSAR-X German sensor which have an antenna size of 5 meters and a pulse bandwidth of 150 MHz the resulting image resolutions are of about 2.5 and 1 meters, in azimuth and slant-range respectively. However, higher resolution can be achieved with other satellite modes such as the spotlight mode (TerraSAR-X, Cosmo-Skymed, Radarsat-2) with up to 1 meter of azimuth resolution (or even less) at the cost of swath width reduction [Sue02].

After the focusing, a complex image is obtained with the SAR response of the ground for each slant-range resolution cell. The amplitude of this signal is directly related with the SAR backscattering of the ground. The higher the amplitude is the higher the total amount of power reflected from the ground. Meanwhile, the phase of the signal is mainly related with the distance covered by the wave when travelling from the sensor to the ground and backwards.

### 2.1.1.1 Image Doppler centroid

Ideally, the closest point of approach of the radar to the ground point target is in the middle of the area illuminated by the antenna. In reality, this condition is not fully accomplished for any of the spaceborne SAR missions. Typically, the attitude of the instrument is controlled in order to

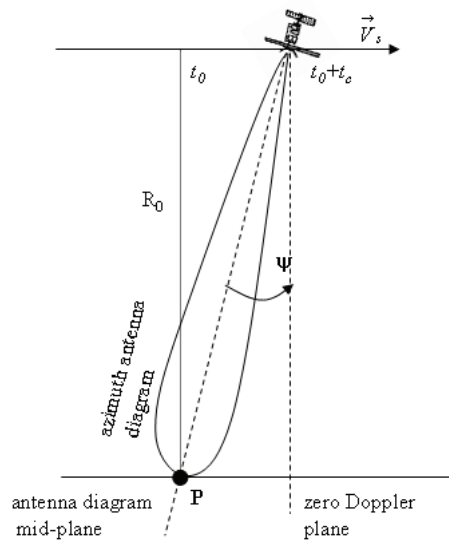


Figure 2.1.6: Illustration scheme of a backward antenna off-pointing. The squint angle  $\psi$  is defined within the plane given by the satellite flight direction vector  $\vec{V}_s$  and the point target on ground P.

minimize the deviation from the perpendicular pointing direction, which is done in adaptive way depending on the its position along the orbit. Hence, it can be found always an offset between the azimuth antenna diagram mid-plane (when the ground target is seen with the maximum gain of the azimuth antenna pattern) and the zero Doppler plane (when the target's range vector is perpendicular to the satellite flight direction), see figure 2.1.6.

The antenna pointing to the target is in correspondence with the maximum gain offered by the antenna diagram, that is the mid-plane of the antenna diagram at  $t_0 + t_c$  in figure 2.1.6. The zero Doppler plane at  $t_0 + t_c$  is also highlighted in figure 2.1.6, where all the point targets which are at closest approach at that azimuth time are located. This zero Doppler plane is orthogonal to the sensor velocity vector  $\vec{V}_s$ . Hence, the angle between the sensor to target line at mid-plane of the azimuth antenna pattern and the zero Doppler plane is defined as the squint angle  $\psi$ . Thus, the beam center time and the Doppler centroid are given by equation 2.1.5[Coo67, Sch93].

$$t_c = \frac{R_0}{\|\vec{V}_s\|} \cdot \tan\psi \tag{2.1.5}$$

$$f_{DC} = -\frac{2\|\vec{V}_s\|}{\lambda} \cdot \sin\psi$$

Aforementioned, the squint angle varies in function of the attitude of the spacecraft. It mainly depends on two of the three attitude angle, the yaw and the pitch. Their relative influence varies in function of the incidence angle (see figure 2.1.8) and in consequence the squint angle will change in range, see [Sch93, Mas08] for further details. In consequence, the squint angle characterizes the image acquisition geometry and also its spectral support. As it was stated in equation 2.1.5 a squint angle is translated into a shift in the location of the targets in the azimuth direction and into a mean Doppler centroid frequency which is not equal zero. In azimuth direction the image spectrum is centered around the zero Doppler frequency or the mean Doppler centroid value. Hence, in case of different squint angles the spectrum support of those acquisitions will be shifted resulting in non-overlapping frequential bands in extreme cases when comparing repeat passes, see figure 2.1.7. Thus, it is a very important image acquisition parameter that should be known. Although the image Doppler centroid can be computed from the sensor attitude, the obtained

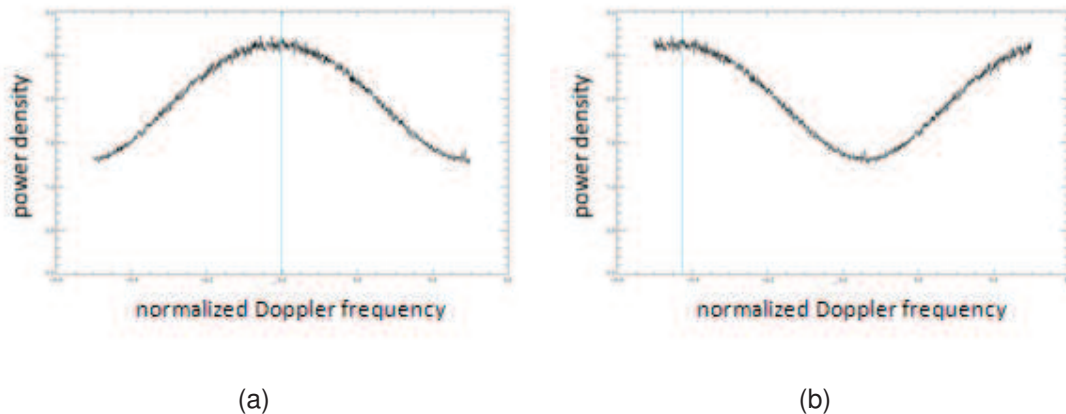


Figure 2.1.7: Doppler azimuth spectrum of two SAR images. a) case of an almost zero mean Doppler (-0.05 cycles). b) case of non-zero Doppler centroid (-0.45 cycles).

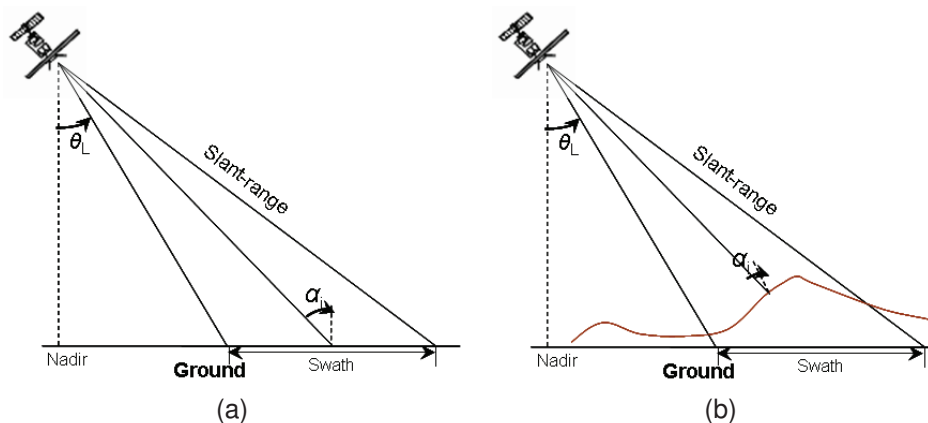


Figure 2.1.8: Side-looking observation geometry of the spaceborne SAR systems. The sampling is performed in the slant-range direction which is defined by the elevation angle  $\theta$  of the antenna. This vector incides the ground in an oblique way defined by the local incidence angle  $\alpha$ , which would depend also on the local topography. In case of flat Earth (a) the incidence angle and the elevation angle are the same. In case of topography there could be found large variations between these two values.

accuracy is often not sufficient for SAR data processing. Usually this parameters is estimated from the SAR image data itself before the SAR focusing.

### 2.1.1.2 SAR image distortions

As it was explained before, the spaceborne SAR systems send microwave pulses to the Earth's surface and receive the echoes. This is done in the range direction which is perpendicular to the flight direction of the sensor (and looking right generally). This range direction is oblique considering the Earth's surface and it is defined by the elevation angle of the antenna, see figure 2.1.8.

Thus, the echoes coming from the ground objects are distinguished between them thanks to this oblique geometry. Therefore, two objects at an identical range distance to the sensor are indistinguishable, even though they are at different places and with a different height on ground. This is the main reason why these kind of radars cannot look directly down to the ground. As the

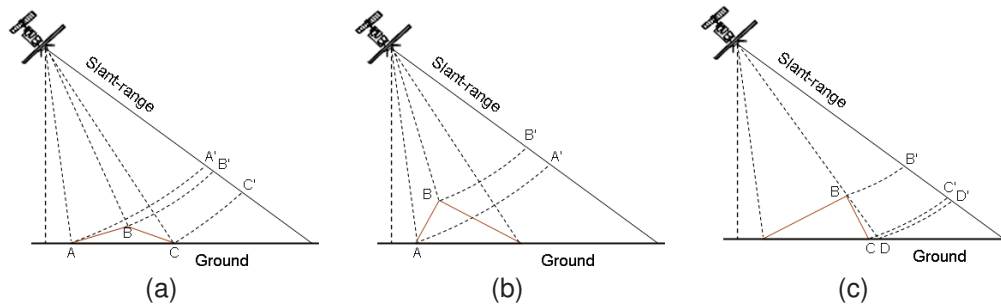


Figure 2.1.9: Main SAR geometric distortions. a) foreshortening. b) layover. c) shadow.

sensor is side-looking, the objects in the ground (defined by its distance to the nadir of the radar, see figure 2.1.8) are arranged as function of their range from the radar.

However, this side-looking geometry has some important disadvantages which arise in case of abrupt terrain. As result, SAR images present geometric distortions which must be perfectly understood. Those geometric artifacts affect their measurements, making them imposible in some cases. They can be classified into three.

### The foreshortening

It appears in the SAR images when the radar samples a topographic relief. As a result of the oblique geometry of the acquisition system the slopes of the hills oriented towards the satellite (A-B in figure 2.1.9.a) are compressed (A'-B' in figure 2.1.9.a) while the slopes oriented away from the satellite (B-C in figure 2.1.9.a) are expanded (B'-C' in figure 2.1.9.a) in SAR geometry, see figure 2.1.9.a. It means, the slopes in the front side of the hills are sampled with less pixels than the one oriented on the back side.

All the ground features thus appear to be tilted towards the satellite. The slopes facing the radar appears compressed and brighter due to the accumulation of ground reflections within the same resolution cell. Any phenomena occuring on this slope will be poorly sampled. In extreme cases, this accumulation of ground reflections from very different areas can result into an aliasing of the signal, making impossible the exploitation of the SAR measurements.

Foreshortening can be corrected under (a visual point of view) with the use of a DEM during the step of geocoding, see chapter 2.2.5.9. The appropriate geometry the slopes can be recovered by means of using interpolation procedures over the SAR amplitude once it has been projected into ground geometry.

### Layover

It is an extreme case of foreshortening. It appears when the incidence angle is smaller than the angle given by the local slope, especially in case of very steep slopes oriented towards the satellite. In that cases tops of mountains, closer to the radar, are sampled before than their basis, see figure 2.1.9.b. This results in extremely severe image distortion as the slopes in SAR images are inverted. See how the points A and B in ground geometry are sorted in an inverse way in slant-range geometry (B' and then A') in figure 2.1.9.b.

Layover cannot be corrected. The signal is completely lost because of the aliasing and the SAR measurements cannot be exploited.

### Shadow

It appears in steep slopes that do not face the satellite. In such cases there are ground areas which are not illuminated by the radar wave, see figure 2.1.9.c. As a result, there is no returned signal coming from those ground terrain regions and no measurements are possible. Those areas appear with a very low amplitude level within the radar images since no backscattered signal is received. Thus, the ground regions between the points B and D are not illuminated by the radar wave in figure 2.1.9.c. Hence, the radar samples compressed between B' and D' will present a very low amplitude level in SAR image.

## 2.1.2 The phase of the SAR signal

In general, the phase value detected by a radar imaging system is the measure of the phase difference between the emitted and the received electromagnetic wave. This magnitude is related basically to three main contributions [Arn97]:

- The travel phase : related to the distance between the antenna and the illuminated object
- The reflection phase : related to the electromagnetic interaction between the wave and the object
- The construction phase : related to the accumulated phase that arrives to the radar within every resolution cell and that is treated as a unique and single reflected echo signal

The recorded phase depends directly on the complex backscattering coefficient of the illuminated surface. It characterizes completely the electromagnetic behavior of the observed ground terrain. In consequence, it could be used for example in order to segmentate and to identify different kinds of terrain and/or land use. The capacity of measuring distance by the signal phase is also a very interesting magnitude. The possibility of detecting very small variations of this distance (below the signal wavelength) make this instrument very useful for monitoring changes in the position of the illuminated object. However, this measure is not straightforward for each single object of the ground because the basic unit of measure of the imaging radars (resolution cell  $\sim$  pixel) is very large in comparison with the used wavelength. Thus, for every pixel what is measured is the contribution of several single targets. This total signal is obtained based on the coherent addition of the returned echoes coming from every target on the ground and which slant-range position lies within the same resolution cell. The power of every echo is governed by the backscattering coefficient of every single scatterer. Hence, it is defined as the construction phase of the pixel. This principle is the responsible of the radiometric pixel noise or "speckle".

### 2.1.2.1 The travel phase

It is directly related to the physical distance between the sensor (which emits the electromagnetic wave) and the target on ground (where the wave impacts). Then, it is a purely geometric measure see figure 2.1.10,.

$$\varphi_{SAR} = \frac{2 \cdot \pi}{\lambda/2} \cdot R \quad (2.1.6)$$



Figure 2.1.10: Illustration of the travel phase detected by the radar.

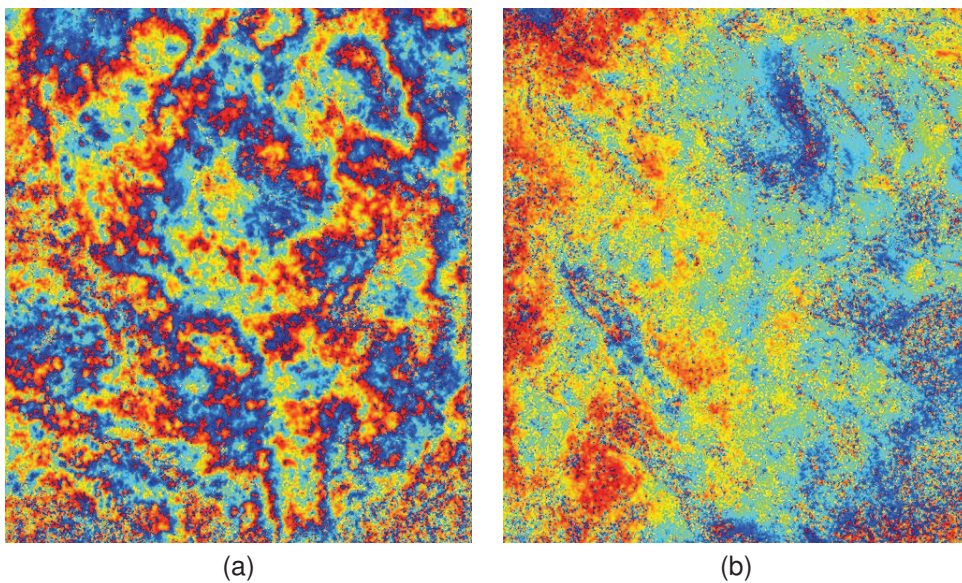


Figure 2.1.11: ENVISAT multilooked interferograms with independent acquisitions and without sensitivity to the local topography. The interferogram in (a) is presenting strong atmospheric artifacts. The variability of the phase values in space is very high, there is a lot of fluctuations between 0 and  $2\pi$  radians. The phase presented in (b) is not so fluctuating. The atmospheric affectation is not so strong as in (a). 

In case of having a unique target, plus a constant wavelength and invariant atmospheric conditions, the measure of the phase will be always the same if the object remains at the same place. In real cases there are a lot of elements reflecting the signal within the resolution cell. It could be said that the measure is related to the mean distance between a large amount of targets and the sensor. The response of the whole target can be understood as only one unique center of phase that falls at some place within the pixel.

However, this phase measure related to the physical distance could be corrupted. During this travel the electromagnetic wave is crossing several layers of the earth's atmosphere. In function of the wavelength this layers will introduce non-homogeneous delays which will be accumulated during the two way travel distance. Further details will be given regarding the impact of the atmospheric artifact on the SAR phase in future chapters. The main constrain is that it is a non-stationary and an unpredictable effect. Each SAR acquisition will have a different atmospheric artifacts which could be more or less important depending on the particular conditions of the atmospheric layers at the acquisition time, see figure 2.1.11 for an example.

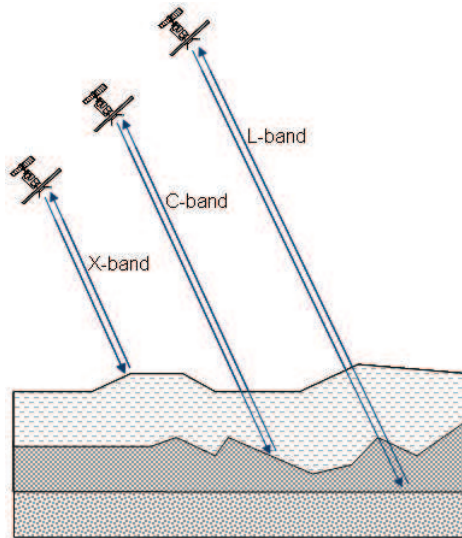


Figure 2.1.12: Different penetration of the radar signal can occur in function of the observed terrain nature and the wavelength.

### 2.1.2.2 The reflection phase

It is directly related to the dielectric properties of the object which is being illuminated by the wave, known as the backscattering coefficient of the object. This backscattering coefficient mainly depends on the nature of the material constituting the object, the local incidence angle, the wavelength, the polarization and the environmental conditions [Sch93].

In practice, it is very difficult to measure the backscattering coefficient of a single object because echoes coming from many different objects on ground are merged within a resolution cell. In addition, the reflection of the wave is not always specular. There could be found reflections at different levels as in function of the wavelength the wave can penetrate into the materials in a different way. In general, signals with large wavelengths can penetrate more than the shorter ones. For example, as it is illustrated in figure 2.1.12, for the same area one can have different backscattering when a L-band, C-band or X-band SAR system is used just because the wave comes from reflection of different layers while the earth's surface still the same.

In general, the observed surface can be interpreted as the volumetric repartition of the elementary targets with variable backscattering coefficient for each one. The SAR imaging is detecting the coherent addition of each of the targets placed within the same radar resolution cell. Then, the construction phase will disturb the measure of the real coherent backscattering coefficient of single objects presented on the scene.

### 2.1.2.3 The construction phase

It could be defined as a mean that describes the geometric distribution of the single targets on ground and the sensor. It is the resulting phase for each slant-range resolution cell due to the coherent addition of the echoes of all the elementary reflecting elements that lies within. It is the responsible of the apparent random behavior of the phase and it is impossible to model and/or to predict. It is important to notice that it is a phase measurement which does not exist physically. It has the origin on the spatial sampling that the radar performs over the ground surface.

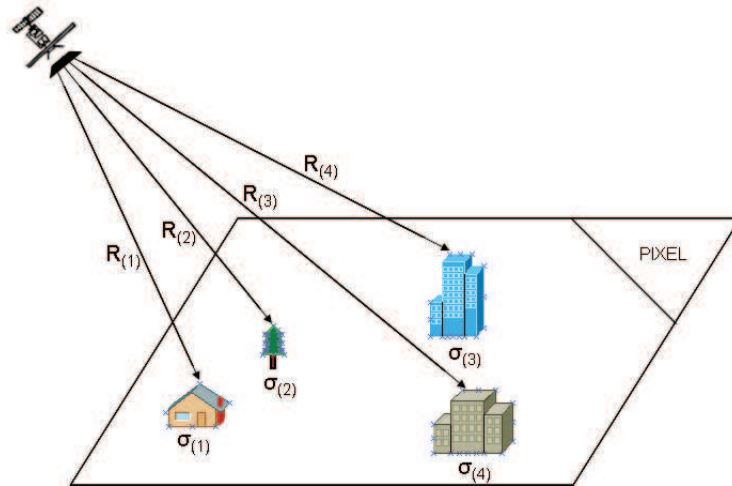


Figure 2.1.13: Every single object presented on the ground surface contributes in a coherent way in the final phase value detected by this slant-range resolution cell. The contribution of every elementary reflector is characterized by its backscattering coefficient and by its distance to the satellite.

This is illustrated in figure 2.1.13 by means of an example. In the presented radar pixel in figure 2.1.13 five single reflectors characterized under an electromagnetic point of view by their backscattering coefficient  $\sigma_i$  (coherent magnitude  $\Rightarrow$  reflection phase). Under a geometric point of view the phase for every single target is characterized by the physical distance between the sensor and the position of every single reflector on ground  $R_i$ . Then, the final measure for this slant-range pixel will be the resulting coherent addition of all the echoes returned by every single elementary reflector, see equation 2.1.7.

$$S_{pixel} = \sum_i \sigma_i \cdot e^{j2\pi \frac{R_i}{\lambda/2}} \quad (2.1.7)$$

The distribution of the single targets within the resolution cell is completely random. Considering that the size of the pixel (in the order of few meters) is larger than the signal wavelength (in the order of few centimeters) there is no way to know if the echoes of each single target are added in a constructive or in a destructive way. It must be considered that the phase signal is wrapped modulus half a wavelength, see figure 2.1.14.

In consequence the echo signal which arrives to the sensor is not directly related with the nature of the terrain. In a extreme situation, there could be found two single targets within the same pixel and presenting a strong backscattering coefficient, but which contributions are added in an opposite way in phase due to geometric reasons leading to a signal loss. This is the origin of the speckle or fluctuation of the amplitude of the SAR images [Bec63]. Due to this effect an homogeneous surface will appear in the SAR amplitude with a textures or with roughness in function of the random addition of the elementary single reflectors that are contained within every pixel, see figure 2.1.15 for an example of speckle perturbation on SAR images.

However, for a random position of the single reflectors on ground and for two consecutive acquisitions in time this SAR roughness (or speckle) should be maintained (if we consider that no physic modification has occurred on the objects). In other words, the construction phase should be the same as the geometry of acquisition between the sensor and the elementary targets on ground is kept. Then, by means of this phase difference between a repeat pass it is possible to

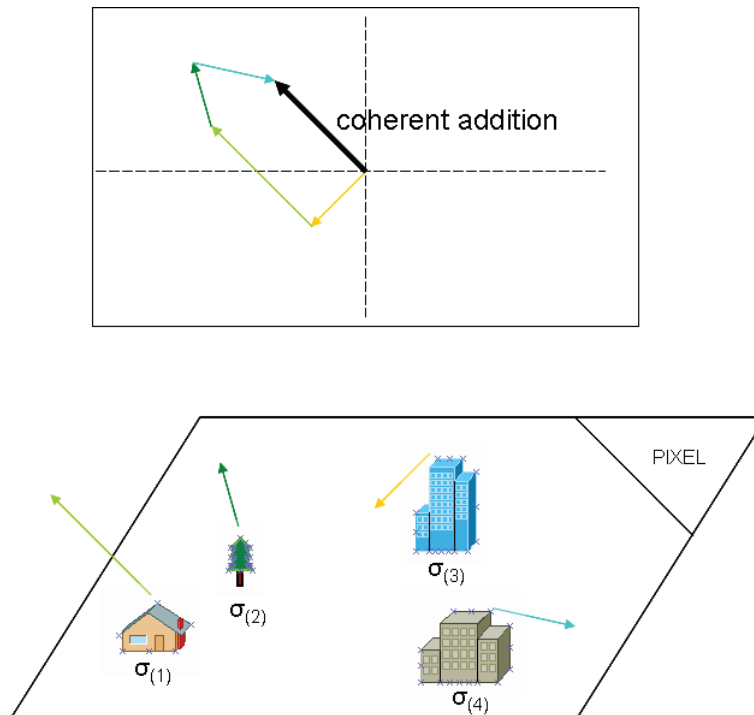


Figure 2.1.14: Each single target will contribute to the final measured pixel radar response in a different way. Every single element has its own coherent backscattering coefficient. The size of the arrow represent the returned power and the orientation the phase offset. In consequence, the final measurement will be lead by the coherent addition of all these vectors (wide black arrow on the image on top).

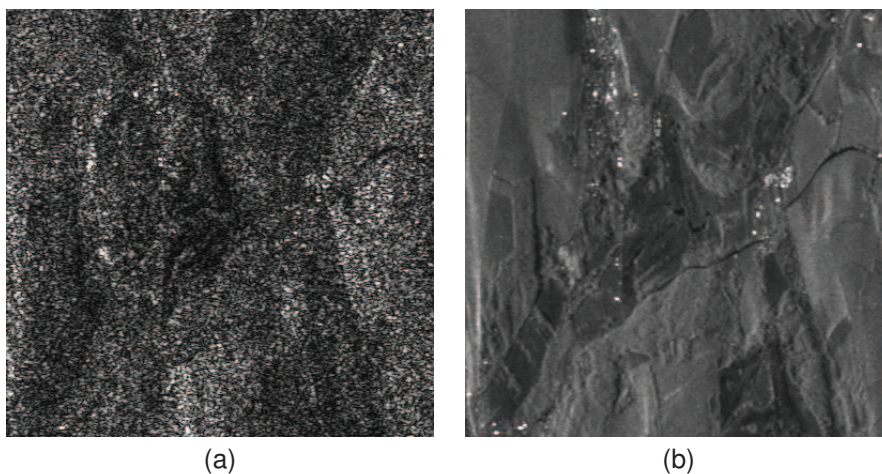


Figure 2.1.15: Example of ENVISAT amplitude image at multilook 1x1 with (a) and without speckle (b).

have access to the reflection and the travel phase. This is in fact the principles of radar interferometry.

## 2.2 SAR interferometry

SAR interferometry (InSAR) is a signal processing technique. It uses two different SAR acquisitions of the same ground surface from slightly different point of views to create an image of the phase differences. This phase difference is known as the interferogram or the interferometric phase [Gra74].

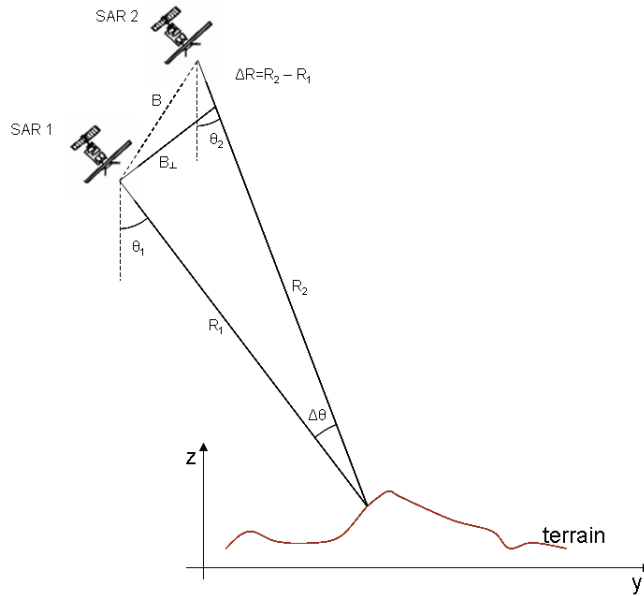


Figure 2.2.1: Geometric approach of an interferometric data pair from [Bam98].

It is desired that the two acquisitions have been taken from more or less the same orbital position. In other words, with the same view angle, approximately the same slant-range distance and at the same time of the day, see figure 2.2.1. Under this constrains the construction phase (see section 2.1.2.3) and the reflection phase (see section 2.1.2.2) will be the same for both images pixel by pixel. In consequence, it can be assumed that the phase difference between the two single acquisitions is a measure directly related to the travel phase (see section 2.1.2.1) difference, see equation 2.2.1. This phase relationship is extremely important as it determines the capacity of the InSAR technique to detect small variations of this range position of the scatterers on ground in repeat passes.

$$\phi_{ima1} = \phi_{travel1} + \phi_{reflec} + \phi_{construc} \quad (2.2.1)$$

$$\phi_{ima2} = \phi_{travel2} + \phi_{reflec} + \phi_{construc}$$

$$\phi_{interf} = \phi_{ima1} - \phi_{ima2} = \phi_{travel1} - \phi_{travel2}$$

## 2.2.1 Phase stability conditions

In general, there are two important parameters which determines the quality of the interferogram. The difference between the two data takes, under a geometric point of view, and the time separation of the two acquisitions. The main geometric parameter that characterize the interferogram is the perpendicular baseline,  $B_T$  in figure 2.2.1. This parameter defines how different the ground surface is sampled considering both data takes. If the baseline is very large the two wave's incidence angles will be very different and in consequence the construction phase of the resulting

pixel will not remain the same from one acquisition to the other, resulting in an increased noise level in the detection of the travel phase.

The same phenomenon occurs with the time separation. If the two acquisitions are taken at two separated epochs, the nature of the ground surface could change (for example, water surfaces decorrelate within tens of milliseconds) and will show no coherence in a repeat pass interferogram. Forests tend to decorrelate due to movement of leaves and branches. Of course, man-made changes such as ploughing of an agricultural area completely destroy coherence. In consequence the reflection phase will change resulting again in an increase of the noise level in the equation 2.2.1. Even if the two acquisitions are taken at different times of the same day it could be found changes in the reflection phase due to possible differences on the temperature, the soil moisture and the atmospheric conditions.

Thus, under the stationary conditions explained above it can be written the expression for the interferogram as the Hermitian product of the two complex magnitudes coming from the two SAR signals as:

$$P_{sar1} = A_{sar1} \cdot e^{j\phi_{sar1}} \quad (2.2.2)$$

$$P_{sar2} = A_{sar2} \cdot e^{j\phi_{sar2}}$$

$$P_{int} = P_{sar1} \cdot \text{conjugate}(P_{sar2}) = A_{sar1} \cdot A_{sar2} \cdot e^{j\phi_{sar1} - \phi_{sar2}}$$

Then, considering the equation 2.2.1 the final interferometric phase value can be expressed as:

$$\phi_{int} = \phi_{sar1} - \phi_{sar2} = \frac{2\pi}{\lambda/2} \cdot (R_1 - R_2) = \frac{4\pi}{\lambda} \cdot \Delta R \quad (2.2.3)$$

As it can be noticed in equation 2.2.3 the interferometric phase can be directly related with the difference of slant-range distance between one acquisition and the other, see also figure 2.2.1. It can be said that the main objective of the SAR interferometry is the detection of this slant-range change of distance between acquisitions.

The main problem is that this phase magnitude is wrapped module  $2\pi$ . As it can be observed in figure 2.2.2 the interferometric phase is estimated by means of the arc-tangent of the resulting Hermitian product of two complex magnitudes. In consequence, this estimated value is contained between  $[-\pi, \pi]$ . This phase wrapping will occur each time the slant-range difference is higher than half a wavelength (in the order of few centimeters for spaceborne systems). Therefore, the interferometric phase is extremely sensitive to the slant-range change of distances in a relative way. In order to have absolute measurements the phase should be unwrapped. In other words, the absolute phase measurement, in terms of multiples of  $2\pi$ , should be recovered. This is performed by means of the phase unwrapping techniques which will be further explained in what follows.

### 2.2.2 Estimation of the interferometric phase quality

With all the stated above it is important to measure the quality of the interferometric phase. For this purposes it is used the interferometric coherence, which is defined mathematically as the amplitude of the complex correlation coefficient of the two signals, see equation 2.2.4 [Arn03, Bam98].

$$\gamma = \frac{E \{P_{sar1} P_{sar2}^*\}}{\sqrt{E \{|P_{sar1}|^2\} E \{|P_{sar2}|^2\}}} \quad (2.2.4)$$

where  $E\{\cdot\}$  is the expected value or mean operator. In practice, expression 2.2.4 is usually approximated by the average operator on a finite number of samples [Bam98]. Then, interferometric coherence is estimated by means of the equation 2.2.5.

$$\hat{\gamma} = \frac{|\sum P_{sar1} P_{sar2}^*|}{\sqrt{\sum |P_{sar1}|^2 \sum |P_{sar2}|^2}} \quad (2.2.5)$$

where the summations are performed over a number of pixels within a window. The interferometric coherence has a value comprised between 0 and 1. As the correlation, it gives a measure of the similarity of the information in the two images. A coherence value equal to 1 indicates that the ground properties are identical in the two images, i.e. that the signal comes from the backscattering sources in the same conditions. A zero value indicates on the contrary that the two signals are completely different. Their interferometric combination is completely decorrelated and it can not be exploited, see figure 2.2.2 for an example.

An important parameter to be defined in the computation of the coherence is the number of elements to consider for the summation. The size of the window must be neither too small, otherwise the computed value would be too unstable and therefore statistically meaningless, nor too large because it can cause loss of details [Bam98]. Typically, those values are of about  $2 \times 10$  or  $3 \times 15$  pixels for ENVISAT images because it represents a sufficient number of samples for the statistical estimation of the coherence while keeping the spatial resolution in the detection of details. It is important to notice the ratio 1 : 5 in the selection of the size of the boxcar, this value makes the resulting image with a uniform spatial resolution for ENVISAT case in azimuth and range, leading to square pixels.

### 2.2.3 Sources of decorrelation

Decrease of the coherence in SAR interferometry can be caused by several effects. Temporal decorrelation is typically one of the major causes. The fact that SAR interferometry is based on repeat pass (images are taken at different epochs) leads to one of the major drawbacks, namely the temporal decorrelation [Zeb92]. It is very difficult to keep the same backscattering properties of the ground in repeat passes, as vegetation growth, climatic changes and the human presence cause all kinds of modifications in the land cover. Although, there are other imaging process that cause a loss of coherence [Zeb92, Bam98]:

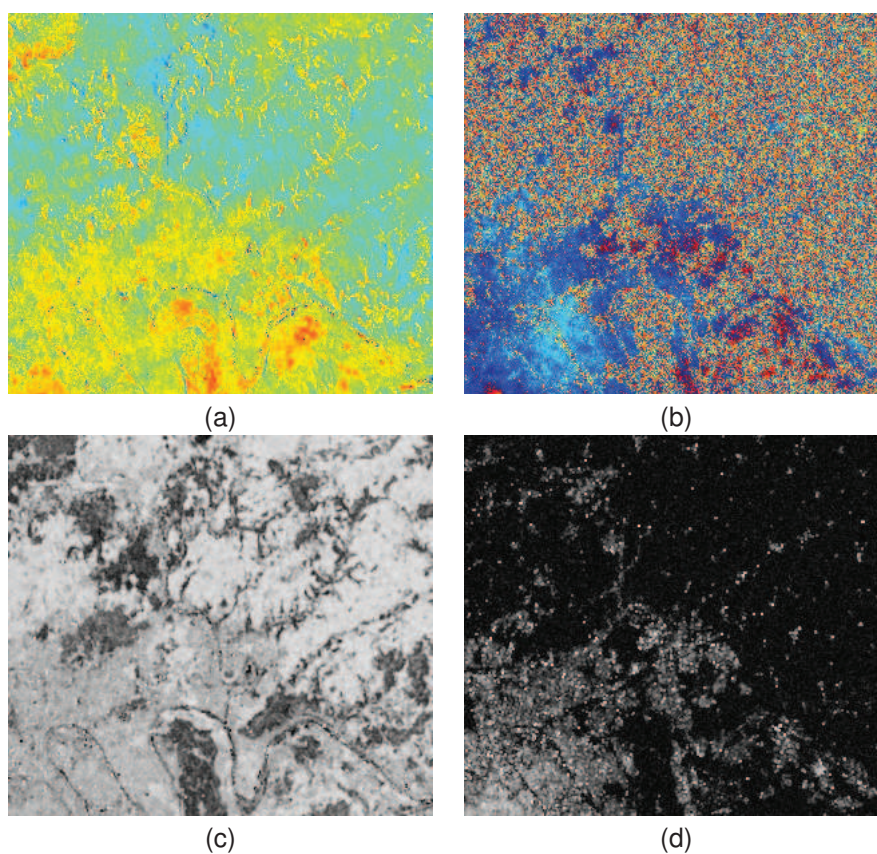


Figure 2.2.2: Example of very coherent and partially incoherent interferograms. In (a) and (c) interferometric phase and coherence detected for a very coherent interferogram (with a reduced time separation and perpendicular baseline). In (b) and (d) interferometric phase and coherence detected for the ground area for a not so coherent data pair (with a moderate large time separation and perpendicular baseline). ENVISAT images were used with a multilook of 10x2 samples in azimuth and range respectively.

- Thermal noise from the instruments
- Data processing errors
- Geometric decorrelation

Then, the interferometric coherence can be expressed in a simplified form in function of these effects as:

$$\gamma = \gamma_{SNR} \cdot \gamma_{geometric} \cdot \gamma_{temporal} \quad (2.2.6)$$

the terms of equation 2.2.6 have a magnitude of less than unity and contribute to the final phase noise.  $\gamma_{SNR}$  accounts for the decorrelation noise introduced by thermal noise added by the instrument during the data take as well as for the noise introduced during the different steps of the data processing. The term  $\gamma_{geometric}$  describes the decorrelation caused by the fact that the two SAR signal have been taken from different points of view. That term accounts in general for both the surface and the volumetric scattering decorrelation mechanism from the scene. This term varies according to the geometrical conditions of the two acquisitions, the carrier frequency used by the imaging system and the land cover of the ground surface. Usually, large baseline is translated into higher loss of coherence. Finally, the term  $\gamma_{temporal}$  accounts for the temporal scene coherence as the two SAR images have been acquired at different times, between the scatterers which may have changed.

### 2.2.3.1 Geometric decorrelation

Jointly with the temporal decorrelation it is one the major causes of decorrelation in SAR interferometry. It appears by the fact that the two acquisitions have a slightly different points of view of the same ground surface. Although, the geometry and the land cover of the observed ground terrain also have an influence on this decorrelation term. The spectral shift has the main contribution to this term. Other effects, as the ground characteristics, the volumetric scattering mechanism and the surface decorrelation, also contribute to the geometric decorrelation [Bam98].

#### Spectral shift

In the frequency domain, the radar imaging can be understood as a bandpass system with a limited bandwidth. The central frequency as well as the width of the filter are determined by the specification of the instrument and the acquisition geometry. Then, the spectral shift in repeat pass appears by the fact that the radar imaging performs a sampling of the ground frequencies based on this limited bandwidth filtering from two different points of view, see figure 2.2.3.

The amount of spectral shift is determined by the equation 2.2.7[Gat94].

$$\Delta f_R = \frac{2B_T}{\lambda R_0 \tan(\theta - \alpha)} \quad (2.2.7)$$

where  $B_T$  is the perpendicular baseline.  $\lambda$  is the sensor wavelength.  $R_0$  the slant-range distance.  $\theta$  is the wave incidence angle and  $\alpha$  is the terrain slope. This effect can be explained

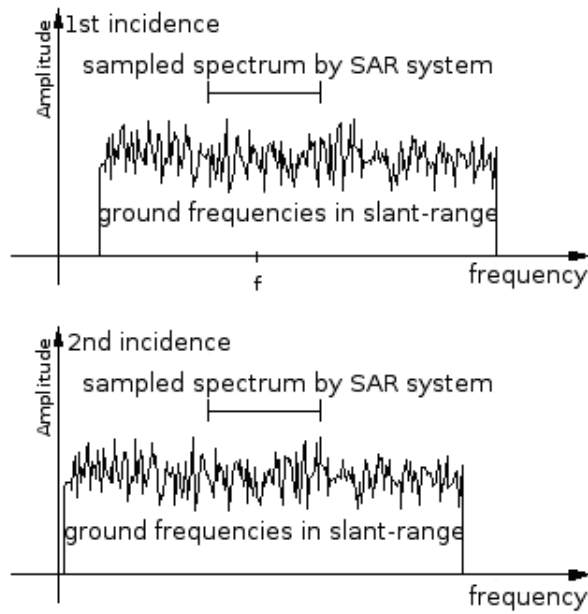


Figure 2.2.3: Ground terrain frequencies projected to the SAR slant-range frequency axis. This ground frequencies appear shifted when comparing the two acquisitions. The SAR system acts in the frequency domain as a bandpass filter determined by the range sampling frequency of the instrument.

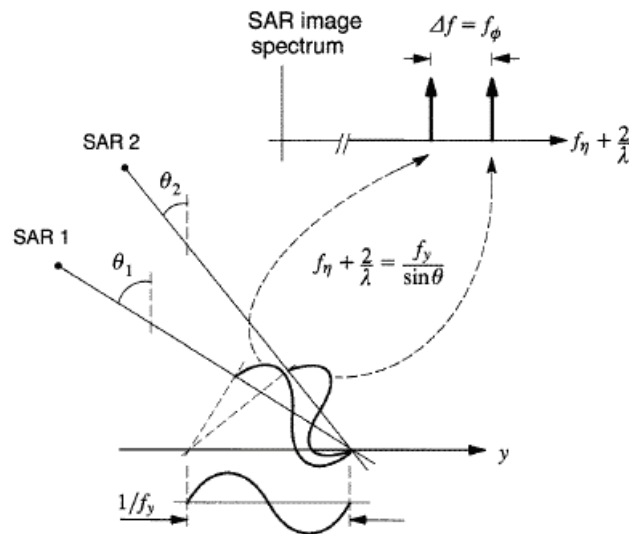


Figure 2.2.4: Geometric interpretation of the spectral shift. As result of the geometric sampling performed from two different point of views a ground frequency  $f_y$  is sampled to two different slant-range frequency positions in function of the wave incidence angle  $f_y/\sin\theta_{inc}$ . Graphic courtesy of [Bam98]

geometrically by figure 2.2.4. Each ground range frequency component is sampled into the SAR signal frequency domain according to the sinus of the local incidence angle, which is different considering the two different points of view of the acquisitions in figure 2.2.4. In that case, the range signal bandwidth contains different ground range frequencies for the two acquisitions. The interferometric information is thus located only in the overlapped part of the spectrum. The non-common spectral components decrease the interferometric SNR, and in consequence should be filtered.

Thus, interferometry will be possible only in case of overlapping of the ground frequencies

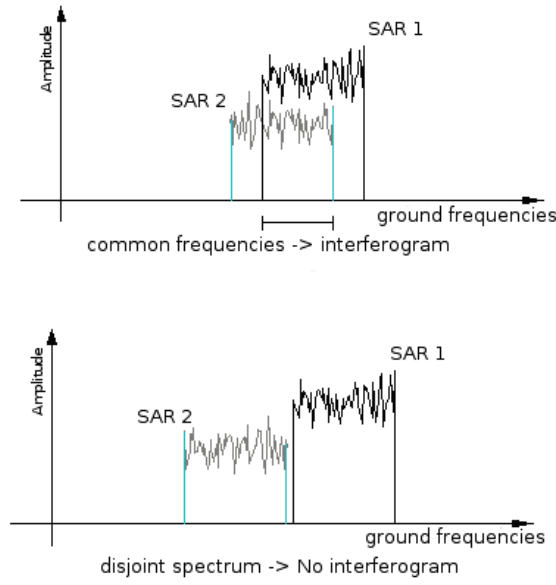


Figure 2.2.5: Schematic representation of the interferometric information in the frequency domain. In case of non-common band interferometry is not possible.

observed by the range spectrum of the two acquisitions. It is impossible to have an interferometric image between two range spectrums that are not representative of the same spread of terrain frequencies, see figure 2.2.5.

In other words, if the spectral shift between both spectrum  $\Delta f_R$  is larger than the range system bandwidth  $F_S$ , given by the range sampling frequency, then there will not exist common band. As it can be noticed in equation 2.2.7, the spectral shift is directly related with the perpendicular baseline, hence to the different acquisition geometries between both images. Therefore, the maximum baseline for which interferometry can be performed is determined by the equation 2.2.8, it is named critical baseline [Arn03].

$$B_{T,critical} = \frac{\lambda R_0 \tan(\theta - \alpha)}{2 PixelD} \quad (2.2.8)$$

being  $\lambda$  the wavelength.  $R_0$  the slant-range nominal distance.  $\theta$  is the wave incidence angle and  $\alpha$  is the terrain slope.  $PixelD$  the size of the pixel in range direction. For example, the critical perpendicular baseline for the ENVISAT case is approximately 1.1 Km, meanwhile for the high resolution TerraSAR-X sensor is of about 1.8 Km, in both cases considering a flat terrain ( $\alpha = 0$ ). It is important to notice the effect of the topographic relief on the spectral shift. For a given baseline, a step terrain slope ( $\alpha$ ) can increase the final amount of spectral separation or vice versa.

Finally, the degradation of interferometric coherence can be quantified by the equation 2.2.9, in function of the acquisition system parameters and the used baseline value.

$$\gamma_{baseline} = 1 - \frac{B_T}{B_{T,critical}} \quad \text{for } B_T \leq B_{T,critical} \quad (2.2.9)$$

### Volume and surface scattering

The effect of scattering in function of the volume on the interferometric correlation will be noticed when objects of different heights are located within the same slant-range resolution cell. Then, there could be found the situation that depending on the volume of the objects different levels of penetration of the incident wave could be given in function of the particular incidence angle of the repeat passes. Hence, when the ground objects have a backscattering coefficient which depends on the vertical penetration of the wave the returned construction phase as well as the reflection phase of those pixels will be complete different in the repeat passes. This is translated directly into a decrease of the coherence.

In case of pure surface scattering and considering the angle induced by the terrain topographic slope changes in the backscattering coefficient of a pixel can be observed as well. Obviously, the different look angles of the two SAR images, even if  $B_T = 0$ , have the effect of decorrelating the signals. The physical reason is that the resulting coherent sum of contributions from the individual elements within a resolution cell on ground varies with the incidence angle.

### 2.2.4 Phase unwrapping

As it has been previously explained the interferometric phase is an ambiguous value, by an integer multiple  $k$  of  $2\pi$ . In order to properly exploit the capacity of measure fine increments of the range distance between repeat passes this ambiguity must be resolved. Then, the unwrapped phase can be defined by means of equation 2.2.10.

$$\phi_{unwrapped} = \phi_{wrapped} + 2\pi \cdot k \quad \text{where } \phi_{wrapped} \in [-\pi, \pi) \quad (2.2.10)$$

The art of recovery this integer number or to reconstruct the absolute phase measurement is the phase unwrapping step. Strictly speaking, phase unwrapping is an impossible problem because an unwrapped phase array (the original one) necessarily contains information that is not available in the corresponding wrapped phase. Effectively, with an ambiguous wrapped phase there is no way to determine which of the many possible integers multiple solutions of  $2\pi$  is correct. Then, all methodologies rely on at least some assumptions, the most basic and common is that the Nyquist criterion is met, at least over more or less large areas of the image. In other words, it is assumed that the spatial sampling is high enough in most parts of the interferogram. Thus, it can be said that the true unwrapped phase values of neighboring pixels has an absolute phase difference below one half cycle ( $\pi$  radians).

Thus, the key point in phase unwrapping lies not in directly finding an estimate of the real unwrapped phase values themselves, but in estimating the unwrapped phase differences between them. This is in agreement with the fundamental premise of phase unwrapping, that under appropriate conditions, an accurate estimate of the unwrapped solution can be performed from the relationships between neighboring phase pixels. Effectively, if this difference between the wrapped phase values is less than half a cycle in absolute value, then the true unwrapped phase differences are equal to the observed wrapped phase differences. However, when this assumption fails the results contain serious errors.

Where the data is sampled adequately the unwrapped phase gradients equal the observed wrapped gradients and the unwrapped estimate can be readily obtained by means of the inte-

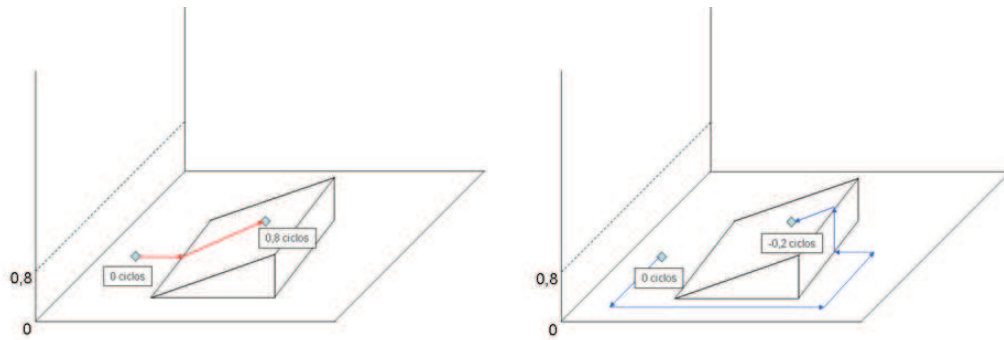


Figure 2.2.6: Path integration should not cross any phase discontinuity in order to avoid unwrapping errors. Following the path in the image on left the unwrapped phase will be properly recovered. In case of crossing a phase jump (or discontinuity), like in the image on right, the recovered phase will have aliasing.

gration of those estimated gradients. The difficulty of phase unwrapping resides in the fact that usually the interferogram contains gradients that exceed one half cycle in magnitude. This is due to a loss of coherence (noise) and/or insufficient sampling of the observed phenomena (presence of fast ground movements). Those high gradients create phase discontinuities in the interferometric image. Another key task of the phase unwrapping algorithm is then to identify and handle properly these phase discontinuities.

Almost all classical phase unwrapping algorithms are based on two main steps. First, an estimation of the phase gradients of the unwrapped phase based on the wrapped phase (input) is performed. Secondly, this estimate is integrated either via one-dimensional summation or by a two-dimensional integration where weighting according to the reliability of gradient estimates can be optionally used. Some of them are listed below. An example of wrapped and unwrapped interferometric phase can be found in figure 2.3.1.

#### 2.2.4.1 Residue-cut algorithm methods

These family of methodologies estimate the phase gradients of the unwrapped phase directly from the wrapped phase and then they integrate these values sequentially by means of some two-dimensional path in the interferogram. These kind of algorithms perform a previous estimation of the ghosts lines or phase discontinuities in order to exclude them from the integration path [Gol] or to use them to correct the phase differences along the detected phase residues by adding integer multiples of  $2\pi$  [Cos96, Fly97] before the integration, see figure 2.2.6 for an illustration of the problem.

An interesting property of these kind of methodologies is that the unwrapped phase is consistent (or congruent) with the wrapped phase. It means that they differ only by an integer number (one multiple of  $2\pi$ ) of one full phase cycle. Then, all the complications appear on finding the phase discontinuities, or in other words, in properly estimating the phase gradient of the unwrapped phase.

#### 2.2.4.2 Least squares estimation techniques

Like the residue-cut algorithms, least squares ones are based on the assumption that the observed wrapped phase is correctly sampled nearly everywhere. Then, instead of performing an

integration of the gradient estimates along some determined paths, a computation of the unwrapped solution is performed based on a minimization of the total squared departure of the estimated unwrapped gradients from their wrapped counterparts. This minimization is performed globally, simultaneously over the whole image. It is very interesting to balance the equations with some kind of weight based on the interferometric coherence or the variance of the estimated phase gradient [Pri96][Ghi94, Hun79].

In the least square problem formulation no gradients are explicitly disregarded as it is done in the residue-cut algorithm. So least square unwrapped estimate is usually very smooth (spatially) and generally not congruent with the wrapped input phase. Thus, despite these kind of methodologies are very efficient and mathematically elegant they often give disappointing results in practice. However, they obtain always a complete solution for the whole image which in some cases constitutes a good compromise.

### 2.2.4.3 Other algorithms

The two kinds of phase unwrapping algorithms briefly introduced above are the most popular and classical ones. However, it exists other methodologies based on different approaches. The existing diversity illustrates the open-ended nature of the phase unwrapping problem.

In case of high coherence interferograms, region growing phase unwrapping techniques have proven to give very good results [Rei97, Xu96]. These kinds of algorithms try to identify regions of high quality and to unwrap them individually. Finally these reliable and isolated areas of unwrapped phase are merged between them in order to have the same reference.

Another very elegant approach is the one based on Kalman filters [Kra96]. By means of this filtering technique, based on the statistic of the observed gradients of the wrapped phase, it is performed a reliable estimation of the local interferometric frequency and an integration of this value in order to obtain a prediction of the unwrapped phase value.

Multiresolution frequency estimators combined with least squares achieve asymptotically unbiased slope reconstruction [Dav96]. They work locally in an adaptive way based on the interferogram quality and adjusting the achieved planimetric resolution.

## 2.2.5 SAR interferometry processing steps

Under a practical point of view the performances of the interferometric processing is divided into several steps. There are a lot of interferometric tools available in the market, which share more or less the same principles. All the interferometric processing within this PhD has been done with DIAPASON software [CNE98], developed by the French Space Agency (CNES) and maintained and upgraded by the company Altamira-information, S.L [ALT]. In figure 2.2.7 the main steps of DIAPASON's software are presented as illustration of the practical procedure required to perform an interferogram. However, this architecture can be extrapolated to rest of interferometric chains.

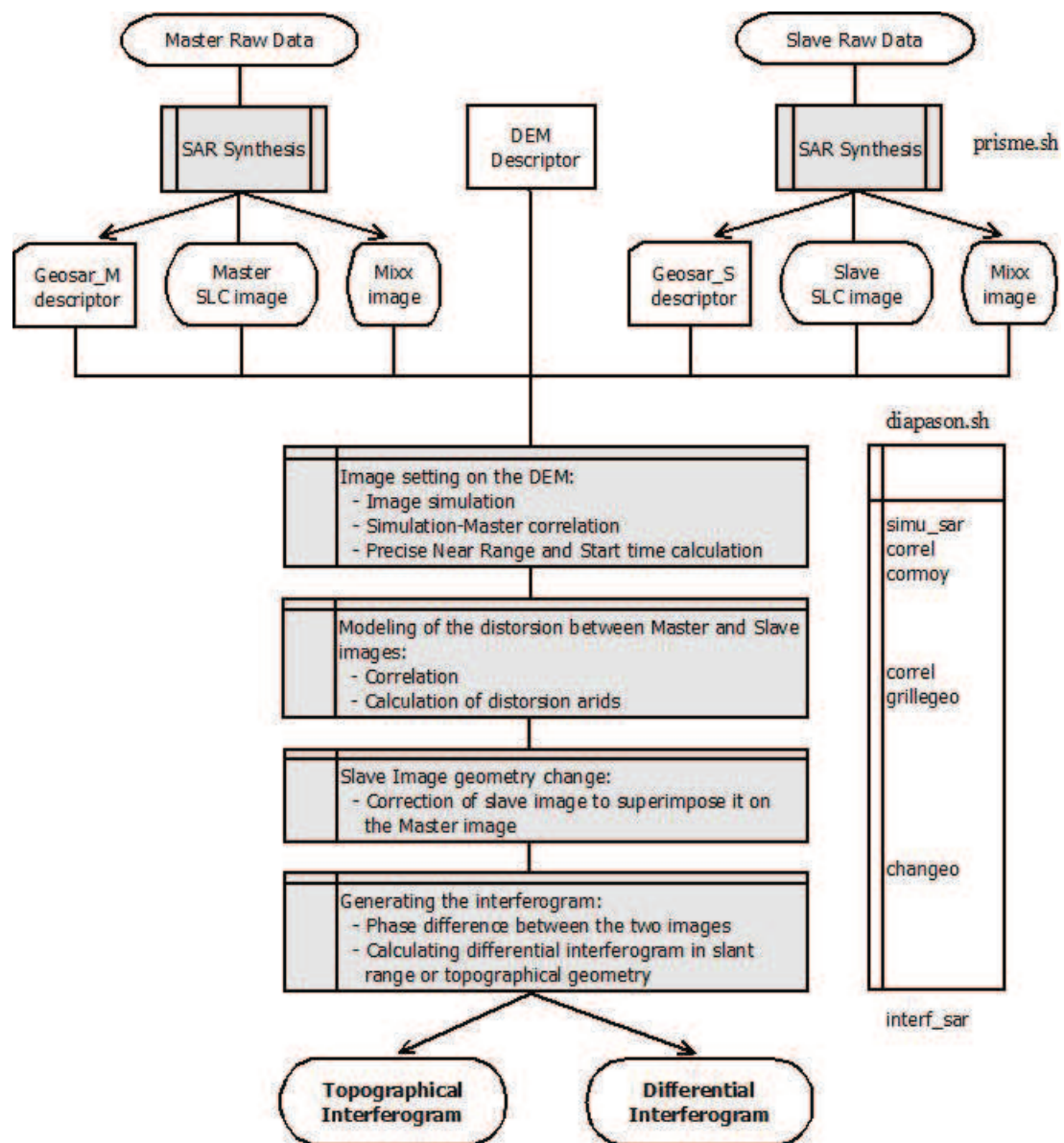


Figure 2.2.7: Main steps for the performance of an interferometric processing. Based on DIAPASON.

### 2.2.5.1 Data extraction

The input data must be always an interferometric SAR data pair, in level 0 (RAW) or in level 1 (SLC). Whatever the case this data must be extracted from the delivered product and put it into a binary file with (setting a particular format). Furthermore, other additional information necessary for the rest of the processing must be extracted from the product annotations such as orbit ephemeris, image timing information and satellite acquisition frequencies. All these product annotations are decoded usually in ASCII files forming an image descriptor which defines the main characteristics of the SAR data.

### 2.2.5.2 SAR focusing

In case of level 0 the RAW data must be compressed or focused by means of the SAR synthesis step in order to obtain a level 1 (or SLC) data.. The focusing step is the responsible of converting the raw data to a complex (I+Q) image with an improved resolution (the nominal one considering the used satellite mode). Previous to the image focusing some important processing parameters such as the azimuth FM rate and the azimuth Doppler centroid value must be estimated carefully for each acquisition, which can be done based on the data itself or based on the product annotation information, achieving in the first case a better accuracy.

### 2.2.5.3 Generation of a descriptor of the illuminated ground surface

It is necessary to describe the ground terrain which covers the area illuminated by the swath of the satellite. This could be done by means of a descriptor file, which specifies the corners of the Area Of Interest (AOI) and a geodetic model of the earth surface. This earth model will be use to remove the interferometric flat earth fringes (to obtain an InSAR). In case of availability of a Digital Elevation Model (DEM) of the AOI it could be used also to improve the compensation of the flat earth fringes from the interferogram by removing the fringes due to the ground topography. In that case the final product will be a differential interferogram (DInSAR).

### 2.2.5.4 Correction of the product annotation timings

The SLC is a raster file which contains information about the SAR reflectivity of the illuminated ground surface in slant-range coordinates (sensor geometry). The acquisition starting time and the near range for the first sample of the raster file is given within the product annotation parameters. These times are used to relate every SAR sample with its correspondent ground position, when compensating the flat earth fringes in the interferogram and when projecting the SAR measurements to ground coordinates. Usually these timing annotations are not accurate enough in order to guarantee a precise geocoding of the products.

This correction is performed by means of the cross-correlation of the SAR amplitude of the master image with a simulated SAR reflectivity based on the DEM. This simulated reflectivity image is obtained as function of the available topographic information of the ground (given by the DEM), the sensor and the image mode characteristics and its orientation (given by the orbit state

vectors). The correlation detects thus the shifts between both geometries (which are a constant value in range and azimuth) and the refinement can be performed.

### 2.2.5.5 Image coregistration

The interferometric data pair are acquired from slightly different point of view. Hence they present different image geometries. Therefore, the SAR couple must be coregistered before any interferometric operation. To coregister a pair of SLC images, one image geometry, called slave image, is transformed into the other one, called master image. To coregister the slave to the master, it is necessary to know the range and azimuth offsets that must be applied to each pixel of the slave image in order to project it onto the master geometry. The coregistration estimates these deformation grids in range and azimuth axis that allows the transformation of each point of the slave images into the master geometry of acquisition, as if all the scenes have been imaged from the same point of view. Usually the coregistration procedure is based in three main steps:

1. **Rough coregistration:** It consists in the estimation of a constant offset between the two images in order to approach both geometries (with a precision of some few pixels). This shift can be evaluated by means of an incoherent amplitude correlation of an undersampled image of the multilook product or approximated by the user that deduced the offsets to be applied from the visual analysis of the multilook products.
2. **Fine coregistration:** uses incoherent amplitude correlation over small windows distributed throughout the image swath, in order to obtain a precise and adaptive estimation of the range and azimuth offsets. However, the quality of these estimates depends on the correlation rate, which is sometimes very low as for example in vegetated areas or inundated (flooded) regions. This estimation is enhanced comparing the correlation grids with a synthetic coregistration grids obtained from the use of a DEM of the area and the orbital files. Due to the inaccuracies of the image timing annotation (in range and azimuth) the synthetic grids are very precise in a relative point of view (correction of the shifts between master and slave), but do not provide the appropriate absolute value for the coregistration offsets. These synthetic coregistration grids give the theoretic offsets between the data pair according to their orbit separation, the ground topography and the acquisition parameters. The result of the fine coregistration is finally composed of two grids containing the offsets that should be applied, in range and in azimuth, to each pixel of the considered slave image. Figure 2.2.8 shows an example of coregistration grids obtained by amplitude correlation and the final interpolated ones.
3. **Application of the grids:** Finally the slave image is resampled in an adaptive way to the master geometry applying to each pixel the offset values indicated by the coregistration grid.

In the bibliography [Gab88] it is demonstrated that a coregistration with an accuracy of 1/8th of a pixel yields to an almost negligible (4%) decrease in the interferometric coherence. Typically, the final coregistration accuracy achieved with DIAPASON is in the order of 0.1 pixel, corresponding to approximately 0.8 m. in ENVISAT and 0.1 m. in TERRASAR-X stripmap modes in slant-range.

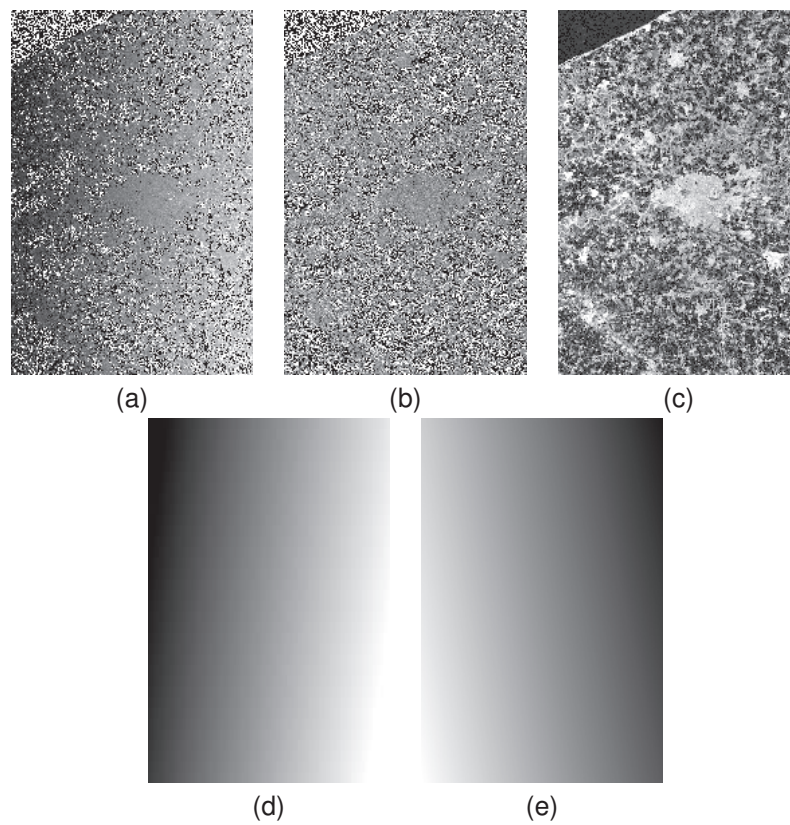


Figure 2.2.8: Example of fine coregistration grids. In (a) and (b) there are the grids with the fine range and azimuth offsets estimated by amplitude correlation between master and slave. The image in (c) is the correlation rate index, which indicates the quality of these estimates. In (d) and (e) there are the final interpolated coregistration grids with the fine offsets that must be applied to the slave image. They are obtained thanks to the use of the orbits state vector, the DEM and the image annotation parameters.

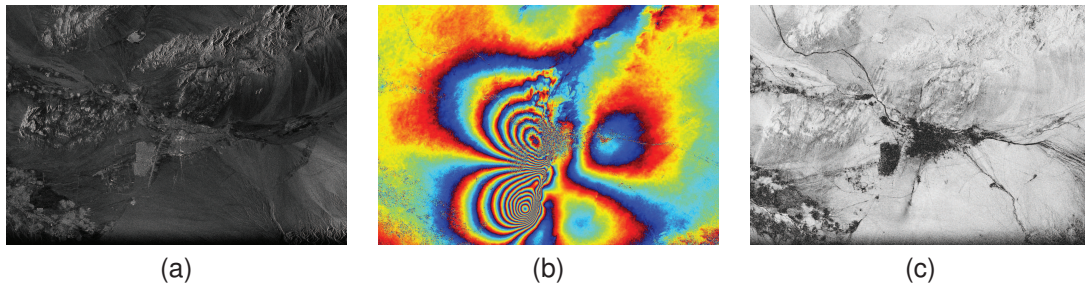


Figure 2.2.9: Example of the three main interferometric products, amplitude (a), phase (b) and coherence (c) over Bam, Iran with ENVISAT image mode data. A strong ground deformation pattern can be observed on the phase image due to earthquake which took place on December 2003. This is possible thanks to have one acquisition before and another one after the earthquake. Each blue-to-red color-cycle (one full phase cycle) equals approximately 2.8 cm of deformation. The dark areas of coherence (very different signals between master and slave) in the center of the image highlights the destruction and the damage caused by the earthquake over the urban area.

### 2.2.5.6 Generation of the interferogram

Within this step the interferometric products are generated. They are obtained by means of the coherent difference between the two coregistered data products in slant-range geometry. It is suitable to define a multilooking factor in order to estimate this mean phase difference for a group of pixels with a good level of signal to noise ratio. This parameter will determine the planimetric resolution of the final product. The main products are:

- The interferometric amplitude: the mean derived from the amplitude of the two input SLC.
- The interferometric phase: image with the phase difference between the two input channels. This phase value is wrapped between  $(-\pi \text{ y } \pi)$ .
- The interferometric coherence: it is a quality index which is directly related with the precision of the estimated phase difference for every interferometric pixel. It is comprised between 0 (no signal) and 1 (very good SNR).

In classical InSAR applications it is commonly performed a common band filtering in both directions range and azimuth taking into account the estimated Doppler centroid and the geometric baseline which characterize the data pair. This is done to enhance the estimated interferometric coherence.

The interferometric phase is related to the physic distance difference that travels the wave considering the master and the slave orbital position and the same target on the ground. In particular, the interferometric phase is measuring the evolution of this differential distance between the adjacent samples. The flat earth phase contribution is automatically compensated within the DIAPASON's interferometric procedure; the phase measured is then the increase of topography between adjacent pixels, considering a geodetic earth surface model. In case of having a DEM of the AOI these topographic phase is also compensated jointly with the flat earth fringes resulting in a Differential Interferogram (DInSAR), see next chapter for further details about InSAR and DInSAR procedures and applications. An example of interferometric product is given in figure 2.2.9.

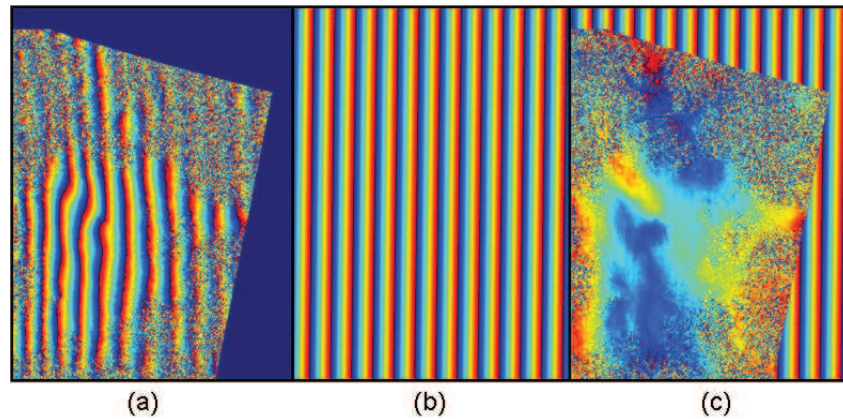


Figure 2.2.10: Illustration example of orbital cleaning procedure. a) Original multilooked interferometric phase. b) estimated phase orbit ramp mainly in range direction. c) final corrected interferogram. After the orbital fringes compensation other phase contributions can be appreciated.

### 2.2.5.7 Compensation of the orbital state vectors inaccuracies

Possible inaccuracies in the used orbital state vectors are translated into linear phase trends in the interferometric phase, typically in range direction [Koh03]. The interferometric softwares usually estimate possible phase slopes or gradients in range and azimuth direction directly from the interferometric phase. Then a synthetic phase ramps is generated in order to compensate these trends over the interferometric phases. An area of good coherence is usually required in order to perform a successful estimation of these phase trends, see figure 2.2.10 for an illustrated example.

### 2.2.5.8 Phase unwrapping

This step performs the unwrapping of an interferometric phase image. It converts the truncated values of path differences into absolute values. Then, the interferometric phase value between any pixel in the image can be compared directly. The unwrapped image of a non-differential interferogram is the first step toward DEM generation.

### 2.2.5.9 Geocoding

The interferometric phase values are in slant-range geometry (sensor geometry). These measurements must be geocoded into some particular ground projection coordinates systems in order to be fully exploited. The projection coordinates should be properly defined in order to be in correspondence with the AOI. Typically, they are the ones defined in the DEM descriptor used within the interferometric process. The planimetric precision is given by the precision of the used DEM and the multilooking factors performed during the interferogram generation steps. The precision of the vertical measurements is given by the interferometric coherence (quality of the phase). See figure 2.2.11 for as an example of illustration of the SAR geocoding.

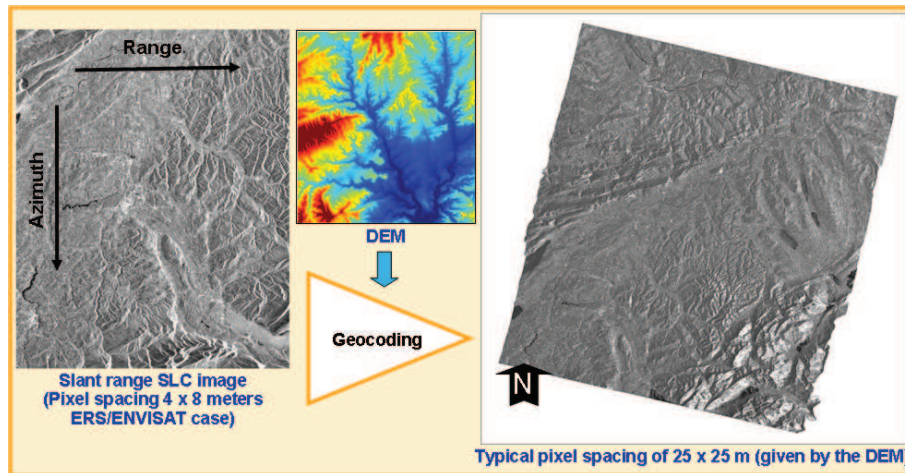


Figure 2.2.11: Example of SAR geocoding procedure. On left, SAR amplitude image in sensor geometry (SLC matrix of  $N \times M$  samples). On right, final geocoded SAR amplitude based on the ground projections defined by the used DEM during the procedure.

## 2.3 InSAR main applications

As it has been introduced in the previous section radar interferometry is a technique that allows to measure phase differences between two radar images. This difference can be originated by several sources, as for example a change of the relative distance between the sensor and the ground and/or changes in the nature of the illuminated ground area.

The main InSAR applications take benefit of the capacity of measurement differences in the travel phase between repeat passes. The first important application of InSAR is the generation of DEMs of the ground surface [Zeb86]. The other important one is the detection of small deformation movements of the ground surface [Mas85]. There are other applications based on radar interferometry as for example change detection based on the interferometric coherence, classification, soil moisture analysis, etc.

Whatever the case, one important limitation common to all the classical InSAR application is the pollution of the measurement produced by the atmospheric artifacts. With only two images (one interferogram) it is very difficult to decorrelate this unwanted phase artifacts from the real measurements, leading in a decrease of the accuracy.

### 2.3.1 Digital Elevation Model generation

As it happens with the optical images, radar acquisitions generated from different point of view can originate a stereoscopic effect. In that case, the same area on ground is observed under slightly different orbital positions, separated by a certain baseline  $B$ , see figure 2.3.1. Due to this geometry the travel phase to the same target on ground is different considering the two acquisitions. This difference detected by the interferometric phase is directly related with the height of the target on ground and with the separation between the two orbits. Thus, the interferometric measurement can be exploited to estimate the height of the observed ground.

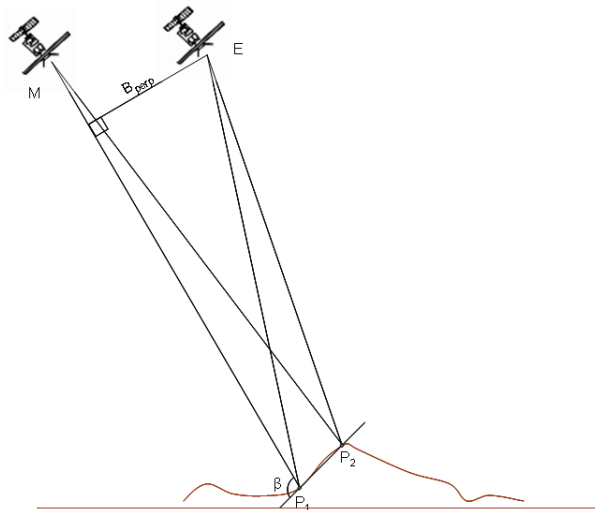


Figure 2.3.1: Geometric interpretation of the relation of the InSAR phase with the ground topography.

### 2.3.1.1 Geometric interpretation

In equation 2.2.1 is already presented that in case of no changes of the ground nature and with the same acquisition geometry the interferometric phase can be directly related with the difference of travel phase between the both signals. This phase can also be analyzed considering the interferometric phase between two consecutive pixel in slant-range direction, it means in the same zero-Doppler plane, see figure 2.3.1.

In that case it can be demonstrated that the increment of range for the second orbit can be approximated by equation 2.3.1[Mas93a]

$$\phi = \frac{4\pi}{\lambda} \Delta R \simeq \frac{4\pi}{\lambda} \frac{B_T}{R} \cdot \tan\beta \cdot PixelD \quad (2.3.1)$$

where  $B_T$  is the perpendicular baseline.  $\beta$  is the complementary angle to the local incidence (which considers the elevation angle induced by the topographical slope) and  $PixelD$  is the size of the interferometric pixel in range. The approximation used in equation 2.3.1 (named far field approach) assumes that the baseline length is much smaller than the slant-range distance from the sensor to the ground  $R$ . This is a reasonable approximation, as  $R$  is typically in the order of some hundreds of kilometers, while the considered baseline  $B$  is usually not larger than a few hundreds of meters.

Some important considerations can be made based on equation 2.3.1:

- The phase difference between two interferometric image pixels is related to the angle of the local slope by means of the term  $\tan\beta$ . Hence, it allows to have a relation with the local relief.
- The magnitude of the phase difference between two consecutive pixels in range is proportional to the perpendicular baseline. Typically the extension of a swath in range is in the order of one hundred of kilometers, and in consequence, the perpendicular baseline will vary in function of the observed point on ground, see figure2.2.4. Usually this change in magnitude is in the order of tens of meters [Arn03]. Then, it can be defined the global sensitivity of an

interferogram to the topographical relief by means of the value of the perpendicular baseline at the center of the scene. However, for DEM generation and in order to estimate with the maximum precision the topographical relief from the interferometric phase, the variations of perpendicular baselines along the scene must be considered. It can be highlighted that if the perpendicular baseline is equal zero then the phase difference will be zero as well. Effectively, it means that the two acquisitions are geometrically aligned and in consequence there is not stereoscopic effect.

- In case of a flat terrain (without topography) the value of  $\tan\beta$  can be considered as a constant. In this case, the interferometric phase between the two consecutive pixels is inversely proportional to the range distance ( $R$ ), which varies in a uniform way between the near range and the far range of the scene (approximately 100 Km). Then, considering a uniform pixel spacing it will be translated into a phase slope oriented more or less in the range direction. This is known as the flat earth contribution or interferometric fringes. They are due to the oblique acquisition geometry of the earth ground surface. As the orbital paths are not strictly parallel between them it can be found variations of the perpendicular baseline also with time (azimuth direction). Due to this non-parallel acquisition geometry the orientation of the flat earth fringes can present some tilt in the azimuth direction.

Further and rigorous details can be found in the literature regarding the above considerations [Mas93a, Arn97]. The basic and important idea for the generation of DEMs by means of InSAR is that the relation of the phase with the local slope induced by the topographical relief is directly related with perpendicular baseline 2.3.1. Then, it can be defined the topographical sensitivity of an interferogram by the equation 2.3.2, which defines the height of ambiguity [Mas93a].

$$A_e = \frac{\lambda R \sin\theta}{2 B_T} \quad (2.3.2)$$

where  $\theta$  is the wave local incidence angle. As it was discussed in the previous section, the interferometric phase is an ambiguous magnitude. It is a value wrapped between  $-\pi$  and  $\pi$ . The height of ambiguity is a parameter which indicates the required height difference between two ground targets in order to create a phase jump of  $2\pi$  in the interferogram.

It is interesting to note that as the baseline increases the altitude of ambiguity decreases. In other words, shorter baselines imply less sensitivity to detect topographic changes on the ground surface. Then, the height of ambiguity is a very important parameter in order to select a SAR interferometric data pair for produce a DEM. It would be desired to have the smallest time separation between the two repeat passes, ideally it may be a simultaneous acquisition, to avoid as much as possible to have changes in the range distances due to any movement of the ground target and/or changes in the nature of the scatterers, but also the same atmospheric induced paths delays. Hence, by selecting an appropriate perpendicular baseline the interferometric phase will be only related to the topographical relief of the scene. Of course, neglecting the effects of the atmosphere on the SAR signal. This can be illustrated by means of the analysis of a practical case like for instance the one presented in figure 2.3.2.

In figure 2.3.2 it is illustrated the effect of the baseline on the detection of ground topography. The same ground relief is sampled by three real interferograms with three different values of height of ambiguity. The first interferogram in figure 2.3.2.a is the one with less sensitivity to

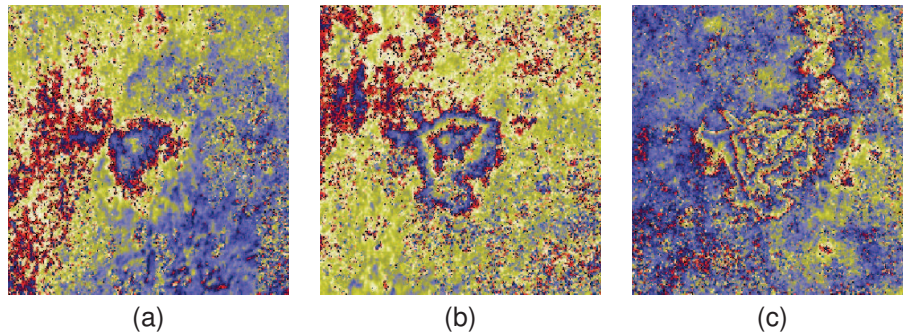


Figure 2.3.2: Affection of the height of ambiguity on the detection of ground topography. Interferograms with 210 m (a), 123 m (b) and -65 m of height of ambiguity respectively. More details of the same ground relief can be appreciated when increasing the interferometric baseline. One cycle of color corresponds to one cycle of interferometric phase cycle ( $2\pi rad$ ) or similarly 210m of vertical height for the first case, 123m for the second and -65m for the last one respectively.

the topography. A full cycle of phase corresponds to a change of about 210 m in the vertical elevation ( $2\pi rad$ ). As it can be observed there is less than a complete fringe for sampling this relief which presents an elevation of about 200 meters from bottom to top of the mountain. The second interferogram in figure 2.3.2.b has a sensitivity of 123 meters. It is presenting almost two complete fringes when sampling this relief from bottom to top, which is in correspondence with the state above for the first case. The last one presented in figure 2.3.2.c shows the highest sensitivity with -65 meters of height of ambiguity. Now the total amount of fringes (phase full cycles) has been increased up to a bit more than 3. As consequence, the topographic relief sampled by the last interferogram in figure 2.3.2 shows a higher level of details of the sampled mountain. It is possible to identify clearly slopes with high elevation gradients, something that was not possible with the previous ones. In addition, it must be highlighted that due to the sign change in the height of ambiguity value the fringe gradients are inverted regarding the a) and b) cases.

It is natural to think that the higher the baseline the higher the precision that one could achieve in the performance of a DEM by means of InSAR. However, it must be considered the geometric decorrelation term introduced in section 2.2.3.1. Large baseline acquisitions are translated into a disjoint of the range spectral contents, in consequence into a degradation of the SNR. In that case common-band filtering is required in order to reduce the noisy band from the spectrum and hence to increase the SNR. The price that should be paid is a degradation of the range resolution as the useful range band is narrow. In practice, a good tradeoff between height sensitivity and spectral shift can be found for values of baseline of about 150 to 400 for the ENVISAT case, taking into account that the time span may be as small as possible whatever case.

Following steps of the DEM generation process consists in the phase unwrapping. As it was explained before the interferometric phase remains wrapped. The phase measurements can not be directly related from one pixel to the other one in the image. Hence, a phase unwrapping operation is required. A lot of possible methodologies are available and depending on the test site one could succeed better than another one. The problematic of phase unwrapping was already presented and briefly discussed in section 2.2.4.

The next step is the conversion of the phase values into vertical heights by means of the inversion of the formula 2.3.1 in an adaptive way and pixel by pixel on the image. The last step is the geocoding of the estimated elevation values, which are in SAR geometry, into some desired ground coordinates system, see section 2.2.5.9. It is highly recommended the use of some ground

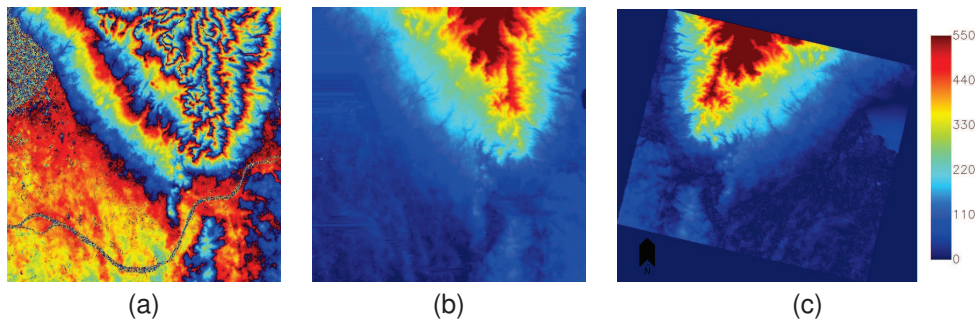


Figure 2.3.3: Illustration of the last InSAR steps required to produce a DEM. a) wrapped interferogram performed over a flat area with a mountain on the top right part of the image. Each color cycle from red to blue means a complete full phase change of  $2\pi$  radians. b) Unwrapped interferogram. Now the phase value of any pixel in the image can be compared in absolute with another one. Now the color table from blue to red it corresponds up to 7 complete phase cycles. c) Final geocoded map with the estimated elevation value for every pixel. This image is in UTM projection north oriented.

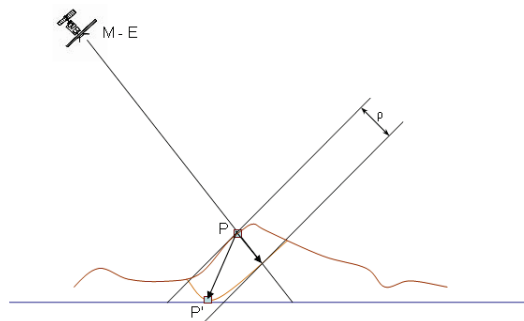


Figure 2.3.4: InSAR acquisition geometry with considering an ideal case of zero baseline. Master (M) and Slave (S) acquisition have the same orbital position. Thus, this interferogram has no sensitivity to the ground topography. If between the two passes occurs a ground displacement ( $\overrightarrow{PP'}$ ) it is possible to detected it by means of the InSAR phase (and its relation with the wave's travel distance). However, the detected deformation magnitude  $\rho$  is the one projected to the line of sight, which will have a magnitude lower than  $\|\overrightarrow{PP'}\|$  in case the line of sight is not parallel to the deformation direction.

control points (GCP) in order to remove systematic errors in the estimates. In case a large number of GCPs distributed all along the image swath is used, it is possible to compensate for possible large scale artifacts in the interferometric phase; for example residual uncompensated orbit errors and atmospheric artifacts, which will be explained in future sections. In figure 2.3.3 all these last steps are illustrated by means of a real case.

### 2.3.2 Estimation of ground deformation maps

Under some specific conditions it is possible to measure ground movements between repeat passes. As was stated above, the interferometric phase can be directly related to the difference of travel phase between the two acquisitions, see equation 2.2.1. If the two images have been acquired under the same point of view (ideal case of zero baseline), possible changes in the travel phase would mean that the ground target has changed its position, see figure 2.3.4. In other words, that there was occurring a displacement of the illuminated ground slice of terrain between the two epochs.

Unfortunately, a zero baseline interferometric acquisition is not a real case. Usually, there is

always a particular value of baseline and a relief of the ground. Then, there is usually a contribution of the ground topography into the interferometric phase. Fortunately, as was explained in the previous section (2.3.1), this contribution is purely geometric. There is a direct relationship of the ground topography with the baseline of the interferometric acquisition. Hence, by knowing this ground topography and the orbital paths this phase contribution can be synthesized and compensated from the interferogram. This results is a Differential Interferogram (DInSAR).

### 2.3.2.1 Complete interferometric phase model

For an interferometric acquisition with a particular perpendicular baseline ( $B_T$ ) and a local incidence angle of  $\theta$  the complete model for the resulting phase can be expressed by means of equation 2.3.3-

$$\begin{aligned}\phi_{InSAR} &= \phi_{FE} + \phi_{TOPO} + \phi_{MOV} + \phi_{ATMO} + \phi_{noise} \\ &= \frac{4\pi}{\lambda R} \cdot \frac{B_T \Delta r}{\tan\beta} + \frac{4\pi}{\lambda R} \cdot \frac{B_T h}{\sin\beta} + \frac{4\pi}{\lambda} \cdot \Delta\rho + \phi_{ATMO} + \phi_{noise}\end{aligned}\quad (2.3.3)$$

The first two phase contributions ( $\phi_{FE}$  and  $\phi_{TOPO}$ ) are due to the scene geometry and the orbital separation of the acquisitions. The third term,  $\phi_{MOV}$ , is due to potential movement of the ground surface. The fourth one,  $\phi_{ATMO}$ , is related to the atmospheric contribution due to the two acquisitions. The last term,  $\phi_{noise}$ , is the component due to the phase noise, which accounts for all the InSAR decorrelation terms and processing errors. The geometric contributions on the interferometric phase can be divided in two: the phase due to the flat earth ( $\phi_{FE}$ ) and the one ( $\phi_{TOPO}$ ) due to the ground local topography. As it can be observed in equation 2.3.3 both are directly related with the perpendicular baseline and with the range separation ( $\Delta r$ ) and the increment of height ( $\Delta h$ ) between consecutive pixels. In consequence, with a geometric model of the ground (DEM) and by knowing the orbital position of the SAR images during the acquisition it is possible to synthesize and to compensate these two phase contributions for a particular repeat pass.

Thus, the remaining phase after the compensation of the geometrical artifacts is the DInSAR phase, see equation 2.3.4.

$$\phi_{DInSAR} = \phi_{MOV} + \phi_{ATMO} + \phi_{noise} = \frac{4\pi}{\lambda} \cdot \Delta\rho + \phi_{ATMO} + \phi_{noise}\quad (2.3.4)$$

As it can be observed in equation 2.3.4 the contribution due to the ground movement is directly related to  $\Delta\rho$ , which is the magnitude of movement detected in the line of sight between the repeat passes. Hence, different atmospheric conditions during the acquisition originate different delays in the travel phase of both acquisitions, leading in detection of false movements. These phase artifacts are completely unpredictable and very difficult to compensate with only one interferometric acquisition, see figure 2.1.11 for an example. Thus, it is an unwanted contribution which may disturb the measurement of deformation. In addition, there could be found another unwanted phase contribution which is due to the different atmospheric conditions in the two epochs, see section 2.1.2.1 plus other noisy terms (see section 2.2.3)

### 2.3.2.2 Detection of movement

DInSAR is an interesting tool for investigating ground deformation events of the earth surface, such as earthquakes, glaciers, tectonics and volcanoes activities as well as small ground subsidences. DInSAR offers large scale coverage of this physic phenomena with a precision in the order of few millimeters. However, important remarks must be done regarding the capacity of detection of movements by means of DInSAR, at least under a geometric point of view originated by the SAR acquisition system.

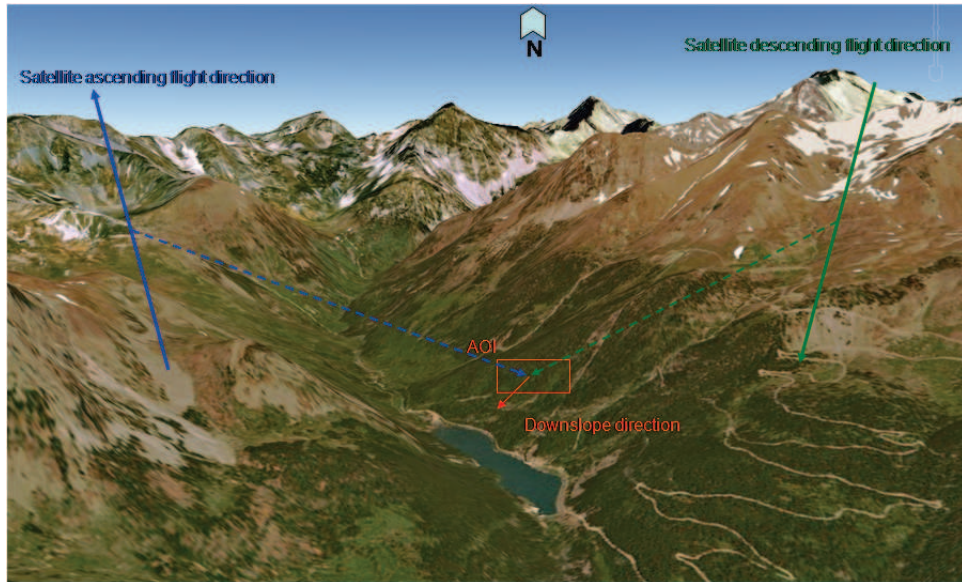
It must be considered that the possible deformations should not change the relative position of the individual reflectors placed within the resolution cell. In case of relative changes in the order of half a wavelength the construction phase (see section 2.1.2.3) of the pixel will not be preserved. In consequence, the stationary conditions made for establishing the InSAR phase relationship with the slant-range change of distance will not be satisfied and the coherence will decrease after the deformation occurred.

The movement must have a magnitude in the order of half the wavelength and must be spatially correlated. In other words, it must present a similar or a gradual varying magnitude between a neighborhood of pixels. This kind of movements do not change the relative positions of the single reflectors that fall within each pixel. They create a uniform shift of all of them. Hence the coherence is kept in the repeat passes. The measurement of this shift is the main scope of DInSAR, as it is related with the ground displacement, see figure 2.3.4 and equation 2.3.4.

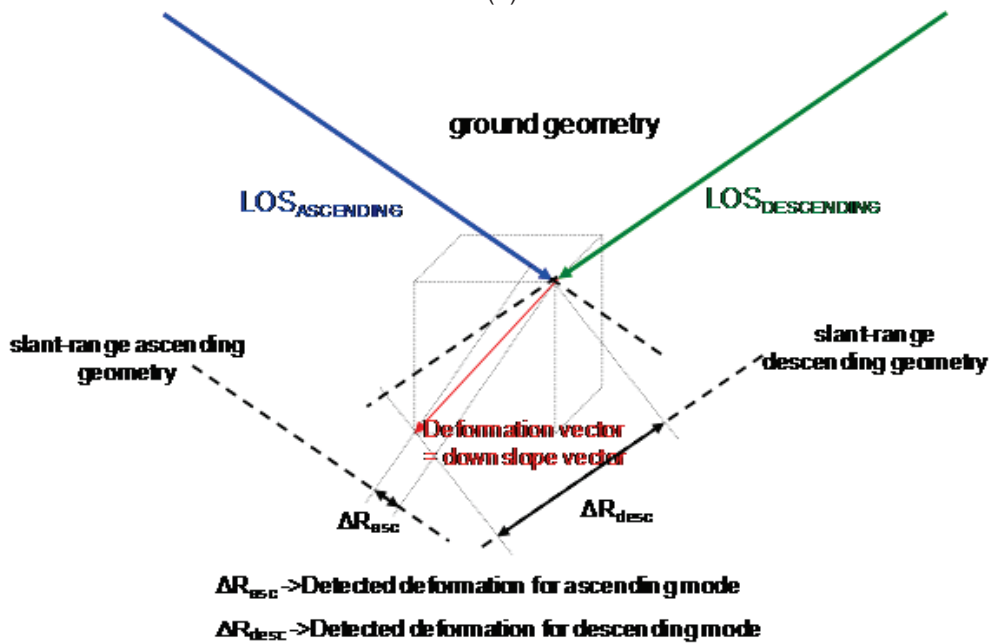
Regarding the oblique acquisition geometry DInSAR mainly measures the ground deformation in the look direction of radar, which is also referred as the line-of-sight (LOS) or slant-range direction. In most of the studies, the assumption of zero or negligible horizontal movement of the deformation was made so that the vertical deformation could be converted directly from the slant-range measured deformation. This is illustrated in figure 2.3.4. The real deformation vector in the three dimension is the one represented by the vector  $P$  to  $P'$ . Although the detected movement is the result of the projection of this vector into the sampling direction which is the slant-range direction,  $\Delta\rho$ .

This assumption of the vertical deformation is not always satisfied when applied to different real cases which can be found in nature, such as for example in case of landslides which generally occur in moderate terrain slopes. Then, it must be considered that not only DInSAR measures land deformation along its LOS direction, but also, that due to its small look angle, it is more sensitive to vertical than horizontal movements of the land surface. For example, one full cycle of phase change in DInSAR is equivalent to a deformation of about half a wavelength along range direction. For the ENVISAT case it represents of about 2.8 cm, this is equivalent to a vertical displacement of 3 cm or a horizontal one of about 7.1 cm. In order to resolve the horizontal deformation vector, the two acquisition modes, in ascending and descending directions, of the satellite must be combined together, see figure 2.3.5. If the deformation is purely vertical, the results derived from both orbits should be the same. Otherwise, it means that there is a contribution due to possible horizontal displacements.

Currently, most of the new SAR sensors provide acquisitions of the same area from different viewing angles, such as ENVISAT with up to seven possible image swath, see table 2.1. Thus, there is the possibility of not only of sampling the same ground deformation phenomena with different LOS, but also with ascending and descending modes, see 2.3.5. In consequence, if exactly



(a)



(b)

Figure 2.3.5: a) illustration of the two main satellite acquisition modes, ascending which generally acquires in the afternoon and descending which generally acquires in the morning. The direction of the LOS versus the north is a very important parameter to consider when one is choosing one mode or another for detecting ground deformations. The background image is copyright Googleearth. b) schematic representation of the estimated deformation (true deformation vector is highlighted in red) in function of the two acquisition modes. In that case descending mode has more sensitivity to the true movement that the ascending one ( $\Delta R_{desc} > \Delta R_{asc}$ ).

the same ground area could be observed under three different perspectives the an estimation of the 3-D deformation vector could be performed. It is only a question of solving an equation system with 3 unknowns shown by equation 2.3.5, which requires a minimum of three observations from different points of view.

$$\begin{bmatrix} -\cos\theta_{sar1} & \sin\theta_{sar1}\cos\varphi_{sar1} & \sin\theta_{sar1}\sin\varphi_{sar1} \\ -\cos\theta_{sar2} & \sin\theta_{sar2}\cos\varphi_{sar2} & \sin\theta_{sar2}\sin\varphi_{sar2} \\ -\cos\theta_{sar3} & \sin\theta_{sar3}\cos\varphi_{sar3} & \sin\theta_{sar3}\sin\varphi_{sar3} \end{bmatrix} \begin{bmatrix} MOV_{UD} \\ MOV_{EW} \\ MOV_{NS} \end{bmatrix} = \begin{bmatrix} MOV_{los1} \\ MOV_{los2} \\ MOV_{los3} \end{bmatrix} \quad (2.3.5)$$

where  $\theta$  is the local incidence angle and  $\varphi$  is satellite track heading angle (flight direction versus the north). Then with three different line of sight vectors sampling the same phenomenon (but at different epochs) it is possible to estimate by means of a geometric analysis the 3-D components of the true vector of deformation (up-down, east-west and north-sud directions). However, under a practical point of view and due to the reduced sensitivity of the radar sampling in the north-south direction the number of unknowns regarding the deformation vector is reduced to only two, up down and east west one.

Just as a final remark, it must be highlighted the importance of the selection of the appropriate acquisition mode regarding the orientation of the true movement that is going to be analyzed, especially if only one interferogram is available. Considering that the sampling of the movement is performed in the satellite LOS direction and that there is a higher sensitivity to the vertical component of the true deformation, it is important to spend look carefully which of the two directions (ascending or descending) are more appropriate and which could be the best incidence angle.

Mission	Origin/Launch	Frequency (GHz)	Polarization	Incidence	Repeat cycle (day)	Resolution (m)	Swath width (Km)
ERS1/2	ESA 1991/1995	C (5.3)	single	23°	1, 3, 35, 176	20x20	100
JERS-1	Japan 1992	L (1.275)	single	35°	44	18x18	75
RADARSAT-1	Canada 1995	C (5.3)	single	20°-50°	24	10x10 fine, 25x28 standard, 100x28 scansar	35 fine, 100 standard, 500 scansar
ENVISAT	ESA 2002	C (5.331)	single, dual pol	15°-45°	35	20x20 image mode, 30x30 AP, 80x20 scansar	100 image mode and AP, 400 scansar
ALOS	Japan 2006	L (1.270)	single, dual and full pol	8°-60°	46	7-88 fine, 100 scansar, 24-89 full pol.	40-70 fine, 250-350 scansar
RADARSAT-2	Canada 2007	C (5.3)	single, dual and full pol	20°-58°	24	3 ultra-fine, 10 fine, 100 scansar, 25 full pol.	50 fine, 170 standard, 500 scansar
TERRASAR-X	Germany 2007	X (9.6)	single, dual and full pol (experimental)	20°-55°	11	1 spotlight, 3 stripmap, 20 scansar	10 spotlight, 30 stripmap (15 dual pol), 200 scansar
COSMO-SKYMED	Italy 2007	X (9.6)	single, dual	20°-55°	1, 8, 16	1 spotlight, 3 standard, 20 scansar	10 spotlight, 60 standard, 250 scansar
SENTINEL-1	ESA 2012	C (5.3)	single, dual pol	20° - 45°	12	5x4 stripmap, 20x5 wide swath, 80x25 extra wide	80 stripmap, 240 wide swath, 400 extra wide

Table 2.1: Main characteristics of past, present and future civilian and most common used spaceborne SAR mission. For further details consult [Mas08] or visit the webpage of the associated space agencies or image providers of each sensor.



## Chapter 3

# Persistent Scatterers Interferometry

Persistent scatterer interferometry (PSI) is an extension to the conventional InSAR techniques described in the previous chapter. It mainly addresses the problem of pixel decorrelation and atmospheric artifacts that constrain classical InSAR. In this chapter the fundamentals and basis of PSI technology will be reviewed. Then, the Altamira Information's PSI technique, named Stable Point Network (SPN) and which is the base of this work, will be presented. Some important key steps of the technique will be analyzed in order to understand and to discuss the actual limitations and how they can be overcome.

### 3.1 Review of PSI technology

PSI methodology is based on the analysis of the InSAR phase considering a stacking of SAR images. Starting from a large data set of acquisitions it is possible to identify pixels presenting a reduced level of noise. Then, over those points and by means of spatio-temporal analysis of the SAR phase some information related with the scatters behavior can be estimated, such as their height, possible displacements and atmospheric perturbations which affect the SAR acquisitions. The image resolution cells where the measurements are possible are known as Persistent Scatterers (PS) or Stable Points (SP) [Usa97], as they are mainly pixels formed by elementary reflectors which presents a stable backscattering over several satellite passes.

The first technique exploiting PS like pixels was presented by [Fer01] as Permanent Scatterers technique (PSInSAR). With this technique PS pixels are identified as the ones whose phase histories match an assumed model of deformation with time. The input is a set of SAR images, these SLC's are then coregistered to a unique master geometry and all the phase differences are generated between all the images and the reference one, whatever the baseline. Hence, there is one interferogram per SLC and the input phases are ordered in time. A bit later, similar processing algorithms have been developed with some important variations regarding the processing flow chart, the image selection and the PS like selection criterion. One of this second generation of PSI algorithms was the one developed by Altamira Information [Arn03, Dur03], although and almost in parallel another techniques arised like for example [Mor01, Mor03], [Ber02], [Wer03], [Ada03].

These methods have demonstrated to be very successful for PSI analysis in areas with a large amount of man-made objects and infrastructures, which tend to be angular objects and quite often produce a good radar reflection that dominates the background scattering (clutter). Generally, these techniques are based on functional model of the temporal displacement to identify PS like pixels, which means that a minimum knowledge of the true deformation phenomena is required a priori. Usually, deformation phenomena that can be found in nature are very complex events which depend on many variables. Hence, it is impossible to define a theoretic deformation model that fits perfectly in almost all the cases. Some of the deformations are assumed to be steady-state (earthquakes) or more or less periodic (thermal dilation). However, it is precisely the temporal nature of the deformation what one wish to determine. For instance, volcanoes often deform in a very episodic and non-steady fashion. Also the temporal patterns of deformation during transient fault slip events and post-seismic ones are not known a priori. In consequence, if the methodology for selecting pixels as PS is based on functional models there is a risk of losing points of measurement when the true deformation pattern does not fit the model.

For this reason some of the methodologies have been invested for the development or the application of phase unwrapping methodologies in order to unwrap the input InSAR phases over the PS like pixels [Pep06, Hoo04, Kam04]. These kinds of approaches have the advantage that they are model free and hence there is no risk (a priori) of not selecting points of measurement because their deformation does not fit the model. However, it must be highlighted that solving a phase unwrapping problem based on sparse data is a very tedious and complicated problem, technically and computationally. In addition, as was already mentioned in section 2.2.4, phase unwrapping generally performs an estimation of the true unwrapped InSAR phase, hence it could fail, and contain false alarms and outliers as any other estimation methodology.

Within this PhD the Stable Point Network technique is going to be set as reference. Several processing steps will be presented and discussed in order to analyze their limitations and to understand the proposed approaches in order to overcome these drawbacks. However, before entering into technical details regarding SPN technology it is interesting to discuss about the nature of a PS.

## 3.2 What is a PS

A PS is any ground target that keeps its reflection properties along a set of SAR acquisitions. It is characterized by a strong and stable radar response, that dominates the SAR resolution cell response. As result these kinds of image pixels have a reduced noise level allowing reliable phase measurements in repeat passes. Generally, temporal changes of the scatterer or its surroundings, different look angles, volume scattering and thermal or processing noise result in a increase of the phase noise within the resolution cell, leading in some cases into a loss of coherence in the repeat passes. However, for this kind of good pixels all these decorrelation effects do not exist or are negligible in comparison with the response of the main target presented within the pixel. As illustration of the explained above, in figure 3.2.1 it is depicted the construction phase of two different kinds of pixels. On the left column it is presented a resolution cell with a lot of single reflectors more or less of equal backscattering and distributed randomly within the pixel. On the right, there is more or less the same situation but with one main target with a strong backscattering

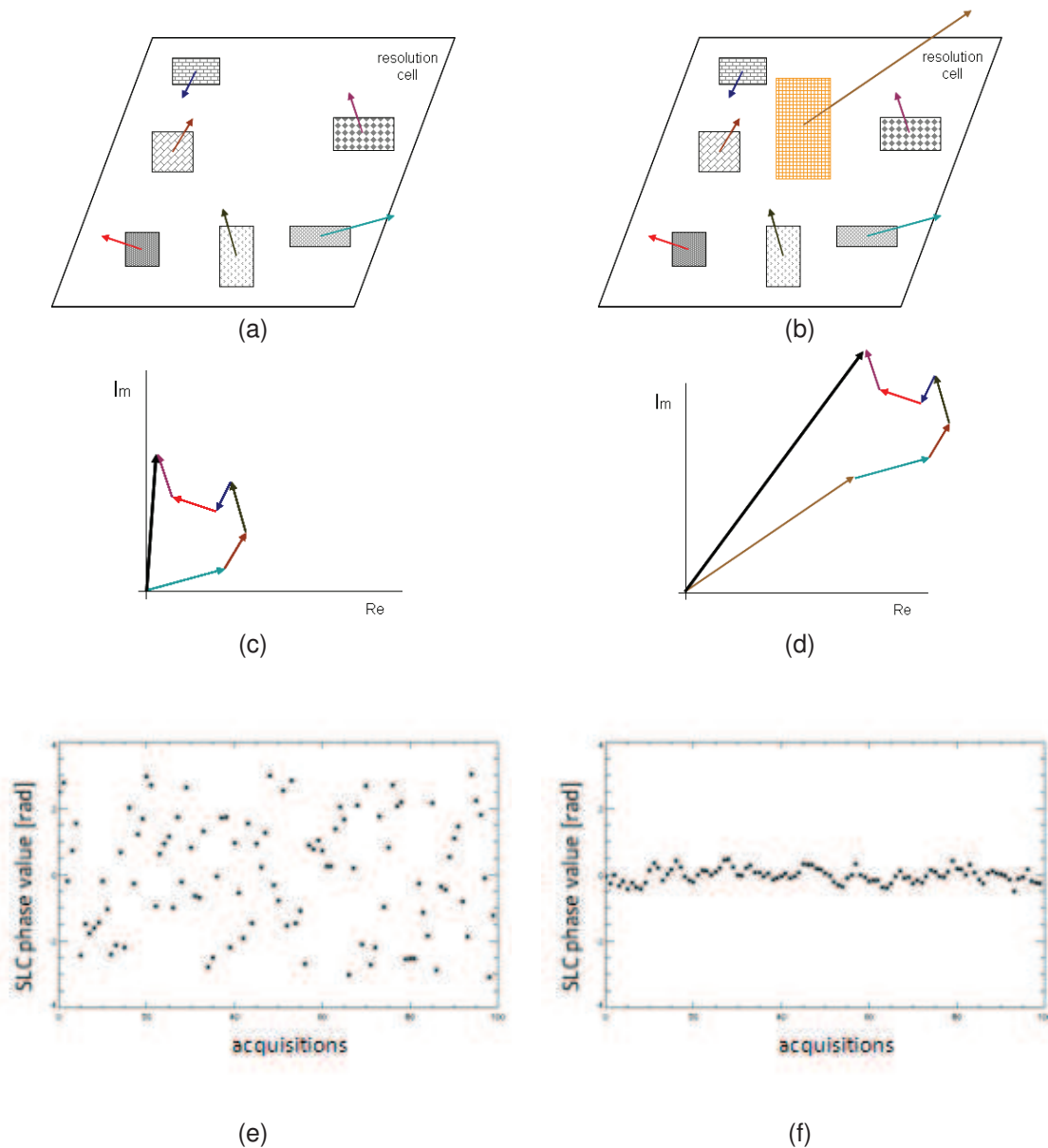


Figure 3.2.1: Illustration of the SAR inter-pixel behavior for a distributed target like pixel (left column) and for a persistent scatterer like pixel (on right). a) the SAR pixel is formed by several spread single targets of more or less equal backscattering. b) the same SAR pixel as in (a) but with a main reflector (the red one) on it presenting a strong radar backscattering regarding the surrounding single targets. c) the construction phase of the pixel as result of the coherent addition all the distributed target's responses contained within the pixel and in d) considering also the contribution of the main reflector with the dominant backscattering. e) estimation of the SLC phase value for a stacking of 100 acquisitions for the distributed target like pixel case and f) for the PS like one. The standard deviation for the second case (f) is extremely lower than in the first case (e) allowing reliable measurements.

coefficient within which dominates completely the SAR response for this pixel (the red one in figure 3.2.1).

As it was explained above in section 2.1.2.3 the degree of decorrelation within a pixel depends on the distribution of the scattering on the ground. The SAR phase of a pixel is the result of the coherent addition of all the single reflections. In the case in which the distributed targets present an equal backscattering level, this kind of addition can be constructive or destructive depending on the particular conditions of each acquisition, like for instance the baseline, the time separation,

the wind conditions, the soil moisture, etc. This is illustrated by means of the images on the left column in figure 3.2.1. As result of the constructive and destructive coherent addition the phase of this pixel for a stacking of SLCs is completely decorrelated, see figure (figure 3.2.1.e).

However, if one good and powerful reflector is presented within the same pixel, then the coherent addition is completely dominated by this high backscattering signal, see images on the right column in figure 3.2.1. In that case, depending on the radiation pattern of the coherent backscattering of this particular object its SAR response can remains stable or unchanged in a stacking of SLCs, see figure 3.2.1.f. Then, the phase detected for this pixel will give almost the same value in a set of acquisitions, allowing to perform reliable estimations of the evolution of the travel distance along the SLCs. The fluctuations of the detected phase in figure 3.2.1.f are due to the variation of the clutter within the set of SLCs when performing the construction phase for each acquisition, see figure 3.2.1.d.

Physically, strong and stable scatterers are present in areas with man-made structures and buildings. Urban areas offers a lot of corners allowing double bounce in the reflection of the radar wave, resulting in a robust and strong backscattered signal under different view angles. However, reliable pixels of measurements can be found also in natural areas like for instance: in presence of a single large rock in country areas; solid lava in volcanoes; sand areas in arid terrain or deserts, etc. [Usa99, Usa00].

### 3.2.1 Why not all targets exhibit a PS behavior?

In reality, complex reflection mechanism occur. They are very complicated to analyze due to the difference between the wavelength and the resolution cell, see sections 2.1.2.2 and 2.1.2.3. In consequence, not all the pixels keep the radar signal reflection stronger and stable for different acquisition configurations. Thus, the stability of a pixel can be defined within a particular set of conditions of existence. Some interesting discussions can be stated in order to analyse the electromagnetic behavior of the targets, and why not all targets or SAR pixels present a PS behavior.

#### 3.2.1.1 Type of reflection As it was highlighted above, different kinds of reflection can occur, as depicted in figure 3.2.2.

As it can be observed in the formulas depicted in figure 3.2.2 each type of reflection presents its own backscattering radiation diagram pattern [Mas08]. In other words, each kind of object (specular, dihedral, trihedral,..) is characterized by its own backscattered power and angular bandwidth, which varies in function of the number of bounces, size of the object with respect to the wavelength and of course the orientation of the object in relation to the LOS. Hence, as it can be observed in figure 3.2.2 the maximum backscattered power corresponds to the specular reflection, but at the same is the object offering the narrower angular bandwidth (in the order of one degree). It means that the returned power will change a lot in function of the baseline and most probably there will not remain stable for a stacking of SLCs. On contrary, the trihedral reflection is offering a extended range of angular bandwidth (of about  $40^\circ$ ) at the price of a reduced maximum backscattered power. This is more convenient because it means that the ground target will keep the reflection properties for a large set of acquisitions, independently of the baseline.

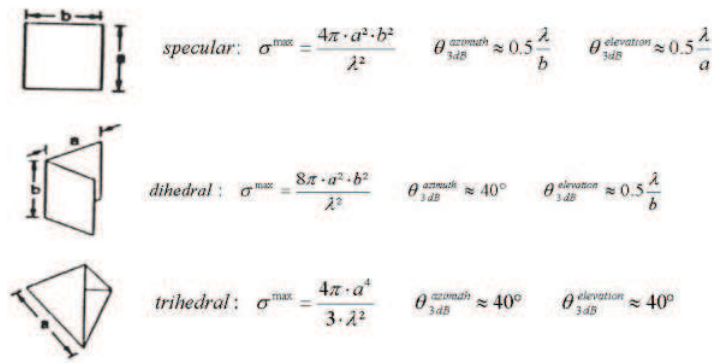


Figure 3.2.2: Different types of reflections for single scatterers in nature in function of the number of signal bounces.

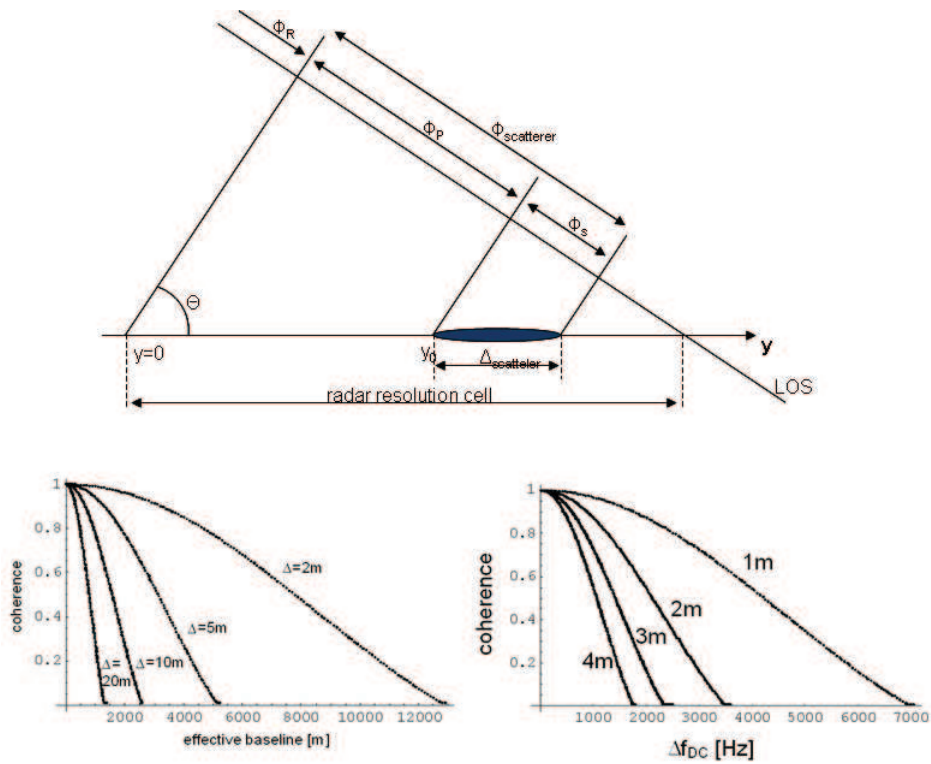


Figure 3.2.3: Estimated decorrelation term in function of the size of the scatterer and the acquisition geometry. The larger the object is the faster the coherence decreases when considering different acquisition geometries [Alt04].

### 3.2.1.2 Ground object size

Then, as it can be inferred from the explanation above, related to figure 3.2.2, that one important parameter to consider if one main target is presented within the pixel, is its size. For example, considering a unique scatterer within the resolution cell, in function of its size and the acquisition geometry of a repeat pass (different baseline, different image Doppler centroid or squint angle [Sch93]) there can be found different levels of decorrelation for the same pixel, see figure 3.2.3 [Alt04].

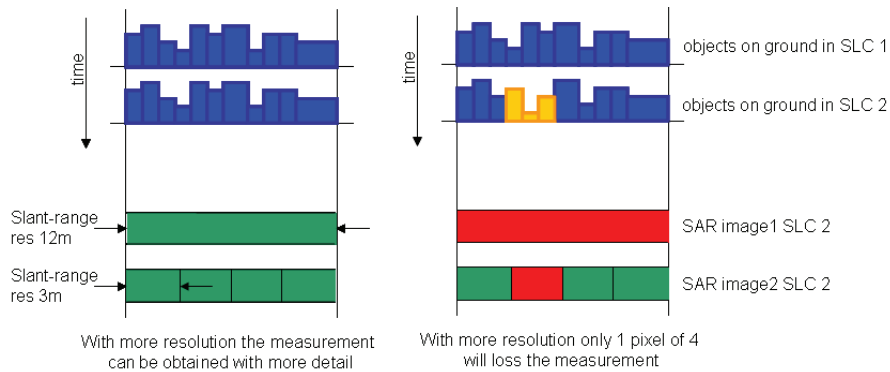


Figure 3.2.4: Illustration of the effect of the image resolution in the chance of having PS like pixels especially regarding temporal decorrelation. If some changes occur during the repeat passes for the objects on ground (affecting the ground objects highlighted in orange on the right column) then the low resolution SAR will lose the measurement over this resolution cell due to the changes in the construction phase induced by the orange one scatterers. However, with the higher resolution sensor only one of the four pixels which sample the same ground area will be affected.

### 3.2.1.3 Wavelength

The operation frequency, and thus the wavelength, must be considered. Large wavelengths are less sensible to changes in the relative distances between single reflectors. Hence, it will support better the inter-pixel decorrelation than smallest wavelength (see equation 2.1.7, as it could be observed the phase is wrapped in function of the range distance in relation with the wavelength).

Furthermore, the penetration of the radar signal inside the medium depends on the observed terrain nature and the wavelength. Depending on the ground layers at where the reflection occurs the backscattering properties can be kept or not in repeat passes. Generally, the penetration depth increases with the wavelength [Mas08]. It means that at lower frequencies (L,P), the wave penetrates deeper than at higher ones (C,X), see figure 2.1.12. It is then important to highlight that depending on the geometric and dielectric properties of the observed terrain the selection of the appropriate operating wavelength can be a very important factor considering the PS density.

### 3.2.1.4 Radar resolution

The resolution of the radar imaging system is also another parameter to consider. Temporal and geometric decorrelation have a lower impact on high resolution data. As the pixel has a reduced size the amount of single reflectors that can be found within a pixel is reduced, especially in pure urban areas where a lot of man-made metallic objects can be found very close one to each others (like for instance the roof of a building with TV antennas, air conditioning systems, solar panels,..). The probability of having a PS like pixel becomes higher when increasing the resolution as there is more chance of having only one main reflector which governs completely the SAR response over the surrounding single reflectors for each pixel, see figure 3.2.4 for illustration of the explained above.

The figure 3.2.4 presents an example of the effect of the resolution on the probability of detecting PS like pixels. The same ground surface (composed of different kinds of targets) is sampled by two imaging sensors with two different SAR resolutions. In particular, one is four times the

other (resolution of 12 meters versus 3 meters). It means that, the same illuminated ground surface results in only one SAR pixel for the first sensor and in four pixels for the second one. Then, if one consider that in repeat passes some changes can occur then in some particular ground targets (the orange ones in the second repeat pass presented on the right column in figure 3.2.4) the reflection and or the construction phase would change completely. In that case the stationary condition in order to perform interferometric measurements will not be accomplished for the whole pixel. However, in case of high resolution data only the pixels which contains the affected ground targets will be polluted, while the other ones still keeping the phase reflection properties for the repeat passes. It means, the coherence will be preserved and allow reliable phase measurements.

### 3.2.1.5 Functional models

Functional models are used in PSI methodologies (in a major or in a minor way) in order to unwrap the input interferometric phases. A very simple and basic model can be written by means of equation 3.2.1[Fer01]:

$$\phi_{int} = \phi_{topo} + \phi_{mov} + \phi_{atmo} + \phi_{noise} \quad (3.2.1)$$

where  $\phi_{topo}$  is the phase due to the height of the target,  $\phi_{mov}$  is the phase due a possible deformation,  $\phi_{atmo}$  is the phase term introduced by the atmospheric delays induced in the travel phase of the scatterer and  $\phi_{noise}$  contains all the other terms not considered in the previous terms plus the decorrelation noise of the target itself. In case of PS like pixels, the major contribution to the wrapping of the phase is the topographic and the deformation terms. Then, a precise phase model which considers these two terms can be written as [Fer01]:

$$\phi_{topo} = \frac{2\pi}{\lambda/2} \cdot \frac{B_T}{R \cdot \sin(\alpha)} \cdot \Delta h \quad (3.2.2)$$

where  $B_T$  is the perpendicular baseline, R is the slant range nominal distance and  $\alpha$  is the wave local incidence angle. Thus, the relation of the phase with the point height  $\Delta h$  (which is the unknown) follows a linear relationship. Meanwhile, for the deformation pattern a possible functional model can be formulated by means of assuming linear deformation pattern of the observed movement as follows:

$$\phi_{mov} = \frac{2\pi}{\lambda/2} \cdot \Delta T \cdot \Delta v \quad (3.2.3)$$

where  $\Delta T$  is the time span of the interferogram (the difference between the two acquisition epochs) and  $\Delta v$  is the unknown which is the linear deformation rate. Then, again a linear relationship between the interferometric parameters and the unknown is used in equation 3.2.3 to derive the deformation quantity, as well as in equation 3.2.2 for the estimate of the topographic term.

The noise term in equation 3.2.1 accounts for the inconsistencies of the stated model. In consequence, what if a target has a very good and stable radar backscattering but a deformation model which is not linear in time, or if within the same resolution cell there is another strong target with a very different height value which pollutes the height model, as depicted in figure 3.2.5. In

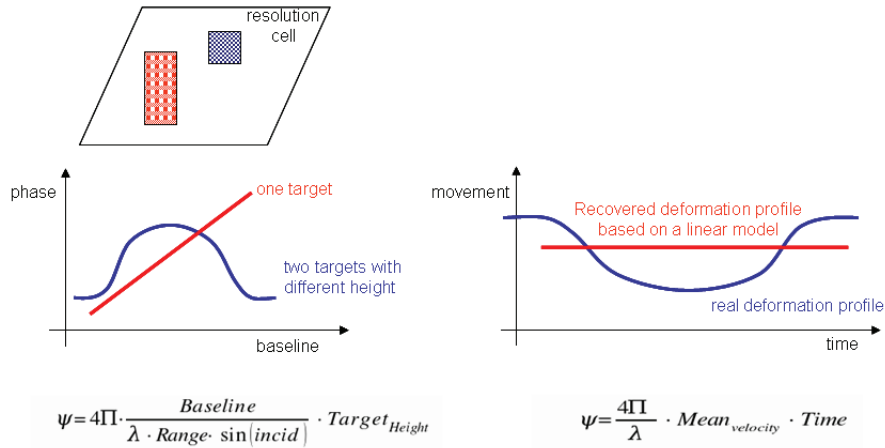


Figure 3.2.5: Illustration example regarding the loss of detection of a PS if the functional model is wrong or does not fit the real situation.

these cases, the point target can be out of model resulting in a very high noise term. Then this point will be discarded as PS.

It is important to highlight that this problem depends on the functional model used by each technique. In particular, it is a problem that affects SPN and hence should be considered.

## 3.2.2 Estimating PS like pixels on radar images

Given a set of SAR images, PSI methodologies exploit only a particular class of pixels, namely those that correspond to points that show a stable electromagnetic behavior over the observation period. PS-like pixels are typically parts of man-made infrastructures and natural features not covered by vegetation or water. Depending on the available number of SAR images and on the type of analysis which must be performed several selection methods can be used for identifying PS like pixels. Some of them are listed and discussed below.

### 3.2.2.1 SAR amplitude stability

The analysis of the SAR amplitude stability over a set of acquisitions of SLCs can be used for selecting PS like pixels [Fer01]. Pixels with low amplitude standard deviation within the stacking of images are selected as radiometrically stable. In [Fer01] is demonstrated by means of a numerical simulation that pixels with a reduced dispersion index  $D_a$  have a reduced phase standard deviation.

$$D_a = \frac{\sigma_a}{m_a} \approx \sigma_{\phi_a} \quad (3.2.4)$$

where  $\sigma_a$  is the estimated amplitude standard deviation and  $m_a$  the estimated mean amplitude when considering a set of SLCs. Then, as it is depicted in figure 3.2.6, for low values of  $D_a$  (below 0.25) it can be observed the same trend as for the pixel phase standard deviation curve. In consequence, this relation enables the identification of pixels with a stable phase without the need of analyzing carefully this magnitude (which is wrapped at this initial step of the processing).

This approach is very suitable for high resolution processing as the dispersion index does not account for neighboring pixels. That enables the selection of isolated points at SLC image full resolution which is not possible with other methodologies, as for example the ones based on a stacking of the interferometric coherence [Mor01]. One of the main drawback is that, as the computed standard deviation method is an estimator of the real magnitude, it depends on the number of samples. In consequence, the estimation is biased when a reduced number of images are used (below 25 [Fer99b]). The real amplitude standard deviation is underestimated. Hence, the number of false detection (noise or non-coherent pixels selected as PS) increases within the performed selection.

The numerical simulation described in [Fer01] has been repeated here, the results are presented in figure 3.2.6. For larger values of the amplitude dispersion index, the relation with the phase standard deviation is no linear. However, points with a lower level of  $D_a$  are expected to have a reduced level of phase noise. Therefore, selecting pixels by means of threshold the  $D_a$  value is a way of detecting pixels with a reduced phase standard deviation. It can be stated that for  $D_a$  below 0.25, both curves follow exactly the same trend. From 0.25 to 0.5 the curves start to be in disagreement although the value for the phase standard deviation remain not very high, (below 0.35 radians). It means that in case of low density of PS this threshold could be relaxed assuming that more noise will be entering in the PSI processing.

It is important to highlight that the number of available acquisitions is a critical parameter when computing the amplitude standard deviation. As depicted in figure 3.2.6 in function of the available number of acquisitions, the standard deviation of the  $D_a$  estimator increases (compare the error bars on the plot on the left (a) -10 SLCs- and on the right (b) -50 SLCs-). In addition, looking carefully the trend for the two curves (phase standard deviation and  $D_a$  estimator) for lower values of noise in both plots in figure 3.2.6 it can be noticed how the dispersion index estimator becomes biased when performing this analysis with a reduced number of images. In other words, the  $D_a$  curve presents a lower value than for the curve on the right, considering the same phase noise standard deviation curve for both cases. Those two facts must be considered when performing a selection by using this methodology in case of few acquisitions are available. In other words, the value for threshold the  $D_a$  may be decreased in order to keep the probability of false alarm or false detection achievable for a large stacking of SLCs.

It is important to highlight that the images need to be radiometrically calibrated in order to allow a reliable estimation of the standard deviation and the mean. Several possibilities can be considered:

- Absolute calibration of the SLCs based on the image annotation parameters [Lau98, Alt04]
- In case in which the annotation parameters are not available, a relative calibration of the SLCs can be roughly performed by means of the equalization of the sigma-zero parameter performed over bright areas distributed all around the image swath [Bov02, Alt04].

### 3.2.2.2 Stacking of the interferometric coherence

The selection of PS like pixels is performed by means of the threshold of the interferometric coherence for a given set of interferograms [Mor01]. The main drawback is the reduction of resolution due to the used coherence estimator, which is performed by means of a window multilooking, see

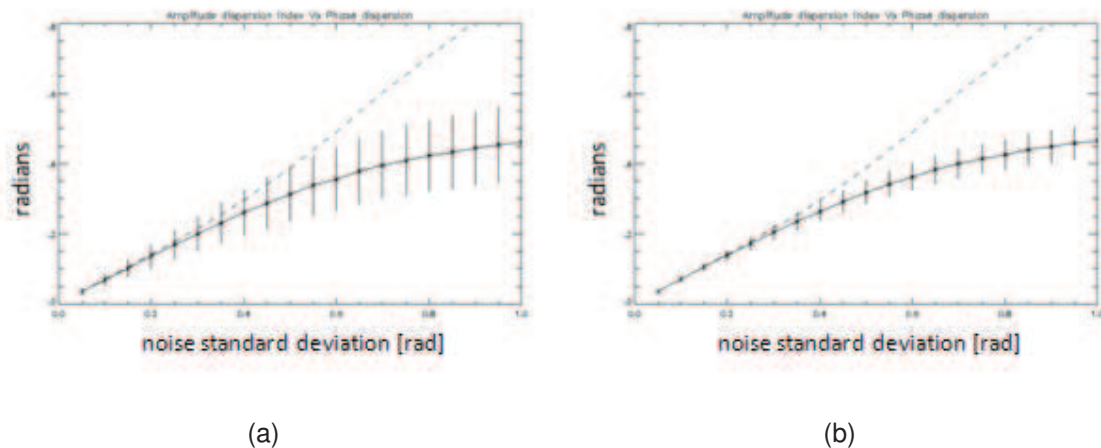


Figure 3.2.6: Numerical simulations for the amplitude dispersion index as presented in [Fer01]. The estimation of the  $D_a$  index is simulated numerically by means of a random addition of phase noise to a complex variable (as one SLC pixel with an I and Q channel). Then, this phase noise per SLC variance is increased gradually analyzing the evolution of the  $D_a$  index, as well as the dispersion of the estimator and the pixel phase standard deviation in function of the noise power level. On the left (a), this simulation is performed for only 10 SLCs while on the right (b) 50 acquisitions were considered. With less samples the  $D_a$  estimator performs worst presenting higher variance and a biased curve.

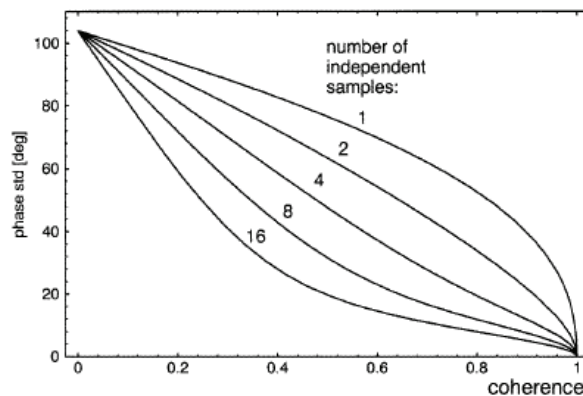


Figure 3.2.7: Standard deviation of the InSAR phase estimated in function of the coherence and in function of the number of samples used in the multilook, extracted from [Bam98].

section 2.2.5. This selection method is usually adopted if a medium or low resolution PSI analysis is required (for example for large scale deformation analysis [Hu06]).

This methodology can also be applied in the case in which few SLCs are available. The fact of working with a multilooked version of the interferometric phase implies (in addition of a loss of resolution) an increase of the phase SNR, see figure 3.2.7. Figure 3.2.7 shows the InSAR phase noise standard deviation in function of the coherence and in function of the number of independent looks (number of samples used in the multilooking). It is important to note that for high coherence values an averaging of  $L$  independent samples are translated into a reduction of the phase noise of about  $1/\sqrt{L}$ . Thus, a tradeoff must be found in terms of increase of the SNR and loss of resolution in function of the number of images and the required density of PS per square Kilometer.

This methodology is suitable not only for selecting PS like pixels when only few SAR images are available but also when the area of interest is a sub-urban or a country area. Thanks to

the spatio-temporal analysis of the interferometric coherence it is possible to detect pixels with a reduced InSAR phase variation in space. In other words, it is possible to detect a high interferometric coherence in areas where the ground surface is very uniform (radiometrically speaking). Like for instance sand or arid terrain free of vegetation and water, lava field close to volcanic areas, rock fields in mountainous areas, etc. [Her09, Hu06].

### 3.2.2.3 Other methodologies

Other methodologies for the PS selection are available. They are less common due to their lower robustness, and sometimes, due to their high computational coast. However, some of them have some interesting advantages that could be considered in special cases [Alt04].

#### Time-frequency image analysis (TFA):

The spectral sub-band image analysis can be used when a very reduced data set of images is available and at the same time, it is mandatory to keep the full resolution of the SLC. By means of this methodology the candidates for becoming PSs are identified within each image by means of a spectral azimuth sub-band analysis. The stable points are then selected by selecting the candidates which are common to the entire SAR image stack. The main basis of the methodology is that in SAR images backscattering may vary over the integration time. Such fluctuations provide additional information on the illuminated objects. A Time-Frequency Analysis (TFA) allows for tracking such instabilities, like for instance through a spectrogram. The behavior of some particular pixels can thus be compared to the one given by a perfect theoretical Persistent Scatterer. Some targets, like man-made metallic plans, have a very directive antenna pattern in space or frequency (specular reflection, see figure 3.2.2). However, other targets such as the trihedrals are isotropic and their backscattering variations is very stable compared to a natural ground target such as grass, trees or water surfaces. However, backscattering diversity is lost in synthesized SAR images and specific and complex signal processing is required to get back this information, see [Tis06].

#### Threshold the Signal to Clutter Ratio (SCR):

With this methodology pixels above a particular threshold of SCR in a set of images are selected as PSs [Ada04]. A direct relation between the SCR and the SLC phase error can be written as :

$$\hat{\sigma}_{\phi} = \frac{1}{\sqrt{2SCR}} \quad (3.2.5)$$

Thus, for a particular value of SCR, the maximum phase standard deviation can be known. The main basis is that for a PS like pixels the SCR must be over a particular value within a set of images. PS like pixels (like man-made artificial trihedral corner reflectors) usually have an isotropic radiation pattern. The main problem resides in the fact that the SCR computation is an estimation of the real SCR which makes the assumption that the power around the pixel is equal to the power inside the resolution cell (around the point target). Thus, if this method is applied in pure urban areas the clutter is likely to be overestimated using this assumption. As it can be commonly observed in SAR images man-made infrastructures, such as buildings, give a very high

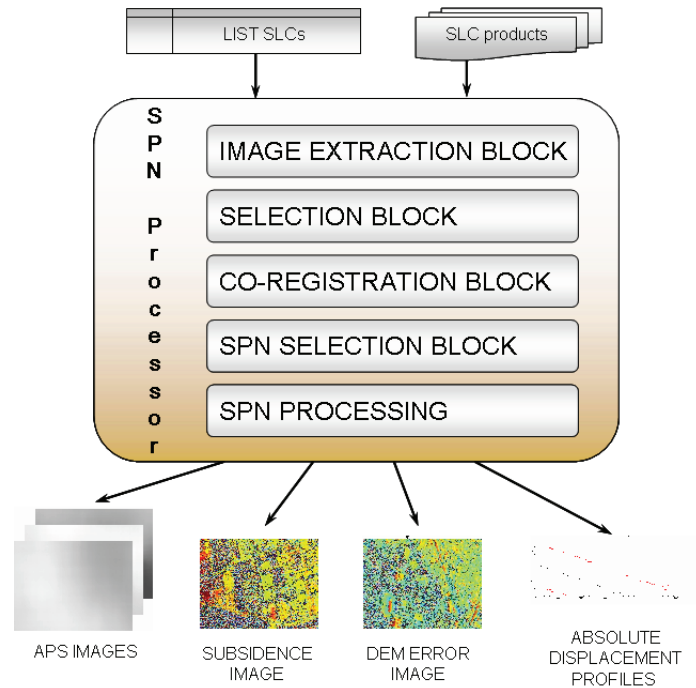


Figure 3.3.1: SPN processor main flow chart.

SAR reflectivity. In that case the SCR would trend to indicate that the power for the signal is equal to the power of the clutter, which can be leading to a lower bound for a particular threshold.

It is a simple methodology which has a very high computational cost. Although it performs very well in country or sub-urban areas where the mean clutter power is not dominated by man-made infrastructures. It works at full SLC image resolution with no limit in the minimum required number of images.

### 3.3 Stable Point Network technique

SPN is a PSI processing technique developed by the company Altamira Information in 2003 [Arn03, Dur03]. It makes use of differential interferometric phase measurements to generate long term terrain deformation and digital surface model maps. The estimation is performed pixel-by-pixel without the use of any spatial interpolation. The algorithm is capable of using all the phase information even in conditions of large baseline or platform instabilities [Mir03]. These effects are handled by precise estimation of the location of the equivalent mean phase center within the SAR pixel. In figure 3.3.1 is depicted the main flow chart of the complete SPN processor.

The processor operation requires as main input a set of SAR acquisitions, in level 0 or level 1 product format. At the end of the processing, the SPN generates three main products:

- The mean linear deformation rate map: it is the the result of the adjustment of a linear model of deformation in time for every scatterer. It assumes that the main part of the energy of the observed deformation signal follows a linear model of deformation in time (the first term in the Taylor's series).

- The digital surface model map: it is the height difference between the elevation given by the DEM used to generate the input DInSAR phases and the elevation of the scatterer (at which the signal is reflected) on ground. In case a very precise DEM of the ground surface is used, this estimate is close to zero for almost all the scatterers. It can be understood as a correction of the height value given by the DEM.
- The accumulated deformation value for every SAR epoch. It is the estimated final time series of the deformation sampled at the epoch of each acquisition. The linear part estimated above is used to unwrap the phases and to recover here the true profile of the deformation in time. Thus, this time series should account for the non-linear part of the deformation pattern in time.

The SPN processor relies on the DIAPASON [CNE98] interferometric chain for all the SAR data handling, coregistration work and interferogram generation. As it is depicted in figure 3.3.1 the SPN processor is based on five main modules:

- Image extraction: SAR data is read from the original media and all the auxiliary parameters are retrieved from the product annotations into ASCII auxiliary files.
- Image selection: Considering the complete set of available images the optimum selection of interferometric couples is set based on the acquisition time, the perpendicular baseline and the Doppler centroid difference of each image.
- Image coregistration: One image is selected as super master. All the other SLC data-sets are then coregistered to the geometry of the super master. It is exactly the same step that the one performed for classical InSAR.
- SP selection: Selection of the initial mask of stable points (PS like pixels), which are pixels with a reduced level of noise component.
- SPN processing: Estimation of the deformation and the point elevation from the InSAR phases

These main points will be detailed below.

### 3.3.1 Image extraction procedure

This procedure extracts the input product data and decodes the product annotations from their media support to the appropriate SPN supported format.

The input to the SPN processing chain is always complex SAR data processed as a single look complex image. These images can be obtained by either processing the RAW data product with the SAR processor integrated in the DIAPASON interferometric software or by using directly data in level 1 format. The extraction procedures are exactly the same as the ones presented in section 2.2.5.1. At the end, a raster file with the SLC image and all the necessary ancillary product information such as the orbital state vectors, the precise timing image annotation for the first image sample and the Doppler centroid image value are available.

### 3.3.2 Image selection procedure

The objective of this module is to generate a list with the best interferometric combinations to be processed for the next steps of the SPN processing chain. The selection of SLC images is based on low interferometric baseline constrains. This procedure also considers the image Doppler centroid values and acquisition times in order to constrain the differential values over the set of images. Low values of Doppler centroid and of time span must be considered in order to reduce the geometric and the temporal decorrelation noise as much as possible.

### 3.3.3 Image coregistration procedure

The objective of this step is to coregister all the SLCs into the super master geometry. The technical routines are based on DIAPASON coregistration process, see section 2.2.5.5. At the end of this step all the SAR images will be in the same geometry, i.e. containing exactly the same ground terrain area for each pixel in all the images.

A key parameter is the selection of the super master geometry. In principle, it may be an image of the data set which minimize a cost function based on the acquisition time, orbital baseline and Doppler centroid value. This cost function can be based for example on the Euclidean distance to the mean baseline, mean Doppler and mean date of the acquisitions. Furthermore it should be an image with a reduced component of thermal noise and atmospheric artifacts. However, it is very difficult to evaluate those terms at this step of the processing.

#### Generation of the interferometric phase

Once all the images are on the same geometry, the interferometric phases can be computed. The procedure is exactly the same as the one presented in section 2.2.5.6. It is important to highlight that the phases must be as clean as possible of fringes. Thus, it is desirable of using a DEM in order to compensate for the topographical fringes, the input to the SPN process are thus DInSAR phases. Furthermore, the orbital fringes must be also estimated and compensated, as it was described in section 2.2.5.7.

### 3.3.4 Initial mask of PS procedure

Two main methodologies are considered for selecting the initial mask of stable points in classical SPN processing. The selection of the suitable methodology depends on the available number of images and on the kind of processing that must be performed. The two methodologies are the analysis of the standard deviation of the SLC amplitude (dispersion index) and the mean interferometric coherence, they are described in section 3.2.2.

- The dispersion index is used when a large data set of images is available and the data must be analyzed at full SLC image resolution. As the selection is based on the estimation of the standard deviation, in case of a reduced number of samples, the estimation is not accurate enough leading in a large number of false detection on the final mask of PSs (noisy points selected as PSs). Furthermore, as the selection is done in a pixel-by-pixel basis over the full

resolution SLC, a higher density of PS per  $\text{Km}^2$  than with multilooking methodologies can be achieved. Typical values for point of good quality spans from 0 to 0.25 or up to 0.4 for cases or areas presenting a reduce PS density.

- PS selection based on mean interferometric coherence is suitable when a reduced number of SLCs is available or when the analysis must be performed at medium SLC image resolution. The interferometric coherence is a direct estimator of the phase noise in each interferogram. The main drawback is that it is required a spatial correlation of the signal, and hence a reduction of the resolution. The multilooked pixels presenting a coherence value higher than a particular threshold in all the interferograms are selected as stable. Typically, these threshold values vary from 0.5 (high quality points) to 0.3 (medium quality points) depending on the desired PS density.

### 3.3.5 Stable Point Network analysis procedure

This procedure is the core of the SPN processor. It has as main scope the isolation of the different phase contributions based on the stacking of DInSAR phases. The starting point is an initial mask of stable points or Persistent Scatterers, the DInSAR phases and other ancillary data related to the acquisition geometry and characteristics. Over this initial mask of points, the software performs an identification and separation of the different phase artifacts based on equation 3.2.1. In other words, it performs an initial estimate of the mean deformation rate and the point height only on the PS, this is named the **low resolution SPN** as the estimates are obtained only on a reduced number of points (a reduced set of locations) giving a low resolution spatial grid of information.

Afterward, the atmospheric phase screen (APS) of each interferometric pair is estimated based on the residual phases of the PSs after removing the initial deformation and height model. This results in an image with the phase value due to the double combination of the signal delays induced by the two different atmospheric heterogeneities of both acquisitions. At the end, the same estimation based on the linear deformation rate and the height of the pixel is performed in a pixel-by-pixel basis without interpolation over the whole swath. This last step is named **high resolution SPN** as the information is obtained for each pixel. In figure 3.3.2 is depicted the block diagram of this important section of the SPN processor.

The software is composed by different modules that can run independently but following always a sequential execution flow. Each of the steps, in which the SPN technique is divided, are implemented as a separate function. The program automatically generates some log files where the user can find some information about the processing. The user can then check the input parameters in order to prove the result consistency without the need of executing the previous steps. Each module requires a minimum number of inputs which initially are defined by default.

One important point of the program is its flexibility: the software can work at any image resolution and with extracted subset of the whole image swath. Furthermore, there is no limit regarding the size of the images that constrains memory requirements, although large images increment considerably the execution time. The procedure works by blocks of lines. One of the most critical step in terms of computational cost is the size of the area of interest when performing the high resolution SPN, as the estimates are performed in a pixel-by-pixel basis increasing a lot the

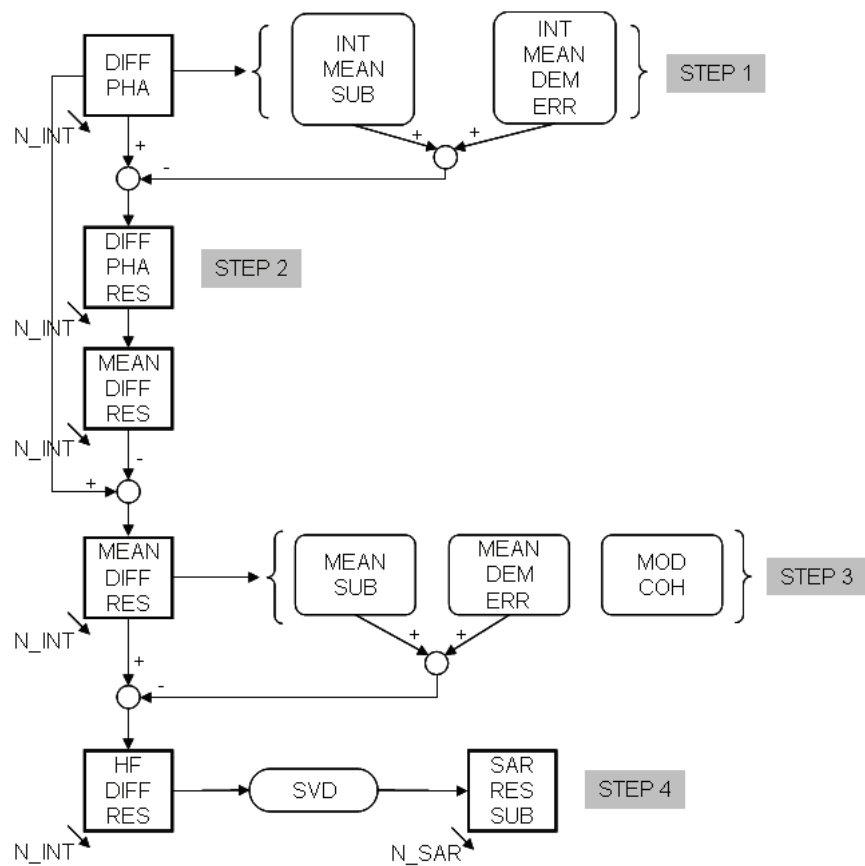


Figure 3.3.2: SPN technique detailed flow chart. It has as main scope the phase artifacts separation based on a particular DInSAR phase model given by equation 3.2.1.

computational burden when trying to analyze the full scene (approximately 2 weeks of processing using a 2 CPU computer for an image of about 5000x20000 samples in range and azimuth respectively).

Below, the different steps of the SPN technique will be detailed briefly. These steps are the base of the improvements performed within this PhD and which constitute the core of the project.

### 3.3.5.1 Relationship establishment

This step takes as input one mask with the stable points obtained by means of the SLC amplitude analysis or by the stacking of the interferometric coherence. The objective is to set a network of relationship between the points of the mask. For this purpose Delaunay triangulation [Lee90] is applied, considering as a constrain in the maximum distance allowed between nearby points, of about 1000 up to 2000 meters depending on the PS density. Afterward the information is vectorized as the useful information is only on the arcs of the network. See figure 3.3.3 for an example of network establishment on a real test site.

The use of the Delaunay triangulation presents two main advantages. First, it helps in the identification of errors in the model fitting procedure by forcing the discrete line integral along any elementary cycle (a triangle itself) to be zero or close to zero. Second, it performs an optimum geometric relationship between nearby points considering the potential of testing the possible irrotational residues. It means, it adds an optimum path redundancy per point which allows to check whether an estimation between two points was correct or not.

### 3.3.5.2 Estimation of the model parameters at network arcs

Within this step a very simple phase model is adjusted based on the interferometric observation at each arc of the network. This network was completely defined by the previous step. Then, for each arc of the network the wrapped interferometric phase difference is obtained, which is the observation (input) of the phase model adjustment (DInSAR phase difference between each two vertexes of the triangles). The phase model considers a linear deformation rate and a possible vertical height value for each arc. This height value is the difference between the elevation given by the used DEM during the DInSAR processing and the real height of the scatterer. Hence, the other common names for this estimated point height in PSI processing, DEM error, DEM correction or DEM refinement. See equation 3.3.1 with the formulation of the adjusted phase model.

$$\Delta \hat{\phi}_{xy}^i = \phi_{PSx}^i - \phi_{PSy}^i = \frac{2\pi}{\lambda/2} \cdot \frac{B_T^i}{R^i \sin(\alpha^i)} \cdot \Delta h_{xy} + \frac{2\pi}{\lambda/2} \cdot \Delta T^i \cdot \Delta v_{xy} \quad (3.3.1)$$

where  $\phi_{PSx}^i$  represents the interferometric phase at PS number x for the  $i^{th}$  interferogram.  $B_T^i$  is the perpendicular baseline value for the  $i^{th}$  interferogram, the same for the range  $R^i$  and the local incidence angle  $\alpha^i$ .  $\Delta T^i$  is the time span for the  $i^{th}$  interferometric data pair. Thus,  $\Delta h_{xy}$  and  $\Delta v_{xy}$  are the unknowns that must be estimated, the increment of vertical height and linear deformation rate between the point PSx and the PSy.

The estimation of the unknowns from the wrapped phases is a non-linear problem that cannot be solved by direct inversion. The solution is obtained by means of the maximization of a cost function which accounts for the sum of the residual phase errors, it is named the model coherence and is defined in equation 3.3.2.

$$\gamma_{xy} = \left\| \frac{1}{N} \cdot \sum_{i=1}^N e^{j\phi_{xy}^i} \cdot e^{-j\hat{\phi}_{xy}^i} \right\| \quad (3.3.2)$$

where  $\phi_{xy}^i$  is the real wrapped phase increment between the PSx and the PSy and  $\hat{\phi}_{xy}^i$  is the phase that must be adjusted. Hence, the coherence is used as a norm. The parameters which maximize the coherence value are obtained by means of a seek through a solution space. The statistical properties of the coherence operator have been described by [Col03], also in the next chapter this coherence function will be reviewed.

The coherence value lies in the interval contained between 0 and 1. A value equal to 1 implies a complete correspondence of the model with the observed phase. It means that the residual phases are exactly 0, thus a perfect match has been obtained. A value close to 0 implies that the phase residuals are very high and in consequence the model is not fitting the observed data.

As was already commented above, the observed phase data are wrapped, it means that are known module  $2\pi$ . The estimation of the parameters can only be successfully performed if the increment of DInSAR phases at the arcs of the network is less than  $\pi$  in absolute value, ( $|\Delta\phi_{xy}| < \pi$ ) in most of the available interferograms. In any case, the residual phase difference  $\phi_{xy}^i - \hat{\phi}_{xy}^i$  is assumed to be small, since the phase components (see equation 3.2.1) which define the complete PSI phase model may be small, like for instance:

- The contribution of the differential atmospheric phase screen term in the phase increment between two close PSs should be small. Typically, it is assumed on PSI processing that in average the atmospheric contribution for points separated by less than 1 Km is below 0.3 rad [Fer00]. This is however not always the case and it mainly depends on several parameters such as the particular atmospheric conditions of the acquisition, the wavelength, the incidence angle, the latitude of the test site or if the acquisition are taken during the day or during the night [Han01].
- The noise terms of the phase should be small as the points involved in the arcs are or should be PS-like pixels, and thus they are suppose to have a reduced noise component. Then, if these points are selected for example with a dispersion index of about 0.25, the equivalent phase noise is approximately below  $\sqrt{2} \cdot 0.25$  rad for all the considered differences.
- Out of model artifacts can cause large phase residual differences in some cases, especially in the case in which important non-linear ground deformation movements arise due to tunneling activities, earthquakes events, landslides, etc. However, the linear model is assumed to be a good approximation for the major number of cases, at least between two nearby points. Furthermore, the height model can be also very difficult to fit when for example there are more than one strong scatterer within the resolution cell and with a very different elevation values. This situation can be found typically in pure urban areas where different scatterers arise due to the presence of balconies, television antennas and other metallic elements with different shapes and sizes.

### 3.3.5.3 Network integration

The performed estimates are obtained in the arcs of the network. These values are thus relative between two nearby points. In order to obtain an absolute value at each point, a path integration procedure is necessary. Like in a classical Region Growing algorithm the values at the points are obtained by integrating the values of the model parameters estimated at the arcs, following a particular guided path. According to the phase model adjustment quality index (the model coherence) the path integration is carried out, from the best arc estimations to the worst ones. The algorithm does not try to connect two isolated integrated zones, below a particular coherence threshold the software stops. Therefore, several zones can be treated in an independent way along the full image swath. Later on, a post processing can be performed in order to connect those areas. However they can remain independent, although each of them are referenced to a particular PS which is the initial seed of the integration. This initial PS is the reference point, all the estimated parameters of the image are referenced to this position, which is set to zero in deformation as well as in elevation.

The selection of this reference PS is a very difficult task. It must be a PS of good quality located in a stable area, not affected by any ground deformation. This selection is thus not straightforward, if no a priori information is available. There are two main possibilities:

- The user can set the area where the PS must be located; then the software selects automatically the reference point within this area based on a quality criteria, which is related to the maximum number of arrival arcs above a particular coherence threshold.
- In case in which no area has been set, the reference point is selected in a completely automatic way. All the PSs are classified based on a quality index criteria. In parallel, their mean position is computed, in range and azimuth. Considering all the possible candidates, one of the best PSs closest to the mean PSs position, is set as reference.

Then, after the integration of the model parameter values the estimates are obtained for each PS. For visualization purposes a spatial interpolation can be performed in order to have a general overview of the result. However, due to the reduced spatial sampling the interpolated map has a very poor quality as the information is only contained at the location of the PSs. In figure 3.3.4 is presented an example of network and of the interpolated low resolution map of the mean deformation linear rate for a real case.

### 3.3.5.4 Estimation of the Atmospheric Phase Screen (APS)

It has been shown that the interferometric phase contribution due to atmospheric inhomogeneities follows a well defined variation laws [Han01]. Generally it is assumed that atmospheric artifacts have a large scale variation in space on SAR images. In addition, they are completely uncorrelated in time. This means that the atmospheric phase screen is completely different on each acquisition. Those contributions are moreover completely unpredictable, as they depend on the particular weather conditions at the acquisition epoch.

The estimation of the atmospheric phase screen term over the interferometric phase is based on a low pass spatial filter. This evaluation is done only over the PSs location, in each interferogram, after the compensation of the low resolution spatial SPN model. In other words, after

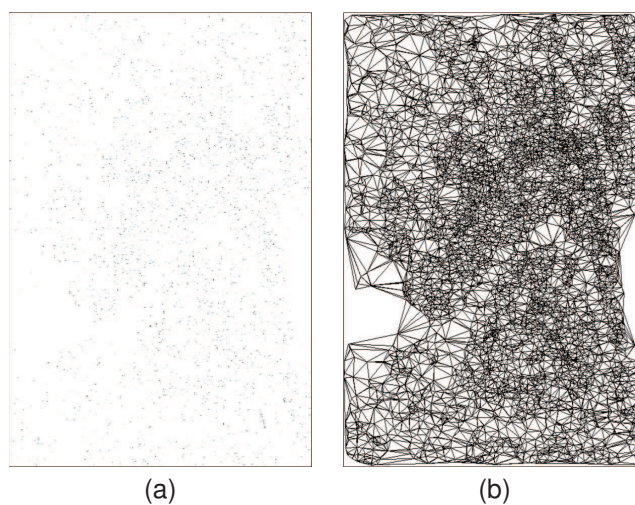


Figure 3.3.3: Example of initial PS mask (a) and the performed network of relationship based on Delaunay triangulation (b).

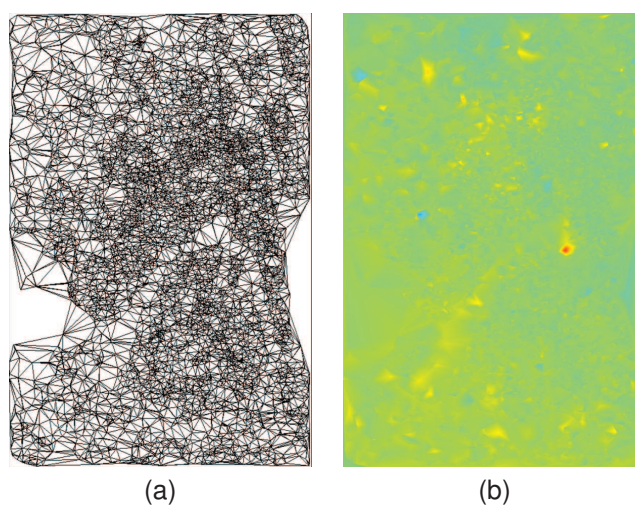


Figure 3.3.4: SPN low resolution PS network based on Delaunay triangulation (a) and integrated and interpolated map with the estimated mean deformation linear rate (b). The color table is coded between -1 (dark red) and +1 (dark blue) cm/year. The image has a size of 1500 x 3000 pixels in range and azimuth with a resolution of 8x4 meters respectively.

the removal of the estimated deformation and the height model their phase residuals of each PS present a reduced variability in space. If this residual phase is high, it would mean that the model that is being removed is not properly adjusted or that the atmospheric perturbation is a very high. It is demonstrated in the bibliography that the mean distance of correlation of the atmospheric phase screen over a SAR image is of about 1 km [Han01]. This value can vary depending on the latitude and on the nature of the test site.

### Model removal

Using the interpolated mean subsidence map and mean height estimation at each PS, a interferometric phase model is synthesized for each interferogram according to the acquisition parameters (baseline, time span, etc.). Those linear terms are subtracted from the true differential interferometric phase obtaining the Differential Linear phase Residue defined in equation 3.3.3:

$$DPR_X^i = \phi_x^i - \hat{\phi}_x^i \quad (3.3.3)$$

where  $\phi_x^i$  is the observation, the wrapped phase for the interferometric couple  $i$  at PS $x$ .  $\hat{\phi}_x^i$  is the corresponding synthesized phase. It is assumed that this residual phase is due to mainly atmospheric artifacts, residual ground deformations which do not fit the linear model and to thermal noise.

In order to ensure the suitability of the adjusted model, the full resolution InSAR phase before and after the model removal can be analyzed. The performed height estimation can be verified, for example, by comparing the phase of an interferogram very sensitive to the surface topography (a tandem pair with a temporal gap of one day) before and after the compensation of the geometrical adjusted model. This is depicted in figure 3.3.5.

As it can be observed in figure 3.3.5.c almost the total amount of fringes presented in the DInSAR original phase (figure 3.3.5.a) has been compensated. By comparing this tandem with the residual phase after the geometric SPN model retrieval (figure 3.3.5.b) it can be realized how much the amount of vertical fringes has been reduced. This interferometric tandem presents a high height of ambiguity value (of about 30 meters) which means that it is very sensitive to the topography of the surface. For that case a DEM has been used to generate the DInSAR phases and compensate for the topographical changes due to the ground terrain roughness. However, as a pure urban area is considered, the height of the buildings and other infrastructures not compensated with the DEM. In consequence, these elements are originating phase fringes in the interferograms, due to the high sensitivity to the topography. After the compensation of the height model for each PS, those fringes disappear from the interferometric phase. The residual phase becomes flat and it corroborates the appropriateness of adjusted model.

The same kind of analysis can be conducted for the SPN deformation model. One DInSAR with a large time span and over an area affected by known ground deformation phenomena can be compared before and after the model compensation for illustration purposes. In figure 3.3.6 is presented one real case as an example. As it can be observed the phase gradient presented in figure 3.3.6.a has disappeared when comparing it with the residual interferometric phase in figure 3.3.6.b. This fact corroborates the estimation of the deformation model under a qualitative point of view. It is important to note that this phase gradient is due to a ground movement and not to an atmospheric artifact (not already compensated at this step). It must be moreover highlighted

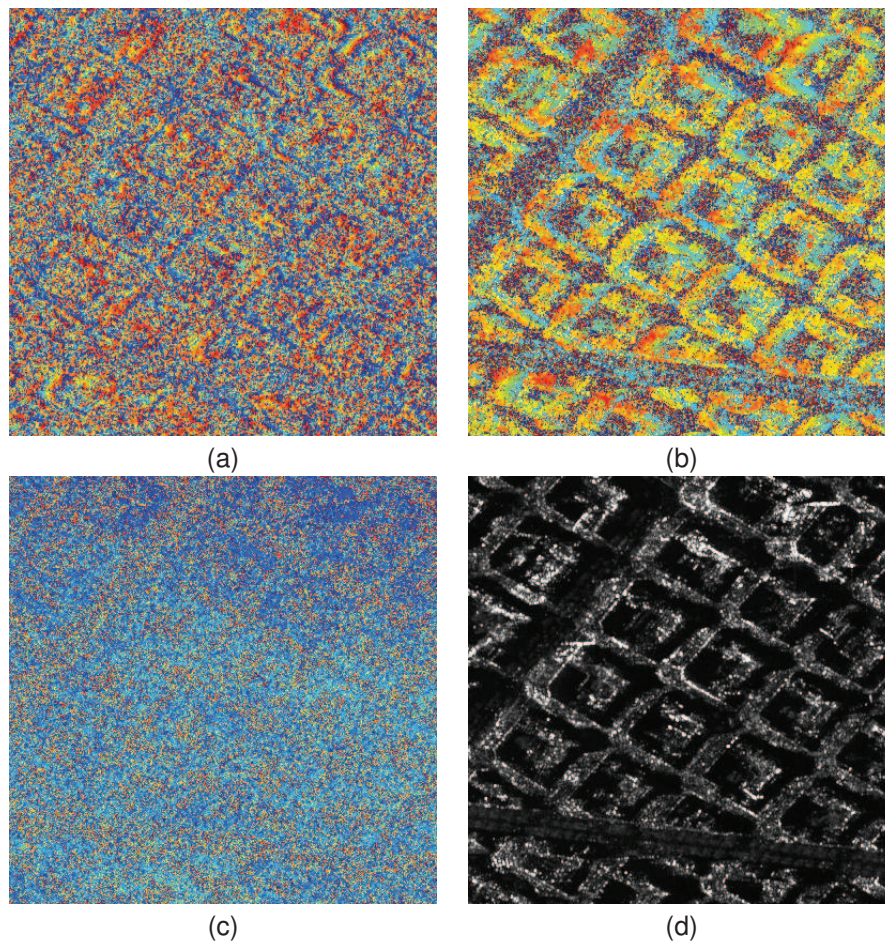


Figure 3.3.5: Illustration example of phase model compensation with TerraSAR-X stripmap mode data. a) DInSAR phase of at full resolution (3x1.5 meters approximately) with a height of ambiguity value of about 30 meters. All the observed fringes (blue to red colorable has been used) are due to the ground surface relief due to the buildings and other man-made infrastructures. That results in this typical pattern of fast fringes in range direction. b) Estimated height value for each pixel based on the ajustement of the SPN phase model given by equation 3.2.2. c) The same interferogram as in (a) after the removal of the SPN geometrical model. As it can be observed the phase has become flatten. The fringes has disappeared. This fact makes reliable the estimated geometrical mode. d) SAR multimean image of the presented pure urban area.

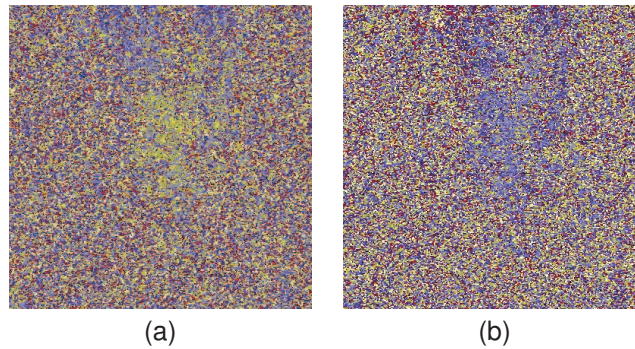


Figure 3.3.6: DInSAR phase of an area affected by ground deformation before (a) and after (b) the compensation of the SPN estimated deformation model. As it can be observed by visual comparison the phase gradient presented in the area within the red circle has disappeared when looking the residual phase in b. The phases are at full SLC image resolution for an area of about 200 x 200 pixels. In consequence, this phase gradient is too fast to be an atmospheric artifact as usually the correlation distance is of about 1 Km.

that the area presented in figure 3.3.6 is of about  $80m^2$ , 200x200 samples. The phase variation due to the atmospheric artifacts over the phase is expected to be very smooth in space when considering small distances.

#### Performance of the APS estimate

The estimation of the atmospheric components is based on application of a low pass over the DPR images. However, these estimates can contain some other artifacts which have the same long wavelength behavior (e.g. possible large scale deformations or residual orbital fringes) not properly removed during the respective SPN steps. The estimation of the APS can be formulated by means of equation 3.3.4:

$$APS_x^i = [DPR]_{low-pass-filter-centered-in-PSx} \quad (3.3.4)$$

However, the pollution of the APS term is not a problem as the orbital fringes is not a signal of interest that should be estimated through the SPN process. It is really difficult to decorrelate the true atmospheric phase screen from a possible residual orbital fringes (it is assumed less than 1 full fringe per swath as residual orbital fringe) as both present a similar spatial variation pattern on the interferometric phase (long wavelength phase artifacts).

On the other hand, the possible corruption of large scale ground deformation movements not properly fitted with the linear model is a critical problem. If this component of the movement is evaluated as part of the atmospheric artifact it is very difficult to recover it later. There is thus a risk of underestimating the real magnitude of the observed deformation phenomena.

In figure 3.3.7 is presented an example of detected atmospheric phase screen for a given interferogram. A large area (20x20 km) is presented in slant range geometry in order to illustrate the smooth variation of this phase component in the spatial domain. As it can be observed in figure 3.3.7.b after the compensation of the phase model (defined by equation 3.3.1) from the original DInSAR input phase (3.3.7.a), the large scale artifacts of the APS become visible. The estimated APS for this interferogram can be observed in figure 3.3.7.c. By compensating this estimated APS from the resulting DPR image of figure 3.3.7.b, it can be noticed how the resulting phase is completely flat, at least considering this large scale phase variations. Phase fluctuations

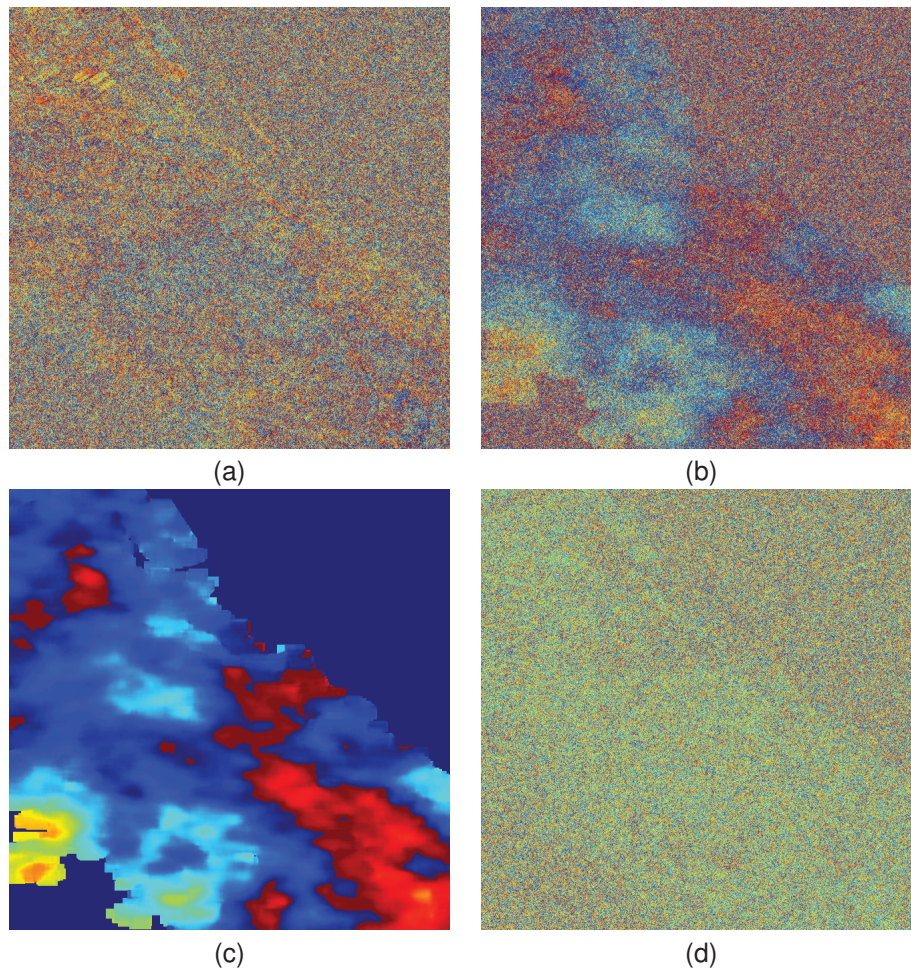


Figure 3.3.7: Illustration example of the estimation and retrieval of the APS for a pure urban area and by using TerraSAR-X stripmap mode data. The interferograms are resampled to highlight the large scale artifacts, they are representing an area of about 20x20 km. a) Original DInSAR phase completely wrapped by the building heights. b) Resulting residual phase after compensation the phase model (see equation 3.3.3). After the removal of the height model other low wavelength artifacts arise. c) Example of detected atmospheric phase screen for this large area. It can be correlated visually the variation presented by the estimated APS with the large scale ones depicted in figure b. d) Residual phase after compensation of the SPN phase model and the APS. As it can be observed the phase is completely flat considering this large scale view. Small fluctuations can be noticed at local scale due to noisy pixels and/or possible out of model residuals.

are still visible in figure 3.3.7.d but they are principally due to noisy pixels, as for example the area on the top right which is a water covered area, and in consequence is completely decorrelated.

### 3.3.5.5 Final spatial high resolution estimation of the SPN model parameters

The original input interferometric phases are compensated by the estimated APS. Two main objectives are achieved. On one hand, the phase is cleaned from this unwanted large scale artifact. On the other hand, the interferometric phases get calibrated in time.

As result, it is obtained a new mean deformation linear rate and a point height value but now per each slant-range pixel without any interpolation. The same optimization procedure as the one described in section 3.3.5.2 is followed in order to maximize the model coherence of each sample. This coherence gives an indication of how well the model is adjusted considering the

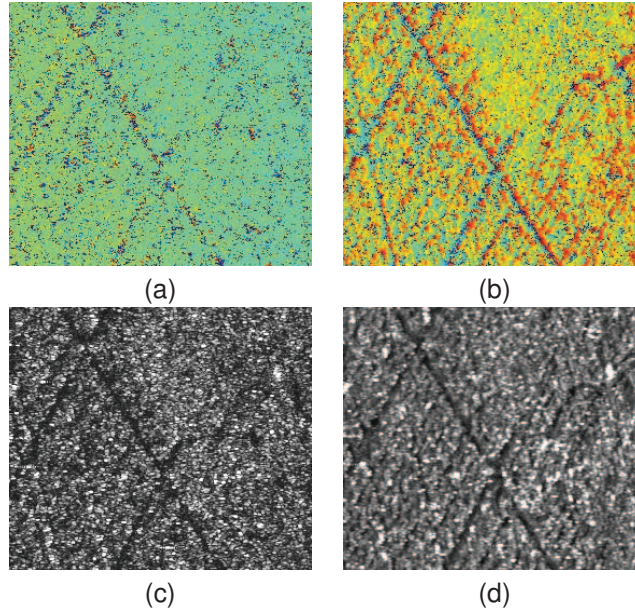


Figure 3.3.8: High resolution SPN outputs. a) mean deformation rate in cm/year (-1 cm/year for dark red and +1 cm/year for dark blue). b) estimated pixel height (-30 meters for dark blue and +30 meters for dark red points). c) SPN model coherence index (0 for dark values -wrong estimates- and 1 for white ones -right estimates-). d) Mean amplitude of the presented urban area in slant-range geometry at SLC full resolution for an area of about 500 x 500 pixels.

available data. Further details regarding the behavior of this model coherence will be given in future chapters. In figure 3.3.8 is presented an example of these estimated products for a pure urban area made with a stacking of a lot SLCs (ERS and ENVISAT). As it can be observed the height estimation follows the shape of the buildings present in the area as it can be inferred by comparing figure 3.3.8.b with the one in 3.3.8.d. Furthermore, as it can be observed there is no cross-correlation between the deformation and the geometric SPN model when comparing the estimated results in figure 3.3.8.a and b. It is important to notice that the model parameters are adjusted for each of the pixels of the image. The model coherence 3.3.8.c indicates the quality and the reliability of this estimate. As it can be observed high fluctuations of the model estimate can be found for areas of low coherence (dark values in figure 3.3.8.c in correspondence with dark red close to dark blue pixels in 3.3.8.a and b). It means that the adjusted model parameters for those pixels are completely random. They don't have any physical sense considering the analyzed ground terrain. It means, it is not possible to have a point with a height of about +30 meters close to another one with a height value of about -30 meters like it can be seen for low coherent areas, which are in correspondence with streets of the city or gardens. The same kind of analysis can be applied to the detected deformation values for completely noisy areas like those ones.

### 3.3.5.6 Estimation of the deformation time series

After the removal of the APS and the SPN phase model for each pixel, the deviation of the estimated deformation from the adjusted linear model can be estimated. The expression for the resulting residual interferograms considering the input DInSAR phases can be expressed by means of equation 3.3.5:

$$DPR_s^i = DPR_s^i - APS_s^i = (\phi_x^i - \hat{\phi}_x^i) - APS_s^i \quad (3.3.5)$$

In principle, this residual phase  $DPR2_s^i$  per pixel (s) and per interferogram (i) should contain terms due to un-modeled deformation (not considered within the linear term defined in equation 3.3.1) and noise (a mixture of thermal noise, geometric interferometric noise, temporal decorrelation noise,...). Hence, for points of good quality, this former term should be very low and only it should present variations with a certain correlation pattern with time.

The estimation of the residual deformation term is done based on a least squares adjustment considering the residual interferometric phases as input; the deformation per each acquisition is set as unknown. The epoch corresponding to the first image is set as reference and the deformations at each of the other epochs relative to this reference one are resolved by means of the following system of linear equations (equation 3.3.6).

$$\bar{b} = A\bar{x} \quad (3.3.6)$$

where  $\bar{b} = [DPR2_s^i, \dots, DPR2_s^{i+M}]$  and  $\bar{x} = [x_s^k, \dots, x_s^{k+N-1}]$  are respectively the set of M residual interferometric phases (observations) and the deformation at each relative acquisition epoch given by the acquisition date of the N available SLCs (the unknowns). This equation system is resolved for each pixel s of the image. The design matrix A is the matrix of connections between each SLC (interferometric couples) and the respective interferometric observations. The shape of this matrix of connections can be observed as illustration example in equation 3.3.7 for a system formed by 5 acquisitions and 10 interferometric combinations.

$$A = \begin{bmatrix} 1 & -1 & 0 & 0 & 0 \\ 1 & 0 & 0 & -1 & 0 \\ 1 & 0 & 0 & 0 & -1 \\ 0 & 1 & -1 & 0 & 0 \\ 0 & 1 & 0 & -1 & 0 \\ 0 & 1 & 0 & 0 & -1 \\ 0 & 0 & 1 & -1 & 0 \\ 0 & 0 & 1 & 0 & -1 \\ 0 & 0 & 0 & 1 & -1 \\ 1 & 0 & 0 & 0 & 0 \end{bmatrix} \quad (3.3.7)$$

In this matrix, each row corresponds to a residual interferometric information, while the columns are related to the acquisitions. Thus, for example, for the interferometric combination  $DPR2_s^i = DPR2_s^l - DPR2_s^j$  related to the row i the values are all zero except at columns i and j, where they are +1 and -1, the sign being determined by the interferometric difference.

The solution vector  $\bar{x}$  of an N-by-N linear system  $Ax = b$  is guaranteed to exist and to be unique if the coefficient array A is invertible. Using a simple algebraic manipulation, it is possible to formulate the solution vector x in terms of the inverse of the coefficient array A and the right-side vector  $\bar{b}$  as showed in equation 3.3.8:

$$\bar{x} = A^{-1}\bar{b} \quad (3.3.8)$$

Although this relationship provides a concise mathematical representation of the solution, it is never used in practice. Array inversion is computationally expensive (requiring a large number

of floating-point operations) and prone to severe round-off errors. An alternate way of describing the existence of a solution is to say that the system  $Ax = b$  is solvable if and only if the vector  $b$  may be expressed as a linear combination of the columns of  $A$ . This definition is important when considering the solutions of non-square (over- and under-determined) linear systems, which is the case of interest. While the invertability of the coefficient array  $A$  may ensure that a solution exists, it does not help in determining the solution. Some systems can be solved accurately using numerical methods whereas others cannot. In order to better understand the accuracy of a numerical solution, it is possible to classify the condition of the system it solves. The scalar quantity known as the condition number of a linear system is a measure of a solution's sensitivity to the effects of finite-precision arithmetic. The condition number of an  $n$ -by- $n$  linear system  $Ax = b$  is computed explicitly as  $\|A\| \|A^{-1}\|$  (where  $\|\cdot\|$  denotes a Euclidean norm). A linear system whose condition number is small is considered well-conditioned and well suited to numerical computation. A linear system whose condition number is large is considered ill-conditioned and prone to computational errors. To some extent, the solution of an ill-conditioned system may be improved using an extended-precision data type (such as double-precision float). Other situations require an approximate solution to the system using its Singular Value Decomposition, which is the case when a linear system is over- or under-determined [Pre07]

### Solution to overdetermined systems

Generally the kind of problems that must be solved within this step of SPN are overdetermined systems. In that cases, when there are more linear equations than unknowns ( $M > N$ ), the vector  $b$  cannot be expressed as a linear combination of the columns of array  $A$ . In other words,  $b$  lies outside of the subspace spanned by the columns of  $A$ . By using the Singular Value Decomposition (SVD) procedure it is possible to determine a projected solution of the overdetermined system ( $b$  is projected onto the subspace spanned by the columns of  $A$  and then the system is solved). This type of solution has the property of minimizing the residual error  $E = \bar{b} - A\hat{x}$  in a least-squares sense.

The core of the solution finding is based on the computation of the SVD of non-square array as the product of orthogonal and diagonal arrays. SVD is a very powerful tool for the solution of this kind of linear systems, and is often used when a solution cannot be determined by other numerical algorithms.

The SVD of an  $(m \times n)$  non-square array  $A$  is computed as the product of an  $(m \times n)$  column orthogonal array  $U$ , an  $(m \times m)$  diagonal array  $SV$ , composed of the singular values, and the transpose of an  $(m \times m)$  orthogonal array  $V$ , see equation 3.3.9 [Pre07]:

$$A = U \cdot SV \cdot V^T \quad (3.3.9)$$

Thus, the solution of the linear system can be expressed as the product of arrays given by equation 3.3.10, which represents the projection of the vector  $b$  into the subspace given by the columns of  $A$  as:

$$\hat{x} = V \cdot SV \cdot U^T \cdot \bar{b} \quad (3.3.10)$$

An example of estimated time series can be observed in figure 3.3.9.

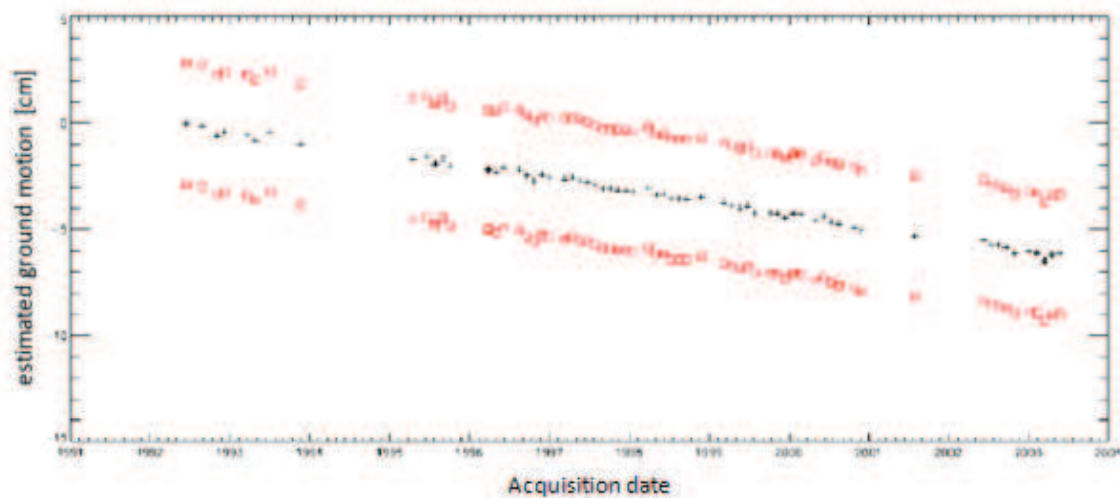


Figure 3.3.9: Example of estimated deformation profile for a large stacking of SLCs. The red squares indicate the position of the possible aliases considering the actual solution. They are placed  $\lambda/2$  above and below the estimated solution. The black crosses are ERS1/2 and the black diamonds are ENVISAT acquisitions.

### 3.3.6 Final selection of points of measurement

The final selection of good measurement points is made at the end of the SPN processing. It is based on the SPN model coherence performed during the high resolution SPN model adjustment, see section 3.3.8. During this step the SPN phase model parameters are estimated pixel-by-pixel. The model coherence indicates how well the observation fits the model for the estimated parameters. It is a quality index that varies between 0 (bad adjustment) and 1 (good agreement).

Hence, by setting a threshold on this value a selection of good points for measurement can be performed. It must be highlighted that this index measures the model goodness-of-fit as well as the level of noise in the input data. Then, relaxing the threshold in order to select more points as stable it will imply as well the inclusion of outliers.

It is interesting to note that the SPN model coherence it is an estimator of quality, and in consequence the performances depend on the available number of samples (especially when few data is available), as it happens with the interferometric coherence (see figure 3.2.63.2.7). One of the innovative work of this PhD is the detailed analysis of the performances of the SPN model coherence, which is done by means of a simulated scenario. The results are presented in sub-section 4.4.1.

Nevertheless some interesting considerations can be formulated when selecting the good points of measurements by thresholding the SPN model coherence. Many factors that can influence on coherence value. They always occur when a large stacking of SLC (more than 25 images) is analyzed, and these factors, presented in what follows, are very difficult to isolate one from each other:

- Phase noise: the presence of noise in the phase values is translated into a degradation of the model coherence. Indeed, the lower the noise, the higher the model coherence. However, in case of reduced number of acquisitions, noisy points can be fitted with extreme model parameter values resulting in high levels of coherence. They are very difficult to detect in slant-range geometry. They can be detected as outlier if their fitted parameter values

are very high (typically  $3\sigma$ , being sigma the distribution of the histogram of the estimated values). Generally in ground geometry those false alarms are located in the middle of areas where are completely incoherent under an interferometric point of view such as water and vegetation covered areas, crop fields, etc.

- Changes of the coherent scatterers: the surface of the analyzed test sites are not static. In urban area, as in vegetated one, the coherence can be reduced due to the scene changes (trees growth or human activities). Sometimes, if this changes are not very drastic, like for instance the collapse of a building, there is a change of phase but the measurement still coherent before and after this event. In those cases the model coherence will be reduced and the precision of the estimated parameters will be reduced, although in mean the measurement will be reliable.
- Out of model ground deformation: non-linear ground movements will be also translated into a degradation of the SPN model coherence. In case of light non-linear movements the adjusted linear model will be good in average. Then, the absolute profile of deformation will be recovered during the last step of the SPN processing, see section 3.3.5.6. However, as the residual phase is high the coherence will decrease like for the case of noise points. The only difference is that for noisy points the time series is noisy and for this kind of non-linear points is fluctuating around the linear model under a more or less correlated way with time. When the non-linear movement is important the fitted linear model is completely wrong leading in a high decrease of the model coherence; this disturbs the possibility of measurement over those kind of good points. This is the worst case because points with reduced level of noise (potential PSs) are lost due to the simplicity the deformation model.

### 3.3.6.1 Methodology for selecting good SPN points of measurement

The principal SPN quality index parameter for selecting which pixels are points of measurement and which not is the SPN model coherence, described in section 3.3.5.2. Considering a test case with many acquisitions (more than 20), the following proposed values can be used as guide for selecting PSs:

- Points with coherence value above 0.8 have a very reliable displacement rate and vertical height estimations (usually the reported precisions are in the order of 1 mm/year and of about 1 meter for the height [Cro08])
- Points with values within the range 0.8 to 0.5 have a reliable displacement rate estimations but with a higher uncertainty value (of about precision 1 - 3 mm/year and 1 - 5 meters for the height). However their time series of deformation are very interesting as this range of values can contain non-linear deformation profiles. In fact, it is this deviation from the linear model of deformation in time, the responsible of the decreasing of the coherence. In other words, due to the bad goodness-of-fit [Pre07] of the model the residuals are large and hence the coherence decreases [Cro08].
- Points with coherence between 0.5 and 0.3 could be affected by a strong non-linear motion (which will not have been extracted correctly using linear modeling methods) and/or they could present a time series showing a high level of noise. Must probably, their time series may show aliasing in the calculation of the average annual rate and/or in the measurement

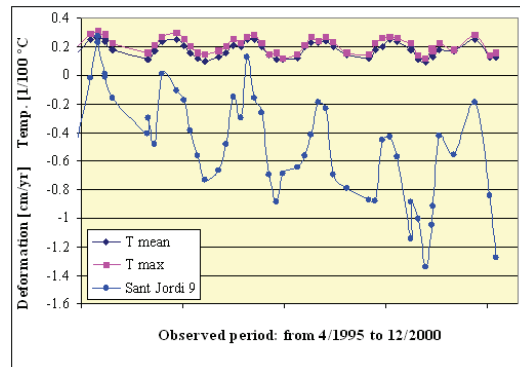


Figure 3.3.10: Illustration example of thermal dilation detected by the deformation time series estimated with SPN. For comparison purposes the mean and maximum temperatures of the days of acquisition. The temperature values have been multiplied by 1/100. Typically those kinds of non-linear profiles give a value of moderate-low SPN model coherence. However, as it can be observed they offer a very precise sensitivity to the deformation (thermal dilation of the roof of a building in that case). The correlation coefficient between temperatures and estimated deformation equals 0.82 for that case.

for each single date. The values of the phase residuals 3.3.5.6 will not be unwrapped properly and the time series cannot be estimated properly (this is the most probably situation).

The main drawback of this indicator is that it gives a description of the goodness-of-fit of the model at the same time as it measures the reliability of the estimated model parameters. Hence, when there is a decrease of the coherence it is impossible to know if the linear model is right but the point has a lot of noise or if the point is radiometrically stable but it has movement completely non-linear with time (out of model). This is the worst case as points of good quality which could be exploited for performing measurements become unselected. For this reason, there are other indexes that aid in the final selection of which points have noise and which ones present possible non-linear movements within the actual SPN methodology.

### **SD\_LIN Standard deviation of the time series with respect to a linear model**

This is a measure of the standard deviation of the estimated deformation time series from the linear model. It provides both a measure of the linearity of the displacement and of the noise in the time series. Low values indicate a reduced variation of the individual deformation regarding the linear model. By considering the SD\_LIN value in combination with the model coherence some conclusions regarding the nature of the time series can be noticed. Since the coherence indicates how well a linear model fits the observed data, a point presenting a high coherence and a high SD\_LIN value (i.e. a point with high dispersion) may be a type showing relatively high variation around a reliable linear displacement rate. An example of such point behavior is a point undergoing (possibly seasonal) sinusoidal displacement with respect to linear movement – e.g. thermal dilation of a metallic structure, or seasonal shrink/swell of clay.

### **Saturation of the calculated parameters**

Generally, values at the edges of the considered span of solutions of the SPN analysis (i.e. at the extreme of the possible deformation rates and of the height search ranges) are related with outlier values. Typically they are very noisy points that fit these extreme values by chance. The decision threshold can be set on  $3\sigma$ , being  $\sigma$  the standard deviation estimated over all the set of solutions.

### Amplitude stability (DA)

This is a measure of the stability of the radar reflection for a particular point. It was already defined and discussed in section 3.2.2. Low values correspond to points which have maintained a consistent reflection amplitude over a span of several acquisitions. It is a normalized measure, thus not penalizes points with very strong reflectance.

As it has been demonstrated theoretically in section 3.2.2, that the amplitude deviation of a point over a set of observations is a useful analogy for the points phase noise standard deviation. Therefore by selecting points with a very low amplitude deviation, typically below 0.25, one can insure that the points of the highest quality are selected, those that have very low phase noise. Points with a DA above 0.25 have a phase noise of more than 0.2 radians, which translates into an error greater than 1mm in the measure of displacement.

This factor can be used to identify potentially very reliable reflector points, for example at the early stages of the SPN processing. It is a fast and very practical technique, however, it should be stressed that the set of reliable points identified at the end of the processing cannot be derived using only the DA as a quality indicator. These points are identified by a combined application of the aforementioned quality parameters, where the combination can be of the form of a threshold applied to each to eliminate the worst cases identified by each parameter but which when taken together identifies a set of reliable points.

### 3.3.7 PS geocoding

As it was presented in the previous subsection, one of the outputs of SPN is the map of the residual topographic errors or the estimated height for each pixel in the SAR image geometry. The residual topographic error is given by the difference between the true height of the scattering phase center of a given pixel, and the height of the DEM employed in the SPN processing to produce the input DInSAR phases. An example of this estimate over a pure urban area can be observed in figure 3.3.8.

The estimated height of the pixel plays a key role for two specific goals. First, it considers the residual topography component of the DInSAR phase: the estimation of the residual topographic error with respect to the DEM. The second goal is the implementation of advanced geocoding procedures for this kind of advanced DInSAR products. The standard methods employ an a priori known DEM to geocode these products (see section 2.2.5.9), is used an approximate value of the true height of the scattering phase center of each pixel, which results in a location error during the geocoding. A more precise geocoding is achieved using the estimated residual topography, this work has been firstly presented in [Dur05]. This may considerably help the interpretation and the exploitation of the PSI results, as it was demonstrated within the validation PSI analysis performed in [Her09]. The formal precision that can be achieved in the estimation of the residual topographic error is a function of the distribution of the normal baselines. Using large baselines, between  $\pm 1200$  m, it can be achieved a standard deviation of about 1 m [Col03].

It is important to note that this parameter describes a rather specific feature, i.e. the height of the radar scattering phase center. This means that it cannot in general be used to improve the quality of the DEM used in the SPN procedure directly but it is of great interest to get a kind of improved "radar DEM" only over the PS selected in the SPN procedure, see figure 3.3.11 for an example. This means that it is possible to distinguish if a PS is over a particular structure

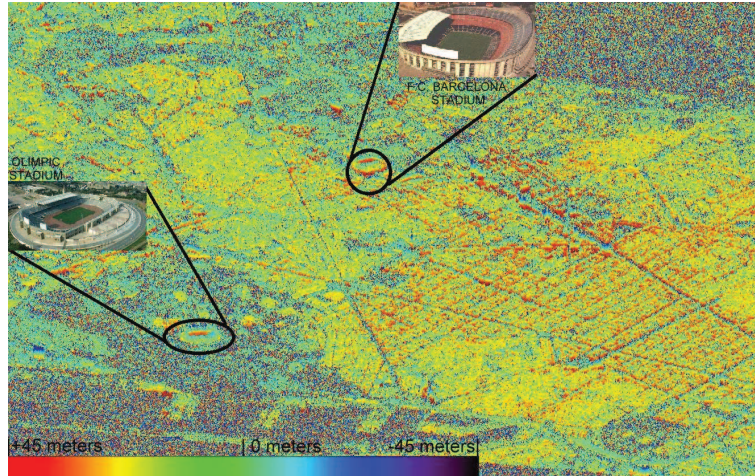


Figure 3.3.11: Example of estimated height for each pixel in slant range geometry as it outputs from SPN. Some structure can be clearly identified even though they are in sensor geometry.

or just over the ground surface, which may be used in the handle of the PSI data for its proper interpretation of deformation measures.

### 3.3.7.1 Precise geocoding procedure

The estimates are performed in sensor geometry or slant range, as stated previously. The SAR geocoding procedure project each image pixel to its corresponding ground position, see figure 2.2.11. The precision mainly depends on the quality of the DEM used to produce the DInSAR phase (typically 25x25 meters), the resolution of the SAR image (of about 20 meters for the C-band ENVISAT case, and of about 3 meters for the TerraSAR-X stripmap case) and the quality of the image timing annotation parameters (which also depends on the used sensor). However, in PSI processing this pixel's final ground position can be enhanced if the estimated vertical height is used.

First of all the satellite track heading angle should be set. That is the angle between the North and the satellite orbital flight direction. As all the missions are polar orbits they have more or less a value of about  $195^\circ$  for the descending path and  $285^\circ$  for the ascending one (considering clockwise direction from the North), taking into account that this value may vary slightly with the latitude and with the used mission, see figure 3.3.12 for clear understanding.

Unitary vectors for the decomposition of the line of sight vector on ground (2-D) can be defined by equation 3.3.11:

$$\hat{u}_{EW} = \cos(\psi) \quad \hat{u}_{NS} = \sin(\psi) \quad (3.3.11)$$

Then, the final ground position of each slant range pixels can be refined on ground by calculating the extra displacement that may be applied to each pixel based on its estimated vertical height within SPN (see equation 3.3.12 and figure 3.3.13).

$$x = \frac{h}{\tan(\alpha)} \quad (3.3.12)$$



Figure 3.3.12: Illustration of the ascending (black) and the descending (red) acquisition mode over the same ground area. The squares represents the swath coverage of each acquisition mode. The LOS vectors represents the slant range direction (perpendicular to the flight direction), it is the direction where the radar performs the measurements of change of distance.

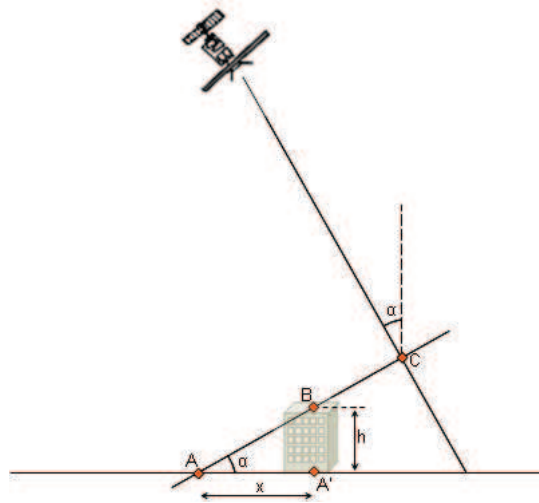


Figure 3.3.13: Schematic view of the precise geocoding procedure.

The target B in figure 3.3.13 with a height h is sampled into the position C in slant range geometry. When projecting this target into the ground geometry, it will be placed into the position given by A. Moreover, if the vertical height of the target is known, the position can be corrected on ground ( $A'$ ) by accounting for the local incidence angle of the wave into the ground ( $\alpha$ ).

In particular, on ground coordinates the final enhanced position of the target is given by the vectors defined by equation 3.3.13.

$$\bar{u}_{EW} = x \cdot \hat{u}_{EW} \quad \bar{u}_{NS} = x \cdot \hat{u}_{NS} \quad (3.3.13)$$

### 3.3.7.2 Example of application

With the precise geocoding procedure the PSs can be projected into any coordinates system. This procedure crucial for the handling and the interpretation of the measurements as the structure responsible of the SAR signal response can be perfectly identified on ground. See figure 3.3.14 for an illustration example of the enhancement of the final PSs position on ground.



Figure 3.3.14: Example of the precise geocoding enhancement of the PS. a) ground location of the PS without accounting for their vertical height. b) Enhanced position of the PS when accounting for their vertical height. c) Aerial orthophoto image for visual correlation of the building shapes with the pattern of the PSs on ground. See the areas within the black circles, the PSs are grouped together on ground following the shape of the buildings. Copyright ICC for the background images.

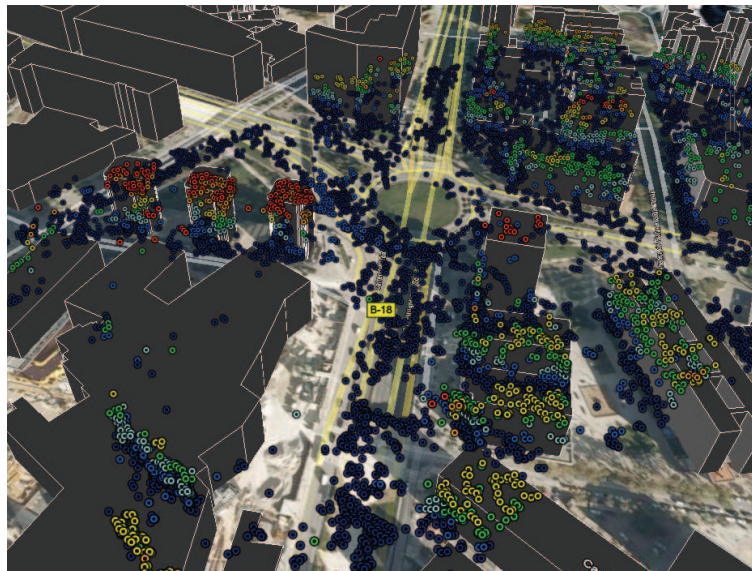


Figure 3.3.15: Example of PSI 3-D geocoding performed with high resolution SAR data (TerraSAR-X stripmap mode). The color-table blue to red represents the vertical height value of each radar points (dark red of about 50 meters and dark blue for ground level). Copyright Googleearth for the background image.

As it can be observed in figure 3.3.14 the final position of the scatterers is drastically enhanced when applying the precise geocoding correction. This is demonstrated by the grouping of the radar points on ground following the shapes of the buildings and the infrastructures presented over the ground surface, see figure 3.3.15.

By setting a threshold into the vertical height value it is possible to discriminate between points placed on the ground level and points placed over buildings and/or infrastructures. The careful analysis of the deformation maps can be done by considering that two points very close one to each other can present a completely different deformation value considering that they are from completely different locations, (see figure 3.3.16).

As it can be observed in figure 3.3.16 a complete analysis of the PSI deformation measurements can be performed when accounting for the enhanced PS final ground position and for its vertical height value. The deformation highlighted by the red square in figure 3.3.16 can be explained by the fact that the point is located over the building, while the surrounding points are

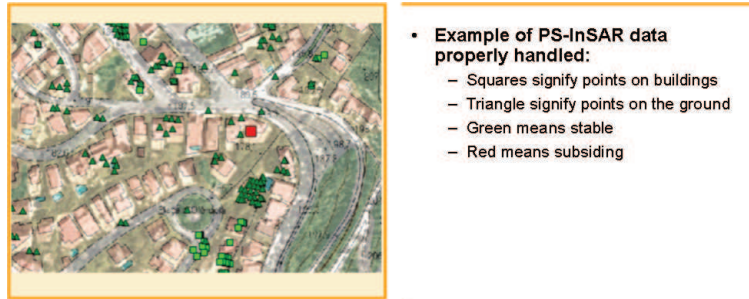


Figure 3.3.16: Illustration example of the proper handling and interpretation of the PSI deformation measurements on ground geometry. Copyright ICC for the background image.

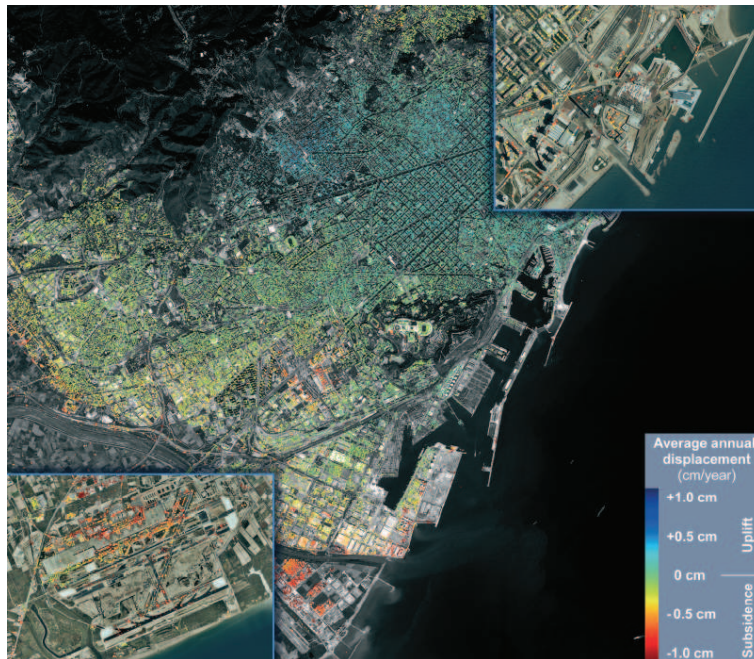


Figure 3.3.17: Example of final geocoded PSI deformation measurements over a urban area superimposed over a spaceborne orthophoto. The processing was done with an stacking of 30 ENVISAT stripmap mode SLCs covering a time span contained between 2003 up to 2008. Background image is copyright SPOTIM-AGE.

directly placed on ground. . It can be inferred that the building is subsiding while the ground is stable. So, it means that it is a problem affecting this particular structure. This work has been published in [Dur07b].

In summary, the final deformation measurement are presented in ground geometry, see figure 3.3.17 for an example of final geocoded PSI product. Typically the final vertical height precision is in the order of 1 meters, which is translated into a precision of about 2.5 meters in the final geocoded ground position. This work was reported in [Dur05, Cro08].



## Chapter 4

# Improvements of the SPN technique

This chapter is the core of this PhD. Some of the technique's major drawbacks identified in the previous chapters will be detailed and reviewed here. The implemented solutions in order to overcome these limitations will be described in the sections of this chapter. These improvements will be evaluated by means of their application and performance on real test cases. These new methodologies are very useful by themselves and each of them represent one single advance of the SPN technique towards a completely automatic processing chain. In particular, one of the major enhancements is the adaptation of the SPN deformation estimates to non-linear ground movements, and especially for long periods of analysis, which the main goal of the PSI analysis

### 4.1 Image coregistration quality control

In PSI, all the available images must be put into a common geometry. Thus, one of the images is selected as super master and all the other ones are coregistered to this common image. In a stacking of several acquisitions the control of the accuracy of this particular procedure is not straightforward. In classical InSAR it can be checked by visual inspection of the amplitude of the images the correctness of this procedure. However, this method can be used when few images are considered. Moreover, errors and inaccuracies at inter-pixel level are sometimes very difficult to detect even by trained-eyes, see figure 4.1.1. PSI and classical InSAR require sub-pixel accuracy in slave image coregistration.

One interesting possibility is to take advantage of the capacity of detecting PS like pixels in a incoherent way at the very early steps of the SPN processing. For example, once the images are coregistered the normalized standard deviation of the stacking of amplitudes can be computed (see section 3.2.2). Thus, pixels with a reduced level of noise can be detected by setting threshold over this index, or in others words, pixels radiometrically stable in the set of acquisitions can be detected. The main idea is to estimate which of the pixels selected have a behavior similar to an ideal point target one. A mask of super PSs is thus produced based on the initial mask of stable points. By detecting and tracking the peak of the main lobe the impulsional response function (IRF) of these points, the accuracy of the coregistration procedure can be evaluated. In normal cases, the mean offset detected for the location of those peaks should be contained within  $\pm 0.1$  fractions of a pixel taking as reference the position of the peak at the super master acquisition.

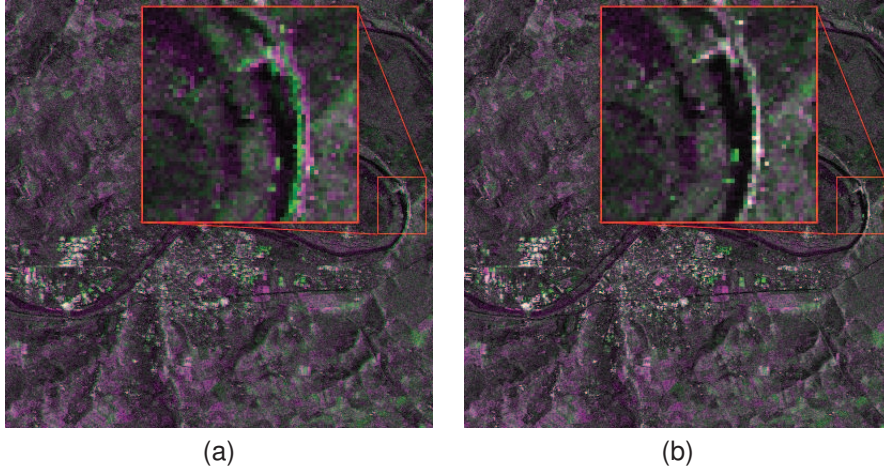


Figure 4.1.1: Example of RGB compose image with the SAR amplitude of 2 not properly coregistered SLCs (a) and 2 perfectly coregistered ones (b). Mis-registrations of about one pixel are very difficult to detect by visual inspection of the amplitudes. See the duplication of the presented structures in the zoomed window in (a) and compare it with the one in (b) where there are more white color, what it means that the RGB channels have the same value over those bright pixels related to a possible harbor and a bridge over the river presented within those red squares.

#### 4.1.1 Detection of super PS

Pixels radiometrically stable based on the stacking of coregistered SLCs are selected (section 3.2.2). Based on this initial mask of PS like pixels the ones with a behavior similar to an ideal point target must be identified. These point are defined as the super PSs. These kinds of pixels may be not only composed by scatterers presenting a reducing level of noise but also they must present a SAR signal response similar to the one given for an ideal target.

For this reason, the IRF of these pixels, selected as PSs, is estimated and analyzed. The IRF of a pixel characterizes its behavior under a radiometric point of view. Then, by comparing the IRF of those PS-like pixels with the one of an ideal target it is possible to make a sub-selection of in order to identify those super PSs within this initial mask of PSs.

##### 4.1.1.1 The impulse response function (IRF)

The IRF is a good tool for analyzing the SAR image quality. It characterizes the SAR response of an ideal point target. The IRF describes the dispersion of the energy coming from a single scatterer, which ideally should be concentrated in one unique pixel of the image. The analytical expression for the SAR IRF can be derived by considering the SAR complete processing as a linear system and as input an ideal impulse, see figure 4.1.2. Thus, the transfer function can be approximated by equation 4.1.1, see [Cum05] for further details.

$$h_{imp}(\tau, \eta) = w_r(\tau - \tau_0) \cdot w_a(\eta - \eta_0) \cdot \exp(-j4\pi R_0/\lambda) \cdot \exp(j\pi K_r(\tau - \tau_0)^2) \quad (4.1.1)$$

where  $\tau$  and  $\eta$  represent the range and the azimuth image coordinates.  $w_r$  and  $w_a$  are the envelopes of the amplitude centered at the target's location  $(\tau_0, \eta_0)$ . The first exponential term is the SAR phase given by the slant-range distance of closest approach radar to scatterer  $R_0$ . The

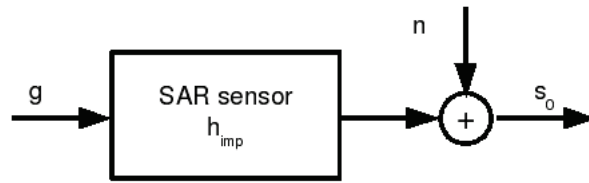


Figure 4.1.2: SAR system model with additive noise.

last exponential is the used chirp range function dominated by the range FM rate  $K_r$ , which is the responsible of the system bandwidth, and hence the resolution of the system.

To obtain the signal model received from a general ground surface, the ground reflectivity  $g(\tau, \eta)$  is convolved with this impulse response in two dimensions to the base-band SAR signal data as depicted in equation 4.1.2.

$$s_o(\tau, \eta) = g(\tau, \eta) \otimes h_{imp}(\tau, \eta) + n(\tau, \eta) \quad (4.1.2)$$

where  $n(\tau, \eta)$  is an additional noise component that is present in all practical systems. The correspondent SAR system model to equation 4.1.2 is shown in figure 4.1.2. This is the matched filtering performed by the SAR system, which allows to detect the desired signal from the noise floor.

However, for simulations purposes the noise can be ignored. The shape of the ideal IRF is shown in figure 4.1.3.

Generally, the shape of the IRF is governed by the applied weighting, such as that physic one, given by the two-way azimuth antenna pattern or artificial weighting applied to azimuth and range frequency spectra during the SAR processing. Both considered within the terms  $w_a$  and  $w_r$  for azimuth and range respectively in equation 4.1.1. The performances of the IRF for each target can be evaluated by means of several parameters. In particular, there are two main parameters which define the radiometric interaction between nearby pixels, the ISLR and the PSLR:

- Integrated Side Lobe Ratio (ISLR): it is the ratio between the total energy contained within the area covered by main lobe and the total energy contained within the area covered by the secondary lobes.
- Peak Side Lobe Ratio (PSLR): it is the ratio between the maximum value of the peak of the main lobe and the maximum value detected for the secondary lobes.

The additional weight applied to the data ( $w_r$  and  $w_a$ ) change the shape of the IRF. The spatial resolution - the width at 3dB of the main lobe in range and azimuth - is favored by uniform weighting, like for instance by unweighting the natural image. Thus, the main lobe is narrow but the side lobes of the IRF are higher, interfering with possible point targets in the surroundings. The weighted image offers a better protection against those interferences of the secondary lobes (plus another ones against the signal ambiguities see [Mas08]), but the width of the main lobes becomes wider (worst resolution). The solution is a tradeoff between spatial and radiometric resolution which must be met during the SAR signal focusing procedure.

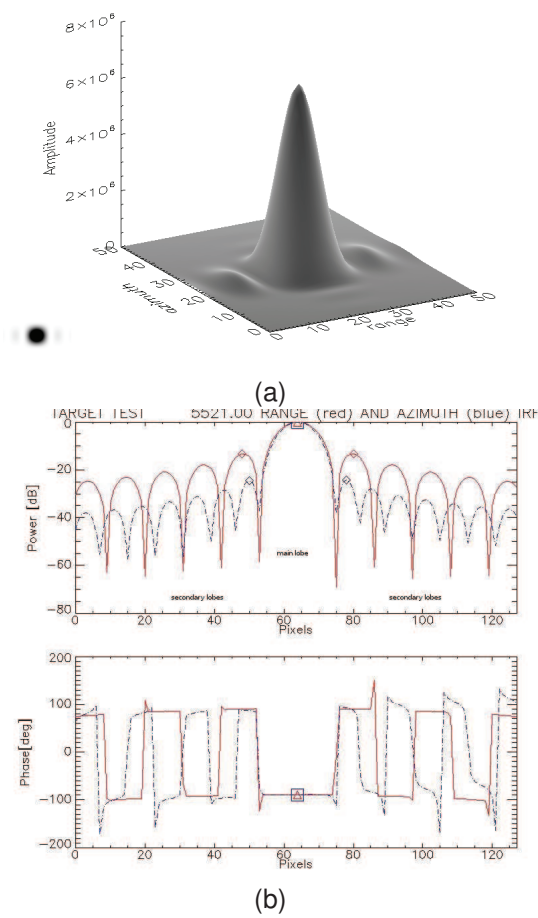


Figure 4.1.3: Ideal SAR IRF in 3-D without added noise (a). IRF cut in range and in azimuth direction for the amplitude and for the phase.

#### 4.1.1.2 Identification of super PSs

In figure 4.1.3 is presented the IRF of an ideal point target obtained by means of simulations. It is understood an ideal target as a target which gives a coherent constant radar backscattering (amplitude and phase) for all the repeat passes. It means, for different geometric point of views. Hence, the target must have a broad bandwidth of backscattering, in range and in azimuth direction.

In real cases, this kind of ideal SAR responses can be obtained on scatterers which presents multiple bounces (natural objects with corners). These reflections give a broad bandwidth of radar response. The ideal case can be found for corner reflectors, see section 3.2. Corner reflectors are scatterers formed by three triangular surfaces (ideally of identical size) placed in a perpendicular way between them resulting in a trihedral. The reflection of the radar wave in those reflectors have always a double bounce ensuring a constant response in amplitude and phase for a broad range of incidences and squint angles. For larger triangles the total amount of returned backscattering is higher and the interference due to the secondary lobes of the nearby points is reduced. The response of this point target prevails over the other ones. The SAR response (IRF) of an artificial metallic corner reflector is very similar of the one given by an ideal target obtained by simulations, presented in figure 4.1.3

Then, these super PS can be defined as the points with a reduced level of phase noise standard deviation and with a backscattering power that prevail over their background in a set of acquisitions. This can be measured by means of the Signal to Clutter Ratio (SCR) of a target, see section 3.2.2. This parameter can be estimated based on the SAR amplitude image [CEO93, Lau98] assuming that the signal return is a deterministic signal polluted by noise due to the clutter. Thus, pixels presenting a high level of SCR in a set of acquisitions are related to targets which dominate the SAR response in a surrounding set of pixels in all the available repeat passes.

#### Estimation of the SCR

The SCR can be computed by several methods. One of them is the CEOS method [CEO93] which is based on the ratio between the total power given by the area covered by the signal (main lobe and secondary lobes) and the area covered by the clutter (estimated by means of the area not covered by the target's IRF response), see figure 4.1.4 and equation 4.1.3.

$$SCR = \frac{\sum_i^{signal} |SLC_i|^2 / AREA_{signal}}{\sum_j^{clutter} |SLC_j|^2 / AREA_{clutter}} \quad (4.1.3)$$

It must be highlighted that this methodology for estimating the SCR assumes stationary conditions of the surroundings, which may not be always valid, especially in urban areas with a high density of strong targets.

#### 4.1.2 Evaluation of the coregistration accuracy

The evaluation of the accuracy of the coregistration is done based on the inter-pixel position of these super PSs in the set of coregistered SLCs. The location of the super PSs in the master

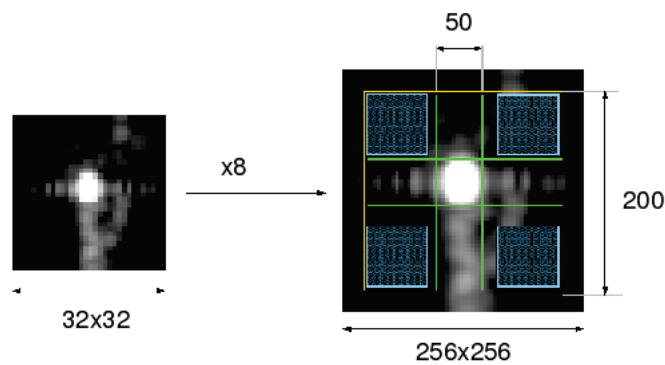


Figure 4.1.4: Illustration of the areas used to estimate the signal (inside the green cross) to clutter (inside blue areas) ratio of power level. The SLC is oversampled by a factor of 8 and then amplitude image is used for the computation of this ratio by means of equation 4.1.3.

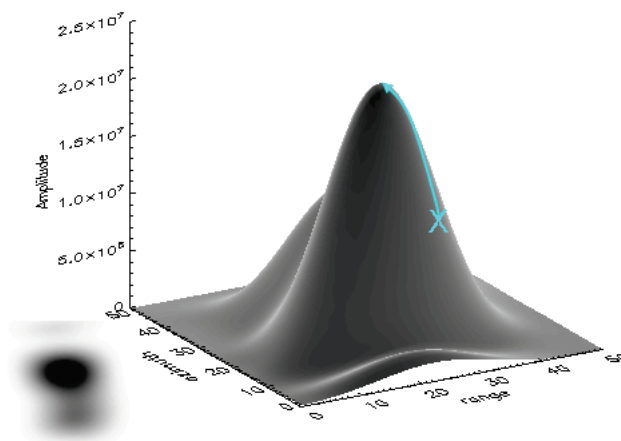


Figure 4.1.5: Illustration of the steep ascent (blue line) methodology used to find the local maximum based on the initial integer coordinates position of the PSs (blue cross) over the estimated IRF of a real point target like pixels..

image is set as reference, the relative inter-pixel positions must be small and should not present any correlation with the position of the target in the image.

First of all, a selection of the super PSs must be performed, the ones with a lower level of amplitude standard deviation and with a high level of SCR (of above 24 dB for all the set of observations). The IRF of the points points contained within the initial mask of super PSs is computed . To compute the IRF the complex SLC images must be oversampled at least by a factor higher than 10 by means of zero padding in frequency domain, see figure 4.1.3 for an example of SAR IRF.

The locations of the point scatterers within the image are obtained by detecting the maximum of the amplitude. Those initial integer coordinates are the starting point for the IRF estimation. The localization of the peak is obtained by means of a steepest ascent path follow algorithm based on the amplitude of an oversampled version of the SLC, see figure 4.1.5.

Thus, the precise location of the target's peak is obtained for all the points identified as super PS and for each coregistered SLC image. The precise location of the points in the master image is set as reference and the difference in pixels is then computed with respect to the other images

for all the points, see equation 4.1.4 for the definition of the relative location for each point  $(x,y)$  and each slave image  $k$ .

$$(\Delta x, \Delta y)_k = (x, y)_{master} - (x, y)_{slave_k} \quad (4.1.4)$$

This relative position can be analyzed in function of the range position for each image and in mean in order to detect systematic errors in the coregistration procedure.

### 4.1.3 Example of application of the methodology

The applicability of the presented procedure has been evaluated by means of several real test cases using ERS and ENVISAT image mode data. The input is a stack of SLCs that have been coregistered into a common master geometry. The objective is to detect point radiometrically stable within the stack and with a IRF similar to the one given by an ideal target, or in other words, to the one given a corner reflector structure.

The first step is to perform an estimation of an initial mask of PSs, like for example the one based on the analysis of the amplitude standard deviation presented in 3.2.2. Then, it is estimated the IRF for those pixels. The width of the main lobe (at 3 dBs of power decrease with respect to the maximum) and the SCR are used in order to points with a IRF similar to an ideal target (narrow and sharp). Values with 50% of variation with respect to the nominal satellite resolution are used for the width at 3 dBs (of about 13 per 7 meters in range and azimuth respectively for the ERS/ENVISAT cases). Values for the SCR are in the order of 5 dBs, when for corners reflectors with a size of about 12 times  $\lambda$  one can have values of about 20 dBs of RCS (target's returned power, added to the clutter level), see figure 3.2.2. The threshold for the SCR may be relaxed when it is applied in pure urban areas as the clutter level usually is very high. Whatever, as the SCR is not the only parameter used (it is combined with the width of the IRF and the radiometric stability analysis within the stacking), the inclusion of possible of false detections is not directly related with this threshold relaxation.

Once the location of the super PSs are known it must be computed their inter-pixel location with the respected to the reference one, the inter-pixel location within the super master image of the stacking. In figure 4.1.6 it can be observed the plot with the mean and the standard deviation of those differential inter-pixel positions for those points per each image (related to an orbit number).

Figure 4.1.6 gives an overview of the coregistration accuracy for each available acquisition, in range and in azimuth. As it can be observed almost for all the estimations the mean location of the inter-pixel relative position is below 0.1, in fact it is very close to zero with a standard deviation of about 0.1. Hence the coregistration accuracy is within the required quality parameters. However, there are a couple of interesting cases outside the expected performances. In figure 4.1.6.b it can be observed one orbit presenting an offset the mean location of the inter-pixel position, the one highlighted with a red arrow. Furthermore there is another orbit in figure 4.1.6.b presenting a high standard deviation, twofold considering the other ones, highlighted with a blue arrow.

The first case (the one highlighted with a red arrow in figure 4.1.6.b) is indicating that there is a mean offset detected in the azimuth inter-pixel locations for those point targets within for this particular acquisition. Further analysis can be conducted by looking at the graphs presented in

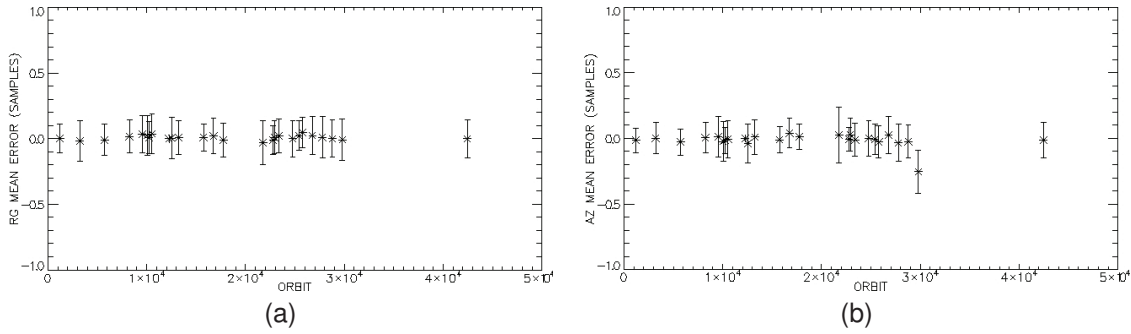


Figure 4.1.6: Evaluation of the coregistration accuracy per each orbit. Mean and standard deviation of the relative inter-pixel location of the point targets for each orbit in range (a) and in azimuth (b) direction. The measurements are performed in pixel units. The accuracy may be in the order of 0.1 pixels.

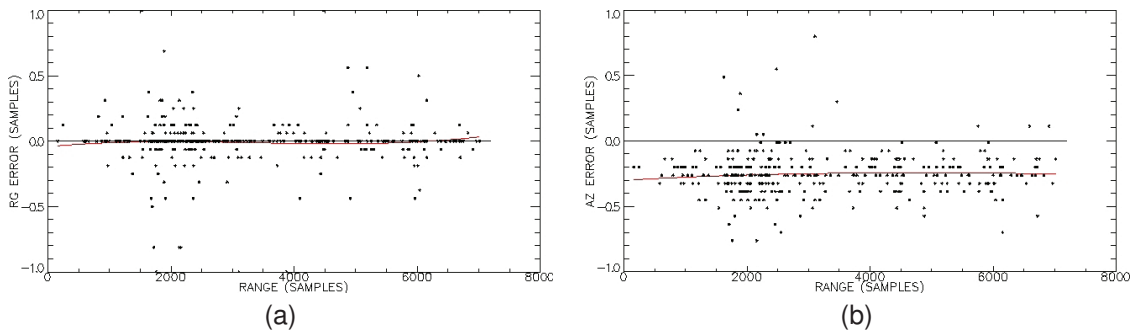


Figure 4.1.7: Range (a) and azimuth (b) relative inter-pixel location detected for point target's like pixels for a particular orbit with a coregistration error of about 0.2 pixels in azimuth. This information is plotted in function of the range in order to analyze possible heterogeneities introduced by the baseline between both acquisitions (which is not the case). The red curve corresponds to a polynomial model of order 3 of the detected shifts in range.

figure 4.1.7 where it is presented the relative inter-pixel position for each point target in function of their range location within the image for this particular orbit.

In figure 4.1.7.b it can be noticed how effectively there is an offset of about 0.2 pixels in the coregistered SLCs, and it is constant in range. However, in range direction (figure 4.1.7.a) the image is not presenting any particular problem. Hence, the coregistration procedure must be refined this particular in order to resolve this inter-pixel shift which may absolutely undetectable by visual inspections of the image amplitudes.

Another interesting problematic case can be found for the one highlighted with a blue arrow in figure 4.1.6.b. For this case the mean offset is correctly placed around zero but the presented spread of the values is larger than for the other cases (twofold). Again, further analysis can be conducted by looking at figure 4.1.8 where it is presented the distribution of these offsets with the range.

As it can noticed in figure 4.1.8.b the distribution of the offsets is completely random. The point targets do not have a relative inter-pixel position close to zero for this particular image for the azimuth direction, in contrary with the range direction (4.1.8.a) where is performing correctly. Thus, one may think that it is a particular problem related only with the azimuth direction that can affect the location of the targets within the image, that is it the image Doppler centroid value.

Effectively, when checking this parameters for this particular image it was corroborated that the Doppler centroid value used for the processing was not the correct one. This fact originates

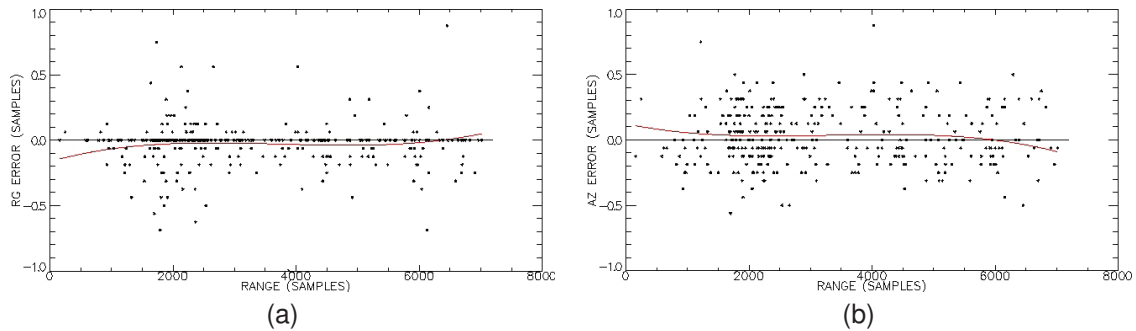


Figure 4.1.8: Range (a) and azimuth (b) relative inter-pixel location detected for point target's like pixels for a particular orbit with a coregistration problem in azimuth. This information is plotted in function of the range in order to analyze possible heterogeneities introduced by the baseline between both acquisitions (which is not the case). The red curve corresponds to a polynomial model of order 3 of the detected shifts in range. The distribution of the values in azimuth direction is completely random.

inaccuracies in the coregistration procedure but also during the estimation of IRF. During the resampling procedures (for coregistration, for the IRF estimation) there are FFTs in azimuth direction what it means that one should account for the appropriate Doppler centroid value. This error has a direct impact on the IRF estimation in azimuth direction as depicted by figure 4.1.9. The shape of the IRF in azimuth direction is not the appropriate one, (compare 4.1.9.a with 4.1.9.b as well as the azimuth profiles in figure 4.1.9.c with the ones in figure 4.1.9.d) as it can be observed it is presenting a fast modulation with a lot of peaks. Thus, the Doppler centroid value must be estimated properly and the image should be reprocessed.

## 4.2 PS-like pixel selection enhancements

As it was already commented the estimation of what pixel has a PS like behavior or not is not straightforward and it can be overcome by different methodologies. SPN, like any other PSI techniques, requires an initial mask with the location of the PSs in order to perform a network of relative measurements. It means, that this estimation of PSs must be done at the very early steps of the processing, hence without entering in the analysis of the phase values (no modeling, no phase unwrapping). An efficient way is to analyze the pixel's radiometric stability. For example by means of an incoherent analysis of the SAR amplitude standard deviation for each pixels in the stacking of images. As it was demonstrated in section 3.2.2 the amplitude dispersion index is directly related with the phase noise standard deviation for low values. For higher values this parameter becomes an underestimation of the real phase standard deviation, hence one can have an idea of the lower bound of the expected noise per pixel.

With this initial mask of stable points SPN establishes a network in order to exploit the phase value of those points. Based on the analysis of the phase in function of the baseline and the time span the atmospheric artifacts can be estimated for every interferogram as it is an artifact completely deco related with these variables. Finally, at the end of SPN a phase model is adjusted pixel-by-pixel. Hence, the final map of stable points with the measurement of the ground deformation is based on this final model estimate goodness-of-fit for each pixel, see section 3.3.5 for further details on SPN methodology and steps.

In summary, SPN requires an initial mask of PSs although the final mask of points of mea-

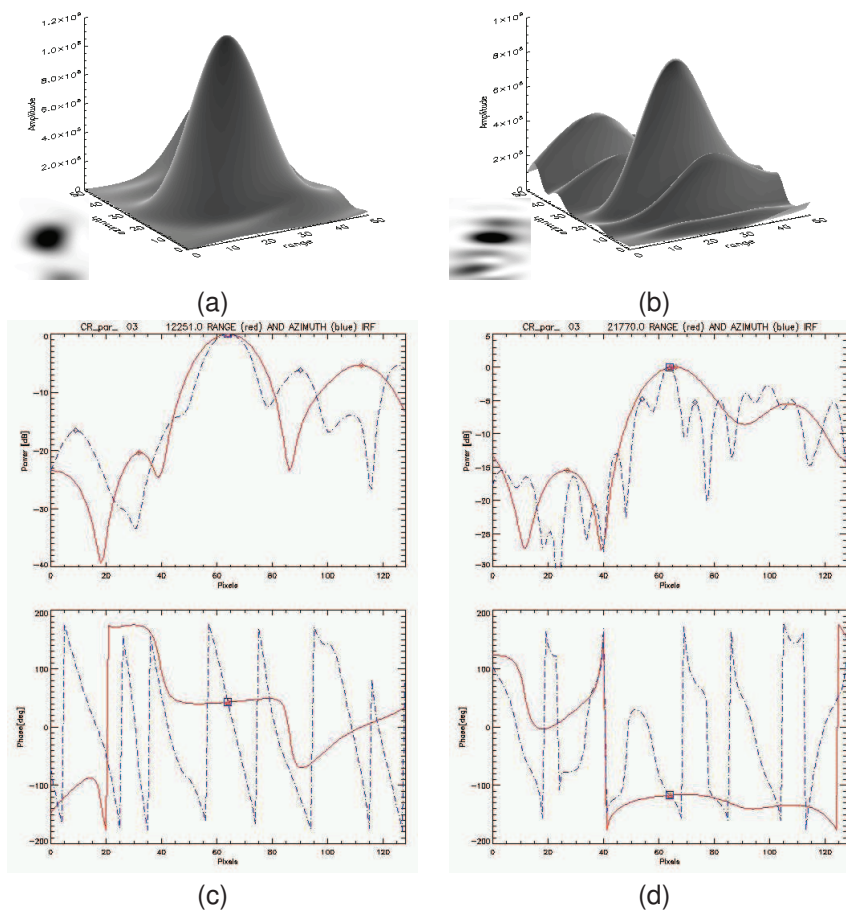


Figure 4.1.9: 3-D shape of the IRF estimated for the same point target with a good (a) and with a bad Doppler centroid value (b). IRF cuts in range and azimuth for the amplitude and for the phase for a processing with good (c) and with a wrong Doppler centroid value (d).

surement is obtained at the end of the phase analysis based mainly on the SPN phase model coherence adjusted for each pixel. The accuracy in the performances of both masks is very important. First, an initial mask of PSs with a lot of false detections or with a lot of noisy points can result into a fail of the network performance or convergence. This would make impossible the separation of the different phase artifacts in an accurate way leading in a fail of the SPN processing. Second, the final selection of the points of measurement is also very important. Possible false detections can lead into false alarms in possible interpretation of ground the deformations. Furthermore, if one is very conservative in this final selection of good points possible huge non-linear ground deformation can become lost or not detected, which is also very grave because this would imply a loss of the detection capabilities of the SAR system.

Thus, the investigation and enhancements in the selection of PSs in both steps is absolutely justified.

### 4.2.1 Enhancements of the initial estimation of PS

Here the amplitude dispersion index [Fer01] will be analyzed in order to improve the initial selection of stable points. The objective of these improvements are twofold, to give robustness to this initial mask and at the same time to increase this number of points within the mask. It must be considered that these two facts are incompatibles considering the current methodology used to achieve this purpose, relaxing the threshold over the dispersion index. This action implies the inclusion of more points within this initial mask but also it leads into an increase of the false alarms or false detections. In other words, the produced mask would be more dense but the noise level presented by the points could be very high, resulting in a complete failure of the SPN processing instead of the high density of points available.

The same effect occurs when the number of available SLCs is reduced. As it could be observed in figure 3.2.6 when this number of images is not large enough (of about 20) the standard deviation of the dispersion index estimator increases drastically (by a factor of 3). As result, the same effect explained just above (related with the relaxation of the threshold) can be noticed.

Another key factor which influences a lot on the accuracy of this estimator is the calibration of the SLCs. In order to analyze the variability of the pixel radiometric level in a set of acquisition it is very important to have all the images perfectly calibrated, specially between them. The objective is to evaluate the stability of the backscattering coefficient given by each pixel, which is directly related with changes in the SAR response due to different facts, noise, geometric or temporal decorrelation, etc.. Hence, if the images are not perfectly calibrated between them this measurement of change can be corrupted by this fact.

#### 4.2.1.1 Relative calibration of the images

Image relative calibration is mandatory before analyzing the variability of the amplitude for each pixel. The absolute calibration of the images is not important because the absolute power is not used in the measurements. Currently, the calibration is based on the computation of a constant power value per each SLC. This constant value is obtained by means of the equalization of the power in particular areas, see equation 4.2.1:

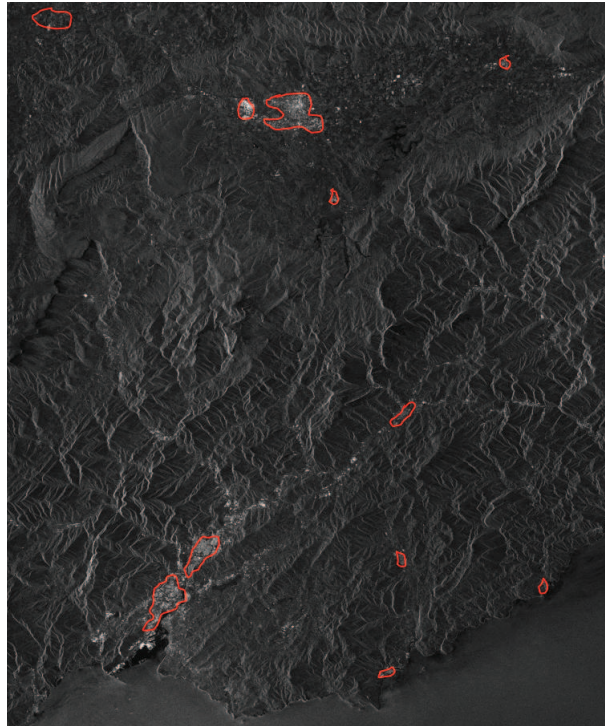


Figure 4.2.1: Example of the selection of the areas for compute the calibration constant based on the visual analysis of the SAR amplitude image.

$$CTE_i = 1/\sum_{areas} |SLC_i|^2 \quad (4.2.1)$$

The selection of these areas is a critical step. That must be performed manually based on the data visual inspection. The idea is to select areas within the SAR geometry which contain infrastructures or man-made objects (bright areas in SAR images) which are assumed to be radiometrically stable (or constant) over time. . These areas may be localized by visual inspection of the SAR image and it is desirable that they are distributed throughout the swath. See figure 4.2.1 for an example.

It must be highlighted that selecting bright areas can be difficult in some special cases, like for example the one depicted by figure 4.2.1. In mountainous or sub-urban areas the presence of man-made objects is not so important. Typically, over those areas this results into the definition of small regions which delimited by small towns detected by visual inspection of the SAR amplitude and distributed along the swath.

It should be noted that these calibration areas are selected roughly and that they could contain a large number of un-stable reflectors (under a radiometric point of view). The estimation of these constant values must thus be refined in some way. Based on [Gua03] it was demonstrated that the azimuth antenna pattern of the instrument can be estimated by means of the exploitation of the SAR amplitude over the PSs along its Doppler history (with level 0 data). It means that, over those point the radiometric quality of the signal is so good that it allow such kind of measurements.

Based on an initial estimation of the calibration constant over those rough areas per each SLC as defined above an initial of mask possible of PSs is obtained. These calibration constants are then refined by performing the computation over the location of the PSs. The initial mask of possible PSs can be updated and the procedure can iterate again. Thus, the proposed methodology

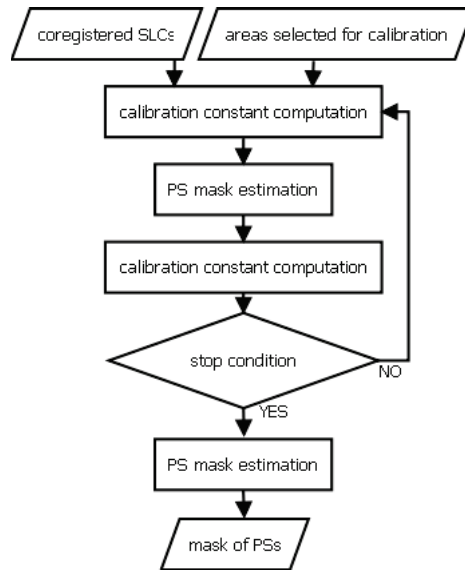


Figure 4.2.2: Flow chart of the iterative methodology performed to improve the detection of initial PSs.

should handle these iterations until some kind of stop condition. One possible exit condition could be based on setting a threshold of less than 0.1 dB in the estimation of the calibration constant of all the SLC, which is approximately the precision reported by the active transponders used for calibration purposes of the SAR instruments [Jac00]. The flow chart of the proposed methodology is shown in figure 4.2.2.

As it is depicted in figure 4.2.2 after the first iteration, the calibration constant is estimated only on the location of the PSs. Then, after the re-computation of the constants a new mask of PSs is obtained and consequently a new estimation of these calibration constants can be performed. This operation can be repeated until some stop condition is accomplished, like for instance based on the convergence of the value of the obtained calibration constants as explained above.

#### 4.2.1.2 Example of application

In order to evaluate the performances of the new proposed methodology a practical case of study based on real data is analyzed. The analysis of the test site is based on a data stack of 28 ENVISAT image mode SLCs. The objective is to evaluate the increase in the amount of PSs selected within the initial mask of good points based on the analysis of the amplitude standard deviation of the stacking of SLCs, see section 3.2.2.

Thus, the first step is the selection of one super master geometry and the performance of the coregistration of all the available SLCs into that common geometry (see section 3.3). Each SLC pixel may contain the radar response reflected from exactly the same ground area.

After the coregistration of all the images to the same geometry (see section 3.3), the first estimation of the calibration constant is done (equation 4.2.1), based on the selected areas distributed along the swath. By using these constant values the images can be calibrated in a relative sense and the evaluation of the variability of the amplitude of each pixel can be performed. The pixels presenting a low dispersion index of the amplitude standard deviation are selected as stable points (typically below 0.25). These two steps are considered as the iteration 0.

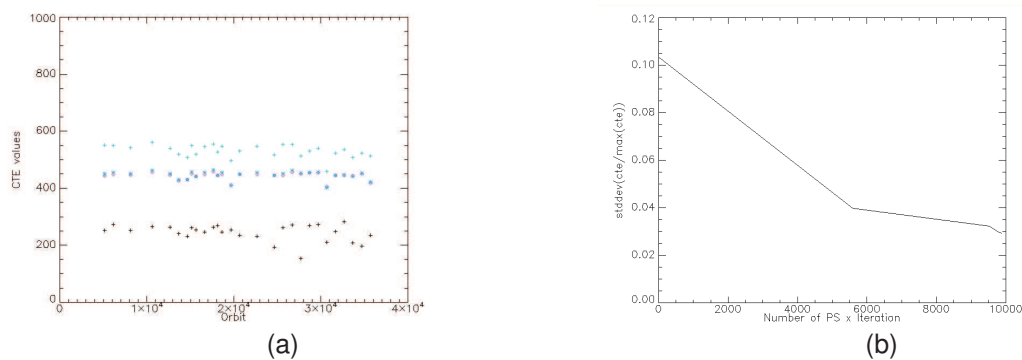


Figure 4.2.3: a) Estimated calibration constant (in power) per SLC in function of the iterations. White crosses for the iteration 0. Red crosses for the iteration 1. Red asterisks for iteration 2. Green diamonds for the iteration 3, the last one. b) Normalized standard deviation (in dBs) of the estimated calibration values in function of the number of pixels selected as PSs for each of the three iterations.

The algorithm is then iterating since the estimated constant per each SLC is not changing (changes below 0.1 dB between consecutive iterations). For this particular test case, the procedure required 3 iterations to reach this requirement.

In figure 4.2.3.a is presented the evolution of the estimated values for each SLC in function of the iterations. As it can be observed the mean of the values change drastically in from the iteration 0 to first one (by a factor of two in power units). After the second iteration the estimated values become almost stable, achieving the exit conditions of the procedure. It is interesting to notice that the spread of the estimated values is reduced with the iterations. This is normal as the points used for performing this estimation are better and better for each iteration under a radiometrically point of view.

In figure 4.2.3.b is shown the evolution of the normalized standard deviation of the estimated calibration values with the iterations in function of the amount of pixels selected as PSs. As it is depicted, the standard deviation of the estimated values is reduced at the same time as the total amount of selected PSs increases. In particular the total amount of PSs is twofold considering the first iteration and the last one (the third), by using always the same threshold for the selection. This is a very important result as the density of PSs is increased without losing radiometric properties.

In figure 4.2.4 are evaluated the performances of the considered procedure under an image point of view. The figures on the left correspond to the iteration zero (classical SPN), while the ones on the right are related to the last iteration (the third one). The SAR multimean amplitude and the final map of selected PSs for the same area between both iterations are compared, the same image histograms stretching have been applied in order to aid the visual comparisons.

As it can be observed by comparing figure 4.2.4.a with figure 4.2.4.b the radiometric quality of the multimean image has been enhanced. In figure 4.2.4.b more radiometric contrast between the different kind of surfaces presented on the image can be appreciated. In particular more details, textures and roughness can be observed when comparing figure 4.2.4.a with figure 4.2.4.b for the

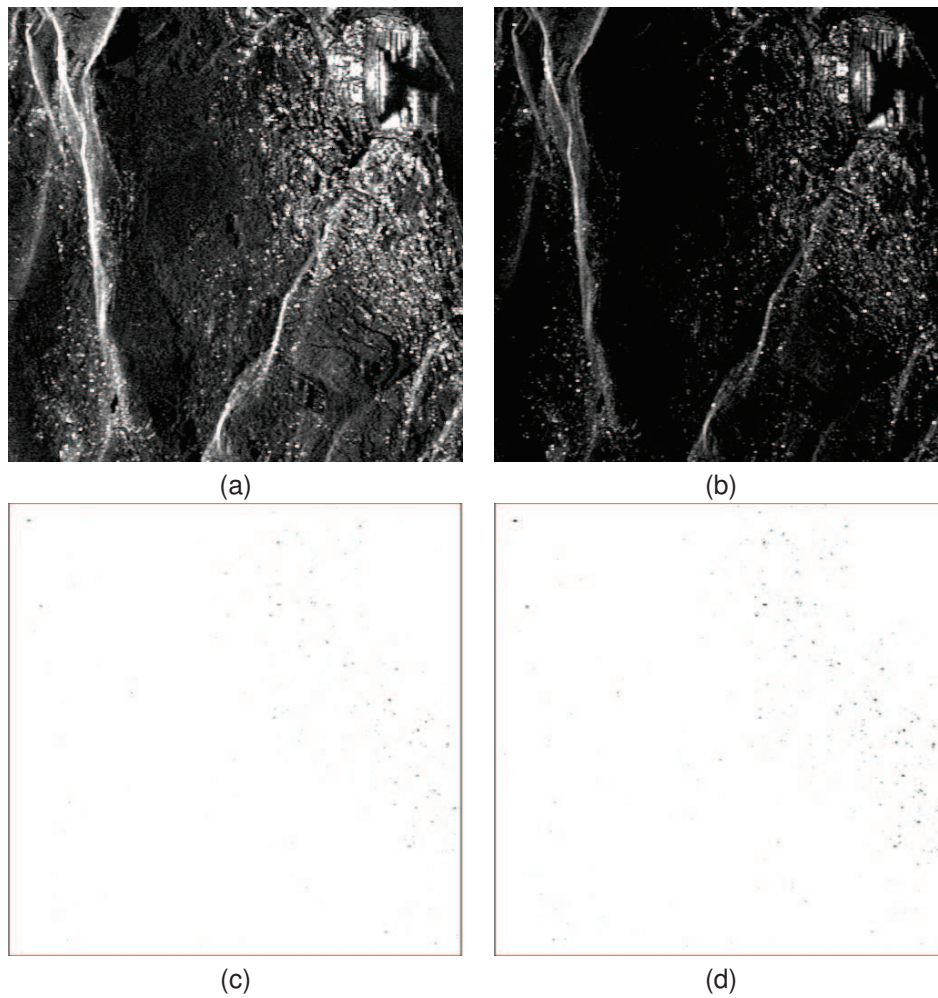


Figure 4.2.4: Example of the image radiometric enhancement induced by the new iterative methodology. a) SAR multimean image at the iteration zero. b) SAR multimean image at the last iteration (the third one). c) map with the locations of the PSs selected for the iteration zero and in (d) for the last one.

urban as well as for the field areas, which corroborates the radiometric resolution improvement introduced by this new methodology.

Another fact that confirms the radiometric enhancement is the selection of more PSs (considering the same threshold for the selection methodology). This can be noticed by means of figure 4.2.3.b, where the increase of the PS numbers in function of the iterations is illustrated. This can be checked also by visual comparison of figure 4.2.4.c with figure 4.2.4.d, more PSs arise in the urban area as well as in the fields.

This methodology is completely justified when using ERS, ENVISAT and RADARSAT data as their radiometric precision is in the order of more than 0.8 dBs [Ros]. However, this radiometric accuracy is extremely improved by the new generation sensors (TerraSAR-X, Cosmo-SkyMed,...). Their radiometric precision is in the order of 0.2 dBs, which is in the same order of magnitude as the precision achieved by the proposed methodology [Sch]. The applicability of this proposed methodology for this type of SAR data is still under investigation.

## 4.2.2 Final selection of PSlike pixels enhancements

As it was commented in the previous sections, the final SPN analysis is made in a pixel-by-pixel basis. The final mask of good point or pixels for measurements is performed mainly based on the model coherence evaluated for each pixel. Not all the interferometric measurements performed over a pixel have a direct correspondence in the real world. Some radar pixels may not be related to existing structures on ground as they are directly generated by the SAR processing itself. For instance, several artifacts can be created in the Synthetic Aperture Radar images due to the signal acquisition system or processing leading in particular artifacts which may be handled properly. For example, azimuth ambiguities and side lobes are two of them which could have a strong impact on interferometric measurements:

- Azimuth ambiguities: they may appear as strong targets in low backscattering areas like forest or water. In consequence they can be interpreted as strong targets within the selection of PSs.
- Side lobes of strong targets: the side lobes of strong targets can pollute lower level signals in the surroundings. Resulting mainly in a false estimation of the real density of points of measurements over the test site.

The main objective of this section is to present the way to identify those artifacts and to analyze their impact on SPN measurements. In summary, it can be said that they can cause ambiguous SPN measurements. This work has been presented in [Dur07b, Dur07a].

### 4.2.2.1 Origin of ambiguous SPN measurements

Two particular SAR artifacts are considered in this study, azimuth ambiguities and range side lobes. The origin of those artifacts will be explained briefly in this section. Some particular characteristics will be remarked in order to study their impact on PSI interferometry.

### SAR azimuth ambiguities

Due to the fact that SAR is a discrete system radar images are affected by some few artifacts such as the range and azimuth ambiguities. The radar acquisition system is generally set to make these artifacts as weak as possible. The ability of the instrument, processing settings or post-processing techniques are very important in order to obtain an acceptable image quality which does not influence the performances for final application. However, the radar signal return is polluted with the contribution of strong ambiguous signal. Such pollution may even partly or fully occlude non-ambiguous signatures. The appearance of an ambiguity is in the form of unwanted signal in the SAR image in terms of amplitude and phase which can be more easily distinguished in areas of low backscatterer such as calm water or field areas covered by vegetation.

Usually, the radar systems may have a poor signal to ambiguity ratio for reasons such as poor resolution performance, reduced antenna size (low-cost design) or improper antenna diagram pattern. In addition, there could be found some processing parameters which may be erroneous such as the Doppler centroid value.

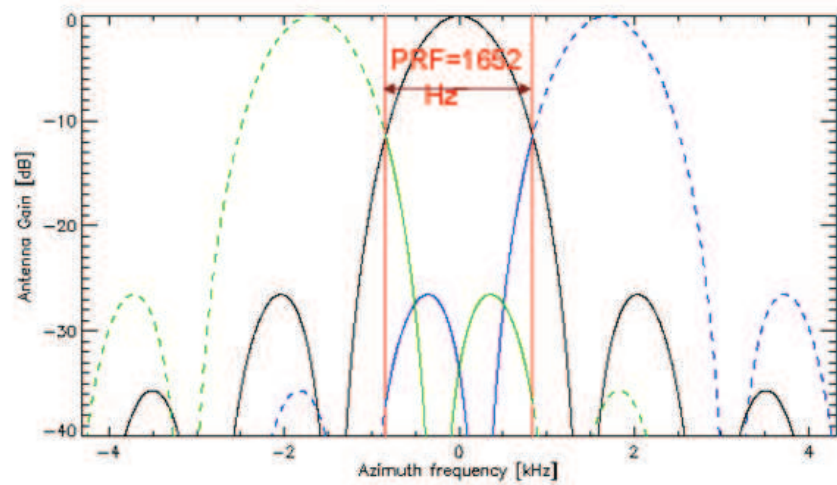
Ambiguities have specific characteristics which differ from unambiguous signals. Azimuth ambiguities are usually defocused since range migrations have not been properly corrected through SAR processing. Their spectral behavior is also modulated by the antenna side lobes patterns. Other important parameters are the PRF, the processing Doppler spectrum and the weighting filter.

Range ambiguities have their own phase history which is different from nominal targets. SAR processing cannot properly correct range migrations and phase history, which produces ambiguity defocusing. Important conditioning parameters are the antenna diagram pattern and the view acquisition geometry.

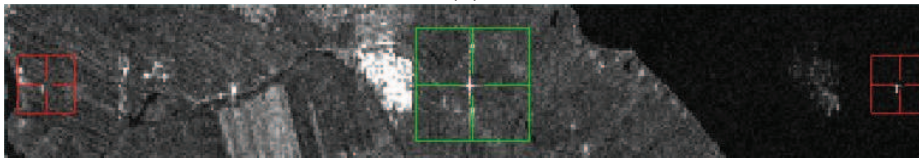
Typically, the impact of range ambiguities in the processed image is usually smaller in comparison with the azimuth ambiguities. The matched filter used for the range compression lead to a defocused of the range ambiguities by the fact that they are processed at range locations which are not the appropriate ones. Even in the cases where the power of the signal received by the edges of the main lobe or from secondary lobes might be comparable to that of the response coming from the images swath given by the main lobe of the antenna, the effect on the image is negligible and, in most cases, does not cause image degradation. For this reason, the impact of azimuth ambiguities on PSI measurements will be considered only [Li83].

Azimuth ambiguities are originated by the SAR signal undersampling in azimuth together with the length of the azimuth response given by the azimuth antenna pattern. The signal received (which is weighted by the azimuth antenna diagram) has a Doppler spectrum wider than the PRF, so the Nyquist sampling rate is not kept. Those frequencies higher than the PRF coming from the side lobe regions of the azimuth antenna are folded into the main part of the signal spectrum centered on the image Doppler centroid (which corresponds to the main lobe of the antenna) so that aliased signals are produced giving origin to ambiguous responses, see figure 4.2.5.a.

In the SAR image azimuth ambiguities appear displaced predominately in azimuth since they are observed a multiple of the integration time before and after the main response is acquired, see figure 4.2.5.b. However they are also displaced in range since the range migration curve of the ambiguous response is different from the one of the main response, see equation 4.2.2 which defines the relative position of the azimuth ambiguities for a given point target within the SAR image, see [Mor93, Gua05] for further details.



(a)



(b)

Figure 4.2.5: a) Azimuth antenna pattern in the frequency domain (dark) and the replicas at  $\pm PRF$  (red and blue) as result of the system sampling performed by the SAR acquisition procedure (given by the PRF). The processing bandwidth is the one contained between  $\pm PRF/2$  delimited by the two vertical red lines. The contribution of the ambiguities are given by the secondary lobes of the replicas that fall within the processing bandwidth (continuous blue and green lines). b) SAR amplitude image with the location of a strong target (green square) and its first azimuth's replicas (red squares). The azimuth ambiguities are perfectly visible in that case because they fall in areas of low backscatterer.

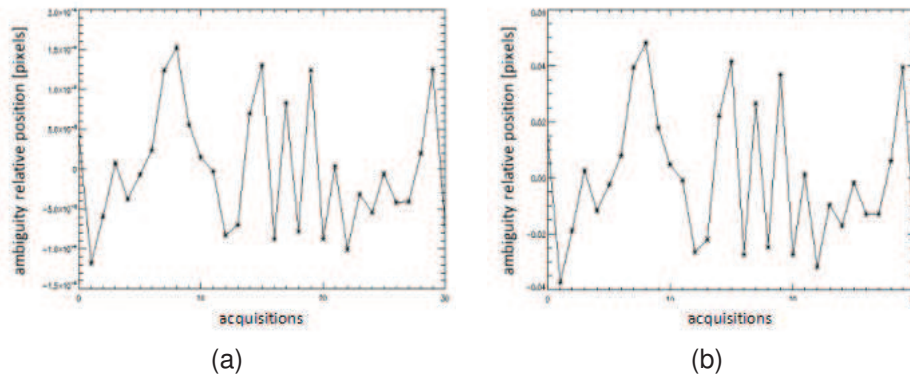


Figure 4.2.6: Pixel relative positions of an azimuth ambiguity in azimuth (a) and in range (b) versus its main target location for a stacking of 31 ERS1-2 images.

$$\Delta x_i = \frac{\lambda R_0}{2v_s} (PRF_i - f_{DC}) \quad \Delta r_i = \frac{\Delta x_i^2}{2R_0} \quad (4.2.2)$$

$R_0$  being the target's slant-range distance of closest approach.  $v_s$  the sensor velocity.  $f_{DC}$  the Doppler centroid frequency. PRF the sensor's Pulse Repetition Frequency and  $i$  the replica number of the ambiguity. From equation 4.2.2 it can be inferred that this displacement mainly depends on the particular image acquisition conditions and the acquisition mode timeline. Typical values for both displacements in the case of ERS-2 satellite are around 5600m in azimuth and 18.5m in range. Then, for similar Doppler rates in a stacking of SLCs (of the same track) the relative position of these ambiguities in azimuth and in range can be calculated for a given point target's location. An example can be seen in figure 4.2.6 for a stacking of 31 ERS1/2 images.

In figure 4.2.6 it can be seen that the position of the azimuth ambiguity remains extremely stable over the SLC's, at least under the expected coregistration precision (which is around 0.1 pixel). Furthermore, and according to the literature, azimuth ambiguities appear slightly unfocused and their phase values are the same as for the main target [Mor93, Gua05]. Following these considerations the selection of azimuth ambiguities as Persistent Scatterers with a strong reflectivity could be an important fact that may be considered.

### Range side lobes of strong targets

The use of chirp signals in spaceborne SAR systems allows a substantial reduction in the peak transmitted power of a radar without reduction of signal-to-noise ratio (SNR). In pulsed radar, a long duration, high bandwidth signal is transmitted. The received data is compressed by applying a matched filter, by correlating it with a reference function, usually a replica of the transmitted chirp signal. Thanks to this operation targets coming from different echoes can be detected from an apparent noisy signal. The resulting time domain waveform for those targets is a sinc function. Its disadvantage is the presence of side lobes.

This results in unsatisfactory performance since low level signals can be masked by the side lobes of higher level signals, see figure 4.2.7. The width of the main lobe corresponds to redundant information with respect to the center of the target response while side lobes express position uncertainty.

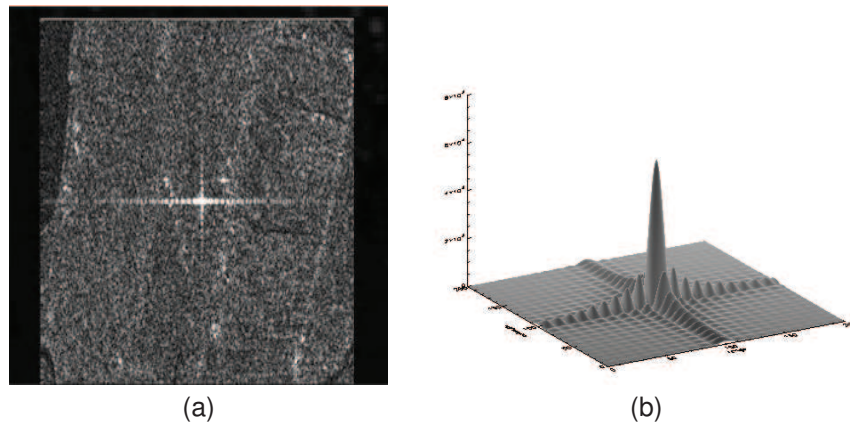


Figure 4.2.7: a) Example of SAR amplitude image with a strong target on it, the side lobes prevails over the background responses. b) Synthesized 3-D IRF for a strong target, the shape of the side lobes are perfectly visible in absence of clutter signal.

Side lobe weighting can be introduced at the processing level in order to overcome this problem. The most widely used weighting function is the Hamming window [Cum05], at the cost of geometrical resolution degradation. Other methods could be used such as SVA [Fis06] which presents a good trade-off between side lobes reduction and geometrical resolution preservation. However the effect of such a technique in interferometric applications is not yet fully assessed.

It is important to highlight that range main lobe and secondary lobes follow the properties of strong radar targets impulse response: stable phase in range and a ramp in azimuth in function of the image Doppler centroid. This can be checked in the IRF of a real strong scatterer presented in figure 4.1.3.

#### 4.2.2.2 Impact of SAR artifacts on SPN measurements

The two SAR artifacts originate ambiguous information at two different scales. Azimuth replicas of strong targets appear about 5600 meters (depending on the used satellite) away from the main target in the SAR image. Meanwhile range side lobes are close to the main target masking the response of neighbors pixels of low backscattering.

The impact of these artifacts on SPN measurements will be analyzed depending of the SPN steps at which they are detected as Stable Points or good points of measurement.. Their impact is thus considered at two different levels:

- Selection of ambiguous pixels as initial mask of stable points.
- Selection of ambiguous pixels as final coherent SPN points of displacement measurement.

#### Impact of SAR azimuth ambiguities in SPN measurements

Taking into account the theoretical studies exposed above the selection of ambiguous pixels within the initial mask of stable points may be expected. To test if it may occur two different datasets of SLCs are generated from a set of 31 ERS1-2 RAW data images:

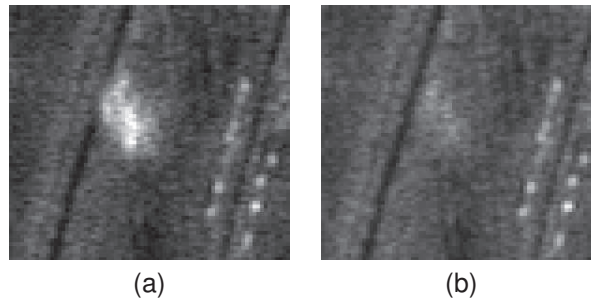


Figure 4.2.8: Example of Multimean reflectivity image in a low-backscattered area with the SLC's focused by taking the full azimuth band (a) and only a 80% (b).

- By focusing the full azimuth band. Resulting in a noticeable presence of azimuth ambiguities clearly visible in dark areas of the image, see example in figure 4.2.5.b.
- By focusing with 80% of the azimuth band (cutting the 20% of the band considering the image Doppler centroid frequency, which is one of the fast and optimum strategies for ambiguity reduction in ERS1-2 & ASAR IS2 mode while focusing). Resulting in a considerable reduction of the azimuth ambiguities.

Then, by differentiating the multimean reflectivity images of each dataset, the azimuth ambiguities can be perfectly distinguished and localized, see figure 4.2.8 for an example.

The next step is the generation of two different masks of stable points which are obtained by exploiting the amplitude stability of the SLC's pixels in both stacks. By comparing both initial mask of stable points, it was detected that almost 90% of the points are common, they have an identical mean reflectivity in both datasets. The remaining 10% of non-common stable points have a very similar mean reflectivity value. The ones presenting a higher differences are due to changes in the amplitude level of part of the azimuth main lobe. This is a normal effect considering that the azimuth spectrum was cut, so this is translated into a spread lobe effect in the slow-time domain.

Thus, for this particular test case no azimuth ambiguity pixels were selected as stable point. Deeper analysis can be driven by looking at the IRF of a strong (in terms of returned power) and very stable target and its azimuth replicas in low backscattering areas. An example is shown in figure 4.2.9.

From figure 4.2.9 it can be observed that the background has a considerable impact on the ambiguity. In general, although the target has a peak to clutter ratio sufficiently high to be well discriminated (see figure 4.2.9.a), the power level for the ambiguity is closer to the background one as depicted in figure 4.2.9.b,. This is normal and due to two main reasons (subsection 4.2.2.1). First the ambiguities are focused at SAR locations which are not the appropriate ones of the target's, then they are slightly defocused on the SLCs. Second, the azimuth replicas are weighted with different parts of the azimuth antenna pattern, which is not the main lobe and in consequence they have a lower power level [Gua05].

This spatial analysis of the main target and its azimuth ambiguity can be extrapolated to the time dimension considering some series of values on the stacking of SLCs as depicted in figure (4.2.10).

As it can be observed in figure 4.2.10 the real target is presenting a more stable amplitude time series meanwhile its ambiguity is showing more variability. It can be inferred that the background

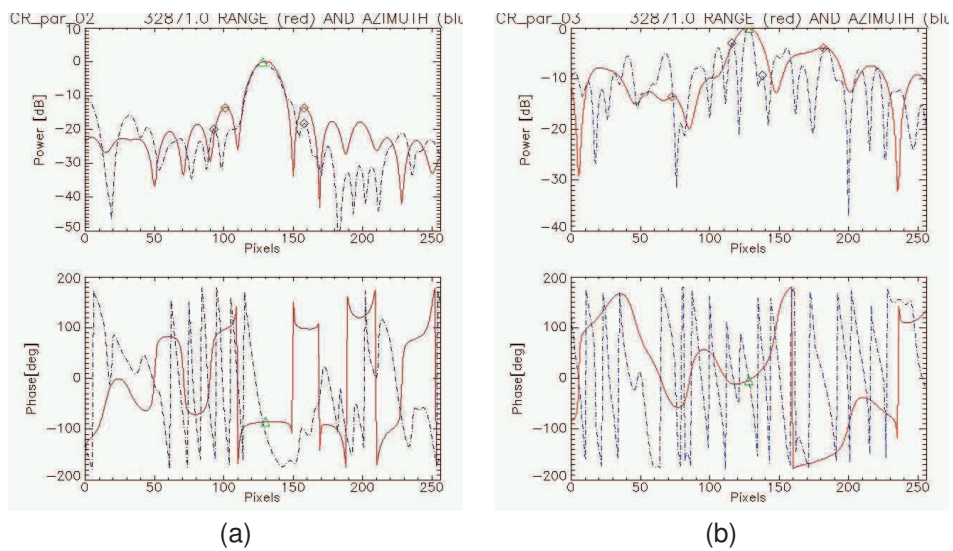


Figure 4.2.9: Example of IRF for a strong and stable target (a) and its first azimuth replica (b) not selected as stable point by means of the analysis of the amplitude stability .

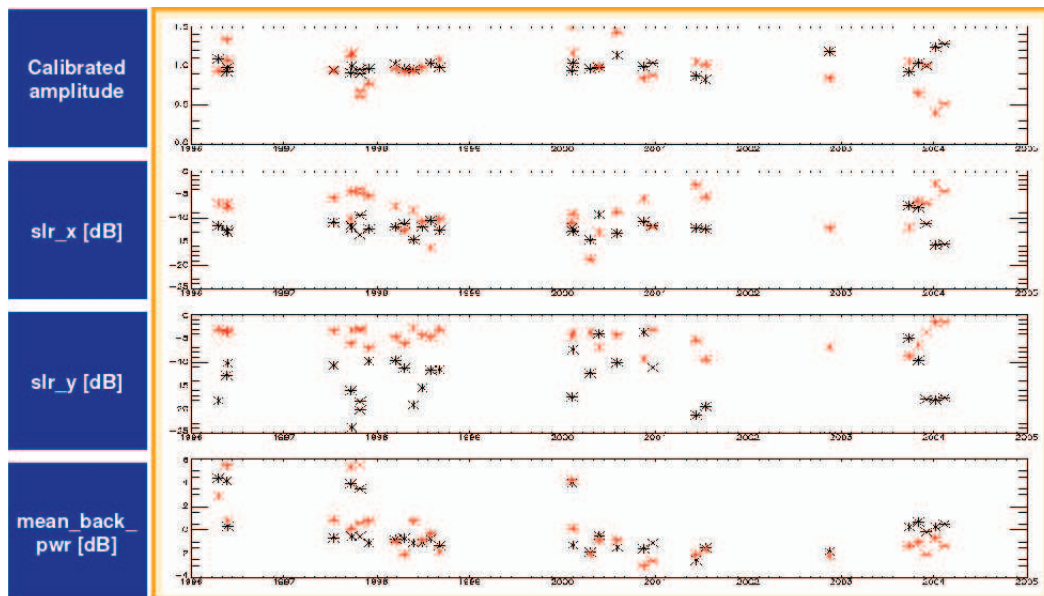


Figure 4.2.10: Real target (dark asterisks) versus its first azimuth ambiguity (red asterisks) -located in an area of low SAR backscattering- analyzed on a stacking of 31 SLCs (ERS1-2). It can be noticed that the phase values per acquisition are not the same for the main target and for its ambiguity. Also the amplitude values fluctuate more for the ambiguity time series than for the main target. The surrounding clutter is corrupting the phase and the amplitude value of the ambiguity.

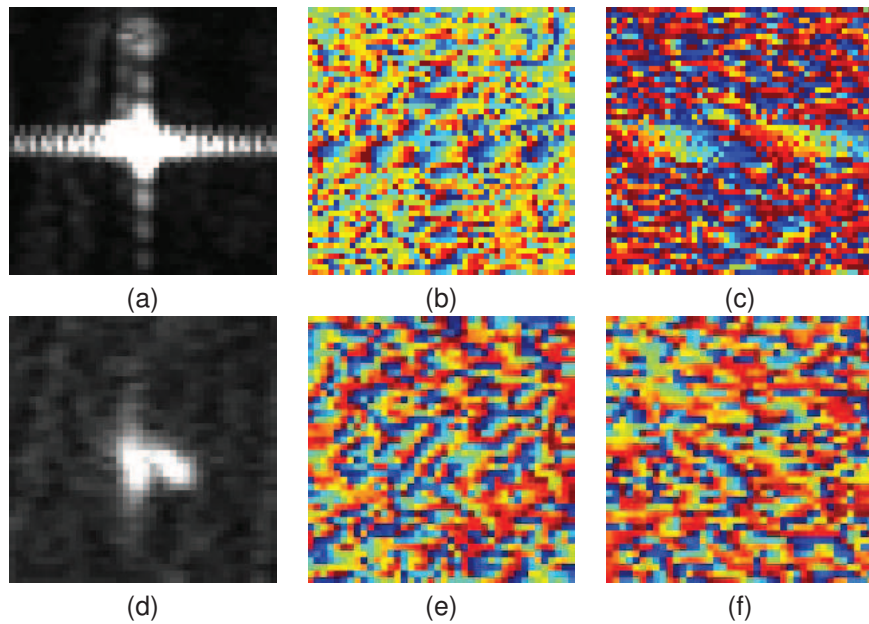


Figure 4.2.11: Example of DInSAR fringes for a real target (a,b,c) and for its azimuth ambiguity (d,e,f). Multimean image for the real target (a) and for the azimuth ambiguity (d). Interferometric phase with height of ambiguity of 40 meters for the real target (b) and for the azimuth replica (e). DInSAR phase with a height of ambiguity of -100 m for the main target (c) and for the azimuth ambiguity (f). The interferometric phase of the ambiguity presents fringes as well as the main target which vary in function of the baseline.

has a considerable impact on the ambiguity, which is normal as the Side Lobe Ratio (SRL) for the azimuth as well as for the range direction is lower for the ambiguity case than for the main target. In general, although the real target has a peak to clutter ratio sufficiently high to be well discriminated, the ambiguity is closer to the background level, due to the simple azimuth antenna pattern weighting [Gua05]. As the background is changing with the temporal conditions (wind, moisture, seasons), it results in an amplitude fluctuation hiding more or less the ambiguity along the temporal SLC data stacking, see figure 4.2.10. It can also be added that the background impacts the ambiguity phase as it is not the same as the main target while theoretically they should be the same target [Mor93, Gua05].

In any case, as it is depicted in figure 4.2.9 the shape of the IRF function of the azimuth ambiguity is very similar to the one of the main targets, but as it was said, with a different phase value versus its main target.

Under an interferometric point of view, this behavior is translated into good coherence in the DInSAR phases. Then on a stacking of interferometric coherence, azimuth ambiguities could be selected within a mask of initial stable points. See figure (4.2.11) for an example.

The interferometric spatial signature of a point target and of its azimuth ambiguity is very similar and it follows the same behavior in function of the baseline (in space), as depicted in the comparison performed in figure (4.2.11). However, even if they have interferometric coherence azimuth ambiguities are not properly modeled under SPN. It means, comparing the interferometric phase value of a point target and of its first azimuth ambiguity in a stacking of acquisitions in function of the baseline it can be noticed how the behavior of the ambiguity it is completely random. Their behavior are similar to any other noisy pixel, see figure (4.2.10) for an example baseline first order modeling over the interferometric phases.

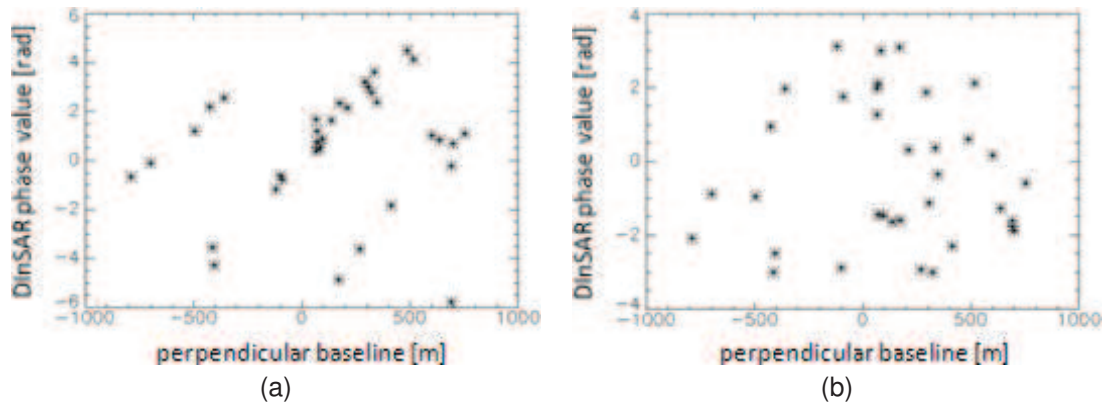


Figure 4.2.12: Example of stacking of interferometric phase values versus the perpendicular baseline for a point target (a) and for its azimuth ambiguity (b). The x-axis represent the baseline values in meters while the y-axis are the DInSAR phase values in radians

As it can be observed in figure (4.2.10) the behavior of the phase value for a point target (a PS) in a stacking of interferogram follow a linear relationship with the baseline values. However, the behavior observed for the azimuth ambiguity do not follow any particular relationship with baseline, see figure (4.2.10) .b. The spread of the values is similar to the one observed for any other noisy point. This reveals that the interferometric phases of those ambiguous pixels are corrupted mainly by these three reasons:

- The phase value is not the same as for its main target response in the SLC image with a real background clutter.
- The local topography used when producing the DInSAR phases is not the correct one for the ambiguity (they are located 5600 m away from its real position within the SAR geometry).
- Likewise for the pixel's atmospheric compensation within SPN. The compensated APS is not the right one for this region of the SAR image where the ambiguity falls.

In conclusion, it can be stated that azimuth ambiguities are not selected as final SPN points of measurements because their stacking of DInSAR phases can not be properly modeled. Due to different phase model mis-compensations the stacking of the ambiguity phases do not follow any particular pattern.

### Impact of range side lobes in SPN measurements

Main lobes and side lobes of strong targets are selected as stable points based on the SLC's amplitude stability as well as on the mean interferometric coherence. Therefore, it is a problem that should be considered in SPN since it occurs at the beginning of the process. See figure 4.2.13..

Range side lobes have a particular phase behavior in relation with the center of the main lobe. They have a constant phase value in range and they follow a ramp in azimuth based on the Doppler centroid characteristics of the SLC, see figure (4.2.9). Thanks to this particular geometrical behavior their interferometric phases can be modeled within SPN in order to set the effective spread of the signal response for strong targets. Side lobes pixels coming from strong and coherent targets can be identified and classified by means of a phase model fitting based on these

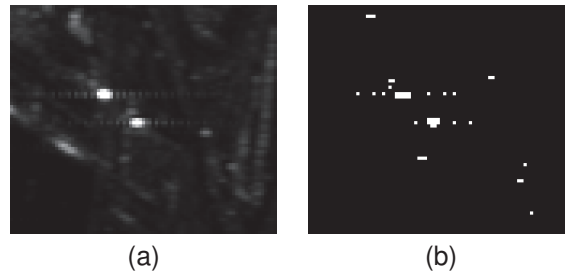


Figure 4.2.13: Example of multimean image (a) and initial mask of pixels selected as stable points by means of the amplitude standard deviation analysis of a stacking of SLCs (b). Usually part of main lobes and secondary lobes of the same ground target are selected as different Stable Points as inputs for the SPN analysis.

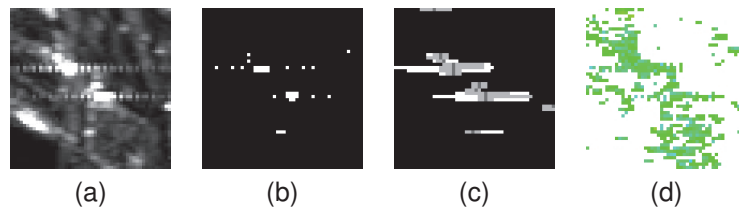


Figure 4.2.14: Example of range side lobes inclusion in SPN analysis. a) Multimean amplitude image. b) initial mask of stable points by means of SLC's amplitude stability analysis, part of the main lobe and some secondary lobes are selected as initial PSs. c) side lobes and secondary lobes pixels detection and classification (dark grey indicates the center of the main lobe, light grey the side lobes, white the secondary lobes and dark means not treated data). d) final deformation mean rate measured in side lobes after the geometrical compensation of the phase. Green means no deformation.

two properties. The phase of these pixels (classified as secondary lobes) can be compensated allowing more reliable deformation measurements, see figure 4.2.14.

In figure 4.2.14 an example of side lobes inclusion in SPN analysis is given. It can be seen that part of the main lobes and secondary lobes of strong targets are included in the initial selection of stable points, figure 4.2.14.a and 4.2.14.b. Then, based on the geometrical phase behavior of the side lobes the spread of the signal response can be set, 4.2.14.c. Pixels included within the same target's SAR response can be identified and classified as center of the main lobe (dark grey in 4.2.14.c), part of the main lobe (light grey in 4.2.14.c) and secondary lobes (white in 4.2.14.c). Thus, the pixels classified as side lobes can be compensated in phase (the light grey and the white ones in figure 4.2.14.c). Thanks to this additional geometrical phase model compensation the SPN measured deformation is consistent for all the range side lobes pixels with the respect to the value detected for the center of the main lobe, as it can be observed in figure 4.2.14d.

However, it is interesting to analyze even further the consistency of the deformation estimates over the side lobes. In figure 4.2.15 the histogram of the mean deformation rate over the side lobes with respect to the estimated value for the center of the main lobe is presented. The histogram is showing that effectively the measured rate is the same as this differential value is centered around zero. The observed width of 0.1 cm/years in the subsidence difference is due to the higher level of noise that can be found in side lobes.

Those pixels are synthetically produced due to the extension of the signal response of strong scatterers and they do not contribute any new information. Hence, by keeping only the center of the target's main lobe two main improvements can be highlighted:

- Efficiency in the quantity and in the quality of the final selected points. In an area of about

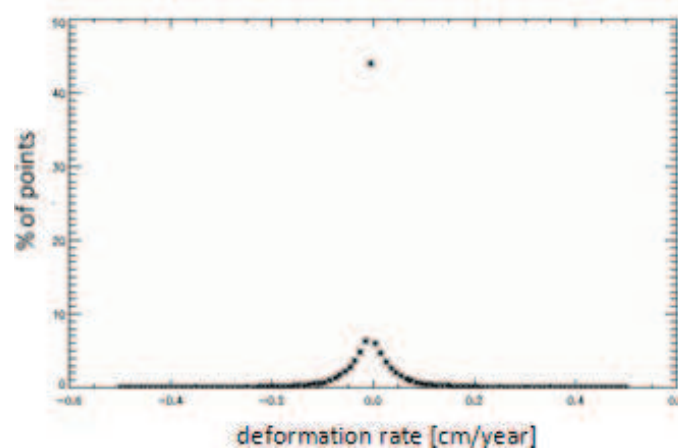


Figure 4.2.15: Histogram with the estimated mean deformation rate difference between the center of the target and the range side lobes for all the strong and coherent scatterers of an extended area of about  $500 \text{ Km}^2$ .

500  $\text{Km}^2$  there has been estimated an optimization of a 30 % in the final amount of good points without loss of information.

- More precise geocoding of the final estimates on ground. This is produced by reducing the position uncertainty introduced by the fact of having so many replicas of the same spread along the projection of the satellite line of sight onto the ground.

In order to illustrate these improvements, a comparison of the final map of PS estimates on ground geometry is conducted and illustrated in figure 4.2.16. It can be noticed how the deformation values measured in the side lobes are consistent with the values given by the center of the target's SAR response. Furthermore, the improvement achieved in the final location of the measurements by removing this redundant and spread pixels (which are related to the side lobes and which do not show any new information) can be appreciated in figure 4.2.16.c and d.

Just to conclude, side lobes introduce redundant information and uncertainty in the geocoding of the final estimates. By considering only the center of the main lobe as point of measurement two main improvements are achieved. One in terms of information efficiency; as the amount of points is reduced by a factor of about 30% without losing detection capabilities. The other one in terms of increase of the geocoding precision; as eliminating the side lobes reduce the location uncertainties of the final position of measurement on ground

### 4.3 SPN linear deformation improvements

As it was explained in section 3.3 SPN is based on a linear model for the estimation of the ground deformation. The linear model is the first order degree of the Taylor's series approach considering a deformation time series in time. It is assumed that the main part of the energy of the analyzed deformation signal can be modeled by means of this first order polynomial. In real cases, each analyzed test case present a particular deformation pattern in time and space which is completely singular and unique. It is very difficult by this reason to define higher order deformation model which match perfectly all the cases. It is better to have a more general and flexible model (only first order) which can be used in almost all the cases, especially when no a priory information is

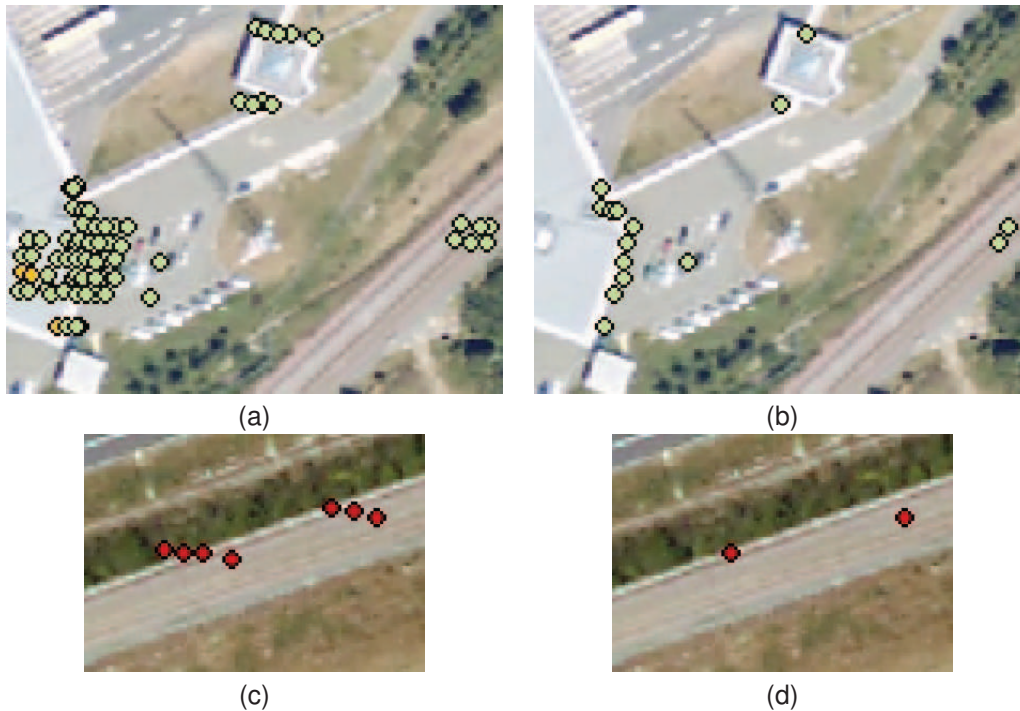


Figure 4.2.16: Example of final geocoded SPN mean deformation rate. Left column (a,c) are the resulting selected PSs based on the SPN model coherence thresholding criteria. Right images (b,d) correspond to the same areas but projecting only the center of the main lobe. Top row (a,b) represents an area without deformation and in the bottom row (c,d) there is an area presenting a moderate deformation values. As it can be observed the detection capabilities are not lost instead of the reduction of PS density. Copyright SPOTIMAGE for the background images.

available (blind cases). In that cases the major improvements come by analyzing carefully the reliability of the performed estimates in order to estimate the precision of the estimates and the goodness-of-fit of the model parameters in order to detect and to handle properly possible outliers. Two main enhancements has been performed:

- Robustness of the linear deformation pattern in time
- Robustness of the linear deformation pattern estimated in space by SPN

### 4.3.1 Robustness of the linear deformation pattern in time

The linear deformation model is adjusted to all the interferometric data pairs which are considered as input to the SPN process. During all the steps of SPN all the interferograms have the same weight. However, not all of them present the same phase variability. They are affected by different levels of noise, understanding noise as all the phase artifacts not considered within the SPN main phase model based on the point height and the ground deformation, see equation 3.3.1. Hence, this noise pattern is characterized by the white noise (thermal noise, processing noise, etc.) and the atmospheric phase screen.

Hence, there is a clear dependence of the SLC phase standard deviation in function of the distance. Before the unknown parameters are estimated a variance component estimation can be performed over each interferogram. The spatial network generated by SPN, see section 3.3.5.1,

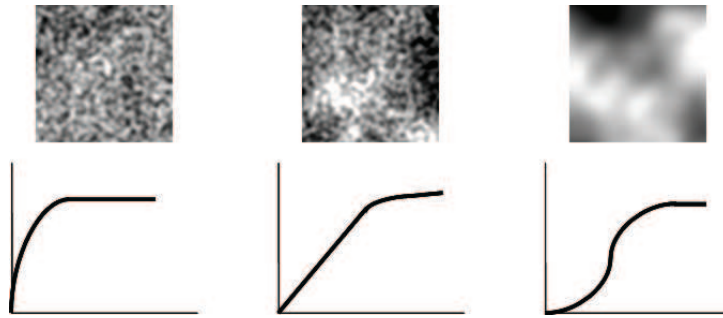


Figure 4.3.1: The variogram function is a very useful tool for measuring the spatial variability of a given field. From left to right it can be observed three fields presenting different variability in space resulting in three very different variogram estimated curves.

can be used for the estimation of the variance components. Thus, this variance function can be used as weight each time a SLC is used in an interferogram within SPN.

#### 4.3.1.1 Variogram definition

The variogram function characterizes the spatial continuity or roughness of a given field. The variogram analysis consists in the experimental variogram calculated from the input data and the variogram model fitted to the data. The experimental variogram is calculated by averaging one-half the difference squared of the values over all pair of observations regarding a specified separation distance and direction. The variogram model is selected from a set of mathematical functions that describe spatial relationship, see figure 4.3.1. The appropriate model is chosen by matching the shape of the curve of the experimental variogram to the shape of the curve of the mathematical function. To account for geometric anisotropy (variable spatial continuity in different directions), separate experimental and model variograms can be calculated for different directions in the data set.

In practice, the variogram of a field  $Z$  is defined as depicted in equation 4.3.1.

$$2\gamma(h) = E \left\{ [Z(u) - Z(u+h)]^2 \right\} \quad (4.3.1)$$

where  $Z(u)$  is the value of the field  $Z$  at the location of  $u$  and  $E$  is the statistical expectation operator. If the function is sampled over a finite set of location, say  $\{Z(u_i)\}$ ,  $i = 1, \dots, N$ , its variogram can be estimated applying the formula of the equation 4.3.2.

$$\hat{\gamma}(h) = \frac{1}{2N(h)} \sum_{i=1}^{N(h)} [Z(u_i) - Z(u_i+h)]^2 \quad (4.3.2)$$

where  $N(h)$  is the number of pairs of points having a distance equal to  $h$ , see figure 4.3.2 for clear understanding.

Thus, the experimental estimation of the variogram function is usually implemented by defining a vector of lag distances  $h_k$ ,  $k = 1, \dots, M$  and then by considering all the pairs of points having distances varying between  $h_k$  and  $h_{k+1}$ . Then, it is computed the mean of the squared differences and equation 4.3.2 can be re-written by means of equation 4.3.3.

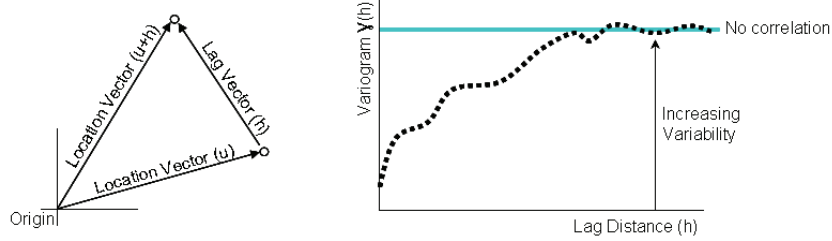


Figure 4.3.2: Illustration of the practical procedure for estimating the variogram of a sampled field.

$$\hat{\gamma}(h_k) = \sum_k \left( \frac{1}{2N_k} \sum_{j=1}^{N_k} \Delta Z_{k,j}^2 \right) \quad (4.3.3)$$

where  $\Delta Z_{k,j} = [Z(u_x) - Z(u_y)]_j$ ,  $h_k \leq \|u_x - u_y\|_j \leq h_{k+1}$  for  $j = 1, \dots, N_k$ . Being  $N_k$  the number of point pairs having a location distance between the lag defined by  $h_k$  and  $h_{k+1}$ . Further details regarding statistic analysis for spatial data can be found in the bibliography [Arm89, Cre91]

#### 4.3.1.2 Estimation of the variogram per SLCs

The objective is to estimate the variogram per each SLC in order to evaluate the variability of the phase as function of the atmospheric artifacts of this particular acquisition. In case of SPN, the input data field is composed by the InSAR phases. The main problem is that they are a wrapped magnitude with values contained between  $-\pi$  and  $+\pi$ . As it was explained in section 3.3 SPN overcomes this problem by means of the fitting of a very simple phase model in a network of relative measurements. Basically an increment of vertical height and differential linear deformation rates between two nearby pixels are estimated, see equation 3.3.1. Thus, if this model is subtracted per each arc and per each interferogram the residual phases must be almost unwrapped. The spatial variability of these residual phases must be dominated by the large scale phase artifacts not considered within the model and which may be correlated in space, say the atmospheric phase artifacts mainly. Those residual phases (see equation 3.3.3) are the input for the estimation of the variogram.

Thus, the established SPN network of measurement and the residual InSAR phases per arc can be used to estimate the variogram of each interferogram. Then, the contribution for each SLC can be computed in the same way as defined in section 3.3.5.6, by inverting the equation system  $Ax = b$ .  $b$  being the observation data, the value of the estimated variogram per each lag distance,  $A$  is the design matrix system which defines the combination of SLCs which forms all the used interferograms and  $x$  is the set of unknowns which is the value of the variogram per each SLC. This is repeated per each lag value.

Finally, a model is adjusted based on the resulting experimental variogram obtained per each SLC. In figure 4.3.3 are presented some of the most common positive definite models used to build a legitimate covariance model for any possible value of the lag distance. There is a great flexibility in modeling variograms with linear combinations of established models.

Visual inspection of the experimental variogram obtained per each SLC showed that the exponential function can fit properly the observed data, see equation 4.3.4. However there are two

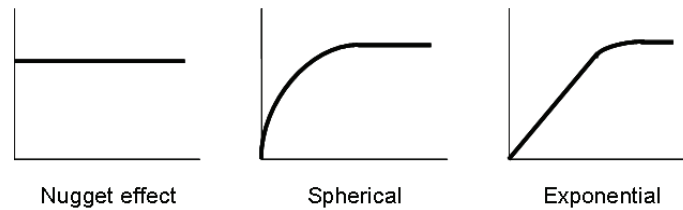


Figure 4.3.3: Some of the most common functions used to model the experimental variogram.

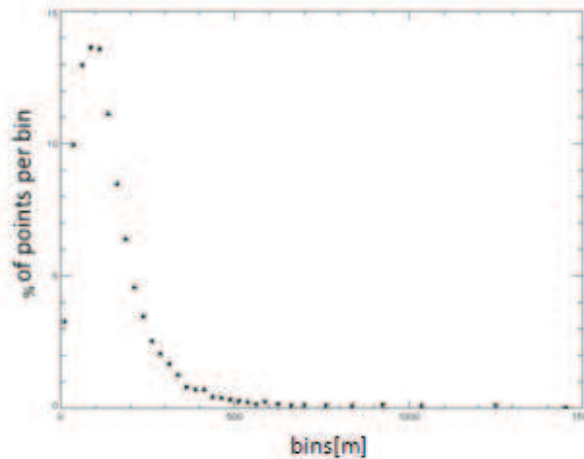


Figure 4.3.4: Example of non-uniform definition of the lag vector for the computation of the experimental variogram based on a SPN network configuration. Mean value for the length of the arcs of the network is equal to 150 m with a standard deviation of about 120 m. Those are typical values for purely urban areas. For rural or field areas these values will increase up to 300 meters.

main problems that must be considered when modeling the variogram:

- The reduced number of samples for large values of lag distances. Due to the properties of the used methodology to perform the network links, Delaunay triangulation, short connections are preferred to large ones (Euclidean distance based on the location of the PSs is used as norm, see section 3.3.5.1). In consequence, large values of distance are not so common as short ones. The solution adopted is to define a non-uniform vector of lag distances to perform the estimation of the experimental variogram. This can be done by analyzing the histogram of the Euclidean distance given by the arcs of the SPN network, see figure 4.3.4 for an example of application. The defined minimum bin size is of 25 meters, if the total amount of samples is below 20 then two consecutive bins are merged up to this minimum number of samples is reached.
- The wrapped nature of the phase. The observed data could present wrapping. Especially for large values of lag distances, more than 500 meters, the presence of important atmospheric disturbances provokes that the phase difference between the two considered points is not base-banded. In other words, there is more than one full cycle of  $2\pi$  between the two residual phase values. This is translated into an increase of noise for the estimated value of the variance magnitude, see figure 4.3.5. The solution adopted is to give more weight to the estimates for the lowest values of lag distances and perform a robust model fitting based on an iterative adjustment with rejection of outliers.

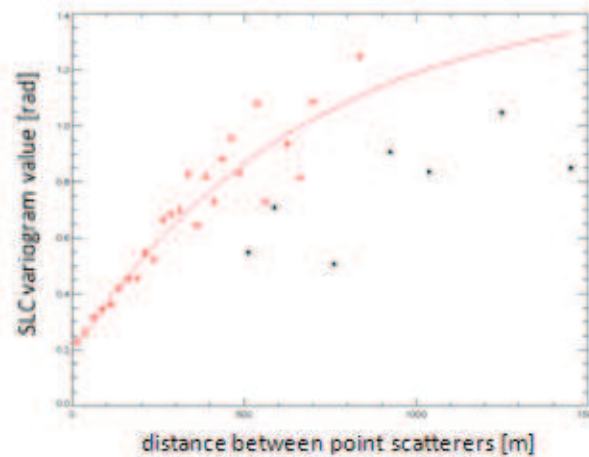


Figure 4.3.5: Example of experimental variogram (asterisks) estimated per one SLC. Red line is the final exponential model adjusted for the variance function. In red are the final values used to fit the model and in black the rejected ones. As it could be observed the level of noise in the samples of the experimental variogram increases drastically with the distance, and especially for values higher than 500 meters.

As it was stated before the used function for the modeling of the variance estimate per each SLC is the exponential semi-variogram one defined in equation 4.3.4.

$$\text{Var}(h) = \begin{cases} C_1 e^{(-3h/A)} & \text{if } h \neq 0 \\ C_1 + C_0 & \text{if } h = 0 \end{cases} \quad (4.3.4)$$

where  $A$  is the range. At distances beyond  $A$  the semi-variogram or covariance remains essentially constant.  $(C_0 + C_1)$  is the nugget, which provides a discontinuity at the origin and  $C_0$  is the sill, which is the variogram value for very large distances. The nugget value indicates the level of “white” noise (thermal noise, processing noise,..), which is a background spurious signal presented in the measure and which is independent of the distance between points. The sill value indicates the level of noise introduced by the atmosphere for large distances. In figure 4.3.6 it can be observed the sill and the nugget value estimated for each SLC.

The information presented in figure 4.3.6.a allows to identify images presenting a high level of noise (processing noise, thermal noise of the instrument, etc..). Additionally, the information presented in figure 4.3.6.b can be used to know which of the SLCs are presenting higher phase variance due to atmospheric perturbations. For example, in figure 4.3.7 two multilooked interferogram are showed for comparison purposes. In 4.3.7.a is presented an interferogram with a sill level of about 4 radians (estimated for one of the orbits which forms the interferogram). In figure 4.3.7.b the interferogram has a detected sill level of about 0.8 radians. Under a qualitative point of view it can be observed that effectively the atmospheric perturbations are originating higher phase dispersion in the interferograms in figure 4.3.7.a than the one in figure 4.3.7.b.

### 4.3.1.3 Application

As it was demonstrated the estimation of the variogram per each SLCs is very useful to know the impact of the atmospheric artifacts over the acquisitions. Furthermore it gives an idea of the noise

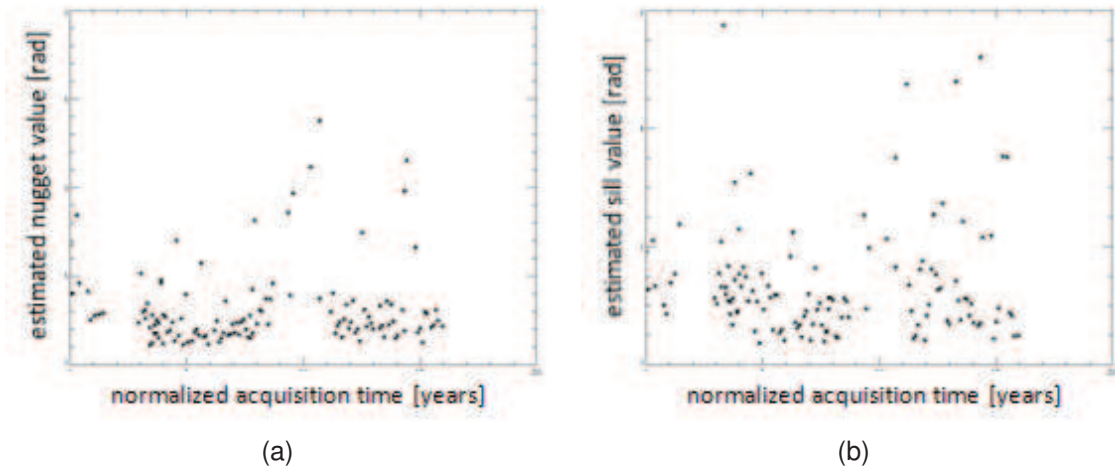


Figure 4.3.6: Example of estimated nugget and sill value for the fitted exponential functions used to model the experimental variogram estimated for each SLC in function of the normalized acquisition time.

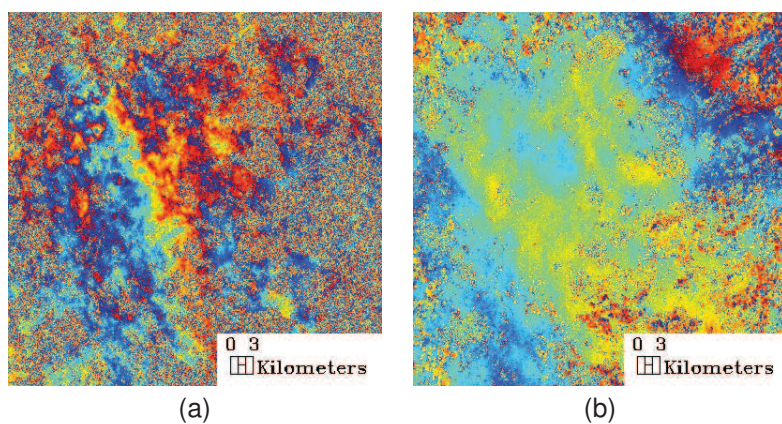


Figure 4.3.7: Example of multilooked (30x6) interferograms with ERS2 data. a) interferogram presenting important atmospheric artifacts (sill value of 4 radians). b) interferogram presenting reduced atmospheric perturbation (sill value of 0.8 radians). The pixel spacing is of about 120 meters. The color table is blue-to-red, corresponding to phase values from  $-\pi$  to  $+\pi$  radians.

level of in each acquisition. This information can then be used in order to weight the contribution of each interferogram during the different steps of SPN. The weight is defined by means of an inverse relation with the estimated variance per each interferogram which is given by the addition of variances of both SLCs. The estimated variance for an interferogram is thus defined by means of equation 4.3.5.

$$\sigma_{INT1-2}^2 = \sigma_{SLC1}^2 + \sigma_{SLC2}^2 \quad (4.3.5)$$

Each time an interferogram is used, it is weighted by the inverse of its estimated variance. This is done in two steps of SPN, during the fitting of the SPN phase model and when the SLC absolute deformation time series are obtained.

### Weighting the observations during the estimation of the deformation time series

The equation system used to estimate the deformation time series (section 3.3.5.6) can be weighted as well, see [Pre07]. The system matrix defined in equation 3.3.6 and can be rewritten as in equation 4.3.6 in case of knowing the measurement errors of the observations  $\sigma_i$ .

$$A_{ij} = \frac{a_{ij}}{\sigma_i} \quad (4.3.6)$$

Hence, the example for system matrix A presented in equation 3.3.7 for a set of 5 SLCs and 10 interferograms results in the following one presented in equation 4.3.7.

$$A = \begin{bmatrix} 1/\sigma_1 & -1/\sigma_1 & 0/\sigma_1 & 0/\sigma_1 & 0/\sigma_1 \\ 1/\sigma_2 & 0/\sigma_2 & 0/\sigma_2 & -1/\sigma_2 & 0/\sigma_2 \\ 1/\sigma_3 & 0/\sigma_3 & 0/\sigma_3 & 0/\sigma_3 & -1/\sigma_3 \\ 0/\sigma_4 & 1/\sigma_4 & -1/\sigma_4 & 0/\sigma_4 & 0/\sigma_4 \\ 0/\sigma_5 & 1/\sigma_5 & 0/\sigma_5 & -1/\sigma_5 & 0/\sigma_5 \\ 0/\sigma_6 & 1/\sigma_6 & 0/\sigma_6 & 0/\sigma_6 & -1/\sigma_6 \\ 0/\sigma_7 & 0/\sigma_7 & 1/\sigma_7 & -1/\sigma_7 & 0/\sigma_7 \\ 0/\sigma_8 & 0/\sigma_8 & 1/\sigma_8 & 0/\sigma_8 & -1/\sigma_8 \\ 0/\sigma_9 & 0/\sigma_9 & 0/\sigma_9 & 1/\sigma_9 & -1/\sigma_9 \\ 1/\sigma_{10} & 0/\sigma_{10} & 0/\sigma_{10} & 0/\sigma_{10} & 0/\sigma_{10} \end{bmatrix} \quad (4.3.7)$$

Also the vector b with the observations in equation 3.3.6 must be weighted with the estimated noise of each interferogram as defined by equation 4.3.8.

$$b_i = \frac{\varphi_{INTi}}{\sigma_i} \quad (4.3.8)$$

With the weighted equation system, the obtained time series estimated for the temporal deformation present a lower dispersion. The deformation for each SLC is estimated with more precision. See next figure 4.3.8 for an example of time series with and without the use of the weights.

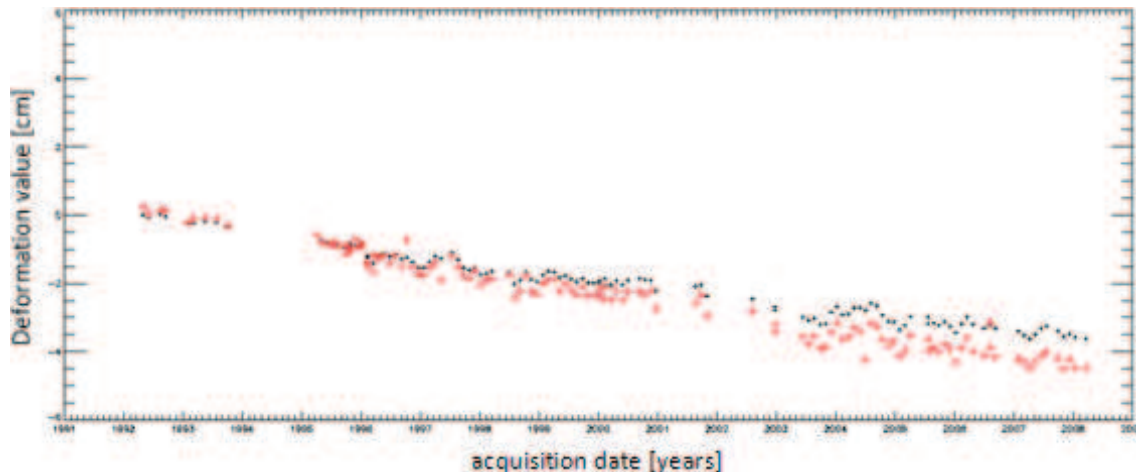


Figure 4.3.8: Final estimated time series of deformation with (black) and without (red) weighting of the observations. The mean deformation rate has changed and the noise of the time series has been drastically reduced. Especially the ERS2 acquisitions from 2002 to the end of the considered period, which present more phase noise due to the platform fluctuations and instabilities (see [Mir03]).

## 4.4 SPN non-linear

Up to here, all the previous sections contained within this chapter have presented improvements in terms of quality control, check of the robustness of the estimates and regarding the efficiency in the selection of the final points (image pixels) of measurement. However, it was not presented yet a solution to one of the main drawbacks of SPN which is related to the loss of measurement points due to fact that the analyzed “true” ground deformation is out-of-model. A new proposed methodology will be presented for dealing with this kind of deformations which are not strictly linear in time (model assumed by SPN).

This study and development will be divided into several steps. First the limits and the specificities of the actual model-fitting methodology will be stressed by means of a simulated scenario. The same controlled environment will be used to introduce the new proposed methodology. Finally, both methodologies will be evaluated in a real scenario which presents a known non-linear deformation event, the test case of the train station of Saint Lazare in the center of the city of Paris in France.

### 4.4.1 Characterization of the SPN linear model fitting procedure by means of simulations

SPN performs a relative phase model adjustment between two nearby points considering a set of differential interferometric phases as inputs, see equation 3.3.1. This model-fitting is based on the maximization of a function defined in equation 3.3.2. In other words, the solution for the model parameters are the ones which minimize the residuals in a coherent way (as the input phase is wrapped). The lomb-scargle periodogram [Lom76] philosophy is used to obtain this solution. In order to analyze and to understand the performance of this minimization methodology a simulation environment has been developed.

The simulator considers the performance of the phase model adjustment between two nearby

pixel, which is performed in time domain. The inputs of the simulator is the number of acquisitions and the total time span covered by the acquisition epochs. The repeat cycle time and the wavelength given by the acquisition system (35 days and 5.6 cm for the ENVISAT case for example and 11 days and 3.1 cm for the TerraSAR-X case). ENVISAT acquisition conditions will be considered for the simulations hereafter. The relative acquisition epoch for each acquisition and the perpendicular baseline are computed randomly.

A noise component can be added to each interferogram and to each SLC. The expected interferometric coherence for each acquisition pair is computed in function of the temporal and the perpendicular baseline. The objective is to simulate different conditions in terms of temporal and geometrical decorrelation. The computation of the coherence is based in the expression described by equation 4.4.1.

$$Coh_{interf} = (1 - \Delta T / \Delta T_{max}) \cdot (1 - B_{perp} / B_{perp max}) \text{ for } \Delta T \leq \Delta T_{max} \text{ and } B_{perp} \leq B_{perp max} \quad (4.4.1)$$

where  $\Delta T$  is the temporal baseline and  $B_{perp}$  the perpendicular one. The maximum allowed values for these parameters define the correlation environment for a given interferometric combination. A simulation with a reduced value for  $\Delta T_{max}$  (of about 2 years for example) or for  $B_{perp max}$  (of about 500 meters) will represent an *environment with huge decorrelation conditions*. For values of about 5 years and 1200 meters respectively will be considered as a *very correlated environment* (almost close to an ideal case). When any of the two values (temporal or perpendicular baseline) are larger than the maximum ones then the coherence is set to 0 for this particular interferometric combination. As it means that the scatterers would be completely uncorrelated for this interferogram. This interferometric coherence is translated into phase fluctuations by means of the following expression defined in equation 4.4.2 [Bam98].

$$\sigma_{interf phase}^2 = \frac{\pi^2}{3} - \pi \arcsin(coh_{interf}) + \arcsin^2(coh_{interf}) - \frac{Li_2(coh_{interf}^2)}{2} \quad (4.4.2)$$

where  $Li_2(\cdot)$  is the Euler's dilogarithm. Equation 4.4.2 sets a relationship between the estimated interferometric coherence and the variance of the phase for a generic case. In figure 4.4.1 is showed the shape of this relationship.

Furthermore, a noise factor is considered for each SLC. This value considers the instrument thermal noise, the possible coregistration inaccuracies, and some other sources of errors specific to each acquisition, like for instance atmospheric perturbations. The simulator considers only the phase model fitting procedure for a given increment of interferometric phase between two nearby points. Then, in function of the distance between these two points and in function of the atmospheric conditions during the acquisition of each SLC this level of noise can vary. Within this simulator this level of noise is simulated by means of a uniformly distribution for each acquisition in a set of 5000 statistic trials. The maximum variance level is increased each time from 0 up to a value close to  $\pi$  in order to evaluate the performance of the model fitting methodology according to:

- The level of noise.

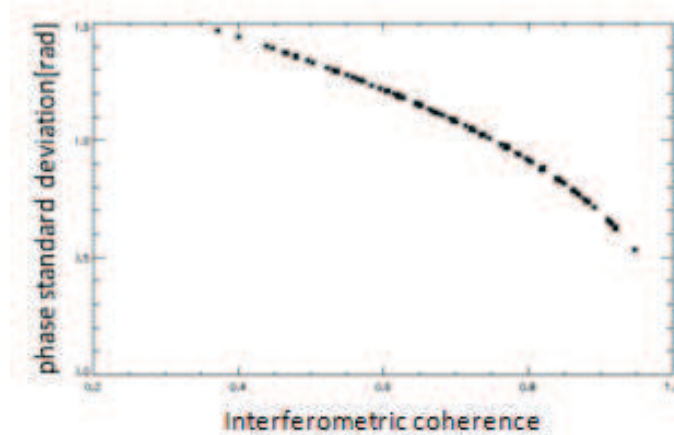


Figure 4.4.1: Standard deviation of the interferometric phase as function of the coherence (considering only one look).

- The number of samples (number of acquisition and number of interferograms used for the model fitting).

The performance of the model fitting are evaluated by means of the analysis of:

- The percentage of false detection: based on the 5000 trials, it is evaluated how many times the solution is not in correspondence with the true value (related with the accuracy).
- The standard deviation of the adjusted model parameters: which determines the precision of the solution (but not the accuracy).
- The shape of the coherence function: which governs the final solution.

Finally, several ground deformations (in time) will be generated for the evaluation of the performances under different cases.

#### 4.4.1.1 Performance of the estimator in function of the noise

The objective of this section is to evaluate the performance of the phase model fitting in function of the level of noise. For this case the generated ground deformation (reference) will be equal zero for all the acquisitions. The number of acquisitions is set to 14 with a span of 3 years. The level of noise per acquisition is increased gradually by setting the phase noise variance from 0 to a value above  $\pi$ . Furthermore, two different temporal and geometrical decorrelation environments are considered as described above. A very relaxed environment (close to an ideal case) is considered with about 5 years and 1200 meters for the decorrelation thresholds, named correlated environment. A more constrained environment with 2 years and 500 meters of baseline as decorrelation thresholds, named partially decorrelated environment. Several investigations are done, based on the observation of the results. They are presented and commented below.

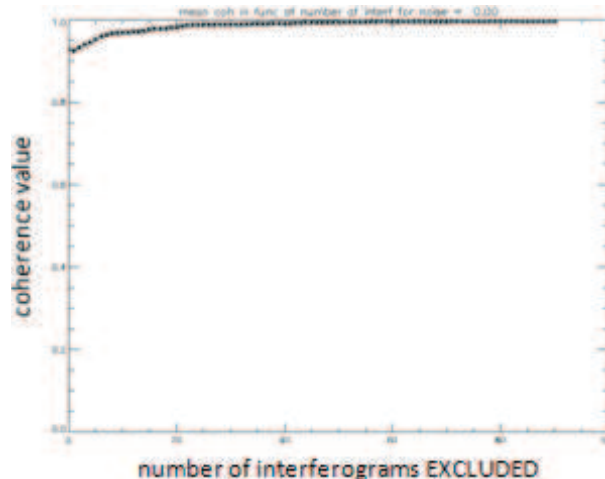


Figure 4.4.2: Coherence value in function of the number of interferograms used to perform the model fitting with a noise variance equal zero for each acquisition.

#### **Ideal case (almost no temporal or baseline decorrelation of the target) and without noise**

The system performs very well independently of the number samples. As it is shown in figure 4.4.2 the coherence for this almost ideal case is close to 1 independently of the used number of interferograms. However, it can be observed that the coherence function is not exactly equal to 1 at the beginning of the analysis, when all the interferograms are used within the model fitting. This is due to the fact that interferograms with large time span (5 years) and large baseline (1200 m) present more phase variance than the shorter ones. It is important to highlight that the removal of interferograms in the model fitting procedure is performed by following an inverse law which removes interferograms with large baseline and large time span at the beginning. A normalization relationship is set, it assumes that 1 years is equivalent to 200 meters of baseline in terms of phase noise.

#### **Ideal case (almost no temporal or baseline decorrelation of the target) and with noise**

The performance of the system degrades with the reduction of the number samples. The introduction of noise in the phase of each acquisition is translated into a degradation of the performances of the SPN model fitting system, see figure 4.4.3. Then, the number of samples used by the model fitting is crucial to keep the performances. As it can be observed in figure 4.4.3.a the coherence function measures a lower value as the noise per acquisition is increased. Also the variance of these values increases. This is completely normal as the phase residuals are higher due to the presence of noise. It is interesting to note that the degradation of the coherence with the noise follow the same shape independently of the number of samples, see figure 4.4.3.b. The only difference is that variance of the coherence estimator increases with noise as it was said above.

As it was expected, the precision of the system is governed by the number of samples. As it can be observed in figure 4.4.3.c the reduction of samples results in a reduction of the precision. Also when the number of samples is very low (blue curve in figure 4.4.3.c) the precision is very sensitive to the noise level, becoming gravely degraded with the increase of noise. Although, the precision is not presenting any special variation with the increase of noise in general (figure 4.4.3.c) the accuracy is seriously degraded, see figure 4.4.3.d. When the noise variance per acquisition is higher than 1 radian the accuracy decreases drastically up to a value above 50% of

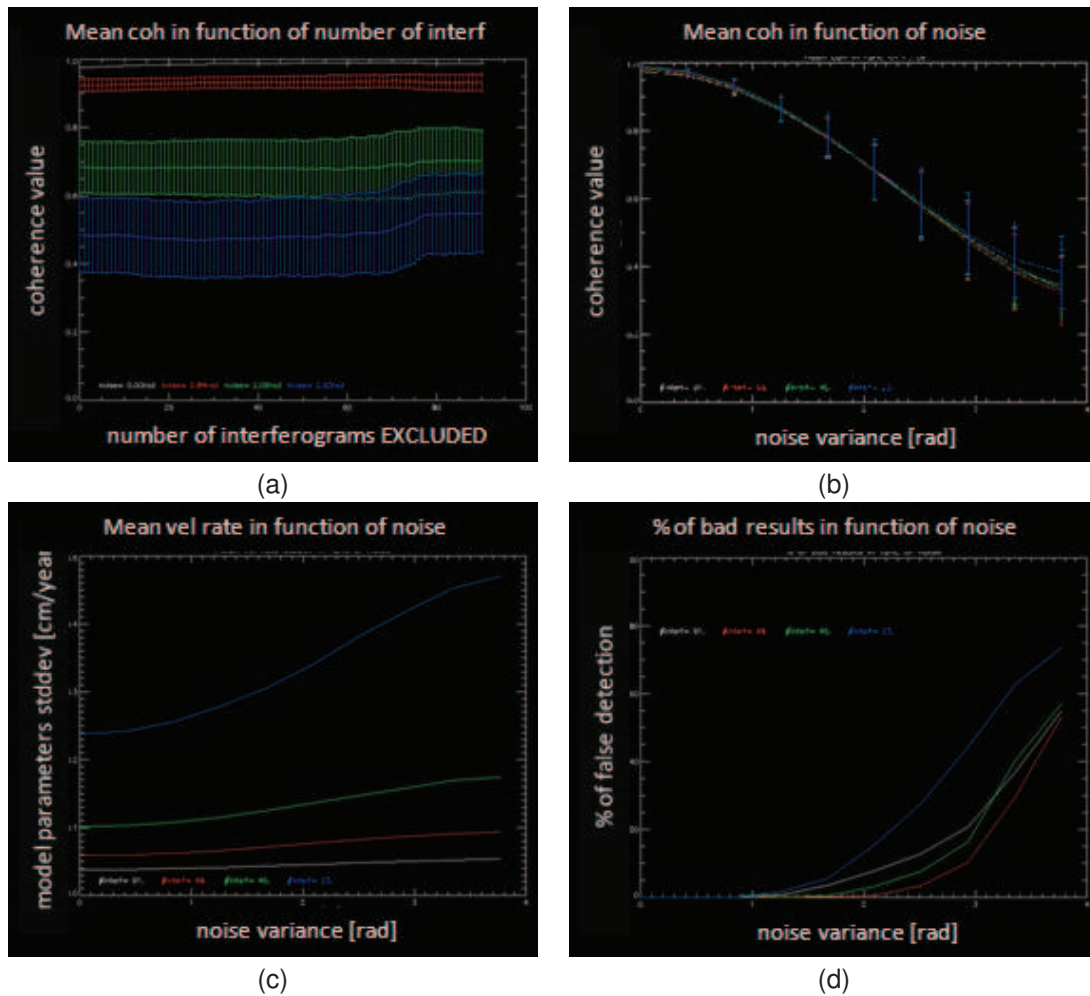


Figure 4.4.3: Performance of the model fitting system in an almost ideal case (almost free of temporal and baseline decorrelation) with 14 acquisitions. a) evolution of the coherence estimator in function of the number of used interferograms for different noise levels. b), c) and d) are respectively the coherence estimator, the estimation of the accuracy and of the precision in function of noise and for different number of interferograms.

false detections. . Furthermore, the shape of the red line in figure 4.4.3.d with respect the other ones indicates that the degradation of the accuracy for this particular number of used interferograms (68) gives the better performances. As it can be observed in figure 4.4.3.d the degradation starts for a noise variance higher than 2 radians instead of the 1 radian measured for the other curves. This is a very interesting result, most probably this curve indicates that the optimum list of interferometric combinations that should be used in order to achieve the better performances during the model fitting (within this almost ideal case).

#### Performance of the system in a partially decorrelated environment

The same analysis is performed but increasing the temporal and the geometric decorrelation noise by a factor of two more or less. In the case an interferogram is completely decorrelated if it achieves a perpendicular baseline of about 500 meters or if it has a temporal span of more than 2 years. The general sense is that the system performs worst, which is normal as the noise level introduced by each interferometric combination is higher as default, see figure 4.4.4 and compare it with figure 4.4.3. The coherence results in a lower value in comparison with the precedent case. The precision is also affected by the increase of noise. Systematically the values are higher than

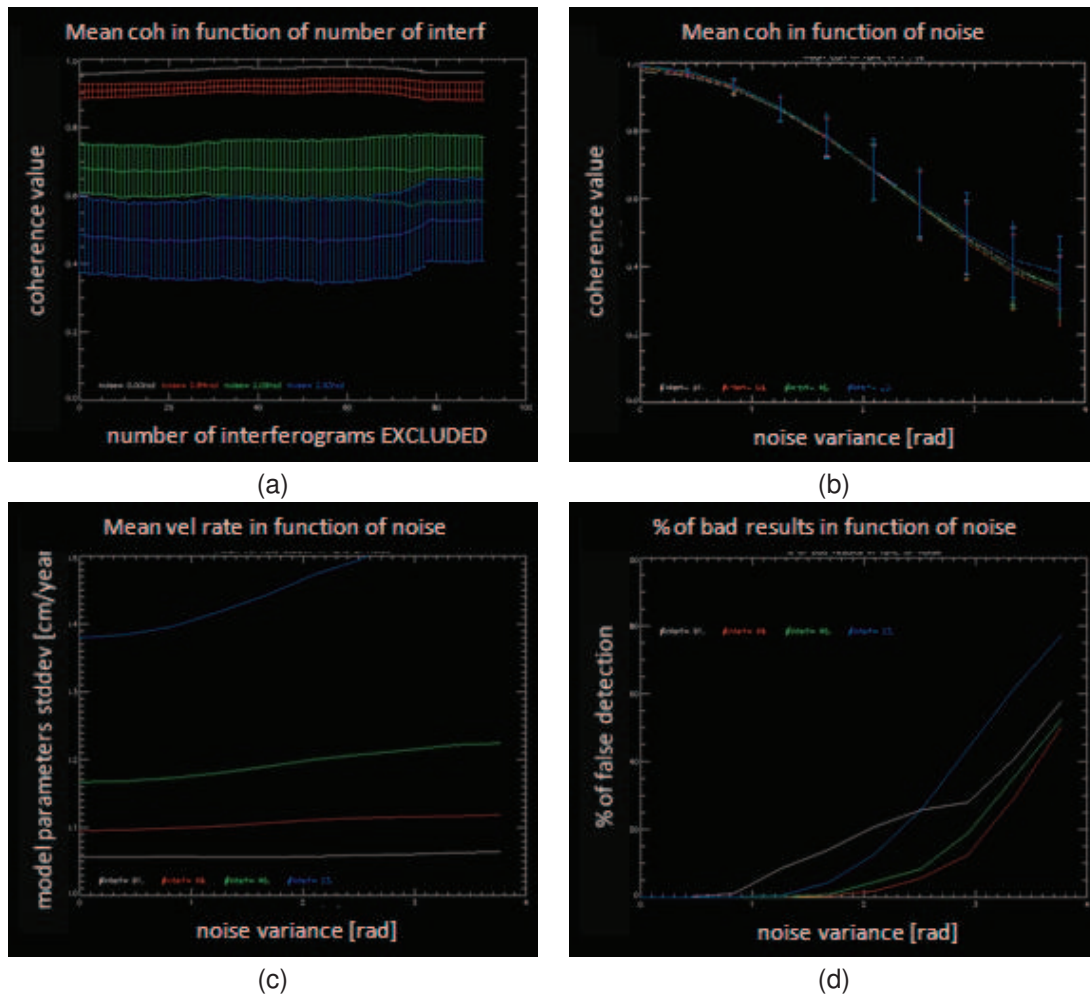


Figure 4.4.4: Performance of the model fitting system in a partially decorrelated environment with 14 acquisitions. a) evolution of the coherence estimator in function of the number of used interferograms for different noise levels. b), c) and d) are respectively the coherence estimator, the estimation of the accuracy and of the precision in function of noise and for different number of interferograms.

in the previous case, compare figure 4.4.4.c with 4.4.3.c.

The more interesting difference is the fact that in the current test, the accuracy of the system is seriously degraded when all the interferograms are used (white curve of figures 4.4.4.d and 4.4.3.d). As it was introduced in the previous section, the use of all the interferograms results in an improvement of the measured precision of the estimated parameters and in an increase of robustness of the estimated coherence function (which is normal as the maximum number of samples are used). However, it results in a grave degradation of the accuracy of the model fitting system as soon as the noise variance per each acquisition is increased significantly, of about 0.5 radians now when before this threshold was detected above 1.2 radians. This demonstrates that for a given acquisition dataset and for a given temporal and geometric decorrelations (given for each particular ground surface properties) it exists an interferometric combination which gives the better performances of the SPN model fitting system.

#### Effect of increasing the number of acquisitions

The same simulation conditions as in the previous subsection (partially decorrelated environment with 14 acquisitions) is considered now with a number of 30 acquisitions. In order to preserve

the sampling interval per year the total time span has been increased twofold, from 3 year to 6 years now. The same graphics are recalculated with this new conditions in order to evaluate the performances of the model fitting system, see the results in figure 4.4.5.

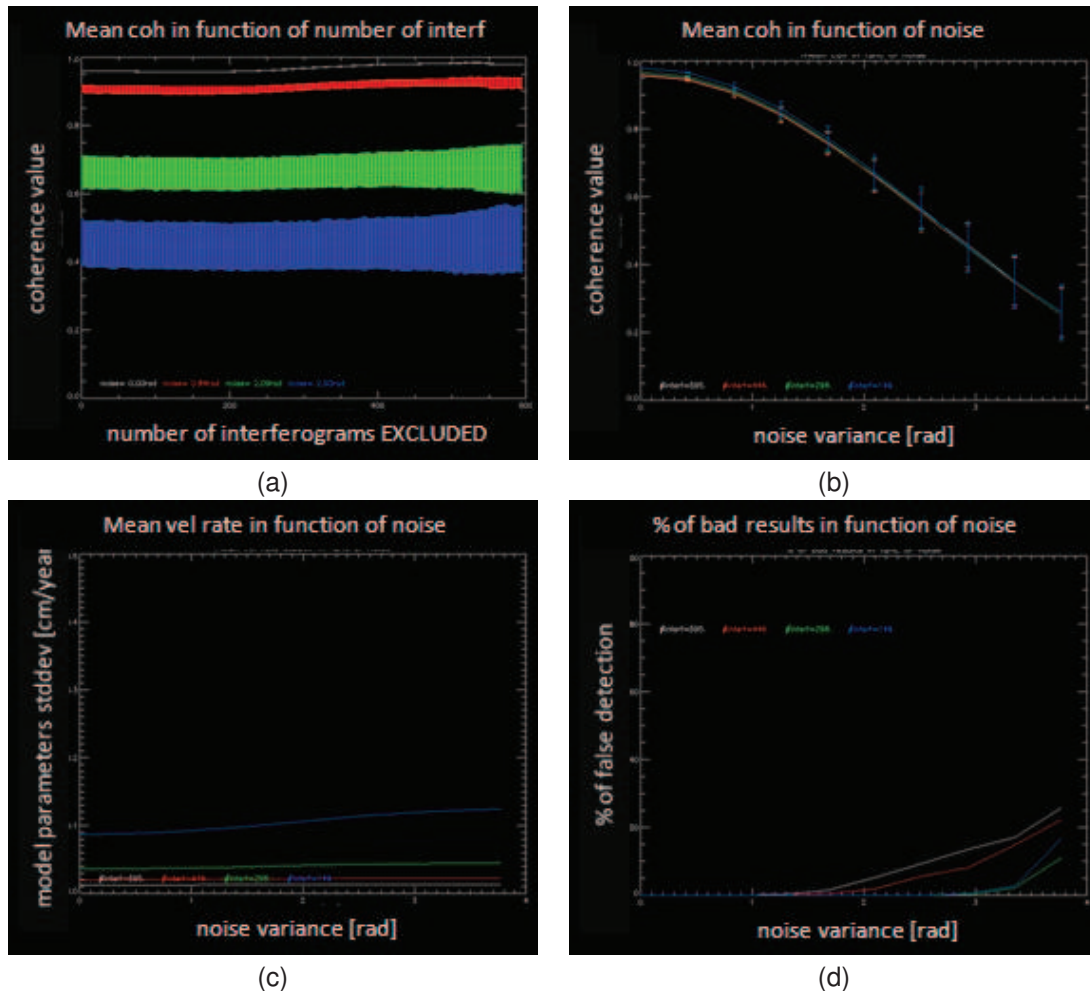


Figure 4.4.5: Performance of the model fitting system in a partially decorrelated environment with 35 acquisitions. a) evolution of the coherence estimator in function of the number of used interferograms for different noise levels. b), c) and d) are respectively the coherence estimator, the estimation of the accuracy and of the precision in function of noise and for different number of interferograms.

By comparing the results obtained in the previous subsection (compare figure 4.4.5 with 4.4.4) it can be stated that the system now performs better as result of the increase of the available number of acquisitions. The variance of the coherence estimator function has been drastically improved, compare the error-bars of the curves presented in figures 4.4.5.a and b with the ones in figures 4.4.4.a and b. Moreover the shape of the performance of the coherence function with the noise level is enhanced. Now the curves in figure 4.4.5.b decrease faster when noise variance increases in comparison with the ones in figure 4.4.4.b.

Furthermore, as it was expected the standard deviation of the estimated parameters have been also improved, see how the curves presented in figure 4.4.5.c present a lower value than the ones in figure 4.4.4.c. However, the more important enhancement of the performances is due to the fact that now the accuracy of the system increases drastically. By comparing the curves presented in figure 4.4.5.d with the ones in figure 4.4.4.d it can be noticed that the percentage of false detections become significant for noise variance above 2 radians, while in the previous case

becomes noticeable for values above 0.5 radians. It must be highlighted that the maximum value reached when noise variance is very high is of about a 20% of false detections when before that value remained above a 50% of the cases.

It has been demonstrated that the performances of the model fitting system are enhanced drastically when the the number of acquisition increases. Moreover, there are combinations of interferograms offering a very robust accuracy in function of noise, see how the blue and the green curves are below the red and the white ones in figure 4.4.5.d.

#### **4.4.2 SPN estimation system for non-linear deformations**

As it was discussed in the precedent subsection non-linear deformations can be detected by the actual SPN model fitting procedure which is based on a linear model of deformation for all the time span. Deformations presenting only one change of trend can be monitored with the actual procedure of SPN when the noise level is low. The problems start to appear when one interferometric combination contains more than one change in its trend (considering time domain). In that cases, those interferograms introduce a high level of uncertainty on the SPN model fitting causing the same effect as if the case of high noise variance. Generally, this is translated into a loss of the measurement, or into a false detection. When the linear model do not fit the observed data the resulting phase residuals are very large. The model coherence is thus low and those out-of-model points may be excluded from the final set of SPN points of measurement.

The natural strategy to overcome this problem is to divide the analysis into different time periods. Different sub-analysis can then be performed within each small time period with more probabilities to succeed with the linear model fitting. In some cases an a priori knowledge of what occurred in the ground deformation can assist in the division of the time span. However, when no information is available, dividing the monitoring period in the most appropriate way is a critical task and it is not straightforward. In any case, by means of a posteriori analysis of the results it is possible to detect possible areas and time periods what do not fit the model.

##### **4.4.2.1 Example of monitoring of non-linear deformations by using a priori information: Katrina hurricane test case**

Knowing the occurrence of particular events when analyzing one test site can assist in dividing the total time span in order to have more success when fitting the SPN linear deformation model. This kind of information can be for example the occurrence of a natural disaster (an earthquake, an eruption of a volcano, flooding, landslides, etc) or of some man-made activities (tunneling activities, water pumping, construction of infrastructures, etc.). Whatever the suspect activity which occurs in the test site during the observation period, it can originate a change in the trend of the temporal evolution of the ground deformation. The study of the ground deformation in the city of New Orleans in United States of America is used as illustration of how to deal with this kind of monitoring in SPN.

This study was conducted for the Canadian Space Agency (CSA) in collaboration with the United States Geological Survey (USGS) and the National Aeronautics and Space Administration (NASA) under an announcement of opportunity launched in August 2006 entitled innovative

research and development into the application of Radarsat-1 interferometric data for subsidence mapping in New Orleans; referred as the DELTA project (see [CSAa]). The primary objective of this cooperative initiative was to stimulate new innovative research and development projects in interferometric applications using RADARSAT-1 data and innovative mapping approaches to better illustrate subsidence.

The main scope of this study was to retrieve ground deformation maps by using Radarsat-1 [CSAb] SLC images. The mean deformation rate maps was one of the final products that should be delivered for this analysis and specially for the geologic interpretation of the results, which is a on going activity performed by USGS. The results of the project were presented within a special session inside the PECORA 17th symposium which took place in November 16-20 in Denver, Colorado (USA) [Dur08]. The main particularity of the test site was the occurrence of a known natural event which occurred during the analyzed time period. That was the Katrina hurricane which originated a terrible flooding in almost all the populated area of the city. The effects of this hurricane was one of the most destructive ever seen in USA. It was suspected that due to the flooding event the deformation pattern could have changed drastically. Thus, it was decided to divide the time period into two different parts. In figure 4.4.6 it can be observed the list of images and their distribution in time with the respect to the occurrence of the hurricane.

PRE KATRINA		POS KATRINA
09May02 - 33992	06Dec03 - 42224	14Sep06 - 51485
26Jun02 - 34678	30Dec03 - 42567	01Nov05 - 52171
20Jul02 - 35021	23Jan04 - 42910	25Nov05 - 52514
13Aug02 - 35364	16Feb04 - 43253	19Dec05 - 52857
06Sep02 - 35707	11Mar04 - 43596	05Feb06 - 53543
28Jan03 - 37765	04Apr04 - 43939	01Mar06 - 53886
21Feb03 - 38108	28Apr04 - 44282	25Mar06 - 54229
17Mar03 - 38451	22May04 - 44625	18Apr06 - 54572
10Apr03 - 38794	09Jul04 - 45311	12May06 - 54915
04May03 - 39137	26Aug04 - 45997	23Jul06 - 55944
28May03 - 39480	13Oct04 - 46683	09Sep06 - 56630
21Jun03 - 39823	30Nov04 - 47369	03Oct06 - 56973
15Jul03 - 40166	17Jan05 - 48055	27Oct06 - 57316
01Sep03 - 40852	06Mar05 - 48741	20Nov06 - 57659
25Sep03 - 41195	23Apr05 - 49427	14Dec06 - 58002
19Oct03 - 41538	10Jun05 - 50113	07Jan07 - 58345

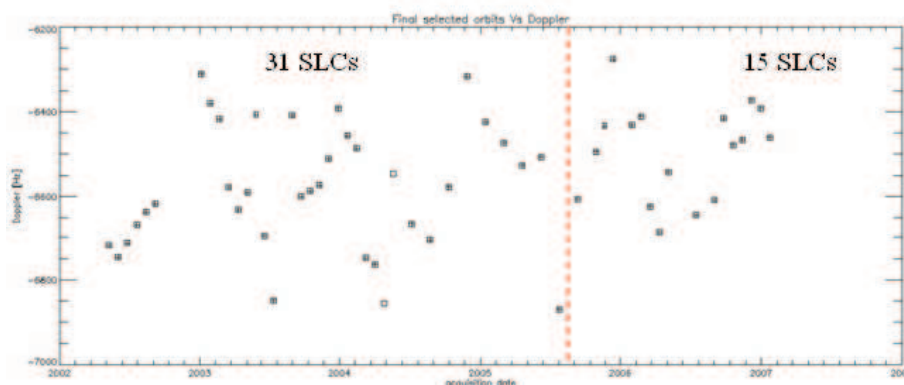


Figure 4.4.6: Top) table with the acquisition dates for each of the 46 available Radarsat-1 SLC images over the city of New Orleans. Bottom) plot of the acquisition time with respect to the estimated image Doppler centroid value. The discontinuous vertical red line indicates the occurrence of the Katrina hurricane.

As it can be observed in figure 4.4.6 the distribution of images is not uniform considering the two periods. In the pre-Katrina period, twice more images were available. As it was highlighted in the previous subsection (see subsection 4.4.1) this would produce different estimation conditions

and in consequence different levels of accuracy and precision for the two estimates. In addition, performing two separated SPN analysis can produce the selection of very different points of measurement not only due to the possible destruction of infrastructures but also to the fact of having different amount of images (the SPN model coherence estimator performs worst with less images).

The adopted strategy consisted in performing a SPN analysis for the entire period in order to identify the scatterers which remain stable (radiometrically speaking) in spite of Katrina's impact. In order to illustrate those changes an analysis of change detection was also conducted by the analysing of the SAR multimean reflectivity image for the two periods. The resulting image can be observed in figure 4.4.7.

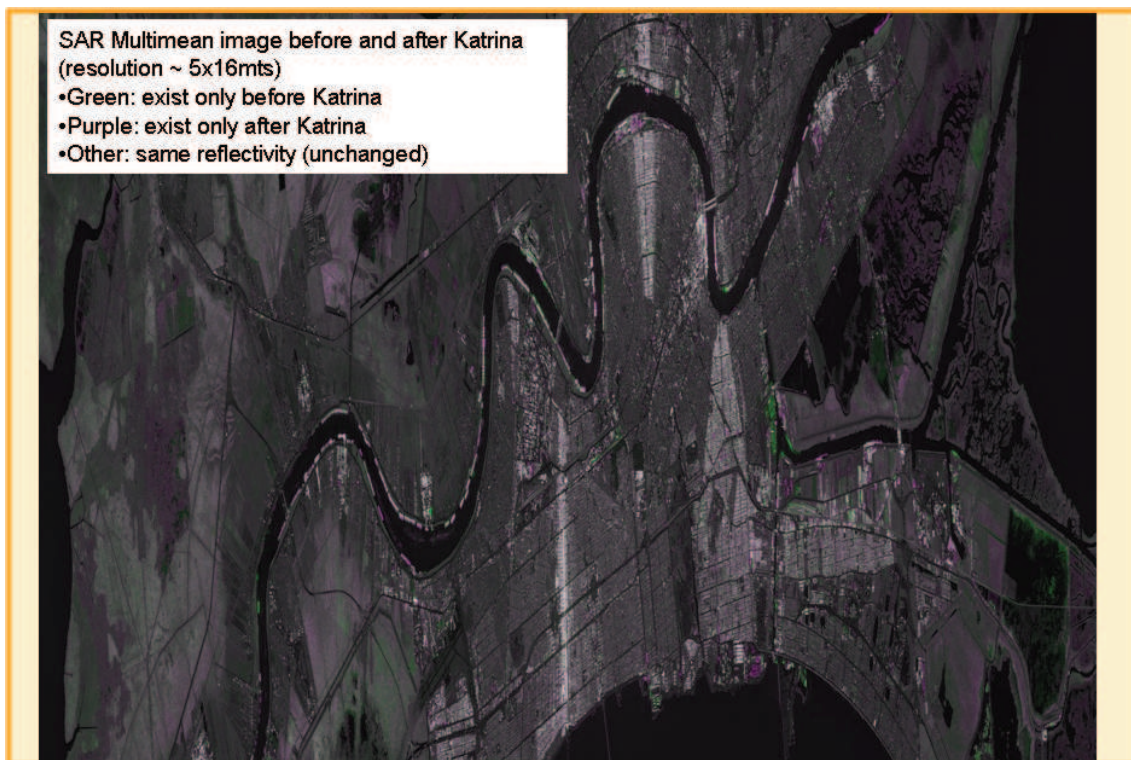


Figure 4.4.7: Radarsat-1 SAR multireflectivity image before and after the Katrina hurricane to highlight changes in the radiometry of the scatterers. The multimean image reduces the speckle while it keeps the resolution of the products, which is 5x16 meters in that case.

In figure 4.4.7, it is highlighted how some particular infrastructures present very different SAR power level. This indicates the hurricane has originated many changes of the ground area covered by those particular pixels. In consequence a full period analysis could not be carried out. In figure 4.4.8, some areas are correlated with orthophotos in order to visually identify changes of the SAR radiometry and changes over the ground surface of the city.

In figure 4.4.8 is presented a particular case of study of special interest. In the zoomed RGB composed image (presented at bottom on figure 4.4.8) it can be appreciated some color changes within this part of the city, which indicates that there were a lot of modifications of the ground surface between the two considered epochs. For example, purple areas indicate scatterers that reflect more power before than after the event or areas presenting new constructions.

A clear and interesting example is the one highlighted within the white square labeled as A in



Figure 4.4.8: Change detection analysis by using the SAR reflectivity. Top) three aerial orthophotos taken over the same part of the city before, during and after the Katrina event to illustrate visually the changes due to the hurricane event. Bottom) RGB combination of the mean SAR reflectivity before and after the event, the same as in figure 4.4.7.

figure 4.4.8. It is one of the dikes that have been broken because of the pressure of the water and which was causing part of the flooding in this part of the city. After the Katrina hurricane, the dike was reconstructed and reinforced making it more wide (and visible for the radar) than before, see the correlation of the orthophotos on the top of figure 4.4.8 over the areas labeled as A.

Meanwhile, the green color pixels within the RGB composed image indicate areas which suffer a lot of damage and that in extreme cases they have completely disappeared. In particular, the harbor area is highlighted within the white squares labeled as B. This area has been completely destroyed by the hurricane as it can be inferred by visual correlation of the aerial orthophotos on the top of figure 4.4.8.

Thus, in order to analyze the evolution of the ground deformation in time and specially to identify possible changes due to the hurricane the points of measurement should be the same for the two periods of analysis. Thus, only the points which kept the reflection properties for all the time period can be exploited for that purposes, which are the points without color on figure 4.4.7. The mean deformation linear rate estimated over those points by means of two the SPN separated time analysis can be observed in figure 4.4.9.

As it can be observed in figure 4.4.9 the estimated mean deformation rate maps before and after the Katrina change drastically. Before the Katrina large scale and smooth deformations have been detected. Several areas were presenting a slightly subsidence deformation pattern, specially the ones close to the water (see figure 4.4.9.a). After the hurricane, the major part of the city was affected by severe and large scale deformations. Areas with important uplift close to zones of huge subsidence can be seen in figure 4.4.9.b. Those areas affected by severe deformation patterns were the ones affected by flooding, compare figure 4.4.9.b with 4.4.9.d.

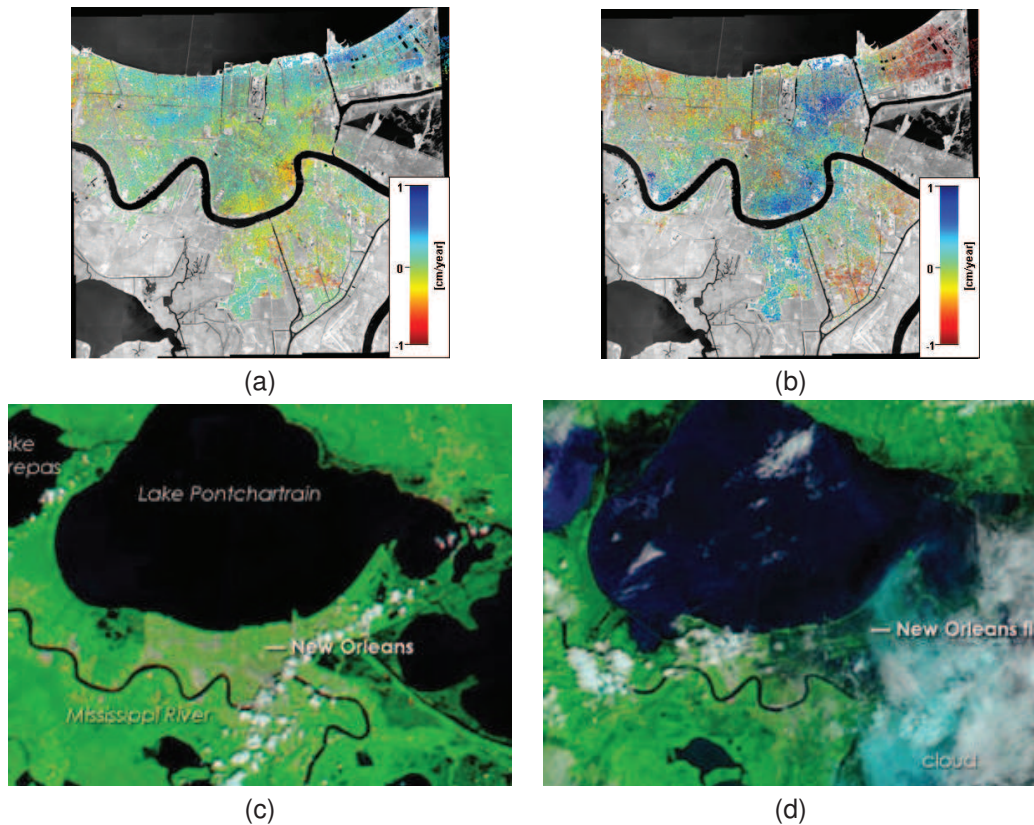


Figure 4.4.9: SPN mean deformation linear rate maps estimated on New Orleans before (a) and after (b) the Katrina hurricane with the Radarsat-1 dataset given in 4.4.6. The measurements are done over the same scatterers common to both periods. c) and d) ASTER [NAS] images before and after the hurricane. Black areas on image (d) represent the major flooded areas on the city which are correlated with the areas presenting huge deformations detected in image (b).

In order to demonstrate that this post-Katrina large scale deformation pattern is not a processing artifact and that it is correlated with the flooding the following analysis was conducted. The spatial shape of several interferograms for a particular area were analyzed in time. The used interferograms have a multilook of  $30 \times 6$  samples in azimuth and range respectively, which results in a square pixel spacing of about 120 meters. This multilooked detected version of the interferograms allowed to analyze those large scale deformation patterns and especially their evolution in time. Thus, several DInSAR phases formed by independent acquisitions were compared, allowing to decorrelate possible atmospheric artifacts associated to one particular epoch. The results are depicted in figure 4.4.10.

As it can be observed in figure 4.4.10 in a qualitative way the deformation pattern estimated by SPN is corroborated by the shape of the phase profiles measured over four independent interferograms. This confirms that the uplift and subsidence shapes detected by SPN (which are very close in space) are correct (see the area crossed by the black arrow over the image on the top left in figure 4.4.10).

In addition, the acquisition epochs of the interferograms are away from the date of the hurricane event, the detected deformation profiles become smooth, see the profiles across the blue arrow presented on the left of figure 4.4.10. This indicates most probably that this particular deformation trend is due to the flooding, and that as the ground dries these deformation smooth, decreasing with time. The ground reacts trying to recover its original state as the water is gone.

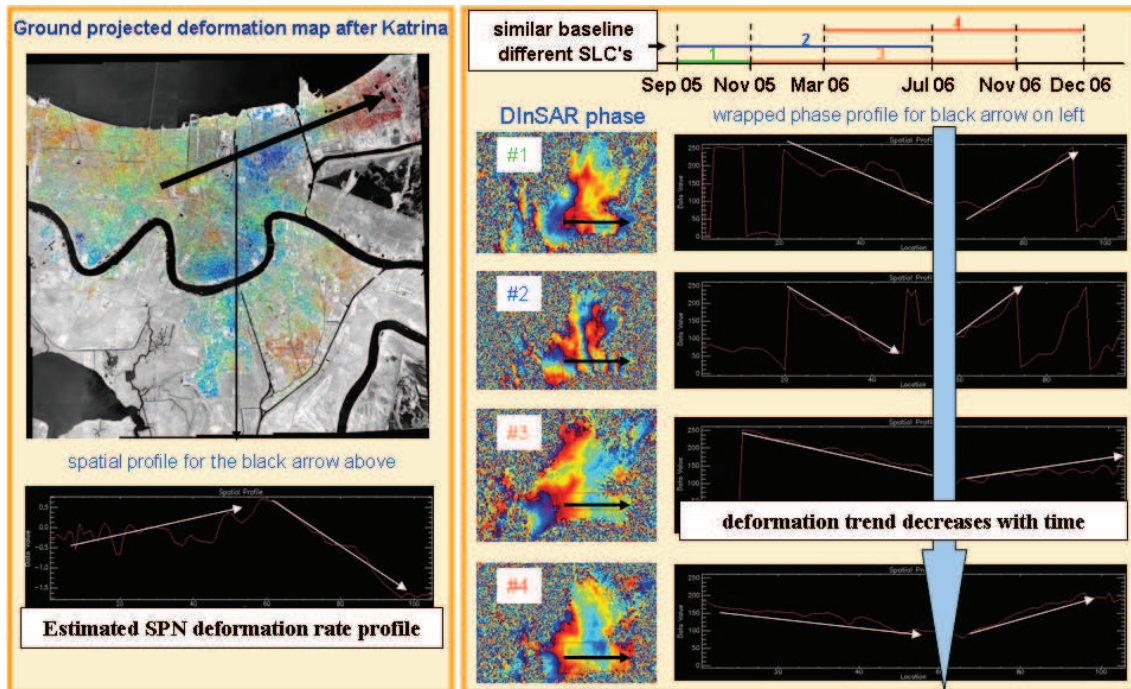


Figure 4.4.10: DInSAR analysis in space and time domain (on the right). The InSAR phase are also compared with the estimated SPN mean deformation rate map for the post-Katrina period (on the left). The spatial profile of four wrapped interferometric phases are showed on the right. These profiles correspond to the same area over the DInSAR phases as well as in the SPN results. The extent and the direction of the profile is indicated with a wide black arrow in all the images (highlighted with a back arrow over the image on the left and over the wrapped phases on the right). The profile of the SPN mean deformation linear rate map is correlated with the deformation trend inferred by interferograms on the right. In addition, as the interferogram is far away from the hurricane epoch the deformation becomes smooth.

#### 4.4.2.2 Guidelines for detecting possible non-linear deformation areas in SPN

In previous subsection it was illustrated by means of a practical SPN processing example how to monitor non-linear ground deformations when some a priori information is available. Although, in the major number of cases this information is not available at all before starting the processing. Then, the unique option is to analyze the complete time span within the same SPN deformation analysis. In that cases, there are some SPN parameters that can be analyzed carefully in order to check for possible non-linearities. This analysis is manual and requires a real expertise. This will be addressed using real test cases.

#### Decrease of the SPN model coherence in areas of good SAR SNR

As SPN phase model fitting is based on a linear deformation model when the ground deformation (the true) does not follow this pattern the model coherence decreases. If this deformation pattern presents some spatial extent this decrease of coherence can be noticed in the results. Typically, this decrease of coherence appears gradually from the stable areas throughout the areas presenting an important non-linear deformation pattern. This can be observed in areas where the SAR signal has a good quality. In other words, in areas presenting a good peak to clutter ratio (SNR) or in areas with a low amplitude standard deviation 3.2.4. Below some examples are presented.

In figure 4.4.11 is presented an example of application for detecting possible non-linear defor-

mations in SPN for an area in the center of the city of Paris in France (St. Lazare Station). The results were obtained using a stacking of about 70 SLC's acquired with the ESA sensors ERS1-2 and ENVISAT between 1995 and 2005. In figure 4.4.11.c it can be observed how the SPN model coherence value decreases in a concentric way. This area of low coherence is correlated with the extension of a detected uplift deformation, see the blue-colored area in figure 4.4.11.d. However, the mean reflectivity is not indicating any special variation of backscattering for this particular area, see figure 4.4.11.a. Although, it is true that exactly in the middle of the hole of coherence there are a lot of bright pixels detected by the analysis of standard deviation of the SAR amplitudes, see figure 4.4.11.b, which indicates that this area is affected by temporal changes of the SAR reflectivity (possible construction works affecting the city's surface).

In summary, what is happening is that potential good scatterers (grey pixel in figure 4.4.11.b) are presenting a low value of model coherence in presence of an estimated SPN linear deformation. In consequence those scatterers will be lost when setting a threshold over the model coherence for selecting the final set of points of measurements. This thus corresponds to a loss of performances, as there is a loss of detection capabilities as points of low noise are not used in the final measurements.

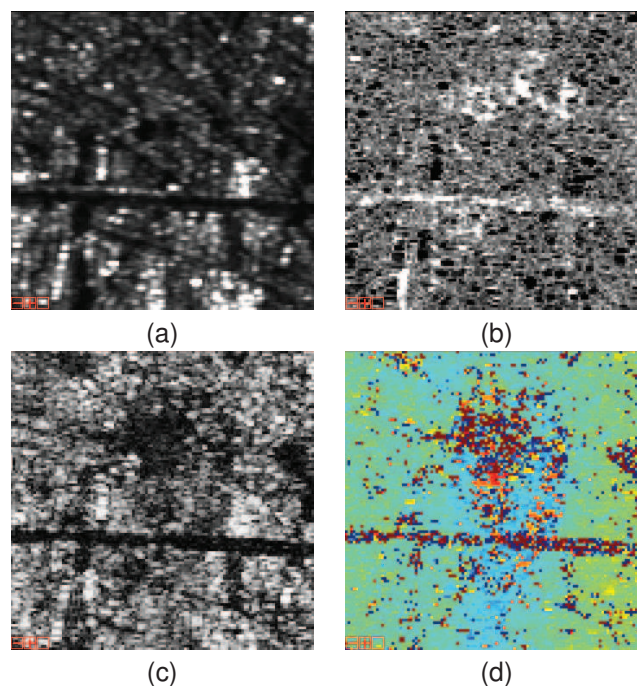


Figure 4.4.11: Example of detection of non-linear deformation in SPN final products for an area close to the Saint Lazare train station in the center of Paris. ERS1/2 and ENVISAT images were used for the processing. a) Mean SAR reflectivity. b) map of amplitude standard deviation, dark values are related with pixels of low amplitude variation and viceversa for the bright ones. c) SPN model coherence, dark means a bad model fitting and white is related to almost a perfect fit. d) estimated linear deformation rate by SPN for the time period 95 to 05. The stretch of the values are from  $+1\text{cm/year}$  for the dark blue ones up to  $-1\text{cm/year}$  for the dark red ones.

In contrary, these non-linear areas can be separated from areas of bad quality signal by several reasons, see for example the street that crosses the images from left to right just in the middle in the figures 4.4.11. The multimean reflectivity image is indicating that those pixels have a low backscattered signal, at least lowest than its surrounding pixels which corresponds to the buildings, see figure 4.4.11.a. Furthermore, the amplitude standard deviation is indicating (bright areas = high amplitude dispersion in figure 4.4.11.b) that those pixels of the road have not only a low

backscattering but also a very high variation of the returned power level to the satellite, which is characteristic of speckle's like pixels. In addition, the model SPN coherence for those pixels are, as expected, very low and which is more important, those pixels present extreme values of estimated mean deformation rate, which are completely outside the confidence limit ( $3\sigma_{deformation}$ ). In summary, those pixels are very noisy but modeled within SPN with insignificant values.

### Aliasing in the deformation time series

Another possible indicator of non-linear deformations is the presence of aliasing in the estimated time series of deformation by SPN. The process of obtaining the time series is described in section 3.3.5.6. As it was addressed the estimation of the evolution of the deformation in time is performed by means of the analysis of the phase residuals (with respect to the linear mode). The contribution of each acquisition to this phase residuals is resolved by means of the solution of a linear equation system. The main assumption which is made is that these phase residuals must be unwrapped. In other words, all the phase residuals may be within the same number of  $2\pi$  cycles in a relative sense. It means, the total amount of cycles is not known (in an absolute way) but it is in a relative way between each interferogram which may be set.

Problems can arise when this relative unwrapping is not performed. For example, when the ground deformation (true movement that must be estimated) presents several trends within the analyzed time period. In that cases SPN tries to fit a linear model with the mean deformation rate estimated for all the period (a mean rate of all the observed rates). In that situation, it is very probable that the estimated mean deformation trend is incorrect resulting in a bad estimation of the deformation over the whole time period. That will result in high phase residuals for some particular periods due to the fact that they are not within the same cycle of phase. Under these conditions, the phase residuals follow a certain correlation with time (high residuals are concentrated in the epochs with changes in the deformation trend) and as result possible aliasing in the final estimated time series can be observed.

As an example of the explained above a simulation was performed based on the software developed under the section 4.4.1, the results are showed in figure 4.4.12.

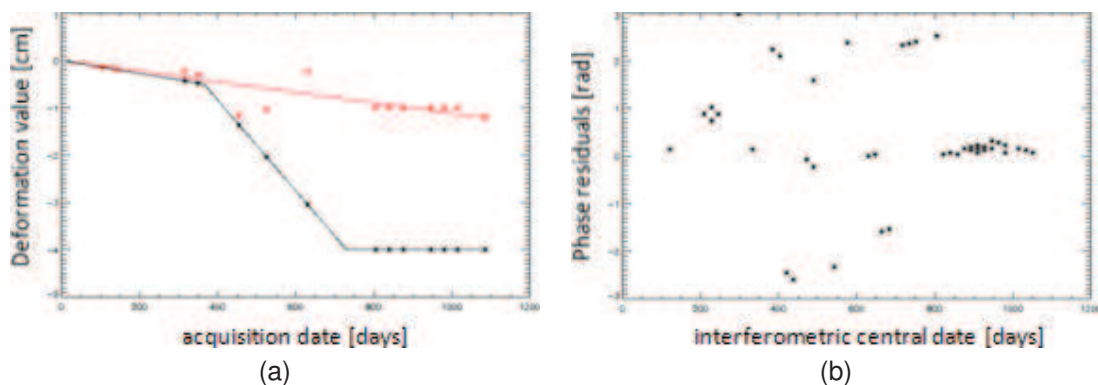


Figure 4.4.12: a) simulated non-linear ground deformation (white line) and estimated time series (red asterisks) with classical SPN based on a linear model (red line). The simulation was performed considering 14 images and noise free and ENVISAT acquisition conditions. b) DInSAR phase residuals as result of the linear model indexed by the mean interferometric time,  $(t_{master} + t_{slave})/2$ .

A ground deformation was generated (always in LOS direction directly) with 3 different regimes in order to synthesize a non-linear movement, see white line in figure 4.4.12.a. The sampling in

time is performed by means of 14 acquisitions randomly distributed but with the constrain of being free of any aliasing a priori. In other words, the random time distribution of the images is accepted if and only the total amount of deformation between two consecutive acquisitions is not higher than  $\lambda/4$ , which for the considered case based on ENVISAT acquisition conditions is equivalent to approximately 1.4 cm. The simulation was performed under free noise conditions. Thus, between two consecutive white asterisks in figure 4.4.12.a, the deformation difference is below 1.4 cm in any case.

The red asterisks in figure 4.4.12.a are the estimated deformation by means of classical SPN. As it can be observed the estimated linear deformation model results in a clear underestimation of the true movement. As a consequence, as the trend of the model is not high enough (red line in figure 4.4.12.a) for the time period of maximum deformation gradient (the one contained within 400 and 700 days in figure 4.4.12.a) the recovered time series present aliasing. This is one of the worst cases where there is an inversion of the trend indicating an uplift when the true deformation is subsiding.

This can be explained by looking carefully the interferometric phase residuals after the retrieval of the linear model, see figure 4.4.12.b. The residuals are indexed in time by means of the mean interferometric time (which is equal to the mean date of both acquisitions which form the interferogram). As it is depicted in figure 4.4.12.b the spread of these residuals is higher for the epochs at which the aliasing is occurring. Thus, this information could help in splitting the total time span into different sub-periods in order to succeed with the classical SPN approach in small datasets.

More examples can be given, but now with real test cases. The first case is presented in figure 4.4.13. A real time series estimated with classical SPN is showed in blue in figure 4.4.13. As it was happening in the simulated test case in figure 4.4.12.a, there is an inversion of the local trend of the time series for a particular time period (see the blue diamonds within the red circle in figure 4.4.12). As it was introduced before, this aliasing or discontinuity in the trend of the time series could be an indicator of non-linearity or of change of trend considering the true ground deformation.

For this test case, the total time span was divided into several subsets. Thus, SPN was performed separately by considering the different time periods. Then, the estimated time series within each single SPN analysis was merged with the other ones considering the total accumulated deformation as reference. For that purposes, there was always a common date between each isolated period of analysis. The results are the ones depicted with the red triangles in figure 4.4.13. As it can be observed a higher rate was obtained and the recovered time series is free of discontinuities or aliasing, arising higher deformation values for this point of measurement.

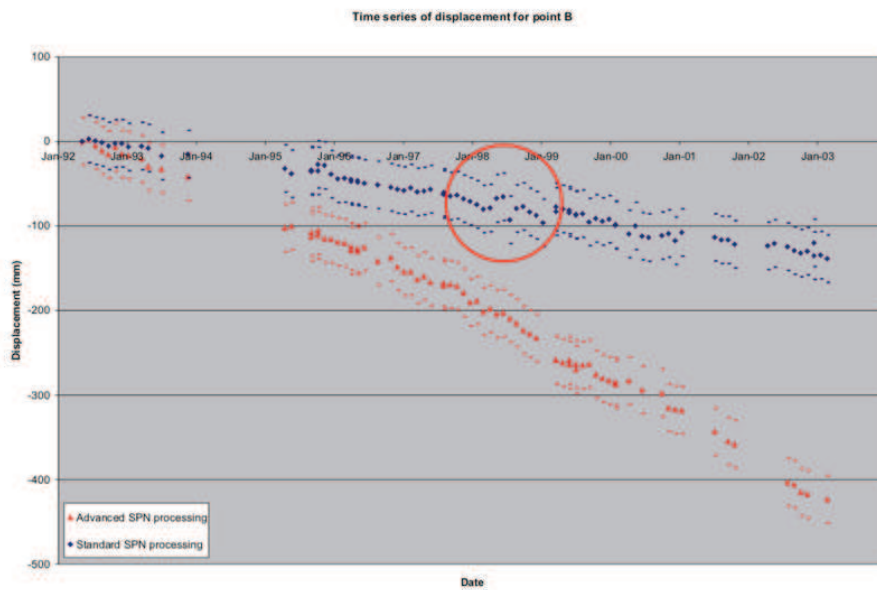


Figure 4.4.13: Example of classical SPN time series with aliasing (red circle) in blue and advanced SPN processing by splitting the time period into several parts (red symbols). The small rectangles (for both colors) are indicating the location of the first possible ambiguity for each resolved position of the time series (placed  $\pm\lambda/4 \approx \pm 1.4\text{cm}$  away from the solution). The time series have been extracted from a real test case located in an area with underground mining activities and imaged with ERS and ENVISAT data.

Unfortunately, this aliasing is not always so detectable, especially in case of presence of noise or huge non-linearities. For instance, when the peak to clutter ratio for a given scatterer is not very high there could be acquisitions presenting more noise than the other ones, as well as severe atmospheric artifacts for a particular acquisition date or severe temporal decorrelation due to the affectation of the snow, etc.. In that cases, the observation of the time series could not indicate any particular problem of aliasing, see figure 4.4.14.a.

In figure 4.4.14 is presented an estimated time series of a real test case of study with a known problem of ground non-linear deformation profile in time. This estimate corresponds to a test site presenting activities of water pumping previous to tunneling works within a pure urban area. As it can be observed in figure 4.4.14.a the aliasing on the time series is not so clear as in the previous examples (figure 4.4.13). The only noticeable fact is that the spread of the time series is higher for the temporal period where the non-linearities are occurring than for the other epochs, see the data within the red circle in figure 4.4.14.a. As it can be observed in figure 4.4.14.b, a splitted SPN analysis (which considers three different regimes) can recover a more precise estimate of the evolution of this ground deformation profile in time.

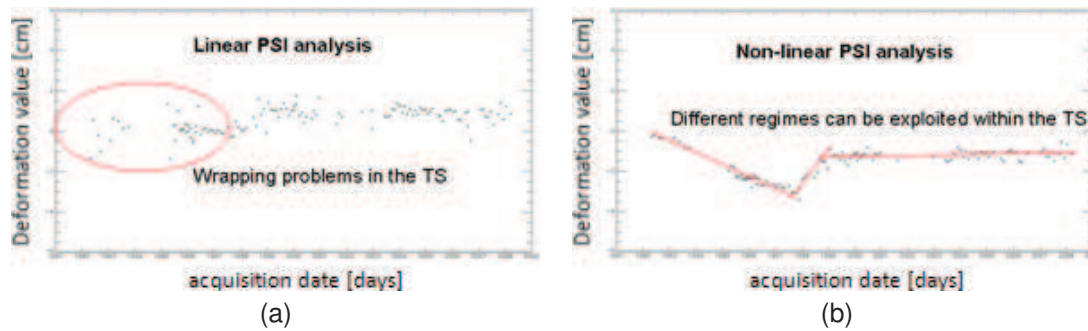


Figure 4.4.14: Estimated deformation time series of a real test site obtained by means of classical SPN (a) and by means of an advanced SPN processing which considers three different time periods of analysis (b). The same list of images has been used for both cases.

#### 4.4.2.3 Advanced SPN for the automatic monitoring of non-linear deformations

As it was introduced in the previous subsection 4.4.2.2, classical SPN succeeds in the detection of time series of deformations when only one change in the trend is occurring, considering the true ground deformation. It was demonstrated that non-linear deformations can be overcome by performing different SPN analysis within small periods of time where the observed deformations are more similar to a linear one. The key parameter is to know when this total time span should be split, which could be suggested by means of having available some a priori information about particular events (natural hazards such as earthquakes, flooding, eruptions, etc. or man-made works such as water pumping, tunneling, etc.) or by analyzing the interferometric phase residuals ordered in time (see figure 4.4.12).

However, those divisions of the total time span can be considered since the beginning. In fact, the sampling of the ground deformation is performed in time by means of the acquisition date. Hence, it is between each two consecutive acquisitions that one can observe (or allow in the considered model) a change of trend. Considering what was stated above, the proposed methodology for automatic monitoring of non-linear deformations is based on a sliding SPN linear analysis between each two consecutive acquisitions. In other words, the SPN model fitting is performed as many times as the number of available data except one. Now, the resulting coherence function already presented in 4.4.1 may consider a two dimensional search space, the possible linear trends and their possible variation throughout time. The analysis of the coherence function becomes a three dimensional matrix, which considers the correlation of the solution in time.

#### 4.4.2.4 Application on Paris test site

The city of Paris is an appropriate test site for the testing of PSI new methodologies; this is due to several reasons. First, there is a large stacking of images acquired by different sensors in different modes such as ERS1/2, ENVISAT and TerraSAR-X. The resulting time span with datatakes is very large, since 1992 up to today. Second, it is known that ground deformations not following a linear pattern are occurring. These deformations are of different nature, which results in completely different pattern in time. Third, the test site is a pure urban area, what it means that the spatial density of good points of measurement is very high. This a very good advantage as the spatial sampling as well as the temporal sampling of the studied ground deformations are very close to

an ideal case, with a density of PSs above  $1000 \text{ PS}/\text{Km}^2$  and more or less a constant sampling in time of one image every 35 days given by the dataset of ERS and ENVISAT C-band SAR data.

The objective of this subsection is to evaluate the performances of the new automatic non-linear estimation methodology presented in the previous 4.4.2.3. For this purposes the classical SPN processing is compared with the new one with special emphasis on the areas affected by deformations. It must be highlighted that the new processing not only account for the automatic non-linear estimation methodology but also for all the other SPN enhancements presented within this chapter. That's it mainly:

- The control of the spatial consistency of the results by means of the check of the rotational of the estimates in close loops of the network and by the application of a parallel and independent parameter integration routine.
- Weighting of the observations in the estimation procedures by means of the computation of the quality of the inputs based on the estimation of the variogram per each acquisition.

The resulting linear deformation rate map in ground projected coordinates is presented in figure 4.4.15. The objective is to identify areas affected by deformation in order to focus the comparison analysis over those specific locations.

The first step is the comparison of the SPN model coherence for these areas affected by deformation in figure 4.4.15. The analysis is presented below. All the comparisons are performed in slant range geometry.

#### **Area A: Grand Palais**

In figures 4.4.16 and 4.4.17 is shown the comparison of both processing for the area close to the Grand Palais. In figure 4.4.16 are presented both coherences jointly with the mean reflectivity image of the area of analysis. As it can be observed the green color prevails, indicating that the coherence of the new processing is higher than the classical SPN one.



Figure 4.4.15: Linear deformation rate as result of the classical SPN processing for the center of Paris. The covered time period is from 1992 up to 2008, and based in the analysis of about 120 ERS1/2 ad ENVISAT SLCs. The main areas affected by deformation are identified by the red circles. Copyright SPOTIMAGE for the background image.

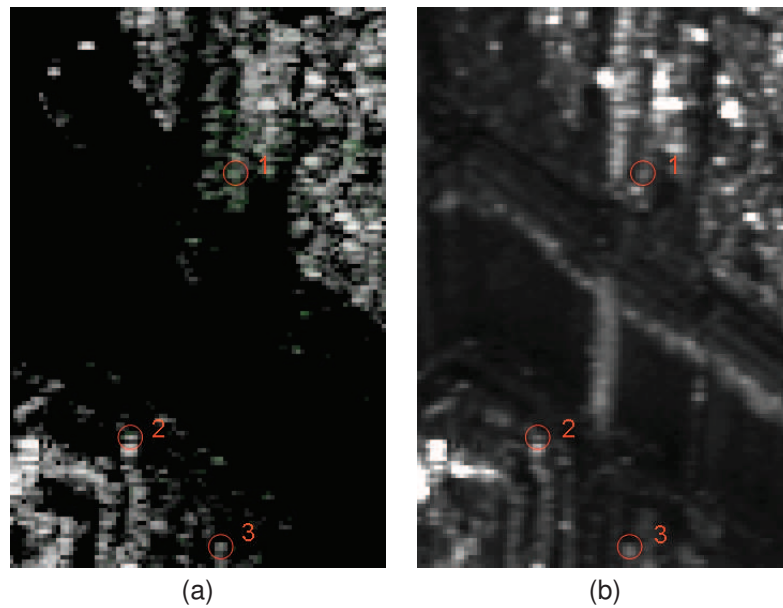


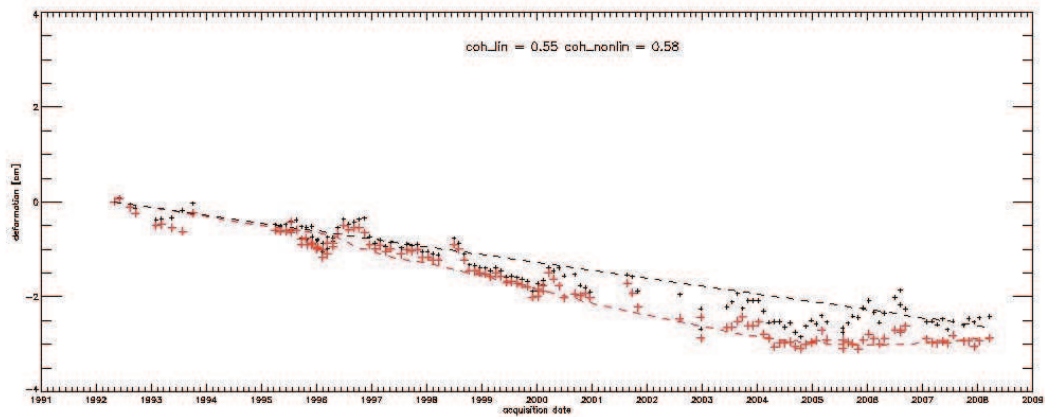
Figure 4.4.16: a) RGB image with the SPN model coherence for the linear and the non-linear processing for the first area as depicted in figure 4.4.15, the area of the Grand Palais. Magenta means that the linear model gives a higher coherence and green vice-versa. Grey values means that both have exactly the same value. b) Mean reflectivity image of the same area.

The estimated deformation time series of some points can be compared in order to evaluate the enhancements of the new methodology. The result can be observed in figure 4.4.17.

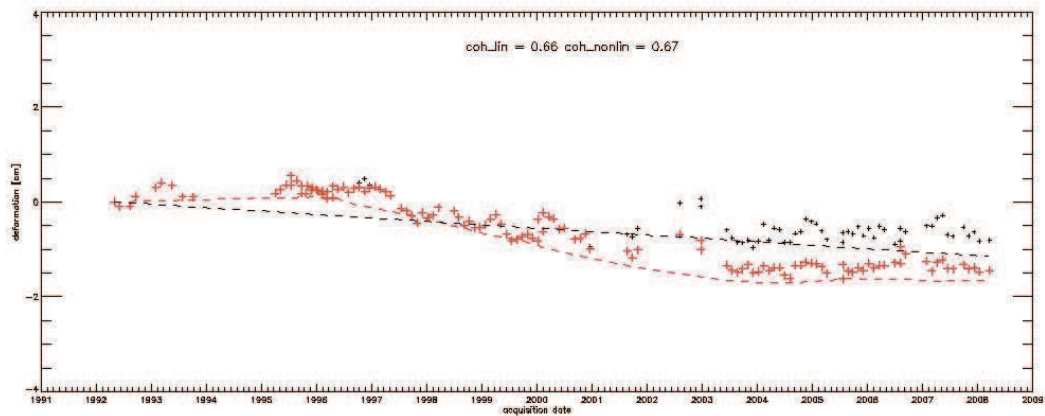
In general, the estimated deformation profiles are slightly different, especially for the last epoch of the time span, where higher differences between the linear and the non-linear model (dark and red discontinuous lines in figures 4.4.17) are observed. Thanks to the non-linear model used to obtain the time series, different trends in the temporal evolution of the deformations can be better identified. Also a reduction of the dispersion in time series can be denoted with the new methodology.

#### Area B: Montmartre

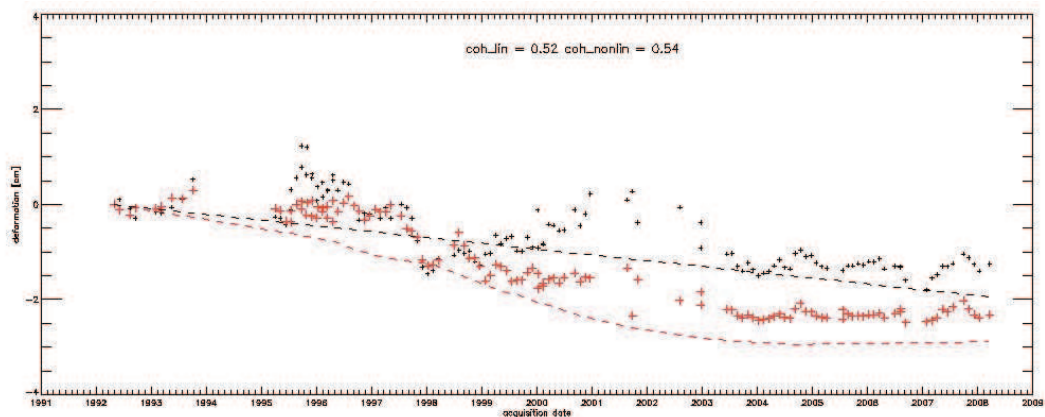
In figures 4.4.18 and 4.4.19 is presented the comparison of both processing for the area of Montmartre. In figure 4.4.18 are presented both coherences jointly with the mean reflectivity image of the area of analysis. As it can be observed the green colour prevails, indicating that the coherence of the new processing is higher than the classical SPN one.



(1)



(2)



(3)

Figure 4.4.17: Deformation time series estimated for the points highlighted in figure 4.4.16. In black is presented the deformation profile obtained with classical SPN and in red the one for the new non-linear SPN processing. The discontinuous lines represent the used functional model to unwrap the phases.

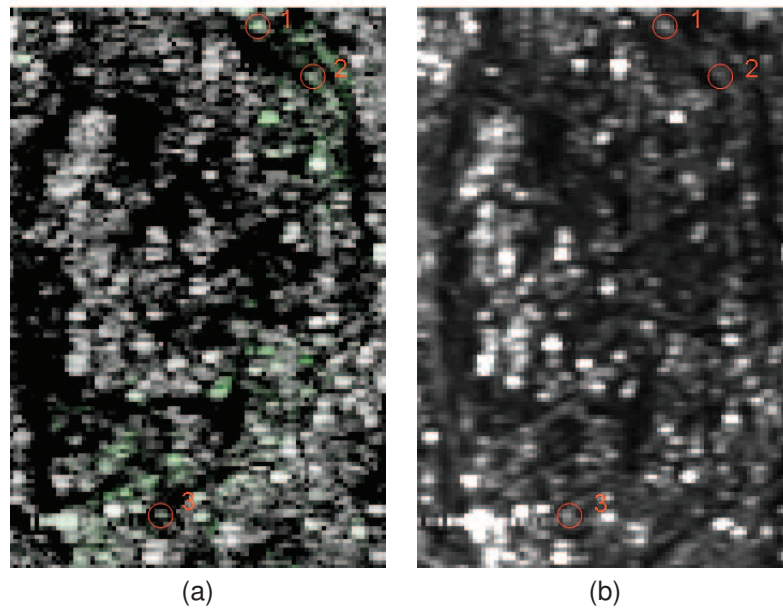


Figure 4.4.18: a) RGB image with the SPN model coherence for the linear and the non-linear processing for the first area as depicted in figure 4.4.15, the area of the Grand Palais. Magenta means that the linear model gives a higher coherence and green vice-versa. Grey values means that both have exactly the same value. b) Mean reflectivity image of the same area.

The estimated deformation time series of some points are compared in order to evaluate the enhancements of the new methodology. The result can be observed in figure 4.4.19

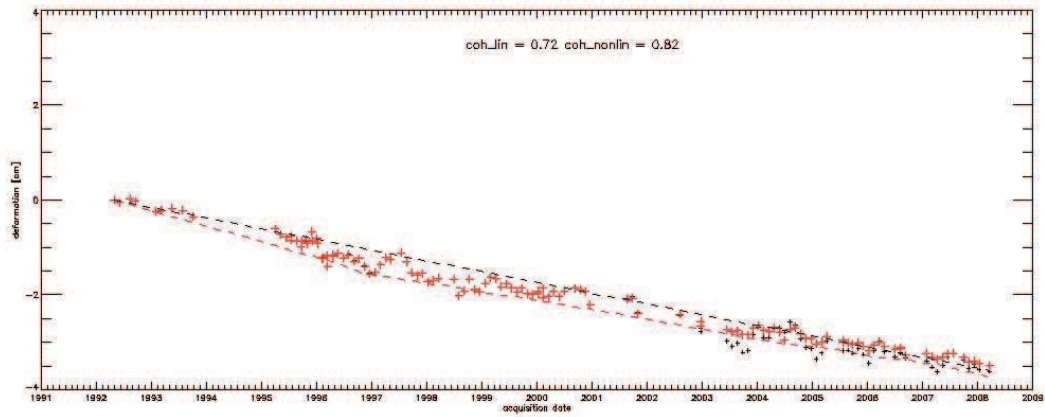
In general, as it was already noticed in the previous case, the estimated deformation profiles are slightly different. However, in that case some variations can be observed. In the last two profiles in figure 4.4.19 (2 and 3) the estimated deformations differ totally, achieving a completely different final value of accumulated deformation. This is indicated also with the model coherence which is slightly higher with the new processing. Although a higher difference can be found in the detected model coherence for the deformation time series presented in figure 4.4.19.1 (twofold than in the previous cases), the resulting profiles are very similar. Moreover, a reduced level of fluctuations can be appreciated with the time series estimated with the new processing.

### Area C: Saint Lazare

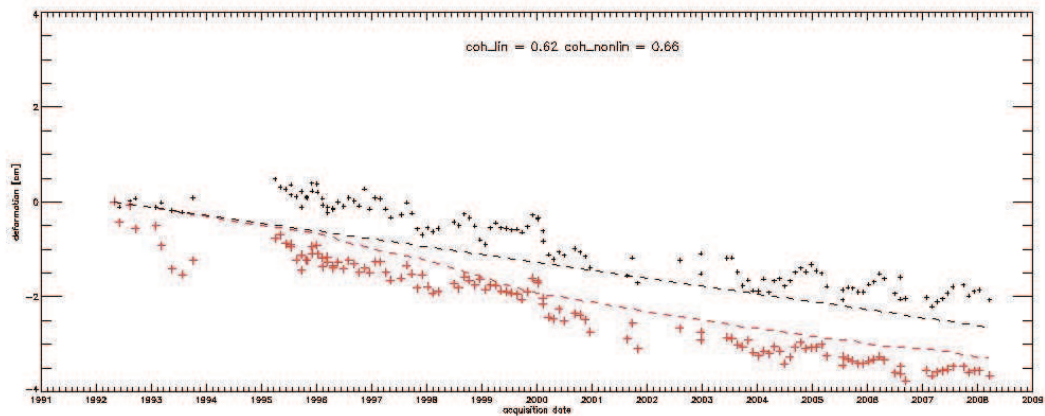
Finally, in figures 4.4.20 and 4.4.21 are presented the last area of analysis, which is located in the vicinity of Saint Lazare train station. Again, in figure 4.4.18 are presented both SPN model coherences jointly with the mean reflectivity image. It can be observed, as in the previous studied cases, that the green color prevails, indicating the increase of coherence achieved by the new processing.

The estimated deformation time series of some points can be compared in order to evaluate the enhancements of the new methodology. The result can be observed in figure 4.4.21.

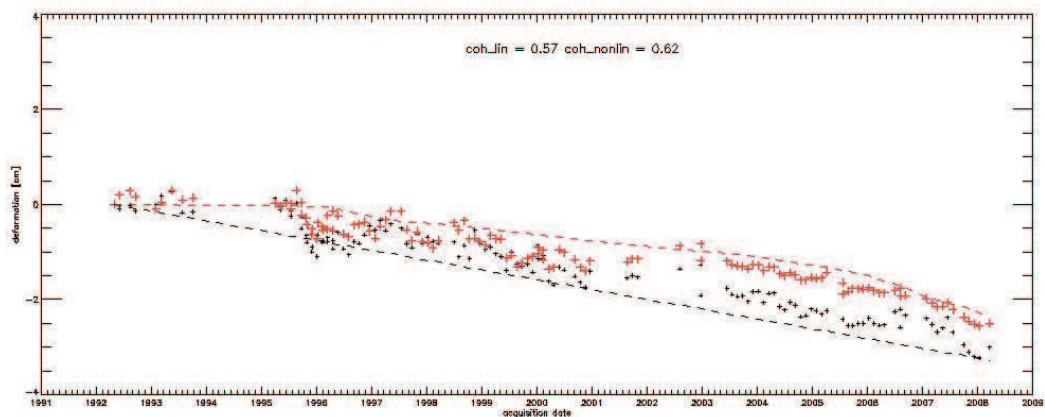
This is the most complicated test area of the three ones. As it can be appreciated in the deformation profiles presented in figure 4.4.21, the ground deformation shows a high non-linearity indicated at least by the different rates over the observations. First there is a high amplitude subsidence (from 1992 to 1995), then a small period of stability (from 1995 to 1998), then a sudden uplift (mid 98), and finally the last years presenting a period of stability. This is a very difficult



(1)



(2)



(3)

Figure 4.4.19: Deformation time series estimated for the points highlighted in figure 4.4.18. In black is presented the deformation profile obtained with classical SPN and in red the one for the new non-linear SPN processing. The discontinuous lines represent the used functional model to unwrap the phases.

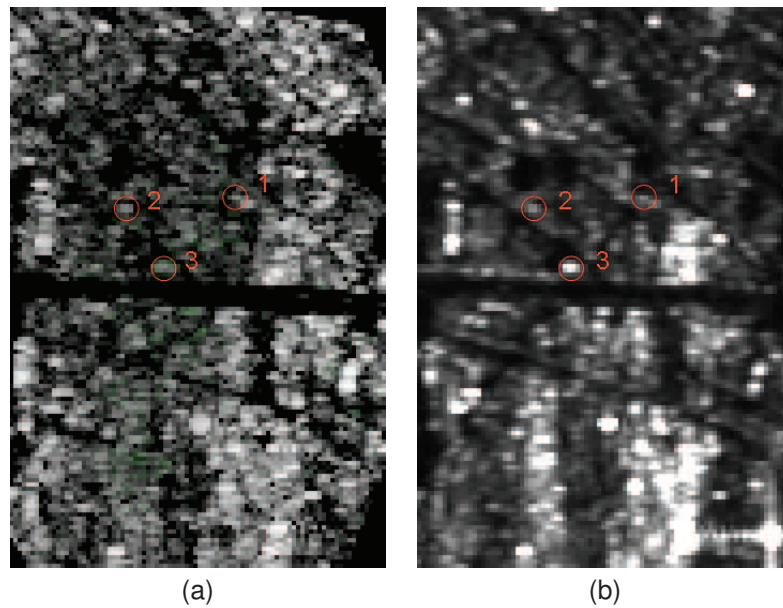
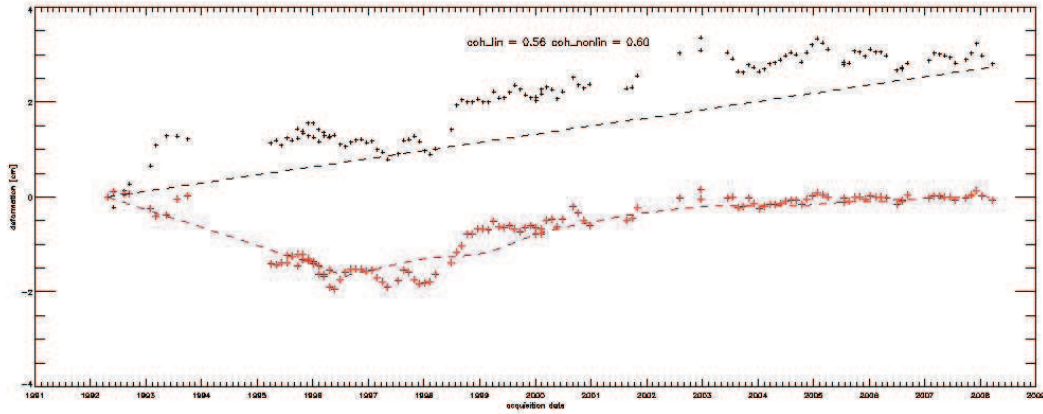


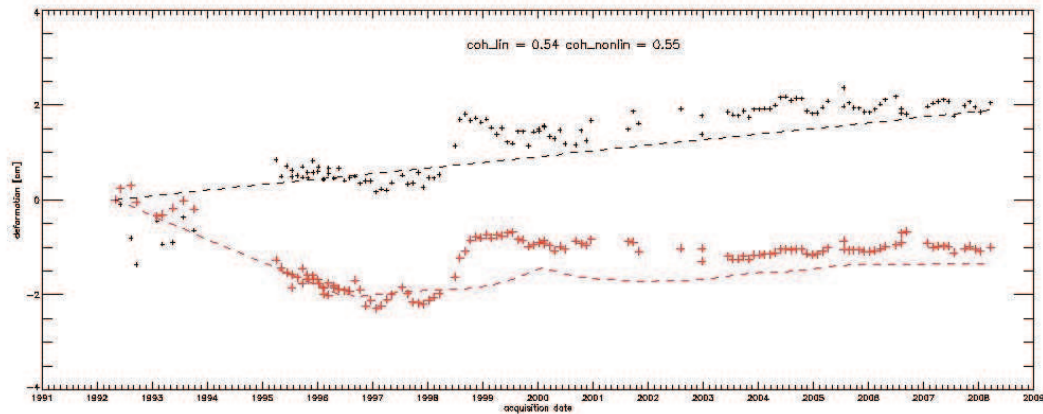
Figure 4.4.20: a) RGB image with the SPN model coherence for the linear and the non-linear processing for the first area as depicted in figure 4.4.15, the area of the Saint Lazare train station. Magenta means that the linear model gives a higher coherence and green vice-versa. Grey values means that both have exactly the same value. b) Mean reflectivity image of the same area.

time evolution to monitor with the time series obtained by means of a linear model. The major drawback here is that the new coherence is not so high with respect the classical SPN one. Most probably, as it is an area affected by constructions, the scatterers over the ground surface are suffering some changes. This results into an increase of noise in the estimated time series, as demonstrated by the deformation values detected by the first acquisitions in 1992 up to 1994 in figure 4.4.21.

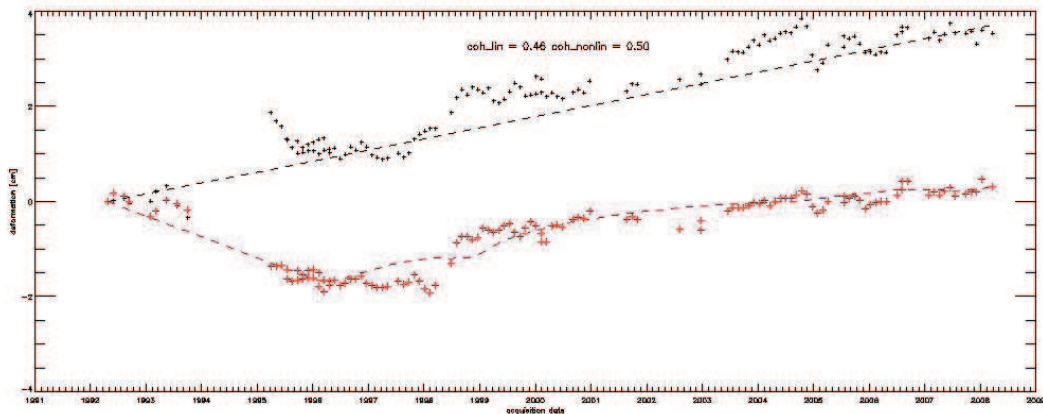
As general conclusion it can be stated that the new methodology allows the monitoring of non-linear deformations better than classical SPN, especially for large time periods of analysis. Furthermore, the final model coherence increases slightly, the improvement depending on the changes occurring during the observed period. For this reason, a better detection of scatterers are expected for areas with deformations when applying a threshold over the model coherence.



(1)



(2)



(3)

Figure 4.4.21: Deformation time series estimated for the points highlighted in figure 4.4.20. In black is presented the deformation profile obtained with classical SPN and in red the one for the new non-linear SPN processing. The discontinuous lines represent the used functional model to unwrap the phases.



## Chapter 5

# Summary and Conclusions

The main objective of this PhD was completely achieved: the development of a new PSI estimation methodology to monitor non-linear ground deformations based on a large stacking of SAR data. The starting point of this work was the PSI technique developed by Altamira Information, called Stable Point Network technique. The main limitations and drawbacks of this methodology were identified and studied in order to develop a new estimation methodology which best fits and enhances the actual one.

Persistent scatterer interferometry is based on conventional synthetic aperture radar interferometry (InSAR). Chapter 2 briefly reviews the basic principles of SAR, classical InSAR and Differential InSAR. The main InSAR applications and drawbacks are also briefly reviewed at the end of this chapter. PSI appears to overcome some of the InSAR limitations. Chapter 3 describes the principles of this type of technique and a summary of the state of the art. Under a general point of view, the base of PSI is a stacking of acquisitions of the same ground area. The basis is the identification of resolution cells which keep the reflection properties within the entire dataset. Then, over those targets a phase analysis is performed in order to extract the contribution of several artifacts: the atmospheric contribution; the vertical height and possible deformation affecting the ground targets. The way in which these contributions are separated sets the main difference between all the existing PSI techniques.

Chapter 3 also introduces SPN, which is the Altamira Information's PSI technique and the base of the developments performed in this work. SPN is based on a phase model fitting to a linear model of deformation in space and time to detect which resolution cell is a PS or not. This has been demonstrated to be a good approximation for small periods of analysis (few years) or for moderate changes in trends of the deformation in time. Especially in pure urban areas where the density of PSs is very high and possible deformations are highly sampled. Thus, the deformation gradient between nearby points may be gradual, allowing a proper monitoring with the linear model. Finally, at the end of the processing SPN is able to estimate with more detail the time evolution of the deformation, recovering the appropriate deformation pattern even if the functional model is based on a linear one.

Finally, Chapter 4 covers the main developments with respect to the classical SPN linear model processing. This chapter is the core of this PhD. The main objective of these enhancements is

the system suitability of the complete processing chain for detecting and monitoring non-linear deformations, especially for long periods of analysis.

The first important improvement is related to the automatic evaluation and quality control of the coregistration procedure of all the stacking of SLCs into the super master geometry. A new methodology is presented based on the analysis of the inter-pixel position of the peak of the main lobe of the SAR amplitude response of some high quality and stronger targets distributed over all the swath. A methodology for detecting these super-targets is also presented highlighting and comparing their SAR impulsional response function with the one given for an ideal target. Some practical cases were discussed in order to highlight the potential of this methodology for detecting possible problems during the processing and the handling of the SLCs. It was demonstrated that in case of no errors, the inter-pixel position for these super-targets should be preserved within the stacking of coregistered SLCs, at least under a precision of about 0.1 pixel.

The second improvement described is the enhancement of the methodologies for detecting PSs or stable points for performing the deformation measurements. From one side it was demonstrated that it is possible to improve the initial mask of PS-like pixels based on the radiometric analysis of the stacking of SLCs by means of enhancing the relative image calibration procedures. This is performed by means of the estimation of a relative offset between images computed in some particular areas of the images. This calibration constant can be refined by an iterative estimation procedure performed only over the selected PSs. These values converge up to a stabilized constant estimated with a dispersion of less than 0.1 dBs. These new constants enhance the final mask of PSs by increasing the total amount of pixels selected as PSs and by reducing the number of false detections. Furthermore, the multimean reflectivity image is radiometrically enhanced, showing more roughness and textures as well as a better radiometric contrast between the different types of ground reflections.

This subsection also demonstrates that not all the pixels selected as PSs are related directly to the reflection of a ground object. It was presented that there are some SAR artifacts (originated during the SAR processing) which could originate ambiguous interferometric measurements. Basically, the range side lobes and the azimuth ambiguities of strong targets are the two main sources of ambiguities in SAR signal processing considered in this work. Within this subsection it was presented that it is possible to perform a classification of the SAR impulsional response of strong targets. Thus, the measurement may be kept only for the pixels in correspondence with the center of the main lobe. The other ones can be discarded without losing detection capabilities in the estimation of ground deformations. Thus, the density of detected PS-like pixels is optimized to a more realistic value.

One original and important point of this section is the performance of an study to analyze the affectation of the SAR azimuth ambiguities in PSI. That was done by processing a stacking of level 0 images with and without filtering the Doppler bandwidth in order to highlight the presence of azimuth ambiguities within the stacking of SLCs. It is demonstrated by means of practical cases that even if they can be observed in the interferograms, they cannot be properly modeled within SPN. In consequence, their model coherence is very low and they would never be selected as good points of measurements.

The third major improvement concerns the enhancement of the estimation procedures within the SPN processing. This improvement comes by weighting the input data (the interferograms). It is demonstrated that by means of the computation of the variogram it is possible to characterize

the level of phase variability presented on each SLC due to the different phase delay introduced by the atmospheric artifacts, the thermal noise, the processing noise and/or the orbit inaccuracies. Then, each SLC can be properly weighted when it forms part of an interferogram. This non-uniform weight of the observation results into an enhancement of the robustness and into an increase of the precision when performing the phase model fitting and the estimation of the time series of deformation.

Finally, the last subsection of Chapter 4 addresses the main improvement achieved within this PhD. The adaptation of the processing methodology to detect and monitor non-linear ground deformation for long periods of analysis. This work was conducted in several steps. First, the SPN model coherence and its performances were analyzed by means of the development of a simulated scenario. This simulator considers the phase model adjustment performed over an hypothetical arc of the SPN network, a relation between two nearby PSs-like pixels. Thus, based on a set of acquisitions the relative DInSAR phase between those two nearby samples is synthesized. The simulator allows to account for some temporal and geometric decorrelation plus an additional normal noise per acquisition (atmosphere) in order to evaluate the affectation of the interferometric sampling (with noise) versus the simulated ground deformation. Then, the SPN phase model fitting procedure was characterized by means of statistics simulations of the same scenario. In particular, the behavior, the precision and the accuracy of the model coherence in function of the noise level and in function of the number of acquisitions. As a main conclusion, it can be stated that the larger the dataset the better the final achieved precision. However, using all the available interferograms does not necessarily increase the accuracy. The selection of the optimum combination list of data should account for the temporal and the geometric decorrelation presented by the analyzed ground surface.

Afterward, the performances of this model function is analyzed in function of different ground deformation profiles, which in some cases differ from the linear model. It is demonstrated by means of simulations that in the case of short periods of analysis the SPN estimation procedure succeeds, allowing to monitor up to three changes of trend in case of noise free conditions. However, with the presence of noise, the performances decrease drastically resulting in a lost of coherence. It is demonstrated by means of real examples how to detect these out-of-model cases in space and in time domains. Under some particular conditions (ground deformation with certain correlation in space) it is possible to observe a gradual decrease of the SPN model coherence in the slant range domain in presence of non-linear movements. In addition, aliasing in time domain can be perceived in the estimated time series of deformation when large changes are occurring. In fact, by ordering the interferometric phase residuals in time, it is possible to identify some correlation of the larger phase residuals with the change of trend in the analyzed ground deformation by means of the use of the developed simulator.

Finally, the end of Chapter 4 presents the new model fitting methodology. First, from a theoretical point of view, by means of the use of the developed simulator and then by applying it to a real test site. The new methodology expands the model coherence function of the classical SPN from 1-D (possible mean linear rate of deformation) to 2-D (possible linear rate in function of the time).

The theory of splitting the time periods into small ones has been corroborated by means of its application in several test cases with real data. One example is the analysis of the evolution of the deformation pattern in the city of New Orleans before and after the hurricane Katrina in August 2005. Two different SPN processing were performed before and after the hurricane obtaining a

completely different deformation pattern which could not be detected in case of analyzing the whole period. Another test site is presented by using a large stacking of ENVISAT data over the city of Paris which covers a very long period of analysis (from 1992 up to mid 2008) with an almost regular sampling every 35 days. The division of the total time period into three parts has introduced some important improvements in the detections of ground deformations. Thus, different deformation patterns arise within this pure urban area of analysis, which in some cases presents strong non-linear profiles.

To complete this work, the new non-linear methodology is applied to the city of Paris in order to evaluate its performances with real data. Three main areas presenting moderate deformations are analyzed with more details by means of the comparison of the results obtained with the new methodology and with the classical one. The obtained results show that the model coherence increases thanks to the use of an advanced model of deformation, but not so much as it was expected at the beginning. Meaning that the phase noise dominates this evaluation of the model coherence. Nevertheless, the shape of the new deformation time series corroborates the improvements by presenting less dispersion in all the cases.

As main conclusion it can be stated that the objectives of this PhD were achieved. Firstly, the main limitations and drawbacks of SPN were identified. Secondly, new PSI methodologies and procedures were developed to improve the robustness, the processing quality control and the PS identification and selection within the technique. Finally, the most important accomplishment was the development of a new estimation methodology to monitor non-linear ground deformations, especially for long periods of analysis.

# Bibliography

- [Ada03] N. Adam, B. Kampes, M. Eineder, J. Worawattanamateekul, and M. Kircher. The development of a scientific persistent scatterer system. *ISPRS Workshop High Resolution Mapping from Space*, 2003.
- [Ada04] N. Adam, B. Kampes, and M. Eineder. The development of a scientific persistent scatterer system: Modifications for mixed ers/envisat time series. *In ENVISAT ERS Symposium*, 6-10 September 2004.
- [All83] D. Allan, T. *Satellite Microwave Remote Sensing*. Ellis Horwood Series in Marine Science, Chichester, 1983.
- [All89] R. Allen and K. Kennedy. Mapping small elevation changes over large areas: differential radar interferometry. *J Geophys Res*, vol. 94(B7):pp. 9183–9191, July 1989.
- [ALT] ALTAMIRA. Altamira information webpage. [Http://www.altamira-information.com](http://www.altamira-information.com).
- [Alt04] Altamira and et al. Development of algorithms for the exploitation of ers-envisat using the stable points network. Tech. rep., Final report, ESA Contract No. 16702/02/I-LG, 2004.
- [Arm89] M. Armstrong, editor. *Geostatistics, volumes 1 and 2*. Iuwer Academic Publishers, 1989.
- [Arn97] A. Arnaud. *Etude et analyse des artefacts dans la construction de l'image interferometrique radar*. Ph.D. thesis, LIMA-IRIT (ENSEEIHT), March 1997.
- [Arn03] A. Arnaud, N. Adam, R. Hanssen, J. Inglada, J. Duro, J. Closa, and M. Eineder. Asar ers interferometric phase continuity. *International Geoscience and Remote Sensing Symposium*, 21-25 July 2003.
- [Bam98] R. Bamler and R. Hartl. Synthetic aperture radar interferometry. *Inverse Problems*, vol. R1-R54(14), 1998.
- [Bec63] P. Beckman and A. Spizzichino, editors. *The scattering of electromagnetic waves from rough surfaces*. Artech House Books, 1963.
- [Ber02] P. Berardino, G. Fornaro, R. Lanari, and E. Sansosti. A new algorithm for surface deformation monitoring based on small baseline differential sar interferograms. *IEEE Transactions on Geoscience and Remote Sensing*, vol. 40(11):pp. 2375–2383, 2002.
- [Bov02] F. Bovenga, A. Refice, and R. Nutricato. Automated calibration of multi-temporal ers sar data. *Proc IGARSS 2002*, vol. 6:pp. 3655–3657, 24-28 June 2002.

- [CEO93] CEOS. Sar calibration sub-group, in ceos sar calibration workshop. *ESTEC, Noordwijk, The Netherlands 20-24 Sept, 1993*.
- [CNE98] CNES. Philosophy and instructions for use of the diapasoninterferometry software. *System Developed at CNES, Centre National d Etudes Spatiales, Toulouse, France, 62 pp, 1998*.
- [Col03] C. Colesanti, A. Ferretti, F. Novali, C. Prati, and F. Rocca. Sar monitoring of progressive and seasonal ground deformation using the permanent scatterers technique. *IEEE Transactions on Geoscience and Remote Sensing*, vol. 41(7):pp. 1685–1701, 2003.
- [Coo67] E. Cook, C. and M. Bernfeld. Radar signals: An introduction to theory and applications. *Academic Press, 1967*.
- [Cos96] M. Costantini. A phase unwrapping method based on network programming. *FRINGE 96 ESA Workshop on Applications of ERS SAR Interferometry, 1996*.
- [Cre91] N. Cressie, editor. *Statistics for Spatial Data*. John Wiley and Sons, New York, 1991.
- [Cro08] M. Crosetto, E. Biescas, J. Duro, J. Closa, and A. Arnaud. Generation of advanced ers and envisat interferometric sar products using the stable point network technique. *Photogrammetric engineering and remote sensing*, vol. 74(4):pp. 443–450, 2008.
- [CSAa] CSA. Delta projects. [Http://www.asc-csa.gc.ca/eng/programs/eoadp/article.asp](http://www.asc-csa.gc.ca/eng/programs/eoadp/article.asp).
- [CSAb] CSA. Radarsat-1 satellite information and sar products. [Http://www.asc-csa.gc.ca/eng/satellites/radarsat1/default.asp](http://www.asc-csa.gc.ca/eng/satellites/radarsat1/default.asp).
- [Cum05] G. Cumming, I. and H. Wong, F., editors. *Digital processing of synthetic aperture radar data*. Artech House, 2005.
- [Cur91] J. Curlander and R. McDonough, editors. *Synthetic aperture radar: systems and signal processing*. John Wiley and Sons, Inc, 1991.
- [Dav96] W. Davidson, G. and R. Bamler. Robust 2-d phase unwrapping based on multiresolution microwave sensing and synthetic aperture radar. (*Proc SPIE*) ed G Franceschetti, C J Oliver, F S Rubertone and S Tajbakhsh, pp. 226–37, 1996.
- [Dur03] J. Duro, J. Inglada, J. Closa, N. Adam, and A. Arnaud. High resolution differential interferometry using time series of ers and envisat sar data. *FRINGE 2003*, 1-5 December 2003.
- [Dur05] J. Duro, J. Inglada, J. Closa, N. Adam, and A. Arnaud. High resolution differential interferometry using time series of ers and envisat sar data. *In ENVISAT ERS Symposium*, vol. 572, Apr 2005.
- [Dur07a] J. Duro, G. Cooksley, N. Miranda, and A. Arnaud. Ambiguous psi measurements. *In ENVISAT ERS Symposium*, 23-27 April 2007.
- [Dur07b] J. Duro, M. Sanchez, N. Miranda, G. Cooksley, and A. Arnaud. Spn examples of subsidence monitoring and validation. *Proc of the 7th Geomatic Week Conference*, Feb 2007.

- [Dur08] J. Duro, E. Biescas, D. Albiol, and A. Arnaud. Innovative research and development into the application of radarsat interferometric data for subsidence mapping in new orleans. *PECORA 17 symposium*, 19 Nov 2008 2008.
- [Ela88] C. Elachi. Spaceborne radar remote sensing: Applications and techniques. *IEEE Press*, 1988.
- [ESAA] ESA. Ers-1/2 satellite information and sar products. [Http://earth.esa.int/ers/](http://earth.esa.int/ers/).
- [ESAB] ESAPSIC4. Esa's psic4 project. <http://earthesaint/psic4/>.
- [Fer99a] A. Ferretti, C. Prati, and F. Rocca. Non-uniform motion monitoring using the permanent scatterers technique. In *Second International Workshop on ERS SAR Interferometry, FRINGE99*, pp. 1–6, 10-12 Nov 1999.
- [Fer99b] A. Ferretti, C. Prati, and F. Rocca. Permanent scatterers in sar interferometry. *International Geoscience and Remote Sensing Symposium*, pp. 1–3, 28 June-2 July 1999.
- [Fer00] A. Ferretti, C. Prati, and F. Rocca. Nonlinear subsidence rate estimation using permanent scatterers in differential sar interferometry. *IEEE Transactions on Geoscience and Remote Sensing*, vol. 38(5):pp. 2202–2212, September 2000.
- [Fer01] A. Ferretti, C. Prati, and F. Rocca. Permanent scatterers in sar interferometry. *IEEE Transactions on Geoscience and Remote Sensing*, vol. 39(1):pp. 8–20, January 2001.
- [Fis06] J. Fischer, I. Pupeza, and R. Sheiber. Sidelobe suppression using the sva method for sar images and sounding radars. *EUSAR 2006, Dresden*, 2006.
- [Fly97] T. J. Flynn. Two-dimensional phase unwrapping with minimum weighted discontinuity. *J Opt Soc Am*, vol. A(14):pp. 2692–701, 1997.
- [Fra99] G. Franceschetti and R. Lanari, editors. *Synthetic Aperture Radar processing*. CRC Press, 1999.
- [Gab88] K. Gabriel, A. and M. Goldstein, R. Crossed orbit interferometry: theory and experimental results from sir-b. *Int J Remote Sens*, vol. 9(5):pp. 857–872, 1988.
- [Gat94] F. Gatelli, A. Guarnieri, F. Parizzi, P. Pasquali, C. Prati, and F. Rocca. The wavenumber shift in sar interferometry. *IEEE Trans Geosci Remote Sensing*, vol. 32(4):pp. 855–865, July 1994.
- [Ghi94] D. Ghiglia and L. Romero. Robust two-dimensional weighted and unweighted phase unwrapping that uses fast transforms and iterative methods. *Jor of the Optical Society of America*, vol. A(11):pp. 107–117, 1994.
- [Gol] R. Goldstein, H. Zebker, and C. Werner. Satellite radar interferometry: Two dimensional phase unwrapping. *Radio Science*, vol. 23(4):pp. 713–720.
- [Gol93] R. Goldstein, H. Engelhardt, B. Kamb, and R. Frolich. Satellite radar interferometry for monitoring ice sheet motion: Application to an antarctic ice stream. *Science*, vol. 262:pp. 1525–1530, 1993.
- [Gra74] L. C. Graham. Synthetic interferometer radar for topographic mapping. *Poc IEEE*, vol. 62 763 8, 1974.

- [Gua03] M. Guarnieri, A. and D. D'Aria. Wide-angle azimuth antenna pattern estimation in sar images. *Proceedings IEEE International Geoscience and Remote Sensing Symposium, IGARSS '03*, vol. 5:pp. 3105–3107, 2003.
- [Gua05] M. Guarnieri, A. Adaptive removal of azimuth ambiguities in sar images. *IEEE trans geosci remote sensing*, vol. 43(3):pp. 625– 633, 2005.
- [Han01] R. Hanssen, editor. *Radar Interferometry: data interpretation and error analysis*. Kluwer Academic Publishers, Dordrecht, Holland, 2001.
- [Her09] G. Herrera, C. Davalillo, J., J. Mulas, G. Cooksley, O. Monserrat, and V. Pancioli. Mapping and monitoring geomorphological processes in mountainous areas using psi data: Central pyrenees case study. *Natural Hazards and Earth System Science*, vol. 9(5):pp. 1587–1598, 2009.
- [Her09] G. Herrera and et al. Validation and comparison of advanced differential interferometry techniques: Murcia metropolitan area case study. *ISPRS Journal of Photogrammetry and Remote Sensing*, vol. 64(5):pp. 501–512, 209.
- [Hoo04] A. Hooper, H. Zebker, P. Segall, and B. Kampes. A new method for measuring deformation on volcanoes and other non-urban areas using insar persistent scatterers. *Geophysical Research Letters*, vol. 31:L23611, doi:10.1029/2004GL021737, December 2004.
- [Hu06] J. Hu, M. Huang, G. Cooksley, J. Duro, A. Arnaud, B. Fruneau, and B. Deffontaines. Neotectonic deformation in sw taiwan as deduced from persistent scatterers sar interferometry and geodetic observation. *AGU Fall Meeting Abstracts*, pp. D534+, dec 2006.
- [Hun79] B. Hunt. Matrix formulation of the reconstruction of phase values from phase differences. *Jor of the Optical Society of America*, (69):pp. 393–399, 1979.
- [Jac00] H. Jackson, I. Sinclair, and S. Tam. Envisat/asar precision transponders. *Journal: SAR Workshop: CEOS Committee on Earth Observation Satellites; Working Group on Calibration and Validation, Proceedings of a Conference held 26-29 October 1999, Toulouse, France*, vol. 450:p. 311, 2000.
- [Jou95] I. R. Joughin, D. Winebrenner, and M. Fahnestock. Observation of complex ice-sheet motion in greenland using satellite radar interferometry. *Geophys Res Lett*, vol. 22:pp. 571–574, 1995.
- [Kam04] B. Kampes and R. Hanssen. Ambiguity resolution for permanent scatterer interferometry. *IEEE trans geosci remote sensing*, vol. 42(11):pp. 2446–2453, 2004.
- [Koh03] O. Kohlhase, A., L. Feigl, K., D. Massonnet, and A. Ferretti. Estimating orbital trajectories from fringe gradients in sar interferograms for measuring crustal strain. *Proc IGARSS*, vol. 6:pp. 3808–3810, 2003.
- [Kra96] R. Kramer and O. Loffeld. Presentation of an improved phase unwrapping algorithm based on kalman filters and combined with local slope estimation. *FRINGE'96 : ESA Workshop on Application of ERS SAR Interferometry*, 1996.

- [Lau98] H. Laur, P. Bally, P. Meadows, J. Sanchez, B. Schaettler, E. Lopinto, and D. Esteban. Derivation of the backscattering coefficient in ers sar pri products. Tech. rep., ESA Technical Report No. ES-TN-RS-PM-HL09, September 2002, <http://earth.esa.int/ESC2>, 1998.
- [Lee90] T. Lee, D. and J. Schachter, B. Two algorithms for constructing a delaunay triangulation. *Int J of Computer and Information Sci*, vol. 9:pp. 219–242, 1990.
- [Li83] K. Li, F. and T. K. Johnson, W. Ambiguities in spaceborne synthetic aperture radar systems. , *IEEE Transactions on Aerospace and Electronic Systems*, vol. AES-19(3):pp. 389 – 397, 1983.
- [Lom76] N. R. Lomb. Least-squares frequency analysis of unequally spaced data. *Astrophysics and Space Science*, vol. 39:pp. 447–462, 1976.
- [Mas85] D. Massonnet and T. Rebaute. Etude de principe d'une detection de mouvements tectoniques par radar. Tech. rep., Centre National d'Etudes Spatiales, 1985.
- [Mas93a] D. Massonnet and T. Rebaute. Radar interferometry: Limits and potential. *EEE Trans Geosci Remote Sens*, pp. 455–464, 1993.
- [Mas93b] D. Massonnet, M. Rossi, C. Carmona, F. Adragna, G. Peltzer, K. Feigl, and T. Rabaute. The displacement field of the landers earthquake mapped by radar interferometry. *Nature*, vol. 364(8):pp. 138–142, July-8 1993.
- [Mas08] D. Massonnet and C. Souyris, editors. *Imaging with synthetic aperture radar*. EFPL Press, 2008.
- [Mir03] N. Miranda, B. Rosich, C. Santella, and M. Grion. Review of the impact of ers-2 piloting modes on the sar doppler stability. *Proceedings of the FRINGE 2003 Workshop*, p. 12.1, 2003.
- [Mor93] A. Moreira. Suppressing the azimuth ambiguities in synthetic aperture radar images. *IEEE trans geosci remote sensing*, vol. 31(4):pp. 885–895, 1993.
- [Mor01] O. Mora, J. Mallorqui, J. Duro, and A. Broquetas. Long-term subsidence monitoring of urban areas using differential interferometric sar techniques. *In International Geoscience and Remote Sensing Symposium*, p. 3, 9-13 July 2001.
- [Mor03] O. Mora, J. Mallorqui, and A. Broquetas. Linear and nonlinear terrain deformation maps from a reduced set of interferometric sar images. *IEEE Transactions on Geoscience and Remote Sensing*, vol. 41(10):pp. 2243–2253, 2003.
- [NAS] NASA. Advanced spaceborne thermal emission and reflection radiometer. <Http://asterweb.jpl.nasa.gov/>.
- [Pep06] A. Pepe and R. Lanari. On the extension of the minimum cost flow algorithm for phase unwrapping of multitemporal differential sar interferograms. *IEEE trans geosci remote sensing*, vol. 44(9):pp. 2374–2383, 2006.
- [Pra90a] C. Prati, M. Giani, and N. Leuratti. Sar interferometry: A 2-d phase unwrapping technique based on phase and absolute values informations. *Proc IGARSS*, vol. 90:p. 2043, 1990.

- [Pra90b] C. Prati, F. Rocca, A. Guarnieri, and E. Damonti. Seismic migration for sar focussing: Interferometrical applications. *IEEE Trans Geosci Remote Sensing*, vol. 28(4):pp. 627–640, 1990.
- [Pre07] H. Press, W., A. Teukolsky, S., T. Vetterling, W., and P. Flannery, B., editors. *Numerical Recipes 3rd Edition: The Art of Scientific Computing*. Cambridge University Press, 2007.
- [Pri96] M. Pritt. Phase unwrapping by means of multigrid techniques for interferometric sar. *IEEE Trans on Geosc and Remote Sensing*, (34):pp. 728–738, 1996.
- [Rei97] A. Reigber and J. Moreira. Phase unwrapping by fusion of local and global methods. *Int Geosc and Remote Sensing Symp IGARSS'97*, pp. 869–71, 1997.
- [Ros] B. Rosich, R. Torres, I. Navas, A. Monti-Guarnieri, and P. Meadows. Asar calibration performance: A review after four years of operation. *6th European Conference on Synthetic Aperture Radar (EUSAR 2006), 16-18 May 2006, Dresden, Germany*.
- [Sch] M. Schwerdt, D. Schrank, M. Bachmann, C. Schulz, J. Doring, B., and J. Hueso. Terrasar-x re-calibration and dual receive antenna campaigns performed in 2009. *8th European Conference on Synthetic Aperture Radar (EUSAR 2010), 7-10 June 2010, Aachen, Germany*.
- [Sch93] G. Schreier, editor. *SAR Geocoding: data and systems*. Wichman, 1993.
- [Sue02] M. Suess, S. Riegger, W. Pitz, and R. Werninghaus. Terrasar-x - design and performance. *Proc of EUSAR2002*, 2002.
- [Tis06] C. Tison, J. Souyris, and N. Clerc-Renaud. Point target behaviour in high resolution sar images: time-frequency versus polarimetric analysis. *EUSAR*, 2006.
- [Usa97] S. Usai. The use of man-made features for long time scale insar. *In International Geoscience and Remote Sensing Symposium*, pp. 1542–1544, 3-8 August 1997.
- [Usa99] S. Usai and R. Klees. Sar interferometry on very long time scale: A study of the interferometric characteristics of man-made features. *IEEE Transactions on Geoscience and Remote Sensing*, vol. 37(4):pp. 2118–2123, 1999.
- [Usa00] S. Usai and R. Klees. An analysis of the interferometric characteristics of anthropogenic features. *IEEE Transactions on Geoscience and Remote Sensing*, vol. 38(3):pp. 1491–1497, 2000.
- [Wer03] C. Werner, U. Wegmuller, T. Strozzi, and A. Wiesmann. Interferometric point target analysis for deformation mapping. *In International Geoscience and Remote Sensing Symposium*, p. 3, 21-25 July 2003.
- [Xu96] W. Xu and I. Cumming. A region growing algorithm for insar phase unwrapping. *Int Geosc and Remote Sensing Symp IGARSS'96*, pp. 4493–9, 1996.
- [Zeb86] H. Zebker and R. Goldstein. Topographic mapping from interferometric sar observation. *Journal of Geophysical Research*, vol. 91(B5):pp. 4993–4999, April-10 1986.
- [Zeb92] H. Zebker and J. Villasenor. Decorrelation in interferometric radar echoes. *IEEE Trans Geosci Remote Sensing*, vol. 30(5):pp. 950–959, September 1992.

- [Zeb94] H. Zebker, P. Rosen, R. Goldstein, A. Gabriel, and C. Werner. On the derivation of coseismic displacement fields using differential radar interferometry: the landers earthquake. *JGR Earth*, May 1994.